Regulation of Cardiac Signaling and Excitability

By

Lu Ren

DISSERTATION

Submitted in partial satisfaction of the requirements for the degree of

DOCTOR OF PHILOSOPHY

in

Molecular, Cellular, and Integrative Physiology

in the

OFFICE OF GRADUATE STUDIES

of the

UNIVERSITY OF CALIFORNIA

DAVIS

Approved:

_____

(Nipavan Chiamvimonvat, MD), Chair

_____

(Manuel F. Navedo, PhD)

_____

(Vladimir Yarov-Yarovoy, PhD)

_____

(Eleonora Grandi, PhD)

Committee in Charge

2021

Acknowledgement

I would like to acknowledge American Heart Association for the predoctoral research award that funded my dissertation project as well as University of California, Davis for awarding me the Dissertation-Year Fellowship. I would like to thank UC Davis and MCIP program for the opportunities I was given for personal and professional growth. In addition, I would like to express my gratitude to all the professors in my MCIP courses, my academic advisors, my qualifying examination committee members and collaborators.

I would especially like to express my sincerest appreciation and deepest gratitude to my major professor, Dr. Nipavan Chiamvimonvat, who has provided incredible support and guidance throughout my graduate education. I would like to thank my dissertation committee members, Drs. Manuel F. Navedo, Vladimir Yarov-Yarovoy, and Eleonora Grandi, whose expertise and advice have been invaluable to my research during my PhD study.

I would also like to acknowledge Drs. Luis Fernando Santana, Claudia M. Moreno, Yang Kevin Xiang, Chao-Yin Chen, Ebenezer N. Yamoah, Xiao-Dong Zhang, Deborah Lieu, Phung N. Thai and Raghavender Reddy Gopireddy for their continued support. I would also like to thank everyone in the Chiamvimonvat lab who has helped me with administrative work, training, and experiments.

Finally, I am forever grateful to my parents for their indescribable and unrelenting support in all aspects of my life and my friends for their enthusiastic encouragement.

Table of Contents

Lu Ren
April 2021
Molecular, Cellular, and Integrative Physiology

Abstract

Background

Sinoatrial node (SAN), the primary pacemaker region in the heart, generates electrical impulses that propagates throughout the heart. SAN activity is tightly regulated by β-adrenergic receptor (β-AR) signaling with adenylyl cyclase (AC) as a key enzyme. However, the main isoform of AC and its functional roles in regulating SAN function remain incompletely understood. SAN dysfunction is well documented in patients with heart failure (HF), but the underlying mechanisms are not fully determined. Additionally, the critical roles of endoplasmic reticulum (ER)-associated degradation (ERAD) in the regulation of cardiac ion channel function in health and disease are only beginning to be recognized.

To this end, we have identified several critical knowledge gaps in our current understanding of the regulation of cardiac excitability in health and disease that form the basis of my dissertation work. Specifically, we tested the hypotheses that distinct AC isoforms are preferentially expressed in the SAN and compartmentalize within critical microdomains to orchestrate heart rate regulation during β-AR signaling (Chapter 2); mitochondrial dysfunction in the SAN in HF directly contribute to SAN dysfunction (Chapter 3); RNF207 regulates *human Ether-à-go-go-Related Gene* (*hERG*) K^+ channel through ER-associated degradation (Chapter 4); different human calmodulin (CaM, a ubiquitous Ca^{2+} sensing protein) mutations, linked to long QT syndrome (LQTS), a hereditary disease that predisposes patients to life-threatening cardiac arrhythmias and sudden cardiac death, disrupt small conductance Ca^{2+}-activated K^+ channel (SK) channel function by distinct mechanisms (Chapter 5).

Methods

To test the hypotheses, we utilized multi-disciplinary approaches, from electrophysiology, cell biology, high resolution imaging to *in vivo* analysis. Specifically, perforated patch-clamp, whole-cell voltage clamp recordings, single-cell RT-qPCR, co-immunoprecipitation, proximity ligation assay, immunofluorescence through confocal microscopy with high resolution Airycan mode, stimulated emission depletion (STED) super-resolution microscopy, fluorescence resonance energy transfer (FRET) imaging, whole-cell Ca^{2+} transient and sarcomere shortening measurements, confocal line scanning, echocardiography and electrocardiography (ECG) telemetry were used.

Results

We demonstrate that Ca^{2+}-activated AC_I is the predominant isoform in SAN that resides in a functional microdomain with caveolin-3, hyperpolarization-activated cyclic nucleotide-gated (HCN)4 channel, voltage-gated Ca^{2+} channel 1.2 ($Ca_v1.2$), and ryanodine receptor 2 (RyR2), and is critical in the sustained rise in local cAMP during β-AR stimulation (Chapter 2); impairment of mitochondria and their microdomain in the SAN contribute to SAN dysfunction in HF (Chapter 3); RNF207 serves an E3 ubiquitin ligase and targets misfolded $hERG_{T613M}$ mutant proteins for degradation (Chapter 4); CaM_{D96V} and CaM_{D130G} mutations linked to LQTS reduce SK currents through a dominant-negative fashion, while specific mutations of phenylalanine to leucine result in conformational changes that affect helix packing in the C-lobe of CaM (Chapter 5).

Conclusions

The cumulative work during my graduate studies has elucidated key mechanisms to help understand cardiac function in normal condition and has demonstrated key mechanisms that may

be exploited in disease. These pivotal findings establish a foundation for future work in cardiac physiology and pathophysiology.

CHAPTER 1

Review of cardiac signaling and excitability in normal and diseased hearts

Abstract

The sinoatrial node (SAN) is the primary determinant of heart rate, which generates spontaneous action potentials (APs) that propagate throughout the heart. SAN automaticity is governed by a complex system that integrates ion channels and transporters on the cell membrane (membrane clock) and calcium handling at the subcellular level (Ca^{2+} clock). The synchronization of the couple-clock system and the tight regulation by autonomic system at subcellular microdomains, enable the SAN to beat rhythmically, in response to physiological demands.

Disease conditions such as heart failure, myocardial ischemia, and mutations of cardiac ion channels and ion channel interacting proteins have been linked to impairment of pacemaker activity, cardiac function, Ca^{2+} dysregulation, cardiac arrhythmias, and sudden cardiac death. Human arrhythmia syndromes, such as Long QT Syndrome (LQTS), or electrical remodeling from cardiac hypertrophy or failure, can result from mutations or alteration in the expression of ion channel or ion channel interacting proteins as well as dysregulation of cardiac ion channels by chaperone, ion channel interacting proteins, microRNAs, or abnormal pH regulation, culminating in defects in trafficking, degradation, post-translational modifications, and function.

This Chapter will provide an overview of our current knowledge in the regulation of cardiac excitability in health and disease and attempt to outline some of the critical gaps in our knowledge that provide the basis of my dissertation work.

1. Cardiac Excitability

1.1 Cardiac Action Potentials

The average human adult heart beats approximately 72 times a minute, 100,000 times a day, 3.6 million times a year and 2.5 billion times during a lifetime[1]. The sinoatrial node (SAN) is the primary pacemaker region in the heart, which produces electrical impulses that propagates across the atria, through the atrioventricular node (AVN), Bundle of His, and Purkinje fibers to orchestrate a coordinated and effective contraction. The process of electrical excitation to cardiac contraction is termed excitation-contraction coupling.[2] Cardiac action potentials (APs) critically depend on the selective permeability of ion channels on the cell membrane. Contractile cardiac myocytes exhibit five distinct phases of the AP, including phases 0, 1, 2, 3 and 4. In contrast, APs of pacemaker cells only consist of three phases—0, 3 and 4.[3]

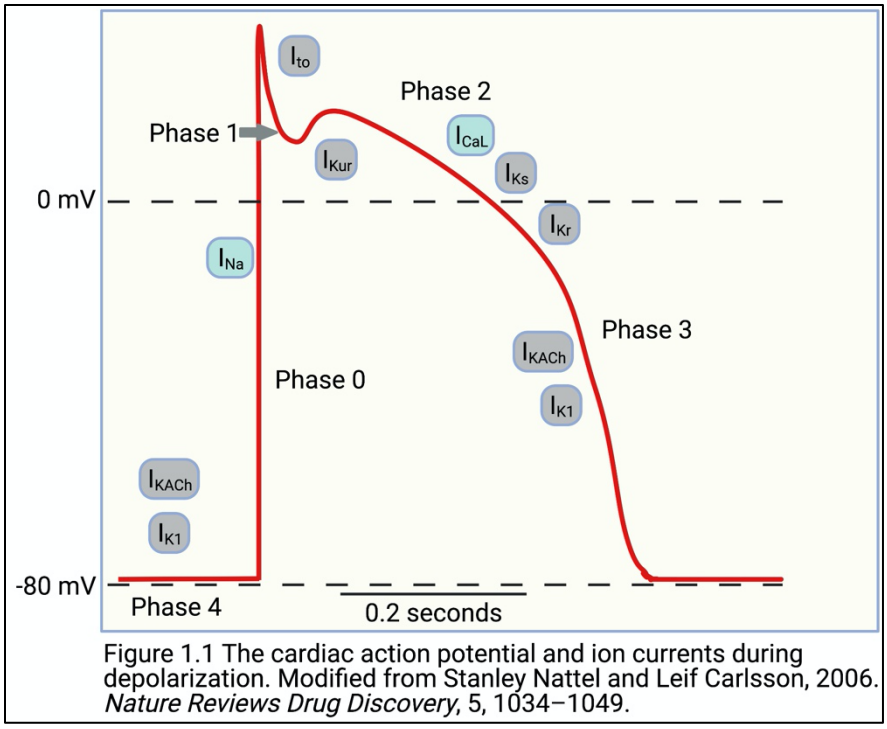

Figure 1.1 The cardiac action potential and ion currents during depolarization. Modified from Stanley Nattel and Leif Carlsson, 2006. *Nature Reviews Drug Discovery*, 5, 1034–1049.

As illustrated in **Figure 1.1**, inward currents are shown in blue boxes and outward currents are shown in gray boxes. During phase 4 or the resting potential in atrial and ventricular myocytes, the cells are impermeable to Na^+ and Ca^{2+} ions, but permeable to K^+ ions. K^+ ions flow out of the cell through the inward rectifier K^+ channel or I_{K1}, which cause the inside of the cell membrane to become more negative, establishing the resting membrane

potential close to the Nernst potential for K^+ ions (E_K). Na^+ influx through voltage-gated Na^+ channels is responsible for the rapid upstroke or phase 0 in contractile myocytes, reversing the membrane potential towards the Nernst potential for Na^+ ions (E_{Na}), leading to a more positive membrane voltage (rapid depolarization). During phase 1 of the AP, there is an early repolarization due to the activation of the transient outward K^+ current (I_{to}). This is followed by phase 2, or the plateau phase, whereby the inward Ca^{2+} and outward K^+ currents are relatively balanced. Ca^{2+} enters the cell through L-type Ca^{2+} channel as inward Ca^{2+} current, $I_{Ca,L}$, triggering Ca^{2+} release from the sarcoplasmic reticulum (SR) in a process termed Ca^{2+}-induced Ca^{2+} release (CICR). The increase of free intracellular Ca^{2+} concentration allows Ca^{2+} to bind to troponin C, which then elicits contraction.[2] This is called excitation-contraction coupling. Phase 3 of the AP is the rapid repolarization phase, which is achieved by the activation of a series of K^+ currents, including ultra-rapid (I_{Kur}) in atrial myocytes, rapidly activating (I_{Kr}), and slowly activating (I_{Ks}) delayed-rectifier currents in atrial and ventricular myocytes.[3]

In contrast, spontaneous phase 4 diastolic depolarization is a unique feature of pacemaker cells. For pacemaker cells such as SAN and AVN cells, there is pacemaker current or I_f, encoded by hyperpolarization-activated cyclic nucleotide-gated (HCN) channels. In addition to I_f, other currents contribute to phase 4 depolarization, such as delayed rectifier K^+ current, Na^+ current, Na^+/Ca^{2+} exchanger (NCX) current, and L- and T-type Ca^{2+} currents (I_{CaT}).[4] In contrast to atrial and ventricular myocytes, phase 0 of the AP in pacemaking cells are initiated by the influx through L-type Ca^{2+} currents and phase 2 is nonexistent in pacemaking cells.

1.2 SAN Automaticity

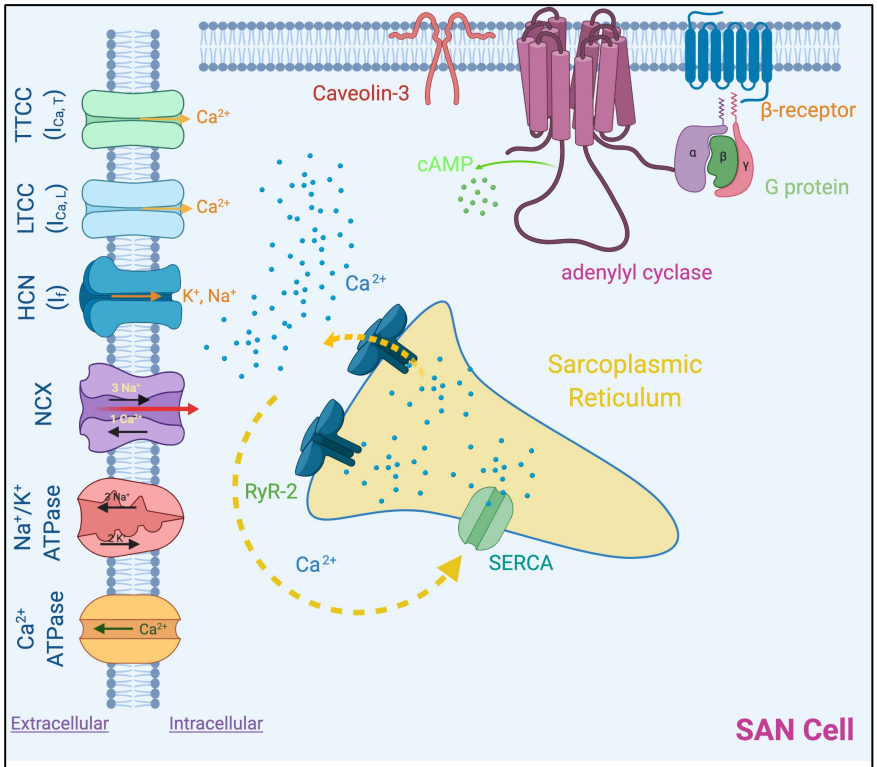

Figure 1.2 The coupled-clock pacemaker system in the SAN. Modified from Edward G. Lakatta, Victor A. Maltsev, and Tatiana M. Vinogradova, 2010. *Circ Res.* 2010 Mar 5; 106(4): 659–673.

Automaticity is a unique feature of the SAN and AVN. Since the SAN lacks a stable resting membrane potential, it is able to spontaneously generate APs. The major ion channels and transporters (and their ionic currents) involved in the pacemaker activities are the L-type Ca^{2+} channels (I_{CaL}), T-type Ca^{2+} channels (I_{CaT}), HCN channels (I_f), NCX (I_{NCX}), delayed rectifier K^+ channels (I_K), and Na^+/K^+ ATPase (I_{NaK}).[5] Spontaneous diastolic depolarization is essential for SAN automaticity. The ion channels together generate spontaneous APs, which is collectively referred to as the "membrane clock". In addition, spontaneous local Ca^{2+} releases from sarcoplasmic reticulum (SR) via ryanodine receptors (RyR-2) during diastolic depolarization induced by cyclic changes in Ca^{2+} are called the "Ca^{2+} clock".[5] Ca^{2+} entry occurs via Ca^{2+} channels, which stimulates the release of Ca^{2+} from the SR via RyR-2. Ca^{2+} is extruded via NCX, which transports 3 Na^+ in exchange for 1 Ca^{2+}, generating a net inward current, as depicted in **Figure 1.2**. The NCX current and other ion channel currents on the SAN cell membrane, synergistically function to generate SAN diastolic depolarization. The two clocks interact with each other and are modulated by Ca^{2+}, membrane

voltage, second messengers, forming a coupled-clock system.[5] G-protein coupled-receptors (GPCRs) signaling regulates pacemaker activities by affecting these modulators.

2. Adenylyl Cyclase in the SAN

The SAN is the primary determinant of heart rate[6, 7] and is tightly regulated by β-adrenergic receptor (β-AR) signaling.[8, 9] Adenylyl cyclase (AC) is a key enzyme in the β-AR pathway that converts ATP into 3-,5-cyclic adenosine monophosphate (cAMP) resulting in a cascade of downstream effects.[9-11] ACs are genetically diverse and encoded by 10 distinct genes. Nine of them are G protein-regulated transmembrane ACs (tmACs), while one is a soluble form.[10, 12] The nine tmACs feature variable N-terminal regions, followed by a six transmembrane helices domain, the first catalytic domain C_{1a}, a second six transmembrane helices domain, and the second catalytic domain C_{2a}[10]. The nine tmACs are relatively conserved in their catalytic domains[12, 13], but quite divergent outside these regions. ACs genetic diversity suggests that different isoforms may serve distinct functions in different regions of the body. ACs can be directly regulated by G proteins following the stimulation of GPCRs. Most ACs can be stimulated by $G\alpha_S$, while a subset of ACs can be inhibited via Gαi/o. (**Table 1.1**)[12] Ca^{2+} can inhibit AC_V and AC_{VI}, and stimulate AC_I and AC_{VIII} by binding to CaM. Some ACs can also be regulated by activated protein kinase, including protein kinase A (PKA), protein kinase C (PKC), and Ca^{2+}/calmodulin-dependent protein kinase (CaMK).[12]

The distribution of the AC isoforms differs significantly between the SAN and ventricular cardiomyocytes. In ventricular cardiomyocytes, AC_V and AC_{VI} are the two main isoforms.[14] In contrast, there is minimal information regarding the main AC isoforms in SAN. One study showed that AC_I is preferentially expressed in guinea pig SAN cells and modulates the funny current

(pacemaker current, I_f)[15]. Another study demonstrated that the most abundant AC isoforms in rabbit SAN are AC_I and AC_V.[16]

	G proteins			Calcium		Kinases		
Isoform	$G\alpha_s$	$G\alpha_{i/o}$	$G\beta\gamma$	Alone	CaM	PKA	PKC	CaMK
AC_I	+	-	-		+			
AC_{II}	+		+				+	
AC_{III}	+	-					+	-
AC_{IV}	+		+				+	
AC_V	+	-		-		-	+	
AC_{VI}	+	-		-		-	-	
AC_{VII}	+						+	
AC_{VIII}	+	-			+	-		
AC_{IX}	+	-						

Table 1.1[12] Regulation of transmembrane ACs by G protein, calcium and kinase signaling. +: stimulate; -: inhibit. Modified from Michelle L. Halls, Dermot M.F. Cooper. *Pharmacology & Therapeutics* 172 (2017) 171–180.

3. SAN Dysfunction in Heart Failure

Heart failure (HF) is a progressive condition that occurs when the heart can no longer generate enough cardiac output to meet the metabolic demands of the body[17]. Approximately 5.7 million people in the United States are diagnosed with HF, with 5-year mortality of greater than 50%[18]. One of the known complications that occurs in HF is bradyarrhythmia from SAN dysfunction, which significantly increases the morbidity and mortality of HF patients[19]. Patients diagnosed with

HF and SAN dysfunction have an increased risk of sudden cardiac death[18, 19]. Hence, it is imperative to develop therapies that specifically target the SAN to improve clinical outcome.

SAN is a highly complex structure consisting of specialized cells which spontaneously fire action potentials (APs) that propagate throughout the heart. Its automaticity is governed by ion channels and transporters that contribute to the membrane [20] and Ca^{2+} [21] clocks. These two cyclic processes are impaired during HF[22]. It has been shown that HCN2 and HCN4 expression are decreased at both the transcript and protein levels in a canine model of HF[23]. In rabbits with volume and pressure overload induced HF, the hyperpolarization-activated "pacemaker" current (I_f) and slow component of the delayed rectifier current (I_{Ks}) are reduced by 40% and 20%, respectively [24]. In a rat model of HF, SAN dysfunction results from an extensive remodeling of ion channels, gap junction channels, Ca^{2+}-, Na^{+}-, and H^{+}-handling proteins and receptors in the SAN[25]. These studies elegantly show the perturbations of key ion channels and transporters involved in the membrane and Ca^{2+} clocks. Table 1.2 summarized the studies on SAN dysfunction associated with HF.

No.	Year	Author	Title	Species	Intervention /disease	Results
1	2000	Opthof et al. [26]	Changes in sinus node function in a rabbit model of heart failure with ventricular arrhythmias and sudden death	rabbit	volume and pressure overload HF	Sympathetic predominance in normal rabbits is preserved in heart failure. The basic cycle length of the isolated sinus node increased.
2	2003	Verkerk et al. [24]	Ionic remodeling of sinoatrial node cells by heart failure	rabbit	volume and pressure overload-induced HF	Intrinsic cycle length ↑, I_f and I_{Ks} density↓ in HF
3	2004	Sanders et al. [19]	Remodeling of sinus node function in patients with congestive heart failure	human	symptomatic CHF	Anatomic and structural remodeling along the crista terminalis with reduced functional sinus node reserve in CHF.
4	2005	Zicha et al. [23]	Sinus node dysfunction and HCN channel subunit remodeling in a canine heart failure model	canine	tachypacing-induced CHF	↓ HCN2 and HCN4 at protein and mRNA levels

5	2007	Du et al. [27]	Downregulation of neuronal sodium channel subunits $Na_v1.1$ and $Na_v1.6$ in the sinoatrial node from volume-overloaded heart failure rat	rat	volume overload-induced HF	↓ Nav1.1 and ↓ Nav1.6 contributes to HF-induced SAN dysfunction
6	2010	Shinohara et al. [22]	Ca^{2+} clock malfunction in a canine model of pacing-induced heart failure	canine	pacing induced HF	Ca^{2+} clock dysfunction in the superior SAN in HF.
7	2011	Yanni et al. [26]	Changes in ion channel gene expression underlying heart failure-induced sinoatrial node dysfunction	rat	ligation-induced HF	Extensive remodeling in ion channel; gap junction channels; Ca^{2+}-, Na^{+}-, and H^{+}-handling proteins; and SAN receptors in HF SAN
8	2015	Verkerk et al. [28]	Ca^{2+} cycling properties are conserved despite bradycardic effects of heart failure in sinoatrial node cells	rabbit	volume and pressure overload-induced HF	Slower Ca transient decay and reduced late diastolic Ca rise during β-adrenergic stimulation in HF SAN cells
9	2016	Chang et al. [29]	Heart failure modulates electropharmacological characteristics of sinoatrial nodes	rabbit	rapid ventricular pacing	Ivabradine resulted in a higher incidence of AP block in HF rabbit SAN cells. HCN4 and RyR were lower in HF compared to control.
10	2018	Chan et al. [30]	Heart failure differentially modulates the effects of Ivabradine on the electrical activity of the sinoatrial node and pulmonary veins	rabbit	ligation induced HF	Ivabradine caused a higher reduction in HF pacemaker activity; led to bradycardia and AF development; induced burst firing in HF

Table 1.2. Studies on SAN dysfunction associated with HF.

The remodeling of the membrane and Ca^{2+} clocks may be secondary to, or potentiated by, alterations that occur within the SAN mitochondria during HF. Spontaneous AP impulses from the primary pacemaker cells disrupts the ionic gradient within the SAN, which needs to be reestablished by energy-dependent transporters on a beat-to-beat basis. The mitochondria provide the bulk energy to fuel the energetically demanding process. Indeed, like ventricular cardiomyocytes, the SAN has a dense network of mitochondria with a high basal respiratory rate [31]. In addition to their primary function of providing energy, they also regulate the life and death of a cell through their roles in reactive oxygen species (ROS) production[32], Ca^{2+} handling[33], and apoptosis[34]. Injury to the mitochondria can thus have detrimental effects to SAN cell viability.

Therefore, it is crucial to investigate the structural and functional changes that occur in the SAN mitochondria during HF, as this will provide insights into better, site-specific therapeutic options.

4. Potassium Channel Dysfunction in Disease

The congenital long-QT syndrome (LQTS) is a life-threatening cardiac arrhythmia syndrome that represents a leading cause of sudden death in the young.[35] Genetic mutations in cardiac ion channels, known as cardiac ion channelopathies, have been shown to cause a significant percentage of LQTS cases.[36-40] Currently, it is estimated that 1 in 5,000 people carry a LQTS mutation. Table 1.3 illustrated the mutations that can cause LQTS.

Gene	Frequency	Protein (Functional Effect)
KCNQ1 (LQT1)	40-55%	Kv7.1 (↓)
KCNH2 (LQT2)	30-45%	Kv11.1 (↓)
SCN5A (LQT3)	5-10%	Nav1.5 (↑)
ANKB (LQT4)	<1%	Ankyrin B (↓)
KCNE1 (LQT5)	<1%	MinK (↓)
KCNE2 (LQT6)	<1%	MiRP1 (↓)
KCNJ2 (LQT7)	<1%	Kir2.1 (↓)
CACNA1C (LQT8)	<1%	L-type Ca^{2+} channel (↑)
CAV3 (LQT9)	<1%	Caveolin 3 (↓)
SCN4B (LQT10)	<1%	Sodium channel-β4 (↓)
AKAP9 (LQT11)	<1%	Yotiao (↓)
SNTA1 (LQT12)	<1%	Syntrophin α1 (↓)
KCNJ5 (LQT13)	<1%	Kir3.4 (↓)

Table 1.3 Mutations associated with LQTS. Functional effects: ↓ loss-of-function or ↑ gain-of-function. Modified from Peter J. Schwartz, Lia Crotti, and Roberto Insolia. *Circulation: Arrhythmia and Electrophysiology. 2012;5:868–877.* [35]

Defects in $K_v11.1$ channel (also known as human *Ether-à-go-go Related* Gene, hERG, encoded by the *KCNH2* gene) are the second leading cause of LQTS. Moreover, hERG channels represent the most common target for drug-induced LQTS.[41-47,48] With the inclusion of drug-induced or acquired LQTS cases, many of whom have the same genetic ion channel defects as those with the congenital LQTS disease, it is estimated that the true incidence of LQTS may be as high as 1 in 1,000.[37, 38, 40] Loss-of-function mutations in hERG channels result in decreased I_{Kr}, causing delayed repolarization and the prolonged QT interval characteristic of LQTS Type 2.[41-44] The fundamental defect in LQTS is prolonged ventricular repolarization, caused by the imbalance of inward and outward currents, and an increase in occurrences of torsades de pointes polymorphic ventricular tachycardia, ventricular fibrillation, and sudden cardiac death.[37, 39, 49]

Recent studies have provided new evidence that LQTS manifests not only from mutations in cardiac ion channels (as in LQT1, LQT2, and LQT3), but also mutations in ion channel interacting proteins (such as calmodulin in LQT14-15).[50-53] One potential ion channel interacting protein is RING Finger Protein 207 (RNF207), encoded by its gene located on chromosome 1. RNF207 is a specialized type of zinc finger protein, shown to be associated with prolongation of the QT interval.[54-58] There is evidence for an interaction between the hERG K^+ channels and RNF207 proteins *via* RNF207's RING domain[56]. This RING domain, as well as RNF207's structural similarity to tripartite motif-containing proteins (TRIM), suggest a potential function of RNF207

as an E3 ubiquitin ligase and a possible role in facilitating protein degradation[59, 60]. However, the exact molecular mechanisms remain unexplored.

Finally, recent studies have provided genetic links between human heritable CaM mutations and several types of cardiac arrhythmia syndrome leading to sudden cardiac death, including long QT syndrome (LQTS),[61-63] catecholaminergic polymorphic ventricular tachycardia(CPVT),[64] and familial idiopathic ventricular fibrillation (IVF).[65] N54I and N98S mutations in CaM are associated with cases of CPVT with altered CaM-ryanodine receptor 2 (RyR2) function; F90L has been shown to be linked to IVF; and D96V, D130G, and F142L are associated with LQTS. Among the known CaM targets, small-conductance Ca^{2+}-activated K^+ (SK) channels are unique, since they are gated solely by beat-to-beat changes in intracellular Ca^{2+}. However, the molecular mechanisms of how CaM mutations may affect the function of SK channels remain incompletely understood.

In summary, we have identified several critical gaps in our current knowledge on the regulation of cardiac excitability in health and diseases. Through the following Chapters, I will outline my dissertation work as well as my contributions to collaborative projects in the laboratory to fill some of the important knowledge gaps and help to lay foundations for future studies.

References

1. Nattel S and Carlsson L. Innovative approaches to anti-arrhythmic drug therapy. *Nat Rev Drug Discov*. 2006;5:1034-49.

2. Bers DM. Cardiac excitation-contraction coupling. *Nature*. 2002;415:198-205.

3. Grant AO. Cardiac ion channels. *Circ Arrhythm Electrophysiol*. 2009;2:185-94.

4. Maltsev VA and Lakatta EG. Dynamic interactions of an intracellular Ca2+ clock and membrane ion channel clock underlie robust initiation and regulation of cardiac pacemaker function. *Cardiovasc Res*. 2008;77:274-84.

5. Lakatta EG, Maltsev VA and Vinogradova TM. A coupled SYSTEM of intracellular Ca2+ clocks and surface membrane voltage clocks controls the timekeeping mechanism of the heart's pacemaker. *Circ Res*. 2010;106:659-73.

6. Chandler NJ, Greener ID, Tellez JO, Inada S, Musa H, Molenaar P, Difrancesco D, Baruscotti M, Longhi R, Anderson RH, Billeter R, Sharma V, Sigg DC, Boyett MR and Dobrzynski H. Molecular architecture of the human sinus node: insights into the function of the cardiac pacemaker. *Circulation*. 2009;119:1562-75.

7. Fedorov VV, Glukhov AV and Chang R. Conduction barriers and pathways of the sinoatrial pacemaker complex: their role in normal rhythm and atrial arrhythmias. *Am J Physiol Heart Circ Physiol*. 2012;302:H1773-83.

8. Irisawa H, Brown HF and Giles W. Cardiac pacemaking in the sinoatrial node. *Physiol Rev*. 1993;73:197-227.

9. Sutherland EW, Oye I and Butcher RW. The Action of Epinephrine and the Role of the Adenyl Cyclase System in Hormone Action. *Recent Prog Horm Res*. 1965;21:623-46.

10. Kamenetsky M, Middelhaufe S, Bank EM, Levin LR, Buck J and Steegborn C. Molecular details of cAMP generation in mammalian cells: a tale of two systems. *J Mol Biol*. 2006;362:623-39.

11. Sutherland EW and Robison GA. The role of cyclic-3',5'-AMP in responses to catecholamines and other hormones. *Pharmacol Rev*. 1966;18:145-61.

12. Halls ML and Cooper DMF. Adenylyl cyclase signalling complexes - Pharmacological challenges and opportunities. *Pharmacol Ther*. 2017;172:171-180.

13. Linder JU and Schultz JE. The class III adenylyl cyclases: multi-purpose signalling modules. *Cell Signal*. 2003;15:1081-9.

14. Timofeyev V, Myers RE, Kim HJ, Woltz RL, Sirish P, Heiserman JP, Li N, Singapuri A, Tang T, Yarov-Yarovoy V, Yamoah EN, Hammond HK and Chiamvimonvat N. Adenylyl

cyclase subtype-specific compartmentalization: differential regulation of L-type Ca2+ current in ventricular myocytes. *Circ Res*. 2013;112:1567-76.

15. Mattick P, Parrington J, Odia E, Simpson A, Collins T and Terrar D. Ca2+-stimulated adenylyl cyclase isoform AC1 is preferentially expressed in guinea-pig sino-atrial node cells and modulates the I(f) pacemaker current. *J Physiol*. 2007;582:1195-203.

16. Younes A, Lyashkov AE, Graham D, Sheydina A, Volkova MV, Mitsak M, Vinogradova TM, Lukyanenko YO, Li Y, Ruknudin AM, Boheler KR, van Eyk J and Lakatta EG. Ca(2+) -stimulated basal adenylyl cyclase activity localization in membrane lipid microdomains of cardiac sinoatrial nodal pacemaker cells. *J Biol Chem*. 2008;283:14461-8.

17. Metra M and Teerlink JR. Heart failure. *Lancet*. 2017;390:1981-1995.

18. Benjamin EJ, Virani SS, Callaway CW, Chamberlain AM, Chang AR, Cheng S, Chiuve SE, Cushman M, Delling FN, Deo R, de Ferranti SD, Ferguson JF, Fornage M, Gillespie C, Isasi CR, Jimenez MC, Jordan LC, Judd SE, Lackland D, Lichtman JH, Lisabeth L, Liu S, Longenecker CT, Lutsey PL, Mackey JS, Matchar DB, Matsushita K, Mussolino ME, Nasir K, O'Flaherty M, Palaniappan LP, Pandey A, Pandey DK, Reeves MJ, Ritchey MD, Rodriguez CJ, Roth GA, Rosamond WD, Sampson UKA, Satou GM, Shah SH, Spartano NL, Tirschwell DL, Tsao CW, Voeks JH, Willey JZ, Wilkins JT, Wu JH, Alger HM, Wong SS and Muntner P. Heart Disease and Stroke Statistics-2018 Update: A Report From the American Heart Association. *Circulation*. 2018;137:e67-e492.

19. Sanders P, Kistler PM, Morton JB, Spence SJ and Kalman JM. Remodeling of sinus node function in patients with congestive heart failure: reduction in sinus node reserve. *Circulation*. 2004;110:897-903.

20. Mangoni ME and Nargeot J. Genesis and regulation of the heart automaticity. *Physiol Rev*. 2008;88:919-82.

21. Maltsev VA and Lakatta EG. Normal heart rhythm is initiated and regulated by an intracellular calcium clock within pacemaker cells. *Heart Lung Circ*. 2007;16:335-48.

22. Shinohara T, Park HW, Han S, Shen MJ, Maruyama M, Kim D, Chen PS and Lin SF. Ca2+ clock malfunction in a canine model of pacing-induced heart failure. *Am J Physiol Heart Circ Physiol*. 2010;299:H1805-11.

23. Zicha S, Fernandez-Velasco M, Lonardo G, L'Heureux N and Nattel S. Sinus node dysfunction and hyperpolarization-activated (HCN) channel subunit remodeling in a canine heart failure model. *Cardiovasc Res*. 2005;66:472-81.

24. Verkerk AO, Wilders R, Coronel R, Ravesloot JH and Verheijck EE. Ionic remodeling of sinoatrial node cells by heart failure. *Circulation*. 2003;108:760-6.

25. Yanni J, Tellez JO, Maczewski M, Mackiewicz U, Beresewicz A, Billeter R, Dobrzynski H and Boyett MR. Changes in ion channel gene expression underlying heart failure-induced sinoatrial node dysfunction. *Circ Heart Fail*. 2011;4:496-508.

26. Opthof T, Coronel R, Rademaker HM, Vermeulen JT, Wilms-Schopman FJ and Janse MJ. Changes in sinus node function in a rabbit model of heart failure with ventricular arrhythmias and sudden death. *Circulation*. 2000;101:2975-80.

27. Du Y, Huang X, Wang T, Han K, Zhang J, Xi Y, Wu G and Ma A. Downregulation of neuronal sodium channel subunits Nav1.1 and Nav1.6 in the sinoatrial node from volume-overloaded heart failure rat. *Pflugers Arch*. 2007;454:451-9.

28. Verkerk AO, van Borren MM, van Ginneken AC and Wilders R. Ca(2+) cycling properties are conserved despite bradycardic effects of heart failure in sinoatrial node cells. *Front Physiol*. 2015;6:18.

29. Chang SL, Chuang HL, Chen YC, Kao YH, Lin YK, Yeh YH, Chen SA and Chen YJ. Heart failure modulates electropharmacological characteristics of sinoatrial nodes. *Exp Ther Med*. 2017;13:771-779.

30. Chan CS, Chen YC, Chang SL, Lin YK, Kao YH, Chen SA and Chen YJ. Heart Failure Differentially Modulates the Effects of Ivabradine on the Electrical Activity of the Sinoatrial Node and Pulmonary Veins. *J Card Fail*. 2018;24:763-772.

31. Yaniv Y, Juhaszova M, Lyashkov AE, Spurgeon HA, Sollott SJ and Lakatta EG. Ca2+-regulated-cAMP/PKA signaling in cardiac pacemaker cells links ATP supply to demand. *J Mol Cell Cardiol*. 2011;51:740-8.

32. Murphy MP. How mitochondria produce reactive oxygen species. *Biochem J*. 2009;417:1-13.

33. Williams GSB, Boyman L, Chikando AC, Khairallah RJ and Lederer WJ. Mitochondrial calcium uptake. *Proceedings of the National Academy of Sciences*. 2013;110:10479.

34. Wang C and Youle RJ. The role of mitochondria in apoptosis*. *Annu Rev Genet*. 2009;43:95-118.

35. Schwartz PJ, Crotti L and Insolia R. Long-QT syndrome: from genetics to management. *Circ Arrhythm Electrophysiol*. 2012;5:868-77.

36. Schwartz PJ, Ackerman MJ, George AL, Jr. and Wilde AA. Impact of genetics on the clinical management of channelopathies. *J Am Coll Cardiol*. 2013;62:169-80.

37. Ackerman MJ. The Long QT Syndrome: Ion Channel Diseases of the Heart. *Mayo Clinic Proceedings*. 1998;73:250-269.

38. Giudicessi JR and Ackerman MJ. Genotype- and phenotype-guided management of congenital long QT syndrome. *Curr Probl Cardiol*. 2013;38:417-55.

39. Kass RS and Moss AJ. Long QT syndrome: novel insights into the mechanisms of cardiac arrhythmias. *Journal of Clinical Investigation*. 2003;112:810-815.

40. Schwartz PJ and Ackerman MJ. The long QT syndrome: a transatlantic clinical approach to diagnosis and therapy. *Eur Heart J*. 2013;34:3109-16.

41. Jonsson MK, van der Heyden MA and van Veen TA. Deciphering hERG channels: molecular basis of the rapid component of the delayed rectifier potassium current. *J Mol Cell Cardiol*. 2012;53:369-74.

42. Sanguinetti MC and Tristani-Firouzi M. hERG potassium channels and cardiac arrhythmia. *Nature*. 2006;440:463-9.

43. Tseng GN. I(Kr): the hERG channel. *J Mol Cell Cardiol*. 2001;33:835-49.

44. Vandenberg JI, Perry MD, Perrin MJ, Mann SA, Ke Y and Hill AP. hERG K+ Channels: Structure, Function, and Clinical Significance. *Physiological Reviews*. 2012;92:1393-1478.

45. Fitzgerald PT and Ackerman MJ. Drug-induced torsades de pointes: the evolving role of pharmacogenetics. *Heart Rhythm*. 2005;2:S30-7.

46. Perry MD, Ng CA, Mann SA, Sadrieh A, Imtiaz M, Hill AP and Vandenberg JI. Getting to the heart of hERG K(+) channel gating. *J Physiol*. 2015;593:2575-85.

47. Sanguinetti MC, Jiang C, Curran ME and Keating MT. A mechanistic link between an inherited and an acquird cardiac arrthytmia: HERG encodes the IKr potassium channel. *Cell*. 1995;81:299-307.

48. Curran ME, Splawski I, Timothy KW, Vincent GM, Green ED and Keating MT. A molecular basis for cardiac arrhythmia: HERG mutations cause long QT syndrome. *Cell*. 1995;80:795-803.

49. Roden DM, Lazzara R, Rosen M, Schwartz PJ, Towbin J, Vincent GM and LQTS* ftSFTFo. Multiple Mechanisms in the Long-QT Syndrome: Current Knowledge, Gaps, and Future Directions. *Circulation*. 1996;94:1996-2012.

50. Abriel H. Cardiac sodium channel Nav1.5 and interacting proteins: Physiology and pathophysiology. *Journal of Molecular and Cellular Cardiology*. 2010;48:2-11.

51. Medeiros-Domingo A, Kaku T, Tester DJ, Iturralde-Torres P, Itty A, Ye B, Valdivia C, Ueda K, Canizales-Quinteros S, Tusié-Luna MT, Makielski JC and Ackerman MJ. SCN4B-Encoded Sodium Channel β4 Subunit in Congenital Long-QT Syndrome. *Circulation*. 2007;116:134-142.

52. Limpitikul WB, Dick IE, Joshi-Mukherjee R, Overgaard MT, George Jr AL and Yue DT. Calmodulin mutations associated with long QT syndrome prevent inactivation of cardiac L-type Ca2 + currents and promote proarrhythmic behavior in ventricular myocytes. *Journal of Molecular and Cellular Cardiology*. 2014;74:115-124.

53. Nakano Y and Shimizu W. Genetics of long-QT syndrome. *Journal of human genetics*. 2015.

54. Andreasen L, Nielsen JB, Christophersen IE, Holst AG, Sajadieh A, Tveit A, Haunsø S, Svendsen JH, Schmitt N and Olesen MS. Genetic Modifier of the QTc Interval Associated With Early-Onset Atrial Fibrillation. *Canadian Journal of Cardiology*. 2013;29:1234-1240.

55. Han QY, Wang HX, Liu XH, Guo CX, Hua Q, Yu XH, Li N, Yang YZ, Du J, Xia YL and Li HH. Circulating E3 ligases are novel and sensitive biomarkers for diagnosis of acute myocardial infarction. *Clin Sci (Lond)*. 2015;128:751-60.

56. Roder K, Werdich AA, Li W, Liu M, Kim TY, Organ-Darling LE, Moshal KS, Hwang JM, Lu Y, Choi BR, MacRae CA and Koren G. RING finger protein RNF207, a novel regulator of cardiac excitation. *J Biol Chem*. 2014;289:33730-40.

57. Newton-Cheh C, Eijgelsheim M, Rice KM, de Bakker PI, Yin X, Estrada K, Bis JC, Marciante K, Rivadeneira F, Noseworthy PA, Sotoodehnia N, Smith NL, Rotter JI, Kors JA, Witteman JC, Hofman A, Heckbert SR, O'Donnell CJ, Uitterlinden AG, Psaty BM, Lumley T, Larson MG and Stricker BH. Common variants at ten loci influence QT interval duration in the QTGEN Study. *Nat Genet*. 2009;41:399-406.

58. Pfeufer A, Sanna S, Arking DE, Muller M, Gateva V, Fuchsberger C, Ehret GB, Orru M, Pattaro C, Kottgen A, Perz S, Usala G, Barbalic M, Li M, Putz B, Scuteri A, Prineas RJ, Sinner MF, Gieger C, Najjar SS, Kao WH, Muhleisen TW, Dei M, Happle C, Mohlenkamp S, Crisponi L, Erbel R, Jockel KH, Naitza S, Steinbeck G, Marroni F, Hicks AA, Lakatta E, Muller-Myhsok B, Pramstaller PP, Wichmann HE, Schlessinger D, Boerwinkle E, Meitinger T, Uda M, Coresh J, Kaab S, Abecasis GR and Chakravarti A. Common variants at ten loci modulate the QT interval duration in the QTSCD Study. *Nat Genet*. 2009;41:407-14.

59. Gong Q, Keeney DR, Molinari M and Zhou Z. Degradation of trafficking-defective long QT syndrome type II mutant channels by the ubiquitin-proteasome pathway. *J Biol Chem*. 2005;280:19419-25.

60. Marin I. Origin and diversification of TRIM ubiquitin ligases. *PLoS One*. 2012;7:e50030.

61. Crotti L, Johnson CN, Graf E, De Ferrari GM, Cuneo BF, Ovadia M, Papagiannis J, Feldkamp MD, Rathi SG, Kunic JD, Pedrazzini M, Wieland T, Lichtner P, Beckmann BM, Clark T, Shaffer C, Benson DW, Kaab S, Meitinger T, Strom TM, Chazin WJ, Schwartz PJ and George AL, Jr. Calmodulin mutations associated with recurrent cardiac arrest in infants. *Circulation*. 2013;127:1009-17.

62. Boczek NJ, Gomez-Hurtado N, Ye D, Calvert ML, Tester DJ, Kryshtal D, Hwang HS, Johnson CN, Chazin WJ, Loporcaro CG, Shah M, Papez AL, Lau YR, Kanter R, Knollmann BC and Ackerman MJ. Spectrum and Prevalence of CALM1-, CALM2-, and CALM3-Encoded Calmodulin Variants in Long QT Syndrome and Functional Characterization of a Novel Long QT Syndrome-Associated Calmodulin Missense Variant, E141G. *Circulation Cardiovascular genetics*. 2016;9:136-146.

63. Reed GJ, Boczek NJ, Etheridge SP and Ackerman MJ. CALM3 mutation associated with long QT syndrome. *Heart rhythm : the official journal of the Heart Rhythm Society*. 2015;12:419-22.

64. Nyegaard M, Overgaard MT, Sondergaard MT, Vranas M, Behr ER, Hildebrandt LL, Lund J, Hedley PL, Camm AJ, Wettrell G, Fosdal I, Christiansen M and Borglum AD. Mutations in calmodulin cause ventricular tachycardia and sudden cardiac death. *American journal of human genetics*. 2012;91:703-12.

65. Hwang HS, Nitu FR, Yang Y, Walweel K, Pereira L, Johnson CN, Faggioni M, Chazin WJ, Laver D, George AL, Jr., Cornea RL, Bers DM and Knollmann BC. Divergent regulation of ryanodine receptor 2 calcium release channels by arrhythmogenic human calmodulin missense mutants. *Circulation research*. 2014;114:1114-24.

CHAPTER 2

Adenylyl Cyclase Isoform 1 Contributes to Sinoatrial Node Automaticity via Functional Microdomains

Lu Ren[1], Phung N. Thai[1,2], Raghavender Reddy Gopireddy[3], Valeriy Timofeyev[1], Hannah A. Ledford[1], Ryan L. Woltz[1,2], Seojin Park[4], Jose Puglisi[5], Claudia M. Moreno[6,7], Luis Fernando Santana[6], Alana C. Conti[8], Michael I. Kotlikoff[9], Yang Kevin Xiang[2,3], Vladimir Yarov-Yarovoy[6], Manuela Zaccolo[10], Xiao-Dong Zhang[1,2], Ebenezer N. Yamoah[4], Manuel F Navedo[3], Nipavan Chiamvimonvat[1,2]

[1]Department of Internal Medicine, Cardiology, UC Davis; [2]Department of Veteran Affairs; [3]Department of Pharmacology, UC Davis; [4]Department of Physiology and Cell Biology, University of Nevada, Reno; [5]California Northstate University; [6]Department of Physiology and Membrane Biology, UC Davis; [7]Department of Physiology and Biophysics, University of Washington School of Medicine, Seattle, WA, [8]Research & Development Service, John D. Dingell VA Medical Center; Department of Neurosurgery, Wayne State University School of Medicine, Detroit, MI; [9]College of Veterinary Medicine, Cornell University; and [10]Department of Physiology, Anatomy and Genetics, University of Oxford, UK

Running title: Adenylyl Cyclase Isoform 1 Regulates Heart Rate

Corresponding authors:
Nipavan Chiamvimonvat, M.D.
Department of Internal Medicine, Cardiovascular Medicine
University of California, Davis
451 Health Science Drive, GBSF 6315
Davis, CA 95616
Department of Veterans Affairs, Northern California Health Care System
10535 Hospital Way
Mather, CA 95655
Email: nchiamvimonvat@ucdavis.edu

Manuel F. Navedo, PhD
Department of Pharmacology
University of California, Davis
451 Health Science Drive, Tupper Hall 2420
Davis, CA 95616
Email: mfnavedo@ucdavis.edu

ABSTRACT

Rationale: Sinoatrial node (SAN) cells are the heart's primary pacemaker. Their activity is tightly regulated by β-adrenergic receptor (β-AR) signaling. Adenylyl cyclase (AC) is a key enzyme in the β-AR pathway that catalyzes 3',5'-cyclic adenosine monophosphate (cAMP) from ATP to activate a cascade of downstream effectors important for regulation of pacemaking activity. At present, it is unclear which AC isoforms are predominant in the SAN and how they regulate the heart's pacemaking activity.

Objective: We hypothesize that distinct AC isoforms are preferentially expressed in the SAN and compartmentalize within critical microdomains to orchestrate heart rate regulation during β-AR signaling.

Methods and Results: Single-cell RT-PCR showed that in contrast to atrial and ventricular myocytes, SAN cells express a diverse repertoire of ACs with AC_I as the predominant isoform. SmFISH confirmed the high expression of AC_I, but also AC_{VI}, in the SAN cells. Although $AC_I^{-/-}$ mice exhibit normal cardiac systolic or diastolic function, they experienced SAN dysfunction. Similarly, SAN-specific CRISPR/Cas9-mediated gene silencing of AC_I resulted in sinus bradycardia with evidence of sick sinus syndrome. Mechanistically, both ryanodine receptor (RyR2) and hyperpolarization-activated cyclic nucleotide-gated (HCN)4 channels of the coupled clock form functional microdomains almost exclusively with AC_I, while L-type Ca^{2+} channels likely compartmentalize with AC_I as well as other AC isoforms. Due to its central characteristic as a Ca^{2+}-activated isoform, AC_I is critical in the sustained rise in local cAMP during β-AR stimulation.

Conclusions: Our study reveals AC_I's critical roles in SAN cells regulation and control of heart rate under basal and β-AR stimulation. The new insight offers unique therapeutic opportunities to modify pacemaking activity, without interfering with contractile cardiomyocytes.

Keywords: cardiac electrophysiology, heart rate, sinoatrial node, Ca^{2+}, HCN, microdomain, adenylyl cyclase

INTRODUCTION

Sinoatrial node (SAN) dysfunction (SND) results in an inability of the heart's natural pacemaker cells to produce a normal rhythm. The prevalence is ~1 per 1000 person-years[1, 2] with a projected incidence of 172,000 people per year by 2060,[3] due to an aging population. SND has a broad etiologic spectrum and affects people from the elderly to children with congenital heart diseases.[4, 5] More than 50% of patients with SND require surgical implantations of pacemakers to restore their sinus rhythms. Electronic pacemakers enable the heart to beat at a regular rate. Still, they exhibit many shortcomings, such as suboptimal autonomic responsiveness, limited battery life, pocket/lead infections, lead fractures, electromagnetic interference, and pacing-induced remodeling.[6] Therefore, research efforts have focused on developing a fully functional biological pacemaker,[7] providing patients with a more physiological response to autonomic stimuli. Significant knowledge gaps in our current understanding of SAN functions need to be filled before the development of a biological pacemaker can be fully realized.

SAN, the pacemaker of the heart, is the primary determinant of heart rate[8, 9] and is tightly regulated by β-adrenergic receptor (β-AR) signaling.[10, 11] Adenylyl cyclase (AC) is a key enzyme in the β-AR pathway that converts ATP into 3',5'-cyclic adenosine monophosphate (cAMP) resulting in a cascade of downstream effects.[11-13] ACs are genetically diverse and encoded by 10 distinct genes. Nine ACs are G protein-regulated transmembrane proteins, while one is a soluble form.[12, 14] ACs genetic diversity suggests that different isoforms may serve distinct functions in different regions of the body. The distribution of the AC isoforms may differ significantly between the SAN and ventricular cardiomyocytes. In ventricular cardiomyocytes, AC_V and AC_{VI} are the two main isoforms.[15] In contrast, there is minimal information regarding the main AC isoforms in SAN. One study shows that AC_I is preferentially expressed in guinea pig SAN cells and modulates the funny current (pacemaker current, I_f).[16] Another study shows that the most abundant AC isoforms in rabbit SAN are AC_I and AC_V.[17] The variability in these studies may be

species-specific or stem from the techniques employed, wherein PCR was used to amplify cells in the vicinity of the SAN, which may have included AC isoforms from the surrounding atrial and other supporting cells.

The function of different isoforms of AC is directly dependent on the concentrations of intracellular Ca^{2+}: AC_I (K_d = 100 nM)[18] and AC_{VIII} (K_d = 500 nM)[19] are Ca^{2+}-activated isoforms while physiological concentrations of Ca^{2+} inhibit $AC_{V\text{-}VI}$.[20] Ca^{2+} is an essential key modulator of the SAN's pacemaker potential *via* the Ca^{2+} clock, [21] during which Ca^{2+} is spontaneously released from the sarcoplasmic reticulum (SR) via ryanodine receptors (RyR), triggering the extrusion of Ca^{2+} from the cytosol *via* Na^+-Ca^{2+} exchanger (NCX). NCX exchanges one Ca^{2+} ion for three Na^+ ions, generating an overall net inward current that contributes to diastolic depolarization.[21] Here, we hypothesize that distinct AC isoforms are preferentially expressed and compartmentalized in SAN to serve a specialized function. Specifically, activated AC_I increases cAMP concentrations, leading to an elevation of intracellular Ca^{2+} (Ca^{2+}_i) through Ca^{2+} channels. The subsequent increase in Ca^{2+}_i activates AC_I in a positive feedback loop, while the rise in Ca^{2+}_i provides negative feedback to other AC isoforms such as $AC_{V\text{-}VI}$. Our study aims to elucidate the critical role of the Ca^{2+}-activated AC_I isoform in the SAN that may provide novel insights into the development of targeted therapeutics, specific to pacemaker cells without interfering with contractile myocytes.

MATERIALS AND METHODS

Animal Models

Male and female WT and $AC_I^{-/-}$ mice[22, 23] 10-15 weeks old in C57Bl6/J background were used for this study. Mice were housed individually in 12 hr light / 12 hr dark environment. The present investigation conforms to the Guide for the Care and Use of Laboratory Animals published by the US National Institutes of Health (NIH publication No. 85-23, revised 1985) and was performed in accordance with the protocols and guidelines approved by the Animal Care and Use Committee of the University of California, Davis.

All the experiments were performed in a blinded fashion by different investigators conducting animal handlings, cardiomyocyte isolations, data collection, and analyses.

SAN Cell Isolation

SAN cells were isolated as described as follows.[24-27] Mice were anesthetized by intraperitoneal injection of 80 mg/kg of ketamine and 5 mg/kg of xylazine. The heart was excised and placed into Tyrode's solution (35°C) containing (in mM): 140 NaCl, 5.0 HEPES, 5.5 Glucose, 5.4 KCl, 1.8 $CaCl_2$, and 1.0 $MgCl_2$ (pH 7.4). The SAN tissue was dissected based on the landmarks defined by the orifice of superior vena cava, crista terminalis, and atrial septum.[28] SAN tissue was digested in low Ca^{2+} solution containing (in mM): 140 NaCl, 5.0 HEPES, 5.5 Glucose, 5.4 KCl, 0.2 $CaCl_2$ and 0.5 $MgCl_2$, 1.2 KH_2PO_4, 50 taurine, pH 6.9, with collagenase B (0.54U/mL, Sigma-Aldrich), elastase (18.9 U/mL, Sigma-Aldrich) and protease type XIV (1.79 U/mL, Sigma-Aldrich) for 30 mins at 37°C. After digestion, the tissue was washed three times with Kraft-Bruhe medium containing (in mM): 100 potassium glutamate, 5 HEPES, 20 glucose, 25 KCl, 10 potassium aspartate, 2 $MgSO_4$, 10 KH_2PO_4, 20 taurine, 5 creatine, 0.5 EGTA, and 1 mg mL^{-1} BSA (pH 7.4). SAN cells were dissociated with a transfer pipette by mechanically stirring and pipetting the tissue chunks. Dissociated SAN cells were used for experiments at room temperature (RT, 22-25°C) or 36 ± 0.5 °C.

Single-cell RT-qPCR

Single cells were identified and isolated with patch pipettes under a microscope. RNA was isolated from single cells using Single Cell-to-CT™ qRT-PCR Kit (Thermo Fisher Scientific, Waltham, MA). Single-strand cDNA was synthesized using Superscript III. The quantitative real-time reverse transcription-polymerase chain reaction (qPCR) was performed using predesigned TaqMan Gene Expression assays probes (Thermo Fisher Scientific), *Adcy 1* (Hs00299832_m1), *Adcy 2* (Hs01058848_m1), *Adcy 3* (Hs01086502_m1), *Adcy 4* (Hs00934099_m1), *Adcy 5* (Hs02890018_m1), *Adcy 6* (Hs00209600_m1), *Adcy 7* (Hs00181579_m1), *Adcy 8* (Hs00905042_m1), *Adcy 9* (Hs00181599_m1), *HCN4* (Hs00975492_m1).

Single-molecule fluorescence in situ hybridization (smFISH)

SmFISH was performed as follows[29] in WT and *AC1* KO SAN sections using probes for AC_I, AC_V, and AC_{VI}. Isolated samples were incubated with 4% DEPC-PFA for 24hr, followed by incubation with 30% sucrose for 2-3 days. Samples were then embedded in the OCT compound and cryo-sectioned (10 μm) on super-frost slides. RNAscope multiple fluorescent detection reagents v2 (Advanced Cell Diagnostics, ACD, #323111) were used for the assay. Probe hybridization was performed according to the manufacturer's instructions (ACD). Sections were immersed in 4% PFA for 15 mins at 4°C and serially dehydrated in 50%, 70%, and 100% ethanol for 5 mins at RT. Sections were then treated with hydrogen peroxidase for 10 mins at RT, followed by proteinase digestion using protease 4 for 30 mins at RT. The following steps were performed at 40°C. Probes were reacted for 2 hours. AMP1, AMP2, AMP3 reagents were used to amplify the signal. The appropriate HRP reagent and Opal dye were used. HRP blocker was then added to complete the reaction. Slides were washed twice after every step at RT. Probes for *Adcy1* (#451241), *Adcy6* (#539861), *GAPDH* (#4471841), and controls were obtained from ACD. For subsequent immunofluorescent staining, slides were treated with 10% goat serum for 30 mins at RT, incubated with primary antibody (hyperpolarization-activated cyclic nucleotide-gated (HCN) 4, 1:500 dilution, Alomone Labs) overnight at 4°C, washed with TBS-0.005% Tween20 three times for 5 mins each, incubated with secondary antibody (FITC, Life Technologies, 1:500) for 2 hours at RT, and again washed with TBS-0.005% Tween20 three times for 5 mins each. Slides were incubated in 4′,6-diamidino-2-phenylindole (DAPI) solution for 30 secs at RT to label cell nuclei. They were then mounted on Fluoromount-G and sealed under a coverslip.

Echocardiography

Echocardiography to assess systolic and diastolic function were performed using Vevo 2100 (VisualSonics, Fujifilm, Toronto, ON, Canada) imaging system and a MS 550D probe (22–55 MHz).[30, 31] Systolic function was assessed using M-mode and two-dimensional measurements in conscious mice. Diastolic function was assessed in mice anesthetized with 1% isoflurane. The measurements represented

the average of six selected cardiac cycles from at least two separate scans performed in random-blind fashion with papillary muscles used as a point of reference for consistency in level of scan. End diastole was defined as the maximal left ventricular (LV) diastolic dimension and end systole was defined as the peak of posterior wall motion. Fractional shortening (FS), a surrogate of systolic function, was calculated from LV dimensions as follows: Fractional shortening (FS), a surrogate of systolic function, was calculated from LV dimensions as follows: FS = ((EDD-ESD)/EDD) x100%, where EDD and ESD are LV end diastolic and end systolic dimension, respectively. E/A ratio (E wave/A wave) was measured to define diastolic function.

Hemodynamic monitoring

Mice were anesthetized by intraperitoneal injection of 80 mg/kg of ketamine and 5 mg/kg of xylazine and maintained at 37 ºC. The arterial catheter was inserted retrogradely into the left ventricle via carotid artery. The recording of pressure and volume was performed by using Millar Pressure-Volume System MPVS-300 (Millar, Inc., Houston, TX), Power Lab, and Lab Chart 6.0 software (AD Instruments, Colorado Springs, CO). The pressure and volume were calibrated before recordings. The volume calibration used fresh heparinized 37 oC mouse blood and a cuvette (P/N 910-1049, Millar, Inc.). To change the preload, a gentle and quick abdominal compression was applied to occlude inferior vena cava.

Electrocardiography (ECG) Telemetry

All telemetry placements were performed 1 week before the start of each experiment. Mice were anesthetized with ketamine/xylazine (80 mg/kg /5 mg/kg) before placement of a transmitter (Data Sciences International (DSI), New Brighton, MN) into the abdominal cavity with subcutaneous electrodes in the lead I configuration. Baseline measurements were recorded for 24 hours and followed by intraperitoneal injection of Isoproterenol (ISO, 0.1 mg/kg, IP) in both AC_1 KO compared to WT animals. Atropine (2 mg/kg, ip) and propranolol (1 mg/kg, ip) were used to block the heart's autonomic control. The analog telemetric ECG signals were digitized at 1 kHz and recorded using PONEMAH software (DSI). R peaks of the ECG signal were detected, and the mean HR was calculated from the RR interval and

averaged for 1 min. For baseline recordings, t=0 corresponds to noon, while t=24 corresponds to midnight. Heart rate variability (HRV) was plotted as RR interval (RR-I) against the next RR interval.

SAN-specific clustered regularly interspaced short palindromic repeats (CRISPR)/Cas9-mediated gene silencing of *AC_I*

A transgenic mouse model expressing a fluorescent Ca^{2+} indicator (GCaMP8) under the control of the *Hcn4* promoter was previously generated and used for the study.[32] CRISPR/Cas9 system containing 3X sgRNA (GeneCopoeia, Rockville, MD) was used to specifically target the AC_I isoform, followed by *in vivo* delivery using liposome and SAN painting technique.[33, 34] A vector containing a scrambled sequence was used as control. Both the targeting and control vectors contained mCherry and were encapsulated in liposomes. The liposomal emulsion was painted onto the SAN region under direct visualization. ECG and echocardiograms were performed 5-7 days after surgery at baseline and after ISO injection. Light Sheet-Based Fluorescence Microscopy (LSFM) was performed in freshly dissected SAN to confirm that the in vivo gene delivery was successful. Green fluorescence protein (GFP) and mCherry signals were simultaneously detected during live SAN imaging.

Light Sheet-Based Fluorescence Microscopy (LSFM)

Freshly dissected tissues were placed in normal Tyrode's solution, immersed in 1.5% agarose in a capillary tube, and mounted inside the Lattice Lightsheet 7 microscope (Carl Zeiss, Germany). During experiments, tissue was maintained at 37°C and constantly gassed with 95% O_2/5% CO_2. Baseline measurements were taken before the application of 1 μM of ISO. Imaris software (Bitplane, Switzerland) was used to perform 3D reconstructions.

Immunofluorescence Confocal Microscopy

Immunofluorescence labeling was performed as follows.[15] Isolated SAN cells were allowed to adhere to coverslips for 10 mins before fixing with 4% PFA. Cells were then washed with PBS (3 x 10 mins). Cells were permeabilized for 10 mins with 1% Triton X-100% and then blocked with 5% donkey serum for 1h at RT. The following primary antibodies were used to incubate the cells overnight at 4°C: (1)

anti-HCN4 (Abcam, 1:300 dilution), a polyclonal antibody raised against rat HCN4, (2) anti-AC_I (Santa Cruz, 1:100 dilution), a monoclonal antibody raised against mouse AC_I and (3) anti-Caveolin-3 (1:300, Thermo-Fisher Scientific), a polyclonal antibody raised against rabbit Caveolin-3. Cells were washed with PBS (3 x 10 mins) and then incubated with anti-rat, anti-mouse, or anti-rabbit secondary antibodies (Jackson ImmunoResearch, 1:500 dilution) for 1 hour at RT. All the antibodies used were diluted in blocking solution with 5% donkey serum. Cells were then washed with PBS (3 x 10 mins). Coverslips were mounted on the slides with ProLong Diamond Antifade Mountant (Thermo Fisher Scientific Inc.). Control experiments performed by incubation with secondary antibody only did not show positive staining under the same experimental conditions. Identical settings were used for all specimens. Cells were sequentially imaged using a Zeiss 900 confocal laser-scanning microscope equipped with an Airyscan detector module, a Plan-Apo 63× 1.4 NA oil-immersion objective and 488/561/647 lasers. Cells for each group were imaged using the same acquisition parameters. Images were background subtracted, pseudo-colored, and analyzed offline using ImageJ. Stimulated emission depletion (STED) microscopy was performed on a Leica STED (TCS SP8 STED 3X) microscope with an HC PL APO 100×/1.4 NA STED objective in STED mode. Using Huygens professional software, deconvolution was limited to 15 iterations and a signal-to-noise ratio of 4 with a manual evaluation of background intensity.

Electrophysiology

Spontaneous APs and AP firing frequencies in single SAN cells were assessed using the perforated patch-clamp technique at 36 ± 0.5 °C. Whole-cell patch-clamp techniques were used to record I_{Ca} and I_f at baseline and after isoproterenol (ISO, 1 μM).

For AP recordings, Amphotericin B (240 μg/ml) was added into the pipette solution. Spontaneous APs were recorded in Tyrode's solution with the pipette filled with (in mM): 30 potassium aspartate, 10 NaCl, 10 HEPES, 0.04 $CaCl_2$, 2.0 Mg-ATP, 7.0 phosphocreatine, 0.1 Na-GTP, with pH adjusted to 7.2 with KOH.

Ca^{2+} currents were recorded using conventional whole-cell patch-clamp techniques at RT. Current-voltage relations were assessed before and after the application of ISO (1 μM). Current-voltage relations were constructed using a family of voltage steps of 300 ms from a holding potential of -55 mV with an interpulse interval of 2 seconds and 20 mV increment to record L-type I_{Ca}. The holding potential for total I_{Ca} recordings was -80 mV. The pipette (intracellular) solution contained (in mM): 120 CsCl, 10 EGTA, 10 HEPES, 10 tetraethylammonium chloride (TEA), 5.0 phosphocreatine, 3.0 $CaCl_2$, 1.0 Mg- ATP, and 1.0 Na-GTP; pH was adjusted to 7.2 with 1.0 CsOH. The bath (extracellular) solution was comprised of (in mM): 137 NaCl, 10 HEPES, 10 glucose, 1.8 $CaCl_2$, 0.5 $MgCl_2$, and 25 CsCl, and pH was adjusted to 7.4 with NaOH.

For pacemaker current (I_f) recordings, patch pipettes were filled with intracellular solution containing (in mM): 120 potassium aspartate, 25 KCl, 4.0 $MgCl_2$, 10 EGTA, 4.0 K-ATP, 2.0 Na-GTP, 2.0 phosphocreatine, 5.0 HEPES, 1.0 $CaCl_2$, and pH was adjusted to 7.2 with KOH. The extracellular solution contained (in mM): 130 NaCl, 5.0 KCl, 2.0 $MgCl_2$, 1.8 $CaCl_2$, 5.0 HEPES, and 5.0 glucose; pH was adjusted to 7.4 with NaOH. 1 mM $BaCl_2$ was applied to block K^+ current. Voltage steps were applied for 2.0 s ranging from −140 mV to −40 mV in 10 mV increments at a holding potential of -35 mV. I_f currents were recorded at 36 ± 0.5 °C.

Proximity Ligation Assay

Protein associations between AC_I and caveolin-3, AC_I and HCN4, AC_I and $Ca_v1.2$, AC_I and RyR-2 were detected by a Duolink In Situ PLA kit (Sigma).[35] Freshly isolated SAN cells were fixed with 4% PFA and washed with PBS. Cells were then permeabilized with 0.25% Triton X-100 (10 min), blocked in 1% BSA for 30 mins at RT, and incubated overnight at 4°C with two primary antibodies 1% BSA + 0.25% Triton X-100 PBS solution. The antibodies used were mouse anti-AC_I (1:100; Santa Cruz Biotechnology), rabbit anti-$Ca_V1.2$ (1:200; Thermo Fisher Scientific), rabbit anti-HCN4 (1:200; Alomone Labs), and rabbit anti-RyR-2 (1:200; Alomone Labs). Cells incubated with only one primary antibody were used as negative controls. PLA probes (anti-mouse MINUS and anti-rabbit PLUS) were used as secondary antibodies to

bind to primary antibodies. Ligase was added to cells to allow hybridization with the probes, and polymerase was added for a rolling circle amplification reaction. Coverslips were mounted on a microscope slide with Duolink mounting medium. The fluorescence signal was detected using a Zeiss confocal LSM 700 microscope. Images were collected at different optical planes (z-axis step = 0.5 mm). The stack of images for each sample was combined into a single-intensity projection image used to analyze the number of puncta/μm^2 per cell. All the data were analyzed in a blinded fashion with the NIH ImageJ software v1.53c.

Whole-cell Ca^{2+} Transient Measurements

IonOptix contraction system (IonOptix LLC, Westwood, MA) was used to detect spontaneous Ca^{2+} transient from whole cells. Freshly isolated SAN cells were loaded with 5 μM Fluo-4 AM (F14201, Molecular Probes) for 15 minutes at RT. Cells were then perfused with Tyrode's solution (36 ± 0.5 °C) continuously. Baseline measurements were taken before ISO was applied in both WT and $AC_I^{-/-}$ mice. The maximal Fluo-4 fluorescence (F) was measured at peak amplitude and was normalized to F_0, the average of baseline fluorescence. Background fluorescence was subtracted for each recording.

Local Ca^{2+} Release and Ca^{2+} Transient Detection via Confocal Line Scanning

Freshly isolated SAN cells were loaded with 5 μM Fluo-4 AM for 15 mins at RT. Cells were then perfused with Tyrode's solution (36 ± 0.5 °C) continuously. Line-scan images across the whole cell were obtained to measure Ca^{2+} signals with 488 nm excitation and 510 nm emission from the SAN cells. Pixel time was 0.76 μs; line time was 0.91 bms. Pinhole was set at 1.00 AU/50 μm. Baseline recordings were performed before ISO was applied in both WT and $AC_I^{-/-}$ mice.

Culture of SAN Cells

SAN cells were first isolated as described above. Glass coverslips (25 mm, size #0, Karl Hecht, Sondheim, Germany) were coated with 100x diluted laminin (Life Technologies, Grand Island, NY) and incubated for 4 hours at 37°C in 5% CO_2. After 4 hours, coverslips were placed in individual wells in a 24-well plate (Falcon, Tewksbury, MA) and washed 3x with sterile PBS (in mM): 137 NaCl, 2.7 KCl, 10

Na_2HPO_4, 1.8 KH_2PO_4, pH = 7.4). Isolated SAN cells were resuspended in M1018 medium (10.7 g/L) supplemented with 1x penicillin-streptomycin-glutamate (PSG), 4 mM $NaHCO_3$, 10 mM HEPES, 10% fetal bovine serum (FBS), 6.25 μM blebbistatin and plated on the pre-coated laminin coverslips and incubated for 4 hours at 37°C in 5% CO_2, before the media was replaced with serum-free M1018.[36]

Adenoviral Transfection of cAMP Biosensors in SAN Cells and Confocal Imaging

For adenoviral transfection, the media was replaced with 500 μL of serum-free medium containing adenoviral vectors carrying different versions of the FRET-based cAMP Universal Tag for imaging experiments (CUTie) sensor.[37] Accordingly, we employed the cytosolic CUTie, the membrane-targeted AKAP79-CUTie, and sarcoplasmic reticulum-targeted AKAP18δ-CUTie. Cells infected with the desired adenoviral vectors were incubated at 37°C with 5% CO_2 for 36 to 40 hours. Adenoviral vectors were produced using the AdEasy system (Qbiogene).[38] A Zeiss LSM700 laser scanning confocal microscope paired with a Zeiss 63x oil immersion lens (numerical aperture = 1.4) was used to collect images at different optical planes (z-axis steps: 0.4 μm) of the YFP fluorescence associated with each FRET construct to confirm expression and expected localization.

Fluorescence Resonance Energy Transfer (FRET) Imaging and Quantification

Glass coverslips with SAN cells were transferred to a glass-bottom culture dish (MatTek, Ashland, MA) containing 3 mL PBS at RT. A Leica DMI3000B inverted fluorescence microscope (Leica Biosystems, Buffalo Grove, IL) equipped with a Hamamatsu Orca-Flash 4.0 digital camera (Bridgewater, NJ) controlled by Metaflor software (Molecular Devices, Sunnyvale, CA) acquired phase contrast, CFP, and YFP images. Phase contrast and CFP480 images were collected with 20x and 40x oil immersion objective lenses, while YFP images were collected using only the 40x oil immersion objective lens. Images for FRET analysis were recorded by exciting the donor fluorophore at 430-455nm and measuring emission fluorescence with two filters (475DF40 for cyan and 535DF25 for yellow). Images were subjected to background subtraction and acquired every 30 s with exposure time of 200 ms for each channel. The donor/acceptor FRET ratio was calculated and normalized to the ratio value of baseline

before ISO. Averages of normalized curves and maximal response to stimulation were graphed based on FRET ratio changes. The binding of cAMP to each FRET biosensor increased the ratio of YFP/CFP and was interpreted as an increase in cAMP levels. Experiments were performed at RT.

Chemicals

All chemicals were purchased from Sigma-Aldrich (St. Louis, MO, USA) unless indicated otherwise. Laminin (cat no: 23017015) was obtained from Life Technology, Blebbistatin (cat no: 13013) from Cayman, 3-isobutyl-1-methylxanthine (IBMX, cat no: 2845) from Tocris.

Statistical Analysis

Data were analyzed using GraphPad Prism (San Diego, CA) software and presented as mean ± SEM. Data were assessed for potential outliers using the GraphPad Prism Outlier Test and for normality of distribution. Statistical significance was then determined using appropriate unpaired two-tailed Student's t-test, nonparametric tests, one-way analysis of variance (ANOVA) or two-way ANOVA for multiple comparisons with appropriate post hoc test. Two-way ANOVA was followed by Holm–Sidak multiple comparison test. General linear model was used for two-way repeated measures and mixed-effect model was used when there were missing values. $p<0.05$ was considered statistically significant.

RESULTS

AC_I is the predominant isoform in the SAN, forming microdomains with key Ca^{2+} handling proteins

To determine the relative abundance of the different AC isoforms, we performed single-cell RT-qPCR. AC_I was the most abundant isoform in the SAN, followed by AC_{VI}, AC_{III}, AC_{IV} and AC_{VII} (**Figure 2.1A**). In contrast, AC_{VI} was the most abundant isoform in both atria and ventricles. In addition to the morphological differences of SAN cells relative to atrial and ventricular cardiomyocytes, we used the HCN4 channel as a marker to accurately identify SAN cells. Single-cell RT-qPCR data are corroborated

by the smFISH experiments (**Figure 2.1B**). Both AC_I and AC_{VI} mRNA expression can be detected in the SAN tissue. HCN4 was used for counter-staining, and the GAPDH probe was used as a positive control.

Caveolin-3 (Cav-3) is a critical scaffolding protein, involved in the organization of signaling microdomains.[39] We have previously shown that AC_V isoform localizes and interacts with caveolin-3 (Cav-3) to regulate Ca^{2+} current in ventricular myocytes.[15] To determine the protein expression and localization of AC_I with respect to Cav-3 and HCN4 channels, we performed immunofluorescence imaging of SAN cells, triple labeled for AC_I, Cav-3 and HCN4, using confocal microscopy coupled with an Airyscan module, with a resolution of ~120 nm (**Figure 2.1C**). AC_I colocalizes with Cav-3 and HCN4, as evidenced by the high Pearson's correlation coefficient and overlap coefficient (**Figures 2.1D-E**). Additionally, stimulated emission depletion (STED) microscopy with a resolution of ~50 nm was used to document the colocalization at a higher spatial resolution. In agreement with Airyscan images, magnified STED images of the SAN cells and subsequent Pearson's correlation coefficient and overlap coefficient analysis revealed that these proteins form clusters with a high degree of overlap at the plasma membrane (**Figures 2.1F-G**). Negative controls are presented in **Supplementary Figure 2.1**.

Proximity ligation assay (PLA) was further used as a complementary technique to determine if two proteins are ≤40 nm apart (**Figure 2.1H**). Red puncta represent close association of AC_I with specific proteins, and nuclei were stained with DAPI. The numbers of puncta per unit area are significantly increased when AC_I was co-stained with HCN4, Cav-3, voltage-gated Ca^{2+} channel ($Ca_v1.2$), or RyR2 compared to negative controls (where only one antibody was used) (**Figure 2.1I** and **Supplementary Figure 2.1**; $p<0.001$ for all comparisons). Taken together, these results suggest that the predominant AC isoform in the SAN is AC_I, which localizes within microdomains with key Ca^{2+} handling proteins and HCN4 channels.

AC_I knockout mice exhibit sinus node dysfunction

How AC_I contributes to overall cardiac function, in addition to the known AC isoforms, remains unclear.[40] We took advantage of *$AC_I^{-/-}$* mice and used echocardiography to quantify cardiac dimensions

and function in $AC_I^{-/-}$ mice compared to wild-type (WT) animals (**Supplementary Figure 2.2**). Genotyping was performed in all mice (**Supplementary Figure 2.3**). To assess systolic function, M-mode images were acquired at the parasternal short axis in conscious WT and $AC_I^{-/-}$ mice (**Figure 2.2A)**. Color and pulse wave Doppler were used to evaluate diastolic function in anesthetized mice, by assessing the ratio of blood flow velocity through the mitral valve during early diastolic filling (E wave) and late diastolic filling (A wave) (**Figure 2.2A**). $AC_I^{-/-}$ mice showed evidence of sinus bradycardia and sinus arrhythmias (**Figure 2.2B**, heart rates were 532±15 compared to 587±6 bpm for $AC_I^{-/-}$ and WT mice, respectively, n=13 and 16, $p<0.001$). However, there were no significant differences in systolic or diastolic function between the two groups (**Figure 2.2C-D**). Normalized heart weight to body weight ratio was not different between WT and $AC_I^{-/-}$ mice with no evidence of cardiac fibrosis (**Supplementary Figure 2.2**). Additionally, there was no evidence of upregulation of AC_V and AC_{VI} isoforms in $AC_I^{-/-}$ mice compared to WT controls (**Supplementary Figure 2.4**).

AC_I knockout mice exhibit blunted heart rate responses to β-AR stimulation

Ambulatory ECG recordings were performed to assess baseline heart rate, followed by β-AR stimulation with isoproterenol (ISO) or autonomic nervous system (ANS) blockade with atropine and propranolol (**Figure 2.2E-F**). There were diurnal variations with lower heart rates during the light than the dark cycles. In addition, heart rates in $AC_I^{-/-}$ mice were significantly lower than WT animals and the differences were most pronounced during the hours when the mice were active. A representative day time (7 AM-7 PM) heart rate variability scatter plot shows that there were more variations in heart rates (**Figure 2.2G**) with significantly higher RR intervals (lower heart rates) in the histogram plots from $AC_I^{-/-}$ compared to WT mice (**Figure 2.2H**). Further analyses revealed that this abnormality persisted at night (7 PM-7 AM), when the mice exhibited the highest activity level (**Supplementary Figure 2.5**).

To determine the intrinsic heart rate, we administered 2 mg/kg atropine followed by 1 mg/kg propranolol intraperitoneally (i.p.) (**Figure 2.2I**). The heart rate after β-AR stimulation (maximum, minimum, and median HR) and after autonomic nervous system (ANS) blockade (intrinsic HR; 536±8

bpm for WT vs. 482±21 bpm for $AC_1^{-/-}$; p=0.0426) were significantly impaired in $AC_1^{-/-}$ relative to WT mice (**Figure 2.2J**).

SAN-specific CRISPR/Cas9-mediated AC_1 gene silencing causes SND

As a complementary experiment to the global knockout model, we took advantage of CRISPR/Cas9 gene silencing techniques[41, 42] to generate a SAN-specific knockout of the AC_1 gene in a transgenic HCN4-GCaMP8 background (**Supplementary Figure 2.3, 2.6 and 2.7**). Control constructs contained scrambled sequences and both constructs contained a reporter gene (mCherry). The constructs in the liposome were delivered to the SAN region.

Mice treated with the control constructs exhibited normal surface ECG before and after ISO stimulation. In contrast, mice treated with the AC_1-targeted construct experienced SND before and after ISO injection (**Figure 2.2K**), with sinus bradycardia and sinus arrhythmias as well as a blunted response to β-AR stimulation (**Figure 2.2L**). SAN tissues were then excised (**Figure 2.2M**), and the mCherry signal was used to validate successful delivery of the construct in each mouse using Light Sheet fluorescence microscopy. GFP signal was used as a marker for the SAN region, showing that the SAN region was successfully transfected in the merged image (**Figure 2.2N**). SAN-specific AC_1-gene silenced mice showed abnormal Ca^{2+} signaling with reduced beating rates (**Figure 2.2O-Q**). Taken together, $AC_1^{-/-}$ mice demonstrate normal cardiac systolic and diastolic function but significant SND with sinus bradycardia and blunted responses to β-AR stimulation.

$AC_1^{-/-}$ SAN cells exhibit reduced action potential (AP) firing frequency

To determine the mechanistic underpinnings for sinus arrhythmias and SND in $AC_1^{-/-}$ mice, APs were recorded from SAN cells isolated from WT and $AC_1^{-/-}$ mice using the perforated patch configuration in current-clamp mode. Under basal conditions, SAN cells isolated from $AC_1^{-/-}$ mice exhibited periods of irregularities with bursting activities (**Figures 2.3A** and **2.3B**). The bursting activities were exacerbated by ISO stimulation. Quantitatively, the beating rate (quantified from within the burst) was lower although not significant in $AC_1^{-/-}$ SAN (174.1±21.29 bpm) compared to WT SAN (227.5±26.07 bpm) cells (**Figure**

2.3C). However, the beating rate in $AC_I^{-/-}$ SAN (281.4±19.03) was significantly lower than WT SAN cells (433.5±31.46) after ISO challenge (p=0.000289). The abnormal automaticity and responses to β-AR are consistent with the ECG findings *in vivo*. There was no significant difference in action potential duration at 90% repolarization (APD_{90}, **Figure 2.3D**), peak potential (**Figure 2.3E**), or maximum diastolic potential (**Figure 2.3F**). Non-firing activity was observed in WT SAN cells as previously described, with periods of regular firing and non-firing.[43-45] However, the percentage of non-firing duration was significantly increased in $AC_I^{-/-}$ SAN (20.98±6.046%) compared to WT SAN (8.031±5.789%) cells (**Figure 2.3G**; $p<0.05$). The non-firing pattern was observed in 41.7% of WT compared to 60% of $AC_I^{-/-}$ SAN cells. ISO completely abolished the non-firing mode in WT and reduced the number of cells with non-firing activity in $AC_I^{-/-}$ SAN cells (30%, **Figure 2.3H**).

$AC_I^{-/-}$ SAN cells show impaired global Ca^{2+} transients (CaTs) with Ca^{2+} alternans and a complete lack of response of local Ca^{2+} releases (LCR) to β-AR stimulation

Since AC_I is a Ca^{2+}-activated AC isoform, we examined global CaT and LCR to determine the mechanisms underlying the observed SND in $AC_I^{-/-}$ mice. Representative traces of global CaTs for WT and $AC_I^{-/-}$ SAN cells are depicted in **Figure 2.4A**. $AC_I^{-/-}$ SAN cells exhibited evidence of Ca^{2+} alternans both at the basal condition and after ISO application. Moreover, $AC_I^{-/-}$ cells showed irregular firing frequency consistent with the AP and ECG recordings. Although there was no difference in the time constant of the rising phase of CaT (τ_{rise}), the time constant of the decay phase of CaT (τ_{decay}) was significantly prolonged in $AC_I^{-/-}$ compared to WT SAN cells after β-AR stimulation, possibly from a decrease in SR Ca^{2+} uptake (**Figures 2.4B-2.4C**). There was no difference in non-firing duration (**Figure 2.4D**) and peak amplitude (**Figure 2.4E**). However, the beating rate was significantly decreased in $AC_I^{-/-}$ compared to WT SAN cells at baseline and after ISO application (**Figure 2.4F**). Indeed, the percentage of cells that exhibited irregular CaT behavior was higher in $AC_I^{-/-}$ SAN cells (**Figure 2.4G**). τ_{rise} at 50%,

70% and 90% and τ_{decay} at 50%, 70%, and 90% of global CaT are summarized in **Supplementary Figure 2.8**.

Analysis of LCRs was performed using IOCBIO Sparks software[46] and a customized interface implemented in LabVIEW to generate 3D reconstructions of Ca^{2+} sparks and transients, as depicted in representative images from WT SAN cells (**Figure 2.4I**). As expected, spark rate, the amplitude of LCR, full width at half maximum (FWHM), and full duration at half maximum (FDHM) significantly increased with β-AR stimulation in WT SAN cells. $AC_I^{-/-}$ SAN cells showed a significant decrease in LCRs (**Figure 2.4H).** Remarkably, the effects from β-AR stimulation on LCRs were abolished entirely in $AC_I^{-/-}$ SAN cells (**Figure 2.4J-M**). Summary data for LCR space rise at 50%, space decay at 50%, τ_{rise} at 50%, and τ_{decay} at 50% are shown in **Supplementary Figure 2.8**. The findings are consistent with the co-localization of AC_I within the microdomain of RyR2 as shown in **Figure 2.1C-I** and support the critical roles of AC_I in mediating the enhancement of the Ca^{2+} clock during β-AR stimulation.

$AC_I^{-/-}$ SAN cells demonstrate blunted responses to *β*-AR stimulation for L-type but not T-type Ca^{2+} currents

β-AR stimulation significantly regulates Ca^{2+} currents (I_{Ca}) in the heart. We tested I_{Ca} response to β-AR stimulation in SAN cells isolated from WT and $AC_I^{-/-}$ mice. Representative total I_{Ca} traces from a holding potential of -80 mV were shown for both groups at baseline and after 1 μM ISO (**Figure 2.5A)** and were superimposed at -25 mV (**Figure 2.5B**). At basal conditions, the I_{Ca} at -25 mV was not statistically different between WT and $AC_I^{-/-}$ SAN cells. However, the response to ISO was significantly blunted in $AC_I^{-/-}$ compared to WT SAN cells (**Figure 2.5C**). The current-voltage (I-V) relationship showed that ISO shifted the peak I_{Ca} potential from -15 mV to -25 mV in WT cells (**Figure 2.5D**), while a leftward shift was not evident in $AC_I^{-/-}$ cells (**Figure 2.5E**). In contrast to the WT SAN cells, the half-activation voltages ($V_{1/2}$) of the normalized conductance of I_{Ca}, fitted with a Boltzmann function, showed a lack of response to ISO in $AC_I^{-/-}$ SAN cells (**Supplementary Figure 2.9**).

To determine which component of I_{Ca} may have been affected, we recorded L-type I_{Ca} ($I_{Ca,L}$) from a holding potential of -55 mV (**Figure 2.5F**). For direct comparison, representative traces at -10 mV are shown for all groups in **Figure 2.5G**. The increase in $I_{Ca,L}$ at -10 mV after ISO application was significantly blunted in $AC_I^{-/-}$ SAN cells (**Figure 2.5H**). Similar to the total I_{Ca}, the I-V curve of $I_{Ca,\,L}$ for WT cells was shifted leftwards after ISO administration (**Figure 2.5I**), but this effect was diminished in $AC_I^{-/-}$ cells (**Figure 2.5J**). The normalized conductance for $I_{Ca,L}$ confirmed a significant decrease in the leftward shift after ISO application in $AC_I^{-/-}$ SAN cells. $V_{1/2}$ and slope factors for $I_{Ca,L}$ are summarized in **Supplementary Figure 2.9**.

In contrast, ISO significantly increased T-type Ca^{2+} current ($I_{Ca,T}$) in both groups relative to the baseline (**Figure 2.5K**). There were no significant differences in $I_{Ca,T}$ between the two groups either before or after ISO application. These data suggest AC_I regulates L-type but not T-type Ca^{2+} channels in SAN cells. Indeed, high-resolution imaging and PLA support AC_I's localization within the microdomain of L-type Ca^{2+} channel $Ca_v1.2$ (**Figure 2.1C-F**).

***$AC_I^{-/-}$* SAN cells show a complete lack of response of pacemaking current to *β*-AR stimulation**

Pacemaking current (I_f), encoded by HCN4 channels, predominantly mediates the slope of phase 4 depolarization and modulates spontaneous AP frequency.[47] We recorded I_f from isolated WT and $AC_I^{-/-}$ SAN cells using whole-cell patch-clamp recordings, from -140 to -35 mV in 10 mV increments from a holding potential of -35 mV (**Figure 2.6**). As expected, β-AR stimulation resulted in a significant enhancement of I_f in WT SAN cells (**Figure 2.6A-C**) with a significant depolarization shift in the normalized conductance (**Figure 2.6D-E**) and increases in both the fast and slow time constants of activation (τ_{fast}, τ_{slow}) (**Figure 2.6G-H**). In contrast, β-AR stimulation failed to enhance the amplitude or activation kinetics of I_f in $AC_I^{-/-}$ SAN cells (**Figures 2.6A-H**) with only a minor shift in normalized conductance (**Figure 2.6D-E**). Specifically, the depolarization shift in $V_{1/2}$ is significantly more robust in WT than $AC_I^{-/-}$ SAN cells ($p<0.05$). There were no differences in the slope factors or deactivation kinetics between WT and $AC_I^{-/-}$ SAN cells at baseline and after β-AR stimulation (**Figure 2.6F, I**). The

findings provide strong evidence for the functional compartmentalization of AC_I and HCN4 channels in SAN cells, which is consistent with the subcellular co-localization of AC_I within the HCN4 microdomain (**Figure 2.1C-I**).

AC_I differentially regulates local cAMP signaling at functional microdomains in SAN cells

Since the product of AC activation is cAMP, we exploited the latest cAMP FRET-based biosensors to elucidate the subcellular mechanism of AC_I-mediated heart rate regulation. Single isolated SAN cells were transfected for 36-40 hrs with cAMP universal tag for imaging experiments (CUTie) sensors localized to the cytosol, membrane (AKAP79), and sarcoplasmic reticulum (SR, AKAP18δ) as shown in representative confocal images (**Figure 2.7A**). The AC activator forskolin (10 μM) and the phosphodiesterase (PDE) inhibitor 3-isobutyl-1-methylxanthine (IBMX, 100 μM) were used to determine the maximal cAMP responses in the three specific regions. **Figure 2.7B** and **Supplementary Figure 2.10A-B** show that SAN cells exposed to forskolin + IBMX exhibit similar maximal responses in the normalized FRET signal (R/R_0), which facilitates comparison of cAMP signal in different subcellular domains. ISO applied to WT SAN cells expressing the cytosolic, membrane or SR CUTie sensors revealed distinctive cAMP production in the different subcellular domains (**Figure 2.7C**). The membrane signal was the highest, followed by cytosolic, and finally the SR.

In WT SAN cells expressing the cytosolic CUTie sensor, ISO induced a dose-dependent production of cAMP with an EC_{50} of 0.51 ± 0.23 nM (**Supplementary Figure 2.10C and 2.10E**). Genetic ablation of AC_I rightward shifted the EC_{50} of ISO-induced cAMP to 224 ± 0.16 nM. Further experiments examining the time-dependent changes in cAMP after β-AR stimulation, found that the localized increase in cAMP in the cytosol, at the membrane and SR were significantly blunted in $AC_I^{-/-}$ compared to WT SAN cells (**Figures 2.7D-F**). Notably, in $AC_I^{-/-}$ SAN cells, there was an initial rise followed by a decay over time after β-AR stimulation, suggesting a lack of sustained AC_I-dependent response.

Next, we pretreated WT (**Figure 2.7G**) and $AC_I^{-/-}$ SAN cells (**Figure 2.7H**) with methyl-β-cyclodextrin (MβCD, 100 μM), a cholesterol remover and caveolar disruptor, after transfection with the three biosensors. MβCD did not significantly alter local cAMP levels at the membrane region but caused a significant increase in cAMP production in the cytosol and the SR region in WT SAN cells after β-AR stimulation. In contrast, MβCD pretreatment in $AC_I^{-/-}$ SAN cells significantly negated the decay in cAMP levels in the cytosol, at the membrane and the SR regions. Subsequently, simultaneous pretreatment with cilostamide and rolipram (cilo+roli, 10 μM each), which are PDE3 and PDE4 inhibitors, respectively, produced similar effects to cAMP levels as MβCD in $AC_I^{-/-}$ SAN cells (**Figures 2.7I-J**). The results were not observed when PDE2, PDE3, or PDE4 inhibitors were applied alone (**Supplementary Figure 2.11**). These results suggest compartmentalization of multiple PDEs and/or their signaling partners via caveolae scaffolding is necessary for regulating local cAMP levels. Collectively, these data support AC_I's critical roles in maintaining the sustained increase of local cAMP required for heart rate responses to *β*-AR stimulation.

DISCUSSION

There are current gaps in our knowledge regarding the dominant AC isoforms of ACs and the specific roles of Ca^{2+}-activated ACs in the SAN. We, therefore, took advantage of SAN-specific CRISPR/Cas9 AC_I-targeted gene silencing and AC_I global knockout mice to determine AC_I's functional significance. The novelty of our study stems from pivotal findings utilizing an array of new and complementary techniques. In stark contrast to atrial and ventricular myocytes, we identify the Ca^{2+}-activated AC_I as the predominant isoform mediating cAMP signaling in SAN that resides within a functional microdomain with Cav-3, HCN4, $Ca_v1.2$, and RyR-2 (**Figure 2.8**). Global or SAN-specific knockout of AC_I results in SND and a significant decrease in heart rate regulation by β-AR stimulation. With pharmacological blockade of the autonomic nervous system *in vivo*, $AC_I^{-/-}$ mice show a lower

intrinsic heart rate. Additionally, maximal β-AR stimulation results in sinus arrhythmia, corroborated by the CRISPR/Cas9 *AC$_I$* gene silencing model. The data strongly support AC$_I$'s critical role in mediating β-AR responses on SAN automaticity.

A diverse repertoire of ACs in SAN compared to atrial and ventricular myocytes: the unique roles of the Ca^{2+}-activated AC isoform in SAN function

cAMP is a critical second messenger that regulates cardiac contractility and chronotropy *via* activities of cAMP-responsive ion channels and pumps.[48, 49] Ten known AC isoforms are localized either in the plasma membrane (transmembrane ACs, AC$_{I–IX}$) or in the cytosol (soluble AC, AC$_X$), all of which produce cAMP. The impact, however, depends on a multitude of factors, including the relative expression and predominant AC isoforms as well as their compartmentalization with effector proteins. However, there exists uncertainty regarding the predominant isoforms and their functional roles in the SAN. In contrast to atrial and ventricular myocytes that express mainly AC$_V$ and AC$_{VI}$ isoforms,[20] we demonstrate diverse AC expression at the transcript and protein levels in mouse SAN cells, with AC$_I$ as the predominant isoform, followed by AC$_{VI}$, AC$_{III}$, AC$_{IV}$ and AC$_{VII}$. The relative abundance and differential expression of the AC isoforms in SAN compared to cardiomyocytes suggest a critical role of AC$_I$ in the SAN function. AC$_I$ is known to be critically involved in learning and memory formation.[50] Moreover, AC$_I$-deficient mice were reported to have disrupted retinotopic ordering. The phenotype can be mimicked by blockade of AP firing.[51, 52] Indeed, SAN cells show a higher basal level of cAMP and PKA than ventricular myocytes.[53] AC$_I$, which is a Ca^{2+}-activated AC isoform, likely contributes to the higher basal level of cAMP *via* positive feedback by intracellular Ca^{2+}.[54]

AC$_I$'s role in SAN automaticity

Recent evidence suggests that both membrane and Ca^{2+} clocks jointly regulate SAN automaticity, and ACs significantly contribute to the coupled clock.[54] Robinson et al.[55] demonstrated the over-expression of AC$_I$, but not AC$_{VI}$, increased cellular cAMP concentration and accelerated beating rate in

cultured neonatal rat ventricular myocytes. AC_I overexpression also increased peak $I_{Ca,L,}$ and the sensitivity of HCN4 to β-AR stimulation.[55] Our current study demonstrates that AC_I ablation significantly blunted β-AR modulation of SAN automaticity (**Figure 2.3**). Mechanistically, knockout of *AC_I* significantly impairs β-AR stimulation of LCRs (**Figure 2.4**), $I_{Ca,L}$ (**Figure 2.5**), I_f (**Figure 2.6**) and AC-dependent cAMP signaling (**Figure 2.7**) leading to irregularity in AP firing with significant periods of AP cessations. The bursting activities of the spontaneous APs observed in the knockout mice are reminiscence of the behaviors observed in the previously reported *NCX* knockout mice.[56] NCX represents the primary Ca^{2+} extrusion mechanism in SAN cells. A decrease in NCX function results in a gradual accumulation of local Ca^{2+} concentration and an increase in the activation of small conductance Ca^{2+}-activated K^+ (SK) currents, documented to be expressed in pacemaking cells,[56] leading to periods of cessation of firing activities. Future studies are required to decipher the intricate interplay of I_{Ca}, NCX, and SK currents in the bursting activities observed in the *$AC_I^{-/-}$* SAN cells. Additionally, CaTs show evidence of Ca^{2+} alternans with a significant increase in the time constant of decay (τ_{decay}) in *$AC_I^{-/-}$* SAN cells. The findings are consistent with a significant decrease in SR Ca^{2+} reuptake by SR Ca^{2+}-ATPase, as recently demonstrated in ventricular myocytes.[57] Knockout of *AC_I* in SAN cells is expected to decrease cAMP-mediated, PKA-dependent phosphorylation of SR proteins, including phospholamban, which may be one of the mechanisms for the increased τ_{decay}.

Functional Compartmentalization of AC_I in the SAN

Synchronization of the coupled clock in the SAN is restricted to precise subcellular microdomains with discrete clusters of ion channels, transporters and regulatory receptors working in concert.[58] Caveolin serves as the scaffolding protein to compartmentalize specialized proteins to initiate diverse molecular signaling.[59] Our group has previously demonstrated that AC_{VI} is localized in the plasma membrane outside the T-tubule in ventricular myocytes[15]. In contrast, AC_V is localized mainly in the T-tubular region, and the direct protein-protein interaction between Cav-3 with AC_V and PDEs is responsible for the compartmentalization of AC_V signaling.[15] Ca^{2+}-activated AC_I and AC_{VIII} are localized within lipid raft

microdomains in the SAN.[17] Mutations in caveolin-1 binding sites impaired AC_{VIII} N-linked glycosylation, and its plasma membrane targeting and functionality.[60] Our current study shows co-localization of AC_I and Cav-3, as well as HCN4, $Ca_v1.2$, and RyR-2 within microdomains of <40 nm based on PLA (**Figure 2.1**). The colocalization was further supported using functional analyses, showing a significantly blunted response of LCRs, I_f and $I_{Ca,L}$ to β-AR stimulation in $AC_I^{-/-}$ SAN cells. In contrast, there are no significant changes in β-AR responses for $I_{Ca,T}$. These data support functional microdomains that play a critical role in the Ca^{2+}-mediated activation of AC_I with the coupled clock.

Closer analyses demonstrate that the effects of AC_I ablation on the β-AR modulation are distinct among the three downstream targets in the coupled clock, LCRs, $I_{Ca,L}$, and I_f. Specifically, AC_I knockout significantly negated the enhancement of LCRs and I_f, with no changes in spark rates, amplitude, FWHM, and FDHM for LCRs and no enhancement in current density or activation kinetics of I_f after β-AR stimulation. In contrast, AC_I knockout results in only diminished effects on $I_{Ca,L}$. The findings suggest that RyR2 and HCN4 channels may form compartmentalization with AC_I almost exclusively. In contrast, Ca^{2+} channels (or possibly different isoforms of Ca^{2+} channels) may form functional units with distinct isoforms of ACs, including AC_I. We have previously shown the functional expression of both $Ca_v1.2$ and $Ca_v1.3$ L-type Ca^{2+} channels in SAN.[28] Future studies are required to decipher the functional significance of compartmentalization of different isoforms of Ca^{2+} channels with ACs.

Critical roles of AC_I in the sustained rise of local cAMP under β-AR stimulation

To directly quantify local cAMP levels, we used FRET-based cAMP biosensors localized to the cytosol, at the plasma membrane or the SR region. The local cAMP responses to β-AR stimulation are significantly blunted in all three regions in $AC_I^{-/-}$ SAN cells (**Figure 2.7**). There is an initial rise in local cAMP levels with β-AR stimulation from other AC isoforms. However, the effects of β-AR stimulation failed to sustain over time, suggesting AC_I's critical roles in sustaining local cAMP in the cytosol, at the plasma membrane and the SR region.

The effects of MβCD (**Figure 2.7G**) on removing cholesterol and disrupting lipid rafts and caveolar domains[61] in WT SAN cells are entirely mirrored by the synergistic effects of PDE3 and PDE4 inhibitors (**Figure 2.7I**), with a pronounced enhancement of local cAMP at the SR. The findings suggest that AC_I's actions at these functional microdomains are balanced and modulated by the localized effects of PDE3 and PDE4 that degrade cAMP. In $AC_I^{-/-}$ SAN cells, the lack of a sustained rise in the local cAMP by β-AR stimulation is negated by MβCD (**Figure 2.7H**) or the combination of PDE3 and PDE4 inhibitors (**Figure 2.7J**), suggesting additional compartmentalization of other AC isoforms with PDE3 and PDE4. Future studies are needed to investigate functional microdomains of other AC isoforms in SAN cells.

In conclusion, SAN cells express a diverse repertoire of ACs with AC_I as the predominant isoform. The diversity of ACs in SAN cells likely provides the needed safety factor for the critical pacemaking activities in the heart. AC_I isoform plays exclusive roles in the chronotropic regulation of the heart with no discernable actions on cardiac systolic or diastolic function. Due to its central characteristic as a Ca^{2+}-activated isoform, AC_I is critical in the sustained rise in local cAMP during β-AR stimulation. Both RyR2 and HCN channels of the coupled clock form functional microdomains almost exclusively with AC_I, while L-type Ca^{2+} channels or different isoforms of L-type Ca^{2+} channels likely form compartmentalization with different AC isoforms. Genetic ablation of AC_I results in SND *in vivo* and impaired SAN automaticity *in vitro*. Collectively, our data suggest a crucial role for AC_I in a functional microdomain with important Ca^{2+} handling proteins and HCN4 channels, that provide critical feedback to, and are driven by, the Ca^{2+}-activated AC_I (**Figure 2.8**).

ACKNOWLEDGEMENTS

This study was supported by American Heart Association (AHA) Predoctoral Award 18PRE34030199 (LR); Postdoctoral Fellowship from NIH T32 Training Grant in Basic & Translational Cardiovascular Science T32 HL086350 and NIH F32 HL149288 (PNT); NIH R01 HL085727, NIH R01 HL085844, NIH R01 HL137228, NIH S10 OD010389 Core Equipment Grant, and VA Merit Review Grant I01 BX000576 and I01 CX001490 (NC); BX005100 (YKX); NIH R56 HL138392 (XDZ); NIH P01 AG051443, NIH R01 DC015252, and NIH R01 DC015135 (ENY); NIH HL147263 (YKX); NIH R01HL098200 and R01HL149127 (MFN). MZ was supported by the British heart Foundation (PG/15/5/31110 and RG/17/6/32944).

The mouse strain HCN4-GCaMP8 was developed by CHROMusTM which is supported by the National Heart Lung Blood Institute of the National Institute of Health under award number R24HL120847.

We would like to thank Dr. Chao-Yin Chen for the use of the ECG telemetry, Dr. Padmini Sirish for helping with plasmid orders, Dr. Ingrid Brust-Mascher for technical support, and James L. Overton, Richard Q. Ngo, Carol E. Nader, Wilson Xu, and Michael J. Haddad for their administrative and mouse colony support.

REFERENCES

1. John Roy M and Kumar S. Sinus Node and Atrial Arrhythmias. *Circulation*. 2016;133:1892-1900.

2. Jensen PN, Gronroos NN, Chen LY, Folsom AR, deFilippi C, Heckbert SR and Alonso A. Incidence of and Risk Factors for Sick Sinus Syndrome in the General Population. *Journal of the American College of Cardiology*. 2014;64:531-538.

3. Virani Salim S, Alonso A, Aparicio Hugo J, Benjamin Emelia J, Bittencourt Marcio S, Callaway Clifton W, Carson April P, Chamberlain Alanna M, Cheng S, Delling Francesca N, Elkind Mitchell SV, Evenson Kelly R, Ferguson Jane F, Gupta Deepak K, Khan Sadiya S, Kissela Brett M, Knutson Kristen L, Lee Chong D, Lewis Tené T, Liu J, Loop Matthew S, Lutsey Pamela L, Ma J, Mackey J, Martin Seth S, Matchar David B, Mussolino Michael E, Navaneethan Sankar D, Perak Amanda M, Roth Gregory A, Samad Z, Satou Gary M, Schroeder Emily B, Shah Svati H, Shay Christina M, Stokes A, VanWagner Lisa B, Wang N-Y, Tsao Connie W and null n. Heart Disease and Stroke Statistics—2021 Update. *Circulation*. 2021;143:e254-e743.

4. Ferrer MI. The sick sinus syndrome in atrial disease. *JAMA*. 1968;206:645-6.

5. Dobrzynski H, Boyett MR and Anderson RH. New insights into pacemaker activity: promoting understanding of sick sinus syndrome. *Circulation*. 2007;115:1921-32.

6. Vardas PE, Simantirakis EN and Kanoupakis EM. New developments in cardiac pacemakers. *Circulation*. 2013;127:2343-50.

7. Cingolani E, Goldhaber JI and Marban E. Next-generation pacemakers: from small devices to biological pacemakers. *Nat Rev Cardiol*. 2018;15:139-150.

8. Chandler NJ, Greener ID, Tellez JO, Inada S, Musa H, Molenaar P, Difrancesco D, Baruscotti M, Longhi R, Anderson RH, Billeter R, Sharma V, Sigg DC, Boyett MR and Dobrzynski H. Molecular architecture of the human sinus node: insights into the function of the cardiac pacemaker. *Circulation*. 2009;119:1562-75.

9. Fedorov VV, Glukhov AV and Chang R. Conduction barriers and pathways of the sinoatrial pacemaker complex: their role in normal rhythm and atrial arrhythmias. *Am J Physiol Heart Circ Physiol*. 2012;302:H1773-83.

10. Irisawa H, Brown HF and Giles W. Cardiac pacemaking in the sinoatrial node. *Physiol Rev*. 1993;73:197-227.

11. Sutherland EW, Oye I and Butcher RW. The Action of Epinephrine and the Role of the Adenyl Cyclase System in Hormone Action. *Recent Prog Horm Res*. 1965;21:623-46.

12. Kamenetsky M, Middelhaufe S, Bank EM, Levin LR, Buck J and Steegborn C. Molecular details of cAMP generation in mammalian cells: a tale of two systems. *J Mol Biol*. 2006;362:623-39.

13. Sutherland EW and Robison GA. The role of cyclic-3',5'-AMP in responses to catecholamines and other hormones. *Pharmacol Rev*. 1966;18:145-61.

14. Halls ML and Cooper DMF. Adenylyl cyclase signalling complexes - Pharmacological challenges and opportunities. *Pharmacol Ther*. 2017;172:171-180.

15. Timofeyev V, Myers RE, Kim HJ, Woltz RL, Sirish P, Heiserman JP, Li N, Singapuri A, Tang T, Yarov-Yarovoy V, Yamoah EN, Hammond HK and Chiamvimonvat N. Adenylyl cyclase subtype-specific compartmentalization: differential regulation of L-type Ca2+ current in ventricular myocytes. *Circ Res*. 2013;112:1567-76.

16. Mattick P, Parrington J, Odia E, Simpson A, Collins T and Terrar D. Ca2+-stimulated adenylyl cyclase isoform AC1 is preferentially expressed in guinea-pig sino-atrial node cells and modulates the I(f) pacemaker current. *J Physiol*. 2007;582:1195-203.

17. Younes A, Lyashkov AE, Graham D, Sheydina A, Volkova MV, Mitsak M, Vinogradova TM, Lukyanenko YO, Li Y, Ruknudin AM, Boheler KR, van Eyk J and Lakatta EG. Ca(2+) -stimulated basal adenylyl cyclase activity localization in membrane lipid microdomains of cardiac sinoatrial nodal pacemaker cells. *J Biol Chem*. 2008;283:14461-8.

18. Wu Z, Wong ST and Storms DR. Modification of the calcium and calmodulin sensitivity of the type I adenylyl cyclase by mutagenesis of its calmodulin binding domain. *J Biol Chem*. 1993;268:23766-8.

19. Cali JJ, Zwaagstra JC, Mons N, Cooper DM and Krupinski J. Type VIII adenylyl cyclase. A Ca2+/calmodulin-stimulated enzyme expressed in discrete regions of rat brain. *J Biol Chem*. 1994;269:12190-5.

20. Willoughby D and Cooper DM. Organization and Ca2+ regulation of adenylyl cyclases in cAMP microdomains. *Physiol Rev*. 2007;87:965-1010.

21. Maltsev VA and Lakatta EG. The funny current in the context of the coupled-clock pacemaker cell system. *Heart Rhythm*. 2012;9:302-7.

22. Wu ZL, Thomas SA, Villacres EC, Xia Z, Simmons ML, Chavkin C, Palmiter RD and Storm DR. Altered behavior and long-term potentiation in type I adenylyl cyclase mutant mice. *Proc Natl Acad Sci U S A*. 1995;92:220-4.

23. Bosse KE, Ghoddoussi F, Eapen AT, Charlton JL, Susick LL, Desai K, Berkowitz BA, Perrine SA and Conti AC. Calcium/calmodulin-stimulated adenylyl cyclases 1 and 8 regulate reward-related brain activity and ethanol consumption. *Brain Imaging Behav*. 2019;13:396-407.

24. Mangoni ME and Nargeot J. Properties of the hyperpolarization-activated current (I(f)) in isolated mouse sino-atrial cells. *Cardiovasc Res*. 2001;52:51-64.

25. Vinogradova TM, Zhou YY, Bogdanov KY, Yang D, Kuschel M, Cheng H and Xiao RP. Sinoatrial node pacemaker activity requires Ca(2+)/calmodulin-dependent protein kinase II activation. *Circ Res*. 2000;87:760-7.

26. Sharpe EJ, St Clair JR and Proenza C. Methods for the Isolation, Culture, and Functional Characterization of Sinoatrial Node Myocytes from Adult Mice. *J Vis Exp*. 2016:54555.

27. Fenske S, Pröbstle R, Auer F, Hassan S, Marks V, Pauza DH, Biel M and Wahl-Schott C. Comprehensive multilevel in vivo and in vitro analysis of heart rate fluctuations in mice by ECG telemetry and electrophysiology. *Nature Protocols*. 2016;11:61-86.

28. Zhang Z, Xu Y, Song H, Rodriguez J, Tuteja D, Namkung Y, Shin HS and Chiamvimonvat N. Functional Roles of $Ca_v1.3$ (α_{1D}) calcium channel in sinoatrial nodes: insight gained using gene-targeted null mutant mice. *Circ Res*. 2002;90:981-7.

29. Yang L, Titlow J, Ennis D, Smith C, Mitchell J, Young FL, Waddell S, Ish-Horowicz D and Davis I. Single molecule fluorescence in situ hybridisation for quantitating post-transcriptional regulation in Drosophila brains. *Methods*. 2017;126:166-176.

30. Li N, Timofeyev V, Tuteja D, Xu D, Lu L, Zhang Q, Zhang Z, Singapuri A, Albert TR, Rajagopal AV, Bond CT, Periasamy M, Adelman J and Chiamvimonvat N. Ablation of a Ca2+-activated K+ channel (SK2 channel) results in action potential prolongation in atrial myocytes and atrial fibrillation. *J Physiol*. 2009;587:1087-100.

31. Thai PN, Daugherty DJ, Frederich BJ, Lu X, Deng W, Bers DM, Dedkova EN and Schaefer S. Cardiac-specific Conditional Knockout of the 18-kDa Mitochondrial Translocator Protein Protects from Pressure Overload Induced Heart Failure. *Sci Rep*. 2018;8:16213.

32. Lee FK, Lee JC, Shui B, Reining S, Jibilian M, Small DM, Jones JS, Allan-Rahill NH, Lamont MRE, Rizzo MA, Tajada S, Navedo MF, Santana LF, Nishimura N and Kotlikoff MI. Genetically Engineered Mice for Combinatorial Cardiovascular Optobiology. *bioRxiv*. 2021:2021.01.21.427692.

33. Gao Z, Rasmussen TP, Li Y, Kutschke W, Koval OM, Wu Y, Wu Y, Hall DD, Joiner ML, Wu XQ, Swaminathan PD, Purohit A, Zimmerman K, Weiss RM, Philipson KD, Song LS, Hund TJ and Anderson ME. Genetic inhibition of Na+-Ca2+ exchanger current disables fight or flight sinoatrial node activity without affecting resting heart rate. *Circ Res*. 2013;112:309-17.

34. Swaminathan PD, Purohit A, Soni S, Voigt N, Singh MV, Glukhov AV, Gao Z, He BJ, Luczak ED, Joiner ML, Kutschke W, Yang J, Donahue JK, Weiss RM, Grumbach IM, Ogawa M, Chen PS, Efimov I, Dobrev D, Mohler PJ, Hund TJ and Anderson ME. Oxidized CaMKII causes cardiac sinus node dysfunction in mice. *J Clin Invest*. 2011;121:3277-88.

35. Fredriksson S, Gullberg M, Jarvius J, Olsson C, Pietras K, Gústafsdóttir SM, Ostman A and Landegren U. Protein detection using proximity-dependent DNA ligation assays. *Nat Biotechnol*. 2002;20:473-7.

36. Reddy GR, West TM, Jian Z, Jaradeh M, Shi Q, Wang Y, Chen-Izu Y and Xiang YK. Illuminating cell signaling with genetically encoded FRET biosensors in adult mouse cardiomyocytes. *J Gen Physiol*. 2018;150:1567-1582.

37. Surdo NC, Berrera M, Koschinski A, Brescia M, Machado MR, Carr C, Wright P, Gorelik J, Morotti S, Grandi E, Bers DM, Pantano S and Zaccolo M. FRET biosensor uncovers cAMP nano-domains at β-adrenergic targets that dictate precise tuning of cardiac contractility. *Nat Commun*. 2017;8:15031.

38. Luo J, Deng ZL, Luo X, Tang N, Song WX, Chen J, Sharff KA, Luu HH, Haydon RC, Kinzler KW, Vogelstein B and He TC. A protocol for rapid generation of recombinant adenoviruses using the

AdEasy system. *Nat Protoc*. 2007;2:1236-47.

39. Vaidyanathan R, Reilly L and Eckhardt LL. Caveolin-3 Microdomain: Arrhythmia Implications for Potassium Inward Rectifier and Cardiac Sodium Channel. *Front Physiol*. 2018;9:1548.

40. Tsunematsu T, Okumura S, Mototani Y, Ohnuki Y, Jin H, Cai W, Suita K, Sato I, Umemura M, Yokoyama U, Sato M, Fujita T and Ishikawa Y. Coupling of beta1-adrenergic receptor to type 5 adenylyl cyclase and its physiological relevance in cardiac myocytes. *Biochem Biophys Res Commun*. 2015;458:531-535.

41. Hsu PD, Lander ES and Zhang F. Development and applications of CRISPR-Cas9 for genome engineering. *Cell*. 2014;157:1262-78.

42. Doudna JA and Charpentier E. Genome editing. The new frontier of genome engineering with CRISPR-Cas9. *Science*. 2014;346:1258096.

43. Fenske S, Hennis K, Rotzer RD, Brox VF, Becirovic E, Scharr A, Gruner C, Ziegler T, Mehlfeld V, Brennan J, Efimov IR, Pauza AG, Moser M, Wotjak CT, Kupatt C, Gonner R, Zhang R, Zhang H, Zong X, Biel M and Wahl-Schott C. cAMP-dependent regulation of HCN4 controls the tonic entrainment process in sinoatrial node pacemaker cells. *Nat Commun*. 2020;11:5555.

44. Bychkov R, Juhaszova M, Tsutsui K, Coletta C, Stern MD, Maltsev VA and Lakatta EG. Synchronized Cardiac Impulses Emerge From Heterogeneous Local Calcium Signals Within and Among Cells of Pacemaker Tissue. *JACC Clin Electrophysiol*. 2020;6:907-931.

45. Clancy CE and Santana LF. Evolving Discovery of the Origin of the Heartbeat: A New Perspective on Sinus Rhythm. *JACC Clin Electrophysiol*. 2020;6:932-934.

46. Laasmaa M, Karro N, Birkedal R and Vendelin M. IOCBIO Sparks detection and analysis software. *PeerJ*. 2019;7:e6652.

47. DiFrancesco D. The role of the funny current in pacemaker activity. *Circ Res*. 2010;106:434-46.

48. Boularan C and Gales C. Cardiac cAMP: production, hydrolysis, modulation and detection. *Front Pharmacol*. 2015;6:203.

49. Efendiev R and Dessauer CW. A kinase-anchoring proteins and adenylyl cyclase in cardiovascular physiology and pathology. *J Cardiovasc Pharmacol*. 2011;58:339-44.

50. Xia ZG, Refsdal CD, Merchant KM, Dorsa DM and Storm DR. Distribution of mRNA for the calmodulin-sensitive adenylate cyclase in rat brain: expression in areas associated with learning and memory. *Neuron*. 1991;6:431-43.

51. Nicol X, Muzerelle A, Rio JP, Metin C and Gaspar P. Requirement of adenylate cyclase 1 for the ephrin-A5-dependent retraction of exuberant retinal axons. *J Neurosci*. 2006;26:862-72.

52. Ravary A, Muzerelle A, Herve D, Pascoli V, Ba-Charvet KN, Girault JA, Welker E and Gaspar P. Adenylate cyclase 1 as a key actor in the refinement of retinal projection maps. *J Neurosci*. 2003;23:2228-38.

53. Vinogradova TM, Lyashkov AE, Zhu W, Ruknudin AM, Sirenko S, Yang D, Deo S, Barlow M, Johnson S, Caffrey JL, Zhou YY, Xiao RP, Cheng H, Stern MD, Maltsev VA and Lakatta EG. High basal protein kinase A-dependent phosphorylation drives rhythmic internal Ca2+ store oscillations and spontaneous beating of cardiac pacemaker cells. *Circ Res*. 2006;98:505-14.

54. Lakatta EG, Maltsev VA and Vinogradova TM. A coupled SYSTEM of intracellular Ca2+ clocks and surface membrane voltage clocks controls the timekeeping mechanism of the heart's pacemaker. *Circ Res*. 2010;106:659-73.

55. Kryukova YN, Protas L and Robinson RB. Ca2+-activated adenylyl cyclase 1 introduces Ca2+-dependence to beta-adrenergic stimulation of HCN2 current. *J Mol Cell Cardiol*. 2012;52:1233-9.

56. Torrente AG, Zhang R, Wang H, Zaini A, Kim B, Yue X, Philipson KD and Goldhaber JI. Contribution of small conductance K^+ channels to sinoatrial node pacemaker activity: insights from atrial-specific Na^+/Ca^{2+} exchange knockout mice. *J Physiol*. 2017;595:3847-3865.

57. Millet J, Aguilar-Sanchez Y, Kornyeyev D, Bazmi M, Fainstein D, Copello JA and Escobar AL. Thermal modulation of epicardial Ca^{2+} dynamics uncovers molecular mechanisms of Ca^{2+} alternans. *J Gen Physiol*. 2021;153.

58. Lang D and Glukhov AV. Functional Microdomains in Heart's Pacemaker: A Step Beyond Classical Electrophysiology and Remodeling. *Front Physiol*. 2018;9:1686.

59. Cohen AW, Hnasko R, Schubert W and Lisanti MP. Role of caveolae and caveolins in health and disease. *Physiol Rev*. 2004;84:1341-79.

60. Tabbasum VG and Cooper DMF. Structural and Functional Determinants of AC8 Trafficking, Targeting and Responsiveness in Lipid Raft Microdomains. *J Membr Biol*. 2019.

61. Zidovetzki R and Levitan I. Use of cyclodextrins to manipulate plasma membrane cholesterol content: evidence, misconceptions and control strategies. *Biochim Biophys Acta*. 2007;1768:1311-1324.

Figure 2.1

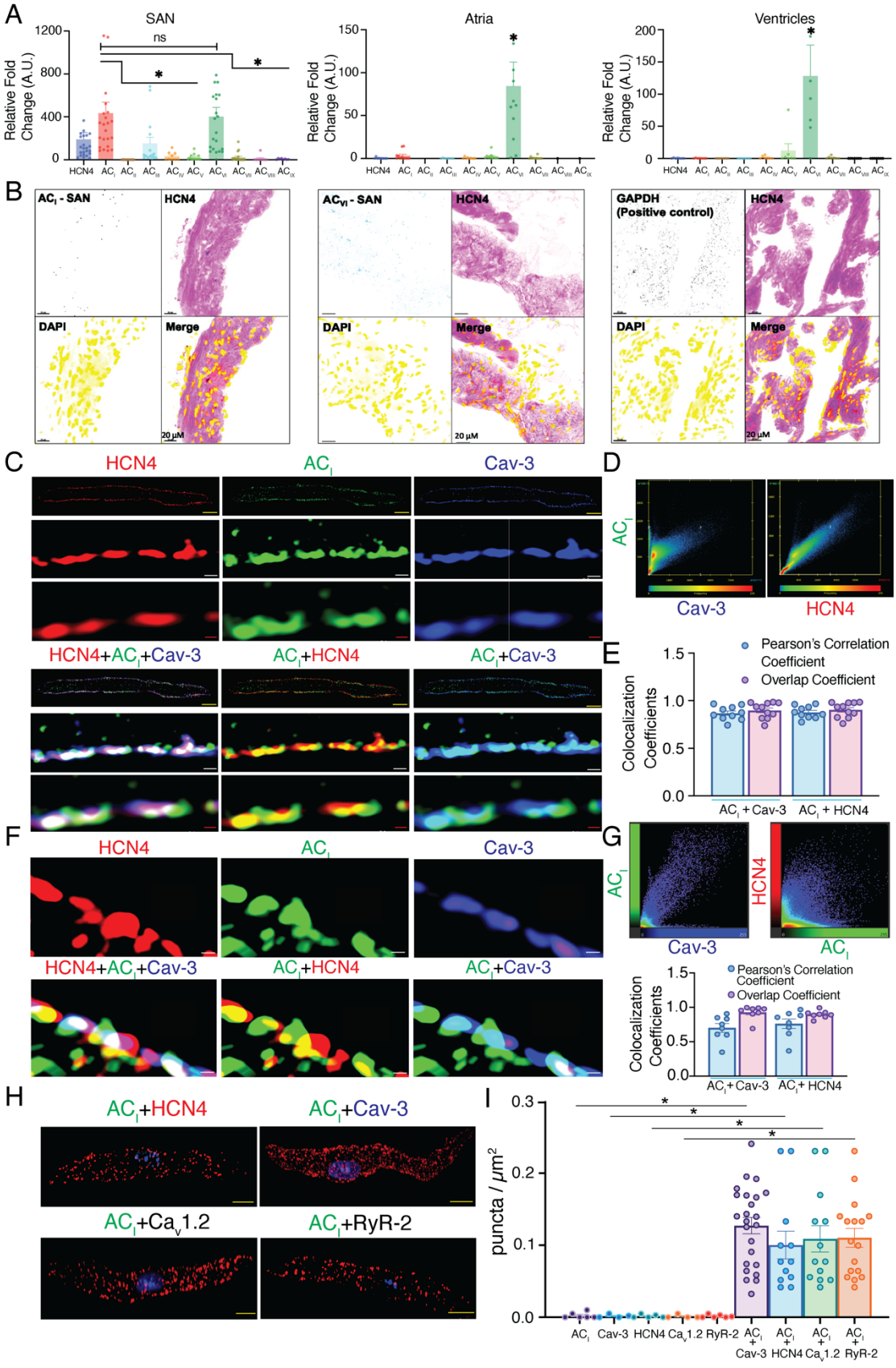
A
SAN
Atria
Ventricles
Relative Fold Change (A.U.)
ns
*
HCN4
B
AC$_I$ - SAN
AC$_{VI}$ - SAN
GAPDH (Positive control)
DAPI
Merge
20 µM
C
HCN4
AC$_I$
Cav-3
HCN4+AC$_I$+Cav-3
AC$_I$+HCN4
AC$_I$+Cav-3
D
AC$_I$
Cav-3
HCN4
E
Pearson's Correlation Coefficient
Overlap Coefficient
Colocalization Coefficients
AC$_I$ + Cav-3
AC$_I$ + HCN4
F
G
H
AC$_I$+HCN4
AC$_I$+Cav-3
AC$_I$+Ca$_V$1.2
AC$_I$+RyR-2
I
puncta / µm^2
AC$_I$ Cav-3 HCN4 Ca$_V$1.2 RyR-2
AC$_I$ + Cav-3
AC$_I$ + HCN4
AC$_I$ + Ca$_V$1.2
AC$_I$ + RyR-2

Figure 2.1. AC_I is the predominant isoform in the SAN, forming microdomains with key Ca^{2+} handling proteins and HCN4 channels. Summary data of relative abundance of $AC_{I\text{-}VIII}$ in single cells isolated from three regions of the heart. (**A**) Single-cell RT-qPCR from SAN, atria, and ventricles (n = 23, 11, 7 cells, respectively, from n=3-5 mice). (**B**) Representative smFISH images of AC_I, AC_{VI}, and GAPDH (positive control) mRNA expressions in the SAN tissue. HCN4 (pink) was used as a counterstain for SAN tissue, and DAPI (yellow) was used to stain the nuclei. (**C**) Representative high-resolution Airyscan images of isolated SAN cells stained with anti-HCN4 (red), AC_I (green) and Cav-3 (purple) antibodies. Images at higher magnifications are shown in the second and third rows for each group. Yellow, white and red scale bars are 10, 0.4 and 0.2 μm respectively. (**D**) Representative scattered plots of colocalization of AC_I with Cav-3 and HCN4 from Airyscan images. (**E**) Summary data of Pearson's correlation and overlap coefficients for AC_I and Cav-3 and AC_I and HCN4 from Airyscan images. n=10-11 cells from 4 mice. (**F**) Representative super-resolution STED images of isolated SAN cells triple-labeled for HCN4 (red), AC_I (green) and Cav-3 (purple). Scale bar: 0.2 μm. (*G*) Upper panel: representative scattered plots of colocalization of AC_I with Cav-3 and HCN4 from STED images. Lower panel: summary data of Pearson's correlation and overlap coefficients for AC_I and Cav-3 and AC_I and HCN4 from STED images, n=8 cells from 2 mice. (**H**) Representative images of PLA in SAN cells for AC_I with HCN4, Cav-3, $Ca_V1.2$, and RyR-2. Scale bar: 5 μm. (**I**) Summary of PLA data, n=12-24 cells from 4-6 mice per group. Data are expressed as mean±SEM. * $p<0.05$ by One-way ANOVA for multiple comparisons, followed by Kruskal-Wallis post hoc analyses.

Figure 2.2

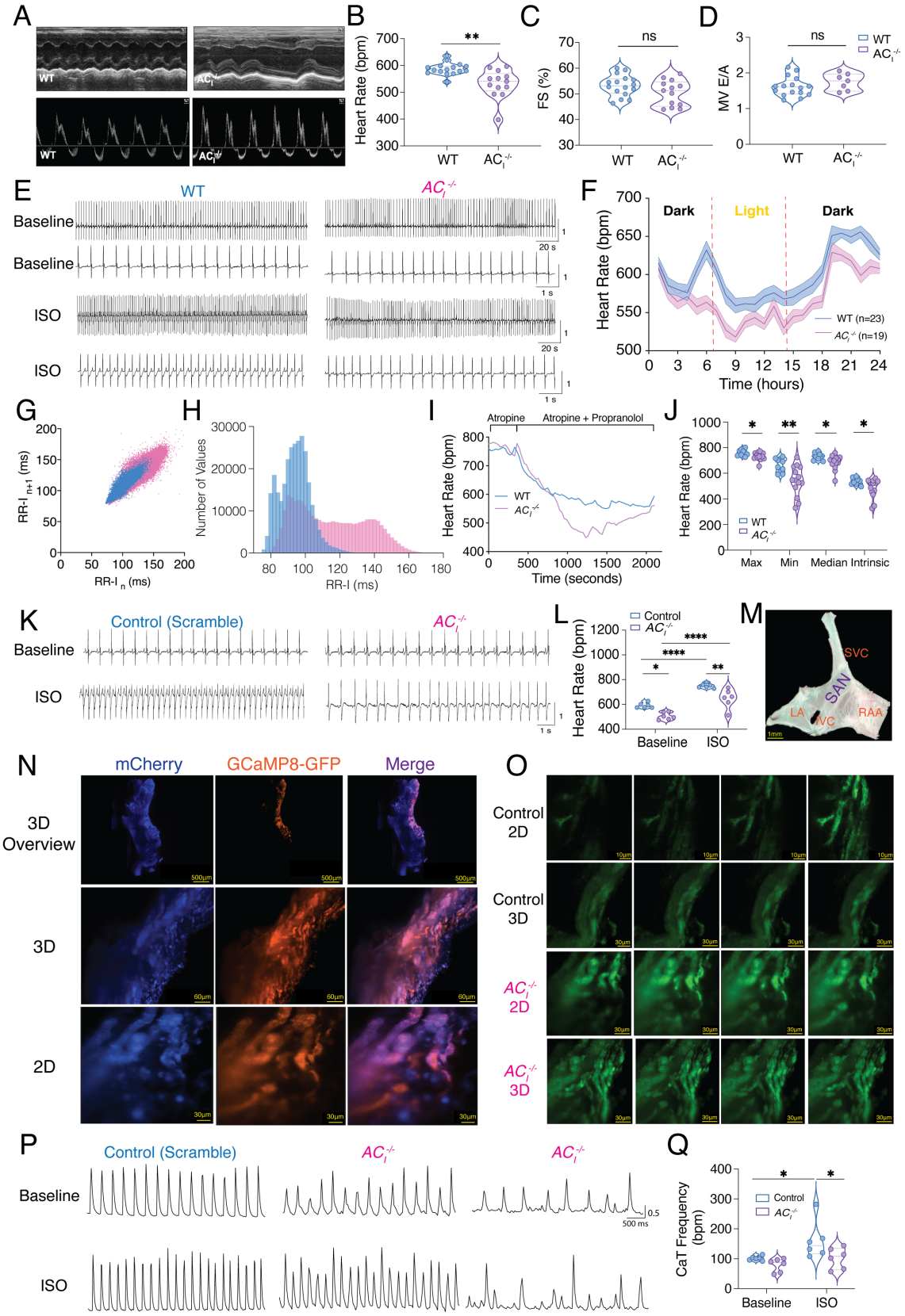
A
WT
AC$_I^{-/-}$
B
Heart Rate (bpm)
**
C
FS (%)
ns
D
MV E/A
ns
WT
AC$_I^{-/-}$
E
WT
AC$_I^{-/-}$
Baseline
ISO
20 s
1 s
F
Heart Rate (bpm)
Dark
Light
Dark
WT (n=23)
AC$_I^{-/-}$ (n=19)
Time (hours)
G
RR-I $_{n+1}$ (ms)
RR-I $_n$ (ms)
H
Number of Values
RR-I (ms)
I
Atropine
Atropine + Propranolol
Heart Rate (bpm)
Time (seconds)
J
Heart Rate (bpm)
Max
Min
Median Intrinsic
K
Control (Scramble)
AC$_I^{-/-}$
Baseline
ISO
L
Control
AC$_I^{-/-}$
Heart Rate (bpm)
Baseline
ISO
M
SVC
SAN
LA
IVC
RAA
1mm
N
mCherry
GCaMP8-GFP
Merge
3D Overview
3D
2D
O
Control 2D
Control 3D
AC$_I^{-/-}$ 2D
AC$_I^{-/-}$ 3D
P
Control (Scramble)
AC$_I^{-/-}$
AC$_I^{-/-}$
Baseline
ISO
500 ms
Q
CaT Frequency (bpm)
Control
AC$_I^{-/-}$
Baseline
ISO

Figure 2.2. *AC_1* knockout and SAN-specific *AC_1*-targeted gene silencing mice exhibit sinus node dysfunction. (**A**) Representative M-mode echocardiographic images for WT and *$AC_1^{-/-}$* mice. Summary data from echocardiography for (**B**) heart rate, (**C**) fractional shortening (FS), and (**D**) mitral valve (MV) E/A ratio. (**E**) Representative ECG tracings of WT and *$AC_1^{-/-}$* mice at baseline and after β-AR stimulation. (**F**) Heart rates (bpm) over 24-hour period recordings are plotted for WT and *$AC_1^{-/-}$* mice (data are expressed as mean±SEM; n = 23 and 19 for WT and *$AC_1^{-/-}$* mice, respectively). Heart rates were averaged after every hour for a 24-hour recording. (**G**) Heart rate variability, plotted as RR intervals (RR-I) for n and n+1 in ms. (**H**) The number of values for each RR-I was plotted as histograms. (**I**) Representative heart rate traces of WT and *$AC_1^{-/-}$* mice after injection of atropine, followed by propranolol to block autonomic nervous system. (**J**) Summary data of the maximum, minimum, median, and intrinsic heart rates from (**I**). (**K**) Representative surface ECG recordings for SAN-specific CRISPR/Cas9 mediated *AC_1*-targeted gene silencing mice at baseline and after ISO stimulation. Scrambled sequence was used for control. (**L**) Summary data for heart rate (bpm) at baseline and after ISO injection (n = 6 for each group). (**M**) SAN isolated from liposome-treated mice with the following landmarks. LA = left atrium. RAA = right atrial appendage. IVC = inferior vena cava. SVC = superior vena cava. (**N**) Representative images of SAN tissue with mCherry signal from the reporter gene and GFP signal from the genetically encoded HCN4-GCaMP8 transgenic mice. (**O**) Ca^{2+} signal is shown for WT and *$AC_1^{-/-}$* SAN tissue. (**P**) Representative CaT traces from SAN-specific CRISPR/Cas9 mediated *AC_1*-targeted gene silencing SAN tissue compared to control mice (treated with scrambled sequence) at baseline and after ISO stimulation. (**Q**) Summary data for CaT frequency (bpm). Summary data in **B-D**, **J**, **L and Q** are shown as violin plots with symbols within the plots representing individual data point and median as well as quartiles indicated as dashed line. *p<0.05, **p<0.01 by student's *t*-test (Panels **B-D** and **J**) or two-way ANOVA with Holm–Sidak multiple comparison post hoc analyses (Panels **L** and **Q**).

Figure 2.3

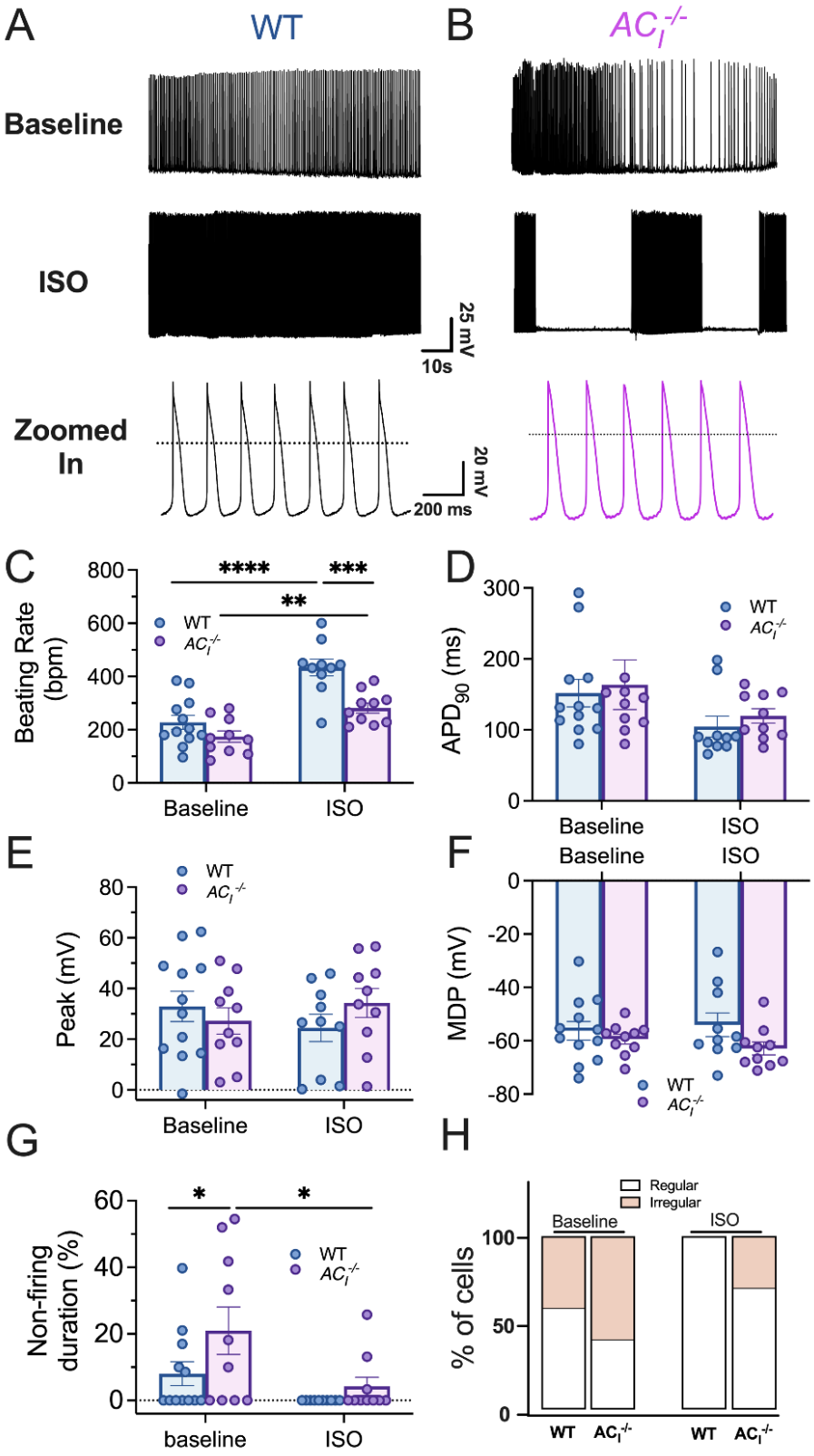
A
WT
B
AC$_I^{-/-}$
Baseline
ISO
25 mV
10s
Zoomed In
20 mV
200 ms
C
Beating Rate (bpm)
****
***
**
WT
AC$_I^{-/-}$
Baseline
ISO
D
APD$_{90}$ (ms)
E
Peak (mV)
F
MDP (mV)
G
Non-firing duration (%)
*
*
baseline
H
% of cells
Regular
Irregular
WT
AC$_I^{-/-}$

Figure 2.3. *$AC_I^{-/-}$* SAN cells exhibit reduced action potential firing frequency.

Representative traces of spontaneous APs at baseline and after ISO from (**A**) WT and (**B**) *$AC_I^{-/-}$* SAN cells. (**C**) Summary data of beating rate (bpm). (**D**) Action potential duration at 90% repolarization (APD_{90}), (**E**) peak potentials, and (**F**) maximum diastolic potentials. (**G**) Percentages of non-firing duration. (**H**) Percentages of cells that exhibited non-firing activity. n=10-12 cells from 5-6 mice per group. Data are expressed as mean±SEM. *$p<0.05$ using two-way ANOVA with Holm–Sidak multiple comparison post hoc analyses.

Figure 2.4

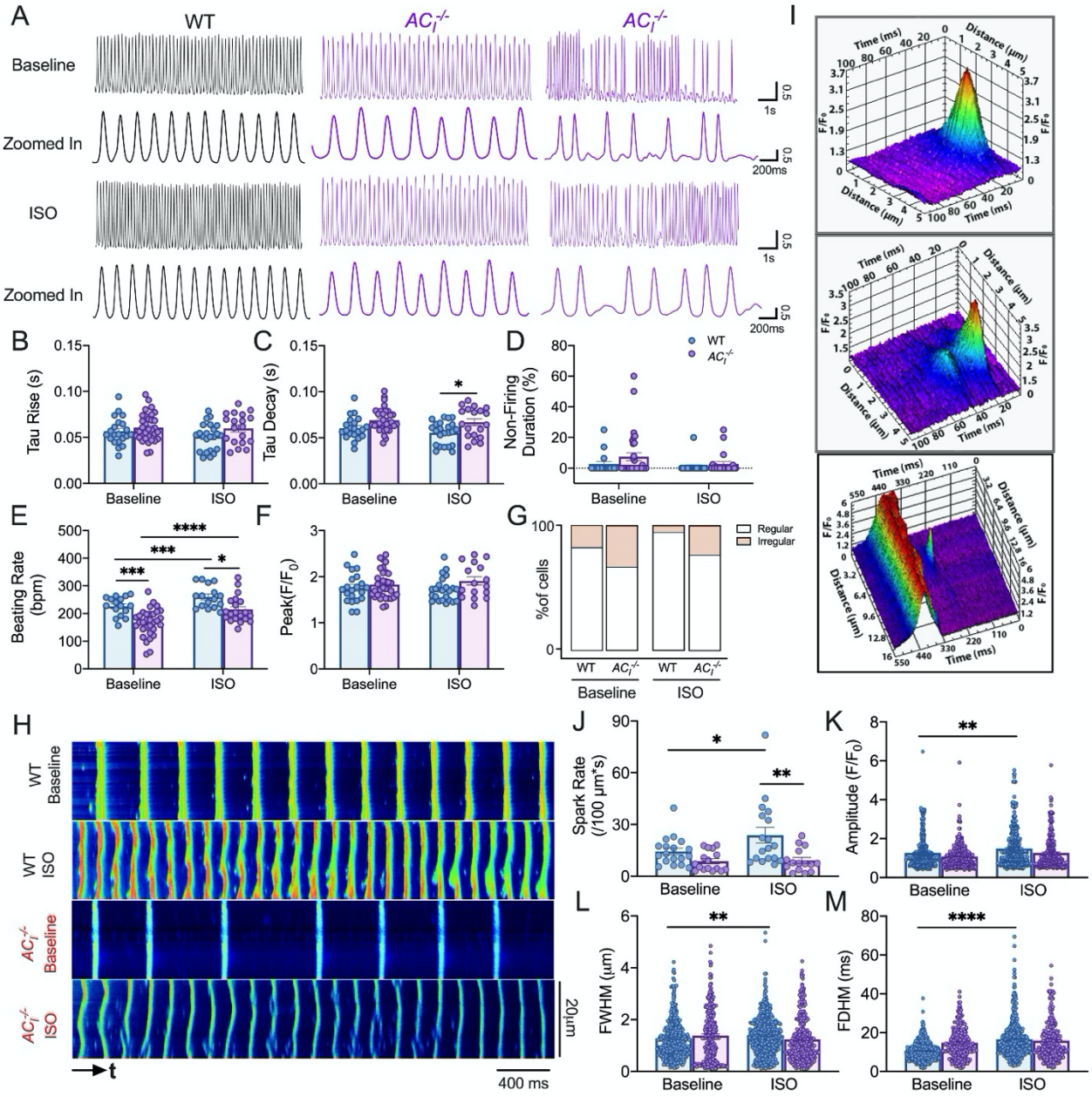

Figure 2.4. $AC_I^{-/-}$ SAN cells show an impaired β-AR response of Ca^{2+} transients (CaTs) and Ca^{2+} alternans and a complete lack of response of local Ca^{2+} release (LCR) to β-AR stimulation. (**A**) Representative whole-cell CaT traces of SAN cells from WT and $AC_I^{-/-}$ mice before and after ISO application. Summary data of (**B**) τ_{rise}, (**C**) τ_{decay}, (**D**) percentages of non-firing duration, (**E**) normalized

peak amplitude, (**F**) beating rate, and (**G**) percentage of cells exhibiting non-firing activity. Number of symbols in the bar graphs represents number of cells. n=19-33 cells from 6-7 mice per group. (**H**) Representative LCR recordings from WT and $AC_1^{-/-}$ SAN cells before and after ISO application. (**I**) Representative 3D reconstructions of Ca^{2+} sparks in WT SAN cells. (**J**) Summary data of spark rate, (**K**) amplitude, (**L**) full width at half maximum (FWHM), and (**M**) full duration at half maximum (FDHM). n=6-7 mice per group. 274-421 sparks from 15-20 cells were analyzed per group. Data are expressed as mean±SEM. *p<0.05 by two-way ANOVA, followed by Holm–Sidak multiple comparison post hoc analyses.

Figure 2.5

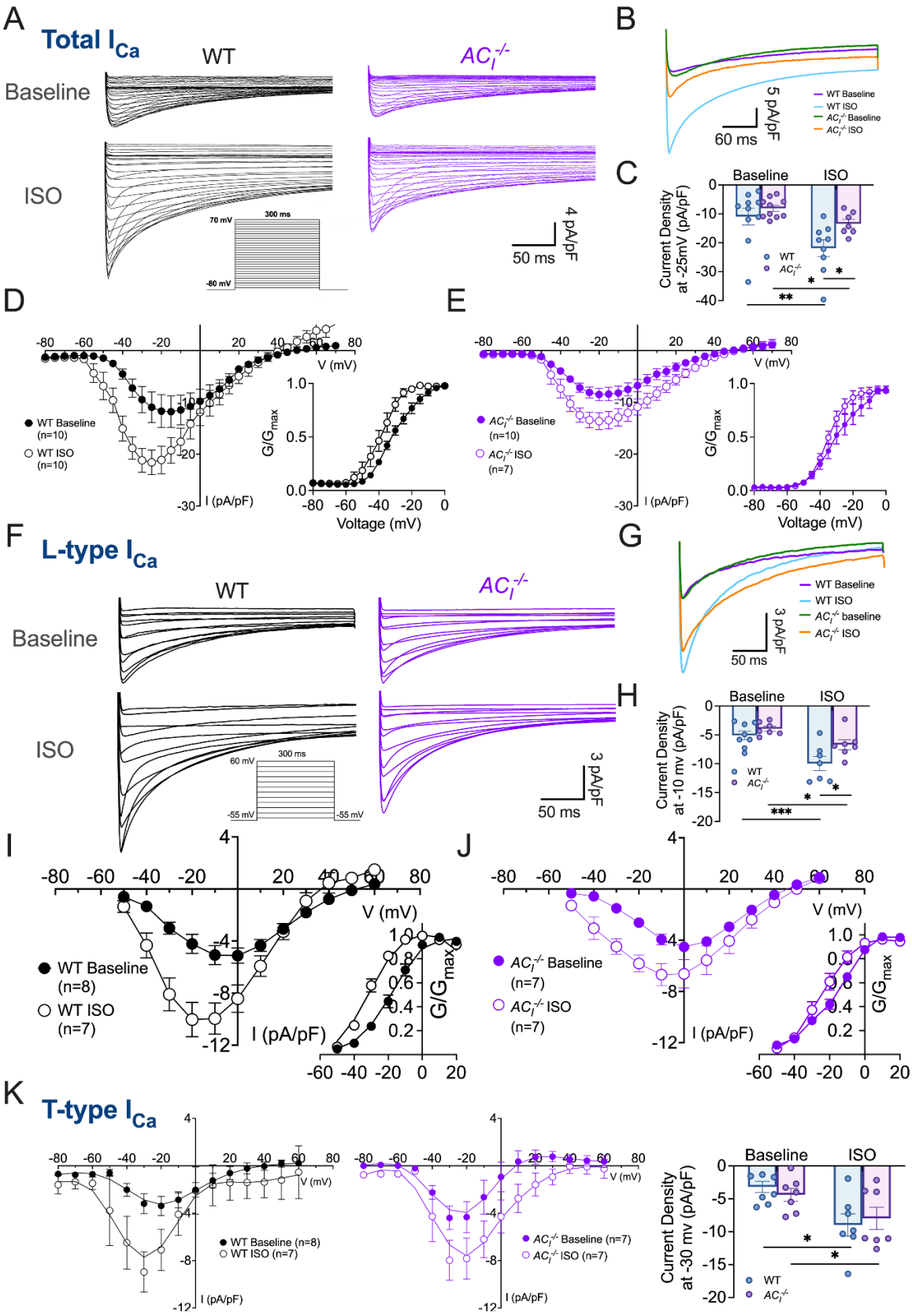
A
Total I_Ca
WT
AC_I^-/-
Baseline
ISO
70 mV
300 ms
-80 mV
4 pA/pF
50 ms
B
5 pA/pF
60 ms
WT Baseline
WT ISO
AC_I^-/- Baseline
AC_I^-/- ISO
C
Baseline
ISO
Current Density at -25mV (pA/pF)
WT
AC_I^-/-
D
V (mV)
WT Baseline (n=10)
WT ISO (n=10)
I (pA/pF)
G/G_max
Voltage (mV)
E
AC_I^-/- Baseline (n=10)
AC_I^-/- ISO (n=7)
F
L-type I_Ca
60 mV
-55 mV
G
3 pA/pF
H
Current Density at -10 mv (pA/pF)
I
WT Baseline (n=8)
WT ISO (n=7)
J
AC_I^-/- Baseline (n=7)
AC_I^-/- ISO (n=7)
K
T-type I_Ca
Current Density at -30 mv (pA/pF)

Figure 2.5. $AC_I^{-/-}$ SAN cells demonstrate a significant decrease in β-AR stimulation of $I_{Ca,L}$ but not $I_{Ca,T}$. (**A**) Representative traces of total I_{Ca} at baseline (top panels) and after ISO perfusion (bottom panels) in WT (left panels) and $AC_I^{-/-}$ SAN cells (right panels). Representative I_{Ca} traces were recorded using 300-ms test pulses from a holding potential of -80 mV to test potentials between -75 to +70 mV with 5 mV increments, using whole-cell patch-clamp mode. Representative traces for each group at a test pulse of -25 mV are shown in panel (**B**). (**C**) Summary data of current density at -25 mV. (**D, E**) Normalized I-V relationship of total Ca^{2+} currents and normalized conductance-voltage relationship before and after ISO stimulation in WT (**D**) and $AC_I^{-/-}$ (**E**) SAN cells. The normalized conductance-voltage relationship from **D** and **E** were fitted with a Boltzmann function ($V_{1/2}$ are -29.6±2.3 and -38.1±2.7 mV (P=0.025423) for WT SAN cells, while $V_{1/2}$ are -27.9±4.4 and -33.1±3.1 mV (P>0.05) for $AC_I^{-/-}$ SAN cells, before and after ISO, respectively. Slope factors are 7.4±0.5 and 3.6±0.4 (p=0.057848) for WT SAN cells and 8.8±2.0 and 6.199±1.281 (P>0.05) for $AC_I^{-/-}$ SAN cells, before and after ISO, respectively. (**F**) Representative traces of $I_{Ca,L}$ at baseline (top panels) and after ISO (bottom panels) in WT (left panels) and $AC_I^{-/-}$ (right panels) SAN cells. (**G**) Superimposition of representative traces for each group at a test potential of -10 mV. (**H**) Summary data of current density at -10 mV. (**I, J**) Normalized I-V relationship and normalized conductance-voltage relationship of $I_{Ca,L}$ before and after ISO perfusion in WT (**I**) and $AC_I^{-/-}$ (**J**) SAN cells. The normalized conductance-voltage relationship from **I** and **J** are fitted with a Boltzmann function ($V_{1/2}$ are -17.1±1.4 and -32.6±1.4 mV (P=0.000012) for WT SAN cells, while $V_{1/2}$ are -16.5±1.8 and -26.3 ±2.4 mV (p=0.000898) for $AC_I^{-/-}$ SAN cells, before and after ISO, respectively). p=0.018206 when comparing WT ISO with $AC_I^{-/-}$ ISO. Slope factors are 7.1±0.4 and 5.3±0.4 (p=0.02) for WT SAN cells and 8.5±0.7 and 6.8±0.4 (P=0.02) for $AC_I^{-/-}$ SAN cells, before and after ISO, respectively. (**K**) Normalized I-V relationship of $I_{Ca,T}$ before and after ISO perfusion in WT and $AC_I^{-/-}$ SAN cells are shown. Summary data of current density at -30 mV for each group are also displayed. All currents were normalized to the cell capacitance. n=7-10 from 4-5 mice per group. Data are expressed as mean±SEM. *p<0.05 by two-way ANOVA with Holm–Sidak multiple comparison post hoc analyses.

Figure 2.6

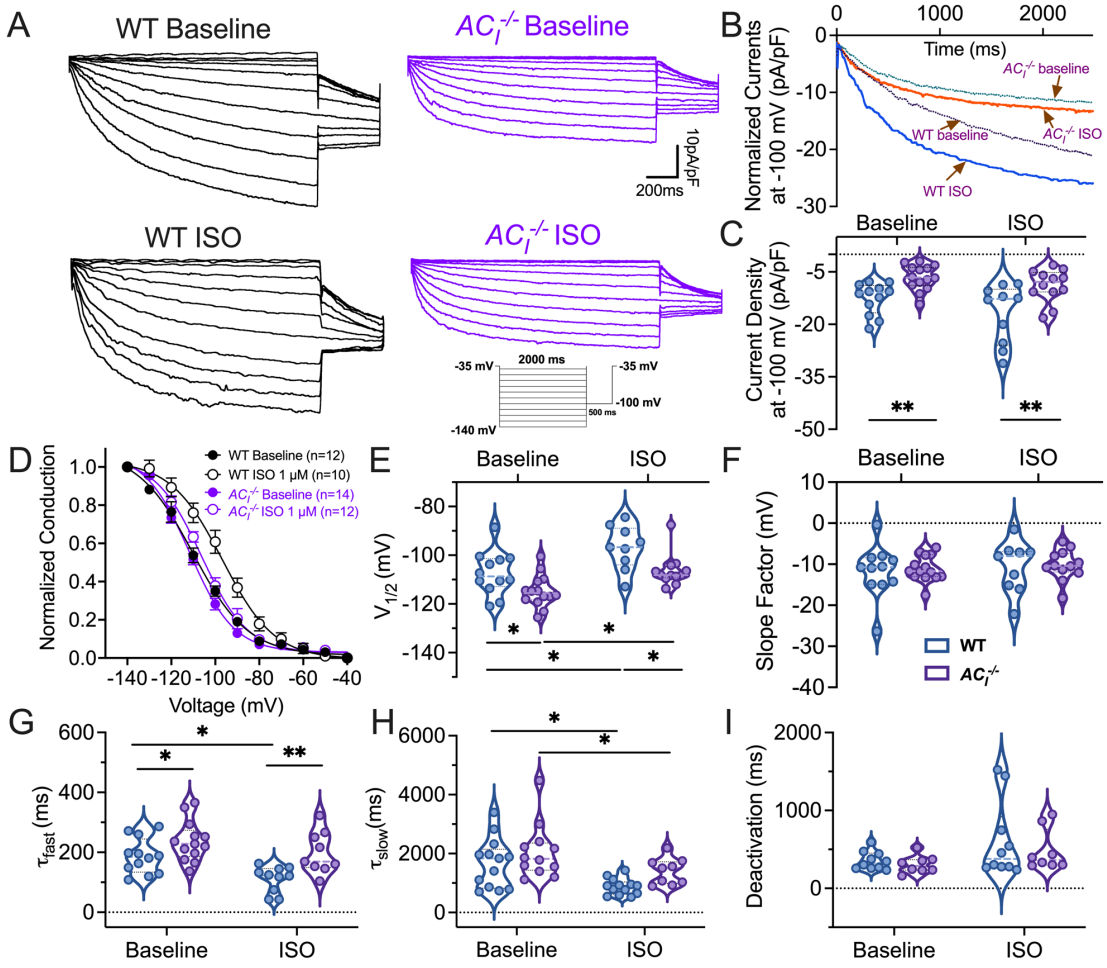

Figure 2.6. *AC$_I^{-/-}$* SAN cells show a complete lack of response of pacemaking current to *β*-AR stimulation. (**A**) Representative traces of I_f for WT and *AC$_I^{-/-}$* SAN cells before and after ISO administration. The inset shows a diagram of the voltage-clamp protocol from -140 mV to -40 mV in 10-mV increments from a holding potential of -35 mV. (**B**) Superimposed individual I_f traces from each group at -100 mV at baseline and after ISO. (**C**) Summary data of current density at -100 mV. (**D**) Normalized conductance at various voltages before and after ISO application, fitted using a Boltzmann function. Summary data for (**E**) half-activation voltage ($V_{1/2}$) (**F**) slope factor, (**G**) τ_{fast} (**H**) τ_{slow}, and (**I**) time constants of deactivation. n=10-14 cells from 4-5 mice per group. Data are expressed as mean±SEM in **C** and **E-I**. *p<0.05 by two-way ANOVA, followed by Holm–Sidak multiple comparison post hoc analyses.

Figure 2.7

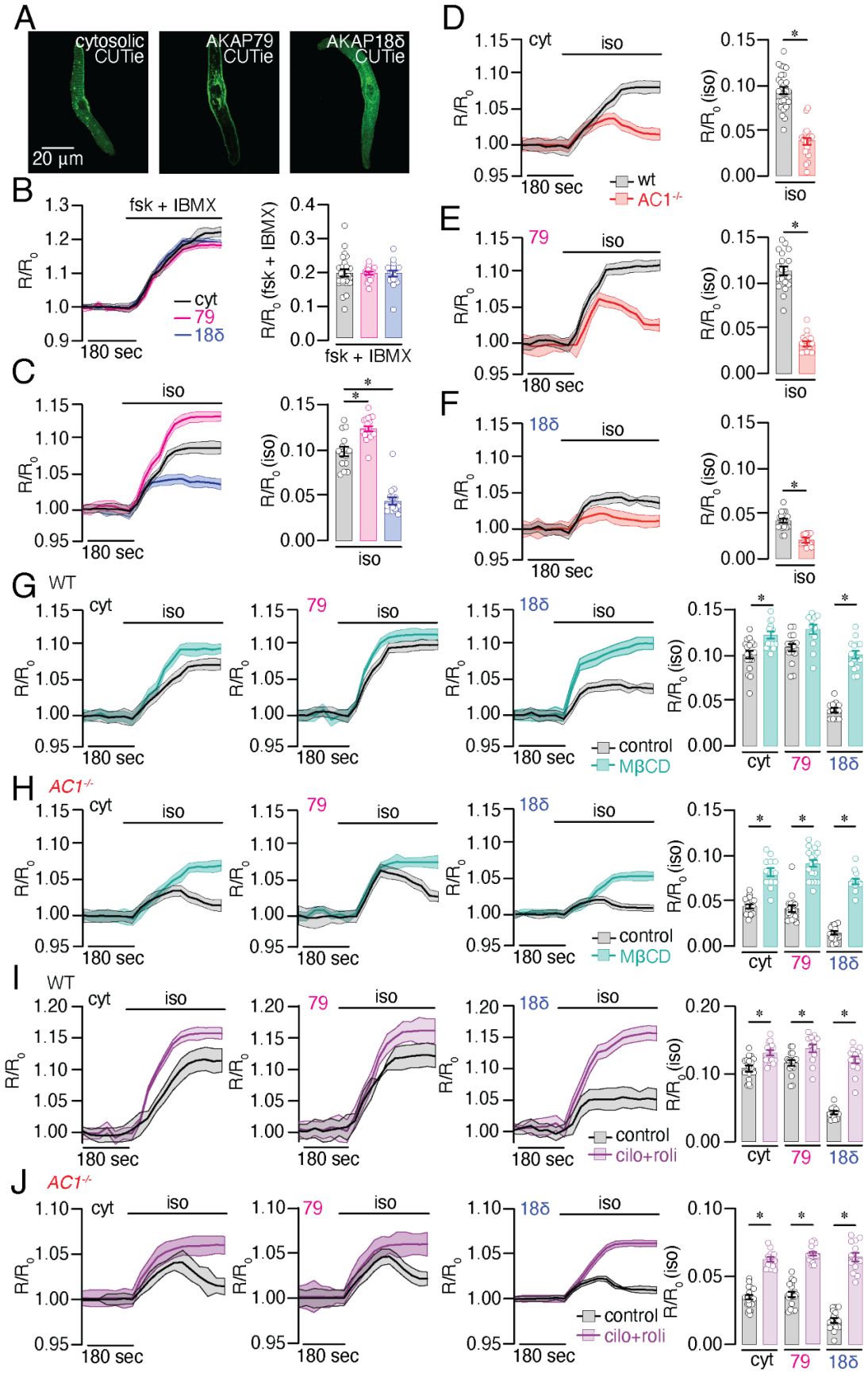
A
cytosolic CUTie
AKAP79 CUTie
AKAP18δ CUTie
20 µm
B
fsk + IBMX
R/R0
180 sec
cyt
79
18δ
R/R0 (fsk + IBMX)
fsk + IBMX
C
iso
R/R0 (iso)
D
cyt
iso
wt
AC1-/-
E
79
F
18δ
G
WT
control
MβCD
cyt
79
18δ
H
AC1-/-
I
WT
control
cilo+roli
J
AC1-/-

Figure 2.7. AC_I differentially regulates local cAMP signaling at functional microdomains in SAN cells. (**A**) Representative confocal images of SAN cells expressing CUTie sensors localized to the cytosol, (cyt) plasma membrane (AKAP79-targeted, 79), and SR (AKAP18δ-targeted, 18δ). (**B-C**) Representative time course of changes in FRET response (R/R_0) in SAN cells expressing CUTie sensors localized to the cytosol (cyt, black), plasma membrane (AKAP79 (79); pink) and SR (AKAP18δ (18δ); blue) upon application of (**B**) the AC activator forskolin (10 μM) and the PDE inhibitor 3-isobutyl-1-methylxanthine (IBMX, 100 μM), and (**C**) the β-AR agonist isoproterenol (ISO, 1 μM). The FRET ratios were normalized to basal levels before treatment. (**D-F**) Time course of changes in the magnitude of normalized FRET responses (R/R_0) in WT (black) and $AC_I^{-/-}$ (red) SAN cells expressing the CUTie sensors after stimulation with ISO (1 μM). Bar graphs on the right show corresponding summary data for the maximal increase in the FRET ratio response to ISO. (**G-J**) Representative time course of changes in the magnitude of normalized FRET responses (R/R_0) in WT (**G** and **I**) and $AC_I^{-/-}$ (**H** and **J**) SAN cells expressing CUTie sensors localized to the cytosol (cyt), plasma membrane (79) and SR (18δ) upon application of ISO (1 μM) in control (black) and SAN cells treated with 100 μM methyl-β-cyclodextrin (MβCD) (aqua, **G** and **H**) or 10 μM cilostamide and 10 μM rolipram (pink, **I** and **J**). Number of symbols in the bar graphs represents number of cells (n≥10) from 4-5 biological replicates (independent SAN isolations). Data are presented as mean±SEM. *p<0.05 by student's *t*-test.

Figure 2.8

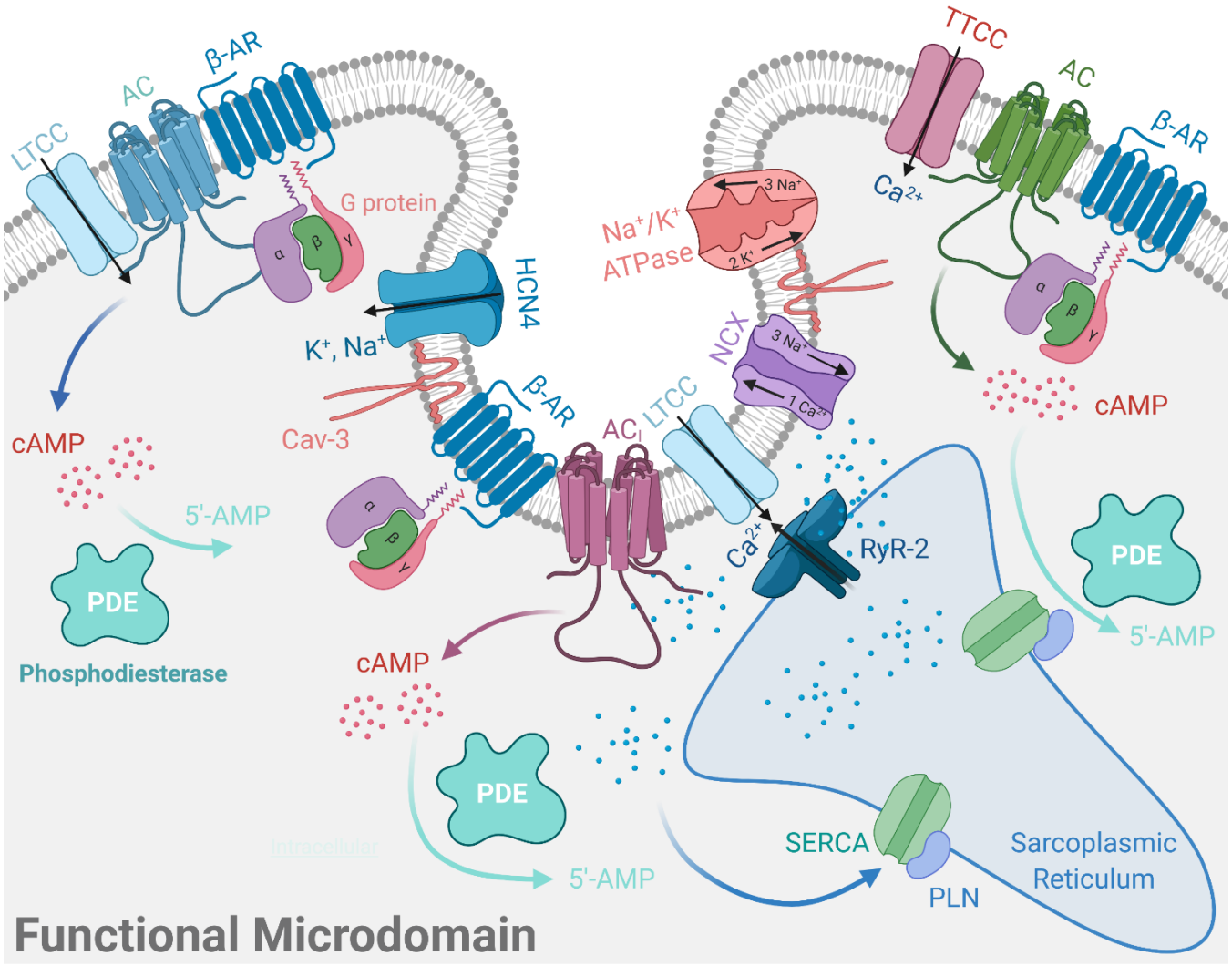

Figure 2.8. Model describing the AC_I functional microdomain. Schematic illustration of interactions of molecules that exist within the functional microdomain (generated using BioRender).

SUPPLEMENTARY FIGURES

Supplementary Figure 2.1

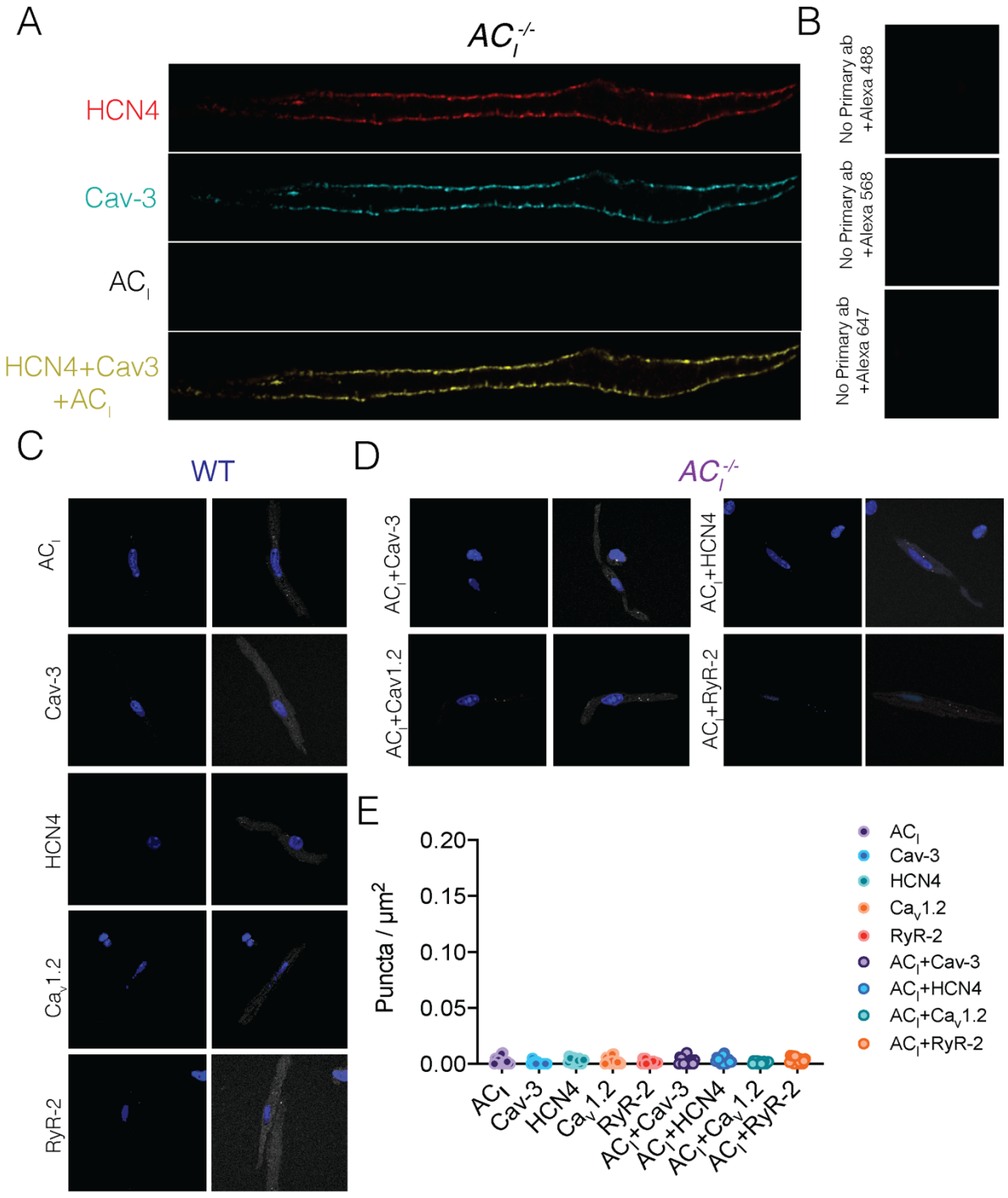

Supplementary Figure 2.1. **ICC and PLA controls**. (**A**) Representative images of $AC_I^{-/-}$ SANCs stained with HCN4, Cav-3, AC_I, or all three antibodies together for ICC. (**B**) Control was performed when SANCs were incubated with only secondary antibodies. (**C**) Images show WT SANCs incubated with various antibodies and (D) $AC_I^{-/-}$ SANCs incubated with AC_I with other antibodies for PLA. (E) Summary data showing that these negative controls exhibited low puncta count per surface area. Data expressed as mean ± SEM.

Supplementary Figure 2.2

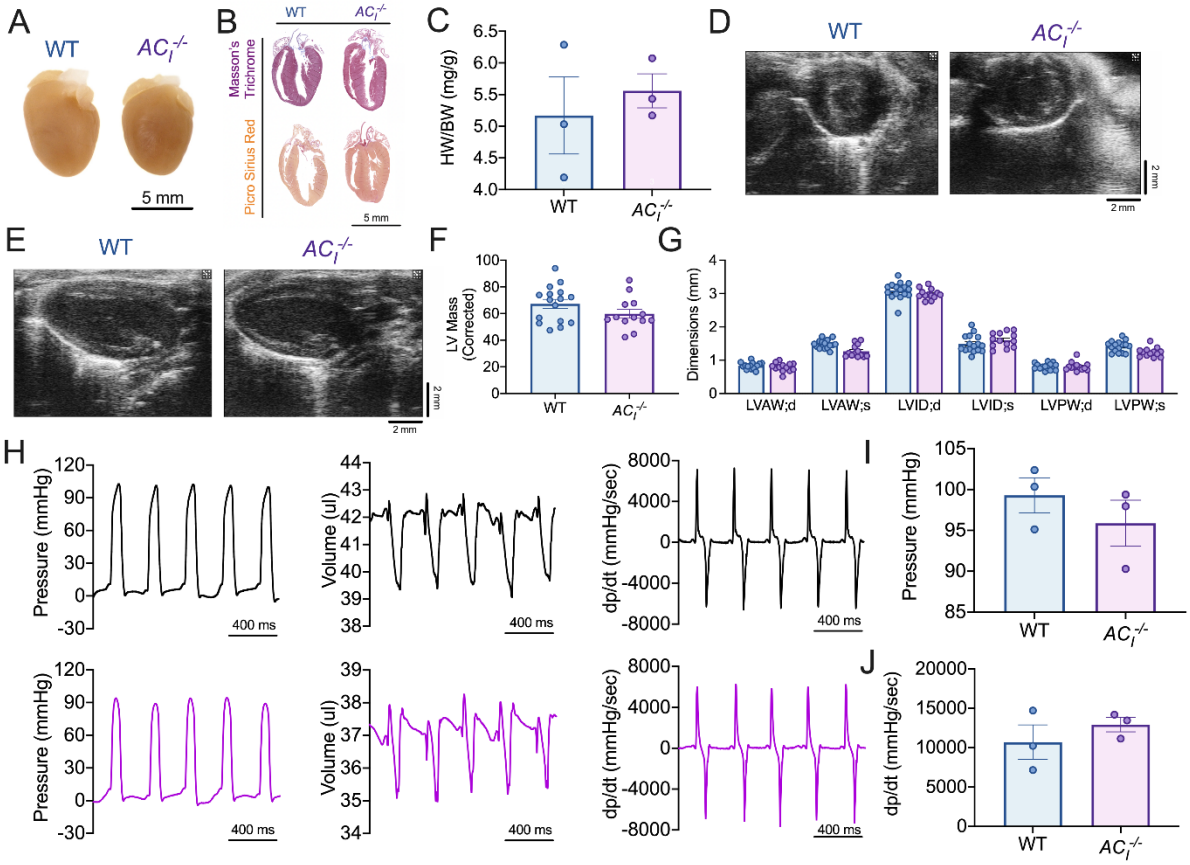

Supplementary Figure 2.2. Cardiac structure and function of $ACI^{-/-}$ mice. (**A**) Representative whole heart images of WT and $ACI^{-/-}$ mice are shown. (**B**) Hearts were fixed, sectioned, and stained for Masson's Trichrome and Picrosirirus red, as depicted. (**C**) Summary data show heart weight (HW) normalized to body weight (BW). (**D**) Representative images of WT and $ACI^{-/-}$ mice hearts are displayed at the parasternal short axis and (**E**) parasternal long axis. (**F**) Summary data of corrected left ventricular (LV) mass and (**G**) cardiac dimensions are displayed. (**H**) Hemodynamics parameters of pressure, volume, and dp/dt are shown for WT (black) and $ACI^{-/-}$ mice (purple). (**I**) Summary data of pressure and (**J**) pressure development are displayed. Data expressed as mean ± SEM. *p<0.05, ** p<0.01 by unpaired student's t test, nonparametric test, Mann-Whitney test. Number of points in graph represent the number of mice used for the experiments.

Supplementary Figure 2.3

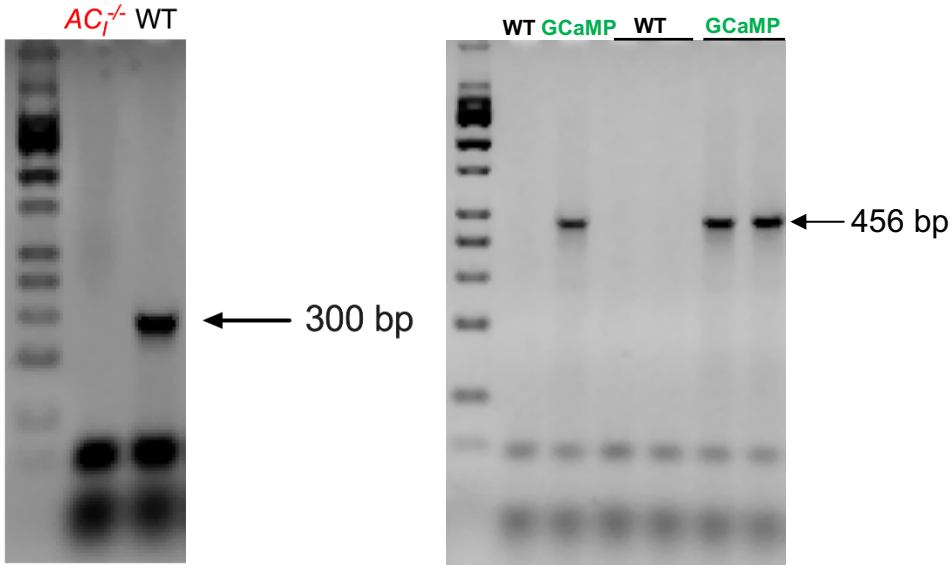

Supplementary Figure 2.3. **Genotype of WT, *AC1*$^{-/-}$ mice and GCaMP8 mice.** Left panel: representative gel image after PCR and DNA electrophoresis of WT and *AC1*$^{-/-}$ mice show a band at 300 bp for WT mice, while *AC1*$^{-/-}$ mice did not exhibit a band. Right panel: representative gel image after PCR and DNA electrophoresis of WT and GCaMP8 mice show a band at 456 bp for GCaMP8 mice, while WT mice did not exhibit a band. Verification of mice's genotype was always done prior to further experiments.

Supplementary Figure 2.4

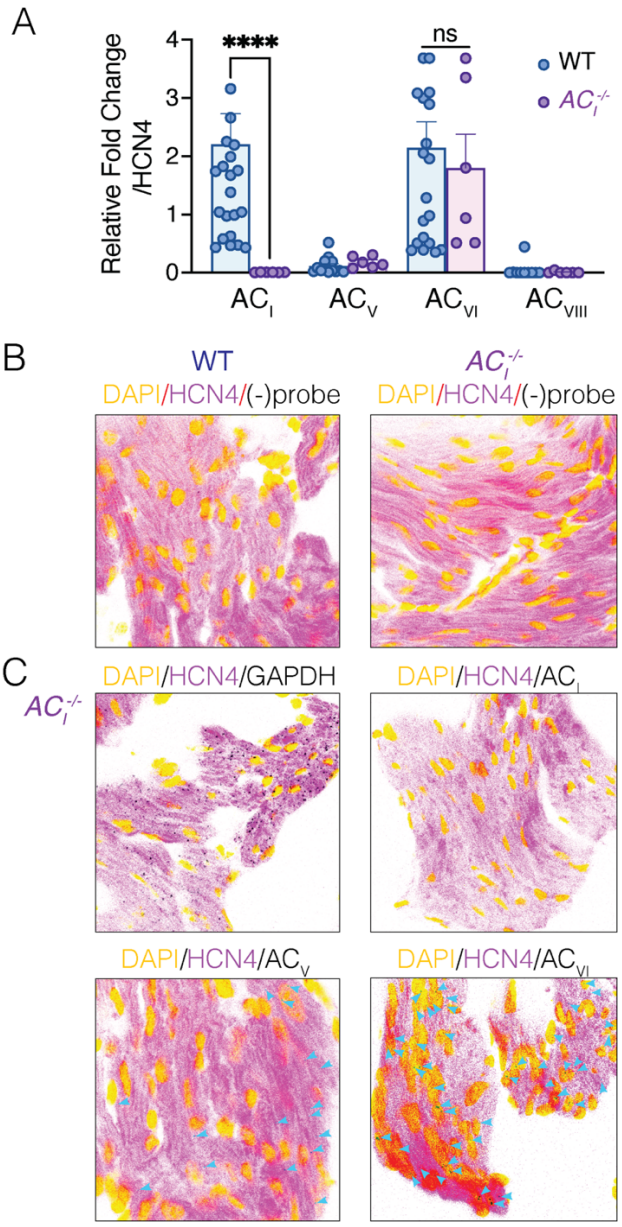

Supplementary Figure 2.4. **Single-cell RT-qPCR and smFISH from *AC$_I^{-/-}$* SANCs**. (A) Single-cell RT-qPCR from WT and *AC$_I^{-/-}$* SANCs (n=6-23 cells from 2-5 mice). AC$_I$, AC$_V$, AC$_{VI}$ and , AC$_{VIII}$ mRNA expressions were normalized to HCN4. Data expressed as mean ± SEM. * p<0.0001 by unpaired two-tail t-tests, followed by Mann-Whitney post hoc analyses. (B) Representative smFISH images of negative control without probes from WT and *AC$_I^{-/-}$* explants. (C) Representative smFISH images of GAPDH (positive control), AC$_I$, AC$_V$, AC$_{VI}$ mRNA expressions in the *AC$_I^{-/-}$* SAN explants. Scale bar: 20 μm.

Supplementary Figure 2.5

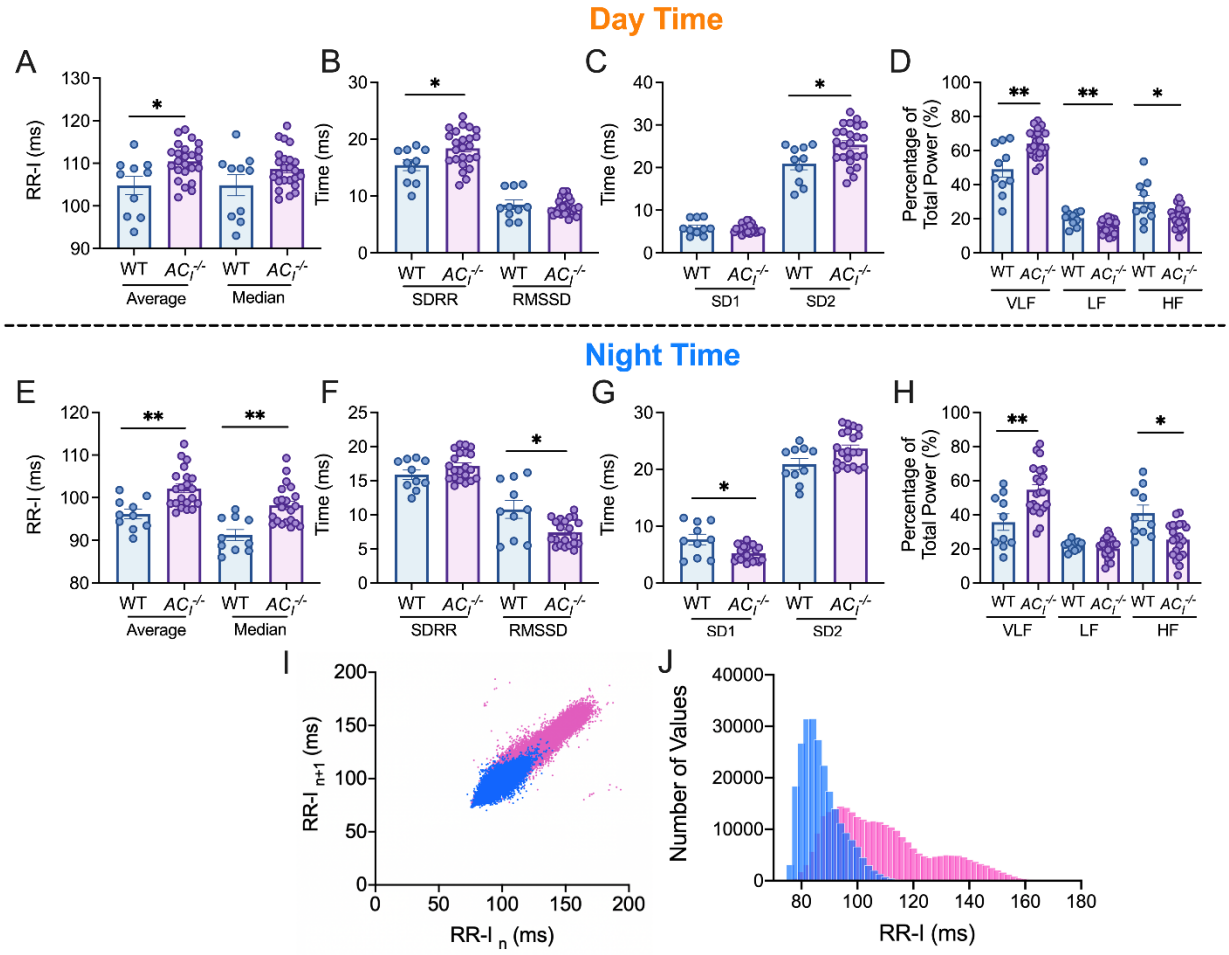

Supplementary Figure 2.5. Heart rate variability (HRV) of *AC1*$^{-/-}$ mice. (**A**) Summary data of the average and medium RR-Interval, (**B**) standard deviation of RR-I (SDRR) and root mean square of successive RR interval differences (RMSSD), (**C**) standard deviation (SD) 1 and 2, (**D**) and very-low frequency (VLF), low-frequency (LF), and high-frequency (HF) bands in WT and *AC1*$^{-/-}$ mice acquired from day time data (7AM-7PM). Similarly, summary of the (**E-H**) same parameters are shown for data obtained at night (7PM-7AM). (**I**) HRV scatter plot of is shown, as well as the (**J**) histogram showing the distribution of the RR-I. Data expressed mean ± SEM. *p<0.05, ** p<0.01 by unpaired student's t test, nonparametric test, Mann-Whitney test. Number of points in graph represent the number of mice used for the experiments.

Supplementary Figure 2.6

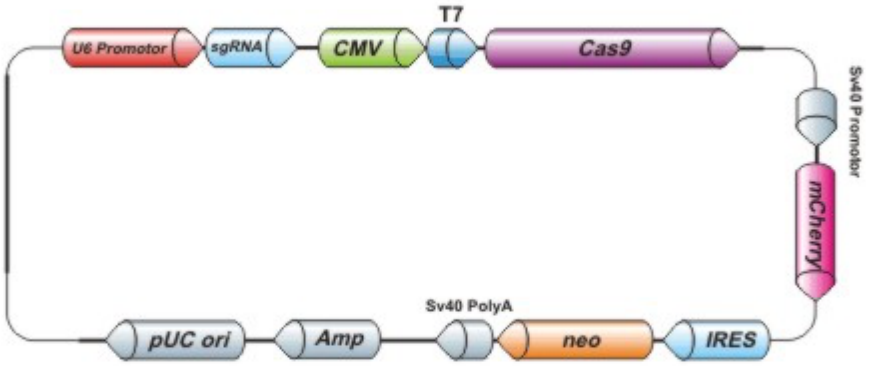

Supplementary Figure 2.6. A map of all-in-one sgRNA plasmid for mouse *adcy1* gene. mCherry was used as the reporter gene. The plasmid contained ampicillin resistance gene. The targeting sites are: GGGGCGCCGCGCGGCCAAGG; GGAGTTCGCGTGCCCCGAGC; and CCGCGGCTACACGTTGC GGC.

Supplementary Figure 2.7

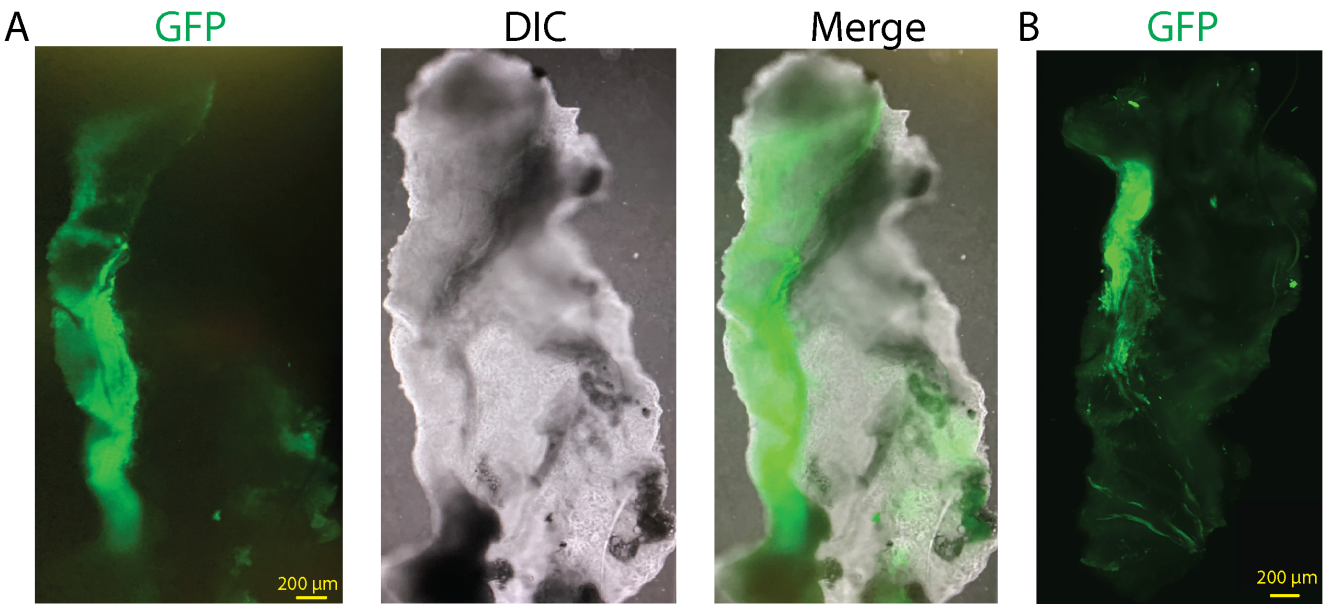

Supplementary Figure 2.7. Ca^{2+} signal from the whole SAN explant from a HCN4-GCaMP8 transgenic mouse imaged using Lightsheet microscopy. (A) Ca^{2+} signal from the whole SAN explant before ISO. left panel: GFP signal; middle panel: differential interference contrast image (DIC); right panel: merged image. (B) Ca^{2+} signal from the whole SAN explant after ISO.

Supplementary Figure 2.8

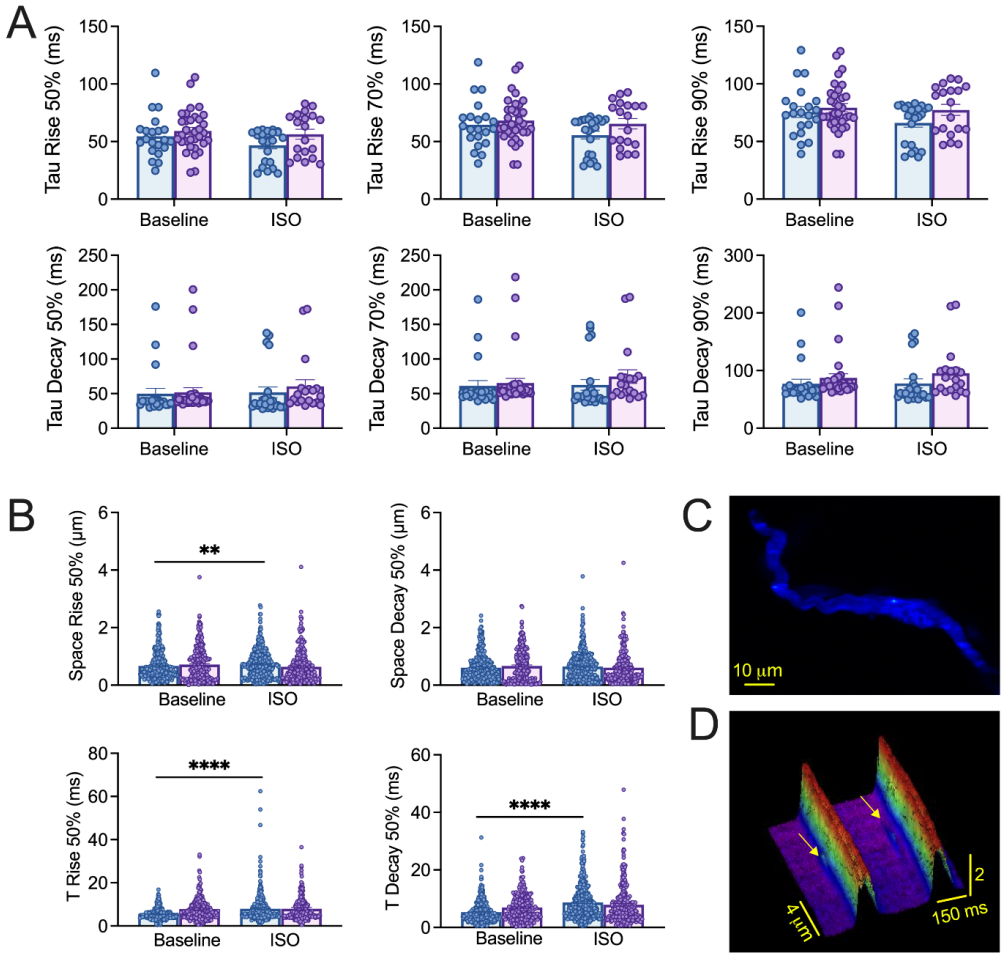

Supplementary Figure 2.8. (**A**) Summary data for τ_{rise} at 50%, 70% and 90% and τ_{decay} at 50%, 70%, and 90% of glocal CaT for WT and *ACI*$^{-/-}$ SANCs before and after ISO application. n=19-33 cells from 6-7 mice per group. (**B**) Summary data for LCR space rise at 50%, space decay at 50%, τ_{rise} at 50%, and τ_{decay} at 50%. Statistical differences were compared between all data sets, and the asterisk highlights those with significance. n=6-7 mice per group. 274-421 sparks from 15-20 cells were analyzed per group. (**C**) Representative confocal image of a WT SANC loaded with 5 µM Fluo-4. (D) Representative 3D plot of Ca^{2+} transients and LCRs. Arrows indicate LCRs. Data are expressed as mean±SEM. **p<0.01, **** p<0.0001 by two-way ANOVA, followed by Holm–Sidak multiple comparison post hoc analyses.

Supplementary Figure 2.9

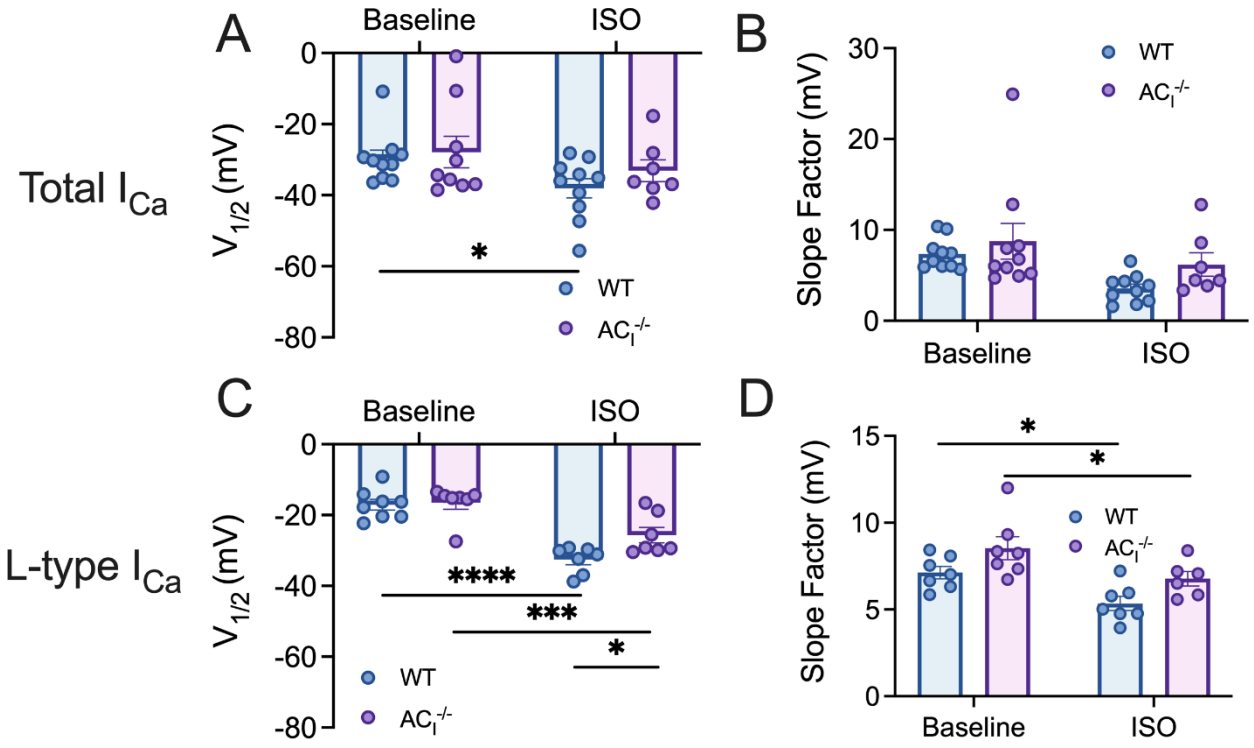

Supplementary Figure 2.9. Summary data for $V_{1/2}$ (A) and slope factor (B) from total Ca^{2+} current recordings. Summary data for $V_{1/2}$ (C) and slope factor (D) from L-type Ca^{2+} current recordings. n=7-10 cells from 4-5 mice per group. Data are expressed as mean±SEM. * $p<0.05$, **$p<0.01$, ***$p<0.01$, **** $p<0.0001$ by two-way ANOVA, Holm–Sidak multiple comparison post hoc analyses.

Supplementary Figure 2.10

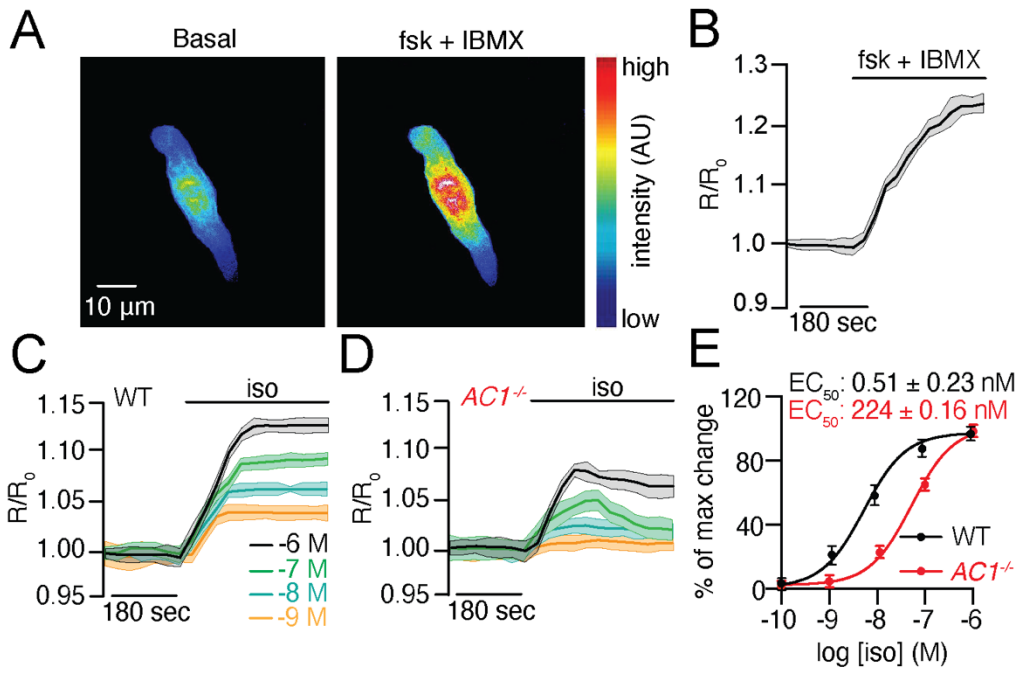

Supplementary Figure 2.10. (**A**) Representative pseudocolour wide-field FRET ratio images of SANCs expressing cytosolic CUTie before (left panel) and after (right panel) 10 µM forskolin + 100 µM IBMX. (**B**) Representative time course of changes in the magnitude of normalized FRET responses (R/R_0) in SAN cells expressing cytosol CUTie upon application of forskolin + IBMX. (**C**) WT and *AC1*$^{-/-}$ SANCs expressing cytosolic CUTie are stimulated with a set of incremental doses of ISO. Time courses show cytosolic CUTie FRET responses after stimulation with specified ISO concentration. (**D**) Normalized ISO-induced dose response curves of cytosolic CUTie biosensor. Data presented as mean ± SEM. n ≥ 10 cells from at least three biological replicates (independent SAN isolations).

Supplementary Figure 2.11

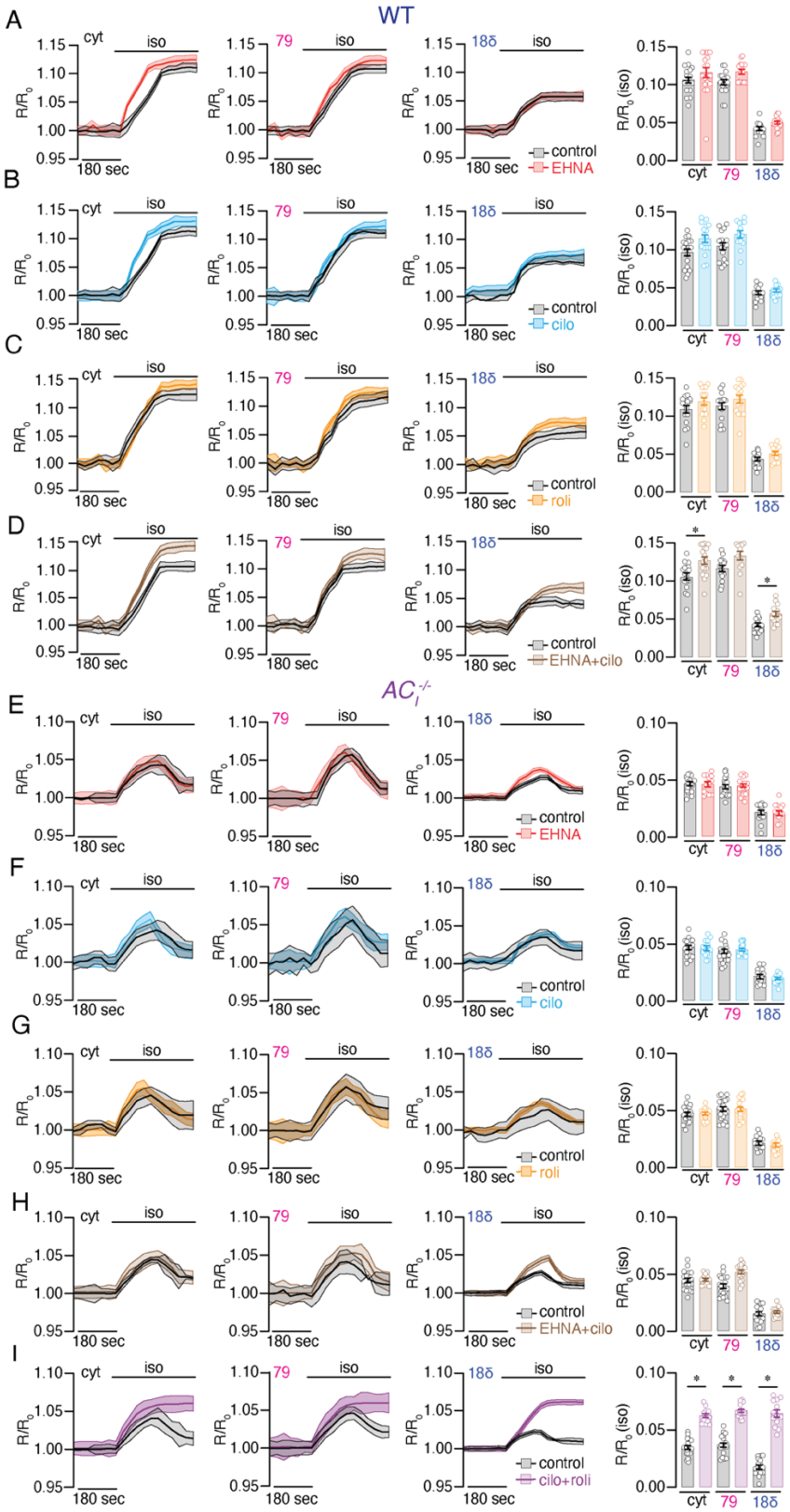

Supplementary Figure 2.11. Representative time course of changes in the magnitude of normalized FRET responses (R/R_0) in WT SANCs expressing cytosolic CUTie, AKAP79-CUTie or AKAP18δ-CUTie upon application of ISO (black) in the absence or presence of (**A**) 10 μM EHNA, (**B**) 10 μM cilostamide, (**C**) 10 μM rolipram, (**D**) or 10 μM EHNA + cilostamide. Representative time course of changes in the magnitude of normalized FRET responses (R/R_0) in $AC_1^{-/-}$ SANCs expressing cytosolic CUTie, AKAP79-CUTie or AKAP18δ-CUTie upon application of ISO (black) in the absence or presence of (**E**) 10 μM EHNA, (**F**) 10 μM cilostamide, (**G**) 10 μM rolipram, (**H**) 10 μM EHNA + cilostamide, (**I**) or 10 μM cilostamide + 10 μM rolipram. Data expressed as mean ± SEM. *$p<0.05$ by Kruskal-Wallis with Dunn's multiple comparisons. Statistical differences were compared between all data sets, and the asterisk highlights those with significance. For all experimental sets $n \geq 10$ from at least three biological replicates (independent SAN isolations).

CHAPTER 3

Structural and Functional Alterations in Sinoatrial Node Mitochondria and Their Microdomain in Heart Failure

Lu Ren[1], Valeriy Timofeyev[1], Yankun Lyu[1], Nathan Grainger[2], James Overton[1], Wilson Xu[1], Luis Fernando Santana[2], Xiao-Dong Zhang[1], Phung N. Thai[1*], Nipavan Chiamvimonvat[1,3,4*]

[1]Department of Internal Medicine, Division of Cardiovascular Medicine, University of California, Davis
[2]Department of Physiology and Membrane Biology, Davis, CA
[3]Department of Veterans Affairs, Northern California Health Care System, Mather, CA
[4]Department of Pharmacology, University of California, Davis

* Denotes equal contribution

Corresponding Authors:

Phung N. Thai and Nipavan Chiamvimonvat
Department of Internal Medicine, Division of Cardiovascular Medicine
University of California, Davis
451 Health Science Drive, GBSF 6315
Davis, CA 95616
Department of Veterans Affairs, Northern California Health Care System
10535 Hospital Way Mather, CA 95655
Emails: pnthai@ucdavis.edu; nchiamvimonvat@ucdavis.edu

ABSTRACT

Introduction: Sinoatrial node (SAN), the primary pacemaker region in the heart, generates electrical impulses that propagates throughout the heart. To faithfully generate electrical impulses on a beat-to-beat basis, it relies on a dense network of mitochondria. SAN dysfunction is well documented in patients with heart failure (HF); however, the underlying mechanisms are not fully understood. Since the mitochondria partake in multiple cellular processes that determine the life or death of a cell, we tested the hypothesis that mitochondrial dysfunction in the SAN during HF directly contribute to SAN dysfunction.

Methods: To test the hypothesis, we subjected C57Bl/6J wild-type (WT) mice to either sham-operation or pressure-overload induced HF by transverse aortic constriction (TAC). We acquired conscious echocardiography and ECG telemetry recordings. Further mechanistic experiments were performed after hearts were harvested for fixation or cell isolation.

Results: After 8 weeks, TAC mice exhibited impaired cardiac function, increased heart and lung weights to body weight ratios, as well as cardiac fibrosis. ECG recordings showed evidence of sinus bradycardia in TAC mice. Ultrastructural imaging using a transmission electron microscope (TEM) revealed an elevated number of clusters of small mitochondria in SAN cells (SANCs) isolated from TAC mice. Functionally, mitochondria from TAC mice exhibited depressed membrane potential, impaired mitochondrial Ca^{2+} handling, which contributed to a reduction in energy production and increased production of reactive oxygen species (ROS) in SANCs from TAC mice. Finally, structural remodeling occurred in the mitochondrial-sarcoplasmic reticulum

(SR) microdomain. Application of a known mitochondria uncoupler, to test the effects of the disruption of the microdomains, results in a significant decrease in the firing frequency of SANCs.

Conclusion: Our findings provided evidence that impairment of mitochondria and their microdomain in the SAN could contribute to SAN dysfunction that occurs during HF. SAN-specific therapies that target the mitochondria could potentially provide comprehensive care in HF patients suffering from SAN dysfunction.

Keywords: mitochondria, heart failure, sinoatrial node dysfunction

INTRODUCTION

Heart failure (HF) is a progressive condition that occurs when the heart can no longer generate enough cardiac output to meet the metabolic demands of the body [1]. Approximately 5.7 million people in the United States are diagnosed with HF, with 5-year mortality of greater than 50% [2]. One of the known complications that occurs in HF is bradyarrhythmia from sinoatrial node (SAN) dysfunction, which significantly increases the morbidity and mortality of HF patients [3]. Patients diagnosed with HF and SAN dysfunction have an increased risk of sudden cardiac death [2, 3]. Hence, it is imperative to develop therapies that specifically target the SAN to improve clinical outcome.

SAN is a highly complex structure consisting of specialized cells which spontaneously fire action potentials (APs) that propagate throughout the heart. Its automaticity is governed by ion channels and transporters that contribute to the membrane [4] and Ca^{2+} [5] clocks. These two cyclic processes are impaired during HF [6]. It has been shown that in a canine model of HF, hyperpolarization-activated and cyclic nucleotide-gated (HCN)2 and HCN4 expression are decreased at both the transcript and protein levels [7]. In rabbits with volume and pressure overload induced HF, the hyperpolarization-activated "pacemaker" current (I_f) and slow component of the delayed rectifier current (I_{Ks}) are reduced by 40% and 20%, respectively [8]. In a rat model of HF, SAN dysfunction results from an extensive remodeling of ion channels, gap junction channels, Ca^{2+}-, Na^{+}-, and H^{+}-handling proteins and receptors in the SAN [9]. These studies elegantly show the perturbations of key ion channels and transporters involved in the membrane and Ca^{2+} clocks. However, no study to date has tested the contributions of mitochondrial dysfunction in the SAN in HF.

The remodeling of the membrane and Ca^{2+} clocks may be secondary to, or potentiated by, alterations that occur within the SAN mitochondria during HF. Spontaneous AP impulses from the primary pacemaker cells disrupts the ionic gradient within the SAN, which needs to be reestablished by energy-dependent transporters on a beat-to-beat basis. The mitochondria provide the bulk energy to fuel the energetically demanding process. Indeed, like ventricular cardiomyocytes, the SAN has a dense network of mitochondria with a high basal respiratory rate [10]. In addition to their primary function of providing energy, they also regulate the life and death of a cell through their roles in reactive oxygen species (ROS) production [11], Ca^{2+} handling [12], and apoptosis [13]. Injury to the mitochondria can thus have detrimental effects to SAN cell viability. Therefore, it is crucial to investigate the structural and functional changes that occur with the SAN mitochondria during HF, as this will provide insights into better, site-specific therapeutic options.

The objective of this study was to investigate the structural and functional remodeling that occurs in the SAN mitochondria during HF. We induced HF in mice using a well-established pressure overload murine model. Concurrent with the development of HF, the animals show evidence of SAN dysfunction with sinus bradycardia. High resolution imaging and electron microscopy demonstrate an accumulation of damaged mitochondria. SAN mitochondria in HF animals are functionally impaired with decreased mitochondrial membrane potential, reduced Ca^{2+} uptake, depressed ATP production, and elevated reactive oxygen species (ROS) generation. At the subcellular level, structural changes within the SAN results in increased distance between mitochondria with the sarcoplasmic reticulum (SR), suggesting the impairment of the mitochondrial-SR microdomain. Application of a known mitochondria uncoupler, to test the effects of the disruption of the mitochondrial-SR microdomains, results in a significant decrease in local Ca^{2+} release, Ca^{2+} transients and the firing frequency of SANCs. Taken together, the data

support structural and functional remodeling in mitochondria in SAN in HF, which may contribute, in part, to the pathogenesis of SAN dysfunction.

MATERIALS AND METHODS

Animal work was performed in accordance with approved protocols of the Institutional Animal Care and Use Committee at the University of California, Davis, which adheres to the guidelines published by the US National Institutes of Health (8th Edition).

Transverse Aortic Constriction (TAC) Surgery

10-16-week-old C57Bl/6J mice were used for this study. Mice either underwent sham-operation, or transverse aortic constriction (TAC) surgery, followed by 8 weeks of recovery. Transverse aortic constriction was performed as previously described [14]. Briefly, the transverse aorta was visualized, and ligated to the size of a 27-gauge needle. Sham procedure was identical, except for the ligation.

Echocardiography

We used the Visualsonics Vevo 2100 ultrasound system with the MS 550D probe to perform echocardiography. Pulse wave doppler was performed at the left and right common carotids after the first week to determine successful ligation of the aorta. Systolic function (B-mode videos and M-mode images) was measured in conscious mice, and diastolic function (tissue doppler and pulse-wave doppler) was measured using 0.5%-1% isoflurane.

Electrocardiography

Transmitters were implanted in mice to record ECGs as previously described. After surgical procedure, mice were allowed to recover for at least 4 days before baseline 24-hour recordings commenced. The next 24-hour recordings were done at 8 weeks, at the time when the TAC mice developed HF, as verified by echocardiography.

Fibrosis Assessment

After 8 weeks, hearts were harvested, fixed in 4% paraformaldehyde solution in PBS, and embedded in paraffin. Five micrometer coronal sections were acquired. Sections were deparaffinized in a series of xylene/alcohol [14]. The sections were stained for hematoxylin and eosin (H&E), Picrosirius Red, and Masson's Trichrome. Fibrosis quantification was performed blindly using ImageJ. Fibrosis percentage was determined as the percentage of the collagen area (red for PSR and blue for MT) per total area of left ventricle.

Sinoatrial Node (SAN) Cell Isolation

SANCs were isolated as described previously [15]. Mice were anesthetized by intraperitoneal injection of 80 mg/kg of ketamine and 5 mg/kg of xylazine. The heart was excised and placed into Tyrode's solution (35°C) containing (in mM): 140 NaCl, 5.0 HEPEs, 5.5 Glucose, 5.4 KCl, 1.8 $CaCl_2$ and 1.0 $MgCl_2$ (pH 7.4). The SAN tissue was dissected out with a dissecting scope according to the landmarks of the heart defined by the orifice of superior vena cava, crista terminalis, and atrial septum. SAN tissue was digested in low Ca^{2+} solution (PH 6.9) containing collagenase B (0.54U/mL, sigma), elastase (18.9 U/mL, sigma) and protease type XIV (1.79 U/mL, sigma) for 30 min at 37°C. After digestion, the tissue was washed with Kraft-Bruhe medium containing (in

mM): 100 potassium glutamate, 5 HEPEs, 20 glucose, 25 KCl, 10 potassium aspartate, 2 $MgSO_4$, 10 KH_2PO_4, 20 taurine, 5 creatine, 0.5 EGTA and 1 mg mL^{-1} BSA (pH 7.4) three times and then SANCs were dissociated with a transfer pipette by mechanically stirring and pipetting the tissue chunks. Dissociated SANCs were placed at room temperature for study.

Proximity Ligation Assay

A Duolink In Situ PLA kit (Sigma) [16] was used to detect complexes consisting of RyR2 and COX IV, RyR2 and mitofustion-2, RyR2 and DRP-1 in isolated sinoatrial node cells. Briefly, cells were fixed with 4% paraformaldehyde and permeabilized with 0.25% Triton X-100. Cell were blocked with 1% BSA for 30 mins at room temperature, and then incubated overnight at 4° C with a specific combination of two primary antibodies in 1% BSA +0.25% Triton X-100 PBS solution: mouse anti-RyR2 (1:200, Abcam), rabbit anti-mitofusion-2 (1:100, CST), goat anti-COX-IV (1:200, Santa Cruz), rabbit anti-DRP-1 (1:200, CST). Cells were incubated with only one primary antibody as negative controls. PLA probes (anti-mouse MINUS and anti-rabbit PLUS) were used as secondary antibodies to bind to primary antibodies. Ligase was added to cells to allow hybridization with the probes and polymerase was added for a rolling circle amplification reaction. Coverslips were mounted on a microscope slide with Duolink mounting medium. The fluorescence signal was detected using a Zeiss confocal LSM 700 microscope. Images were collected at different optical planes (z-axis step = 0.5 mm). The stack of images for each sample was combined into a single-intensity projection image that was subsequently used for analysis of number of puncta/μm^2 per cell.

Immunofluorescence Confocal Microscopy and Stimulated Emission Depletion (STED) Microscopy

Immunofluorescence labeling was performed as described previously described [14]. The following primary antibodies were used: mouse anti-RyR2 (1:200, Abcam), rabbit anti-mitofusion-2 (1:100, CST), goat anti-COX-IV (1:200, Santa Cruz), rabbit anti-DRP-1 (1:200, Sigma). The cells were treated with primary antibodies overnight at 4° C. Anti-mouse or anti-rabbit secondary antibodies (Jackson ImmunoResearch, 1:500 dilution) were used to incubate the cells for 1 hour at room temperature. Slides were imaged using a Zeiss confocal LSM 700 microscope. Control experiments performed by incubation with secondary antibody only did not show positive staining under the same experimental conditions. Identical settings were used for all specimens. STED microscopy was performed on a Leica STED (TCS SP8 STED 3X) microscope. Deconvolution was done using Huygens Professional software. Colocalization was analyzed by the Imaris software.

Transmission Electron Microscopy

Hearts were harvested, and the SAN tissues were isolated and placed in fixative containing 2% paraformaldehyde and 2.5% glutaraldehyde in 0.1M sodium phosphate buffer overnight. The tissues were then rinsed in 0.1M sodium phosphate buffer twice at 15 minutes each, followed by 45 minutes in 1% osmium tetroxide. After incubation, the tissues were rinsed with ddH_2O two times at 15 minutes each. They then underwent a series of ethanol-induced dehydration, followed by propylene oxide. Pre-infiltration was performed overnight in half propylene oxide, half poly/bed Luft resin (Poly/Bed 812, dodecenyl succinic anhydride, nadic methyl anhydride, DMP-30). Infiltration was done for 5 hours in 100% Poly/Bed Luft resin. We then embedded the tissues

in fresh Poly/Bed Luft resin, and allowed the resin to polymerize for 24 hours at 60°C. Sections of the tissues were taken at approximately 100 nm, and collected on copper grids. Sections were stained with 4% aqueous uranyl acetate, rinsed in water, followed by 0.3% lead citrate in 0.1N sodium hydroxide before a final rinse in water. FEI Talos L120C was used to image the sections. Data analysis was done using ImageJ as described [17].

Mitochondrial Ca^{2+} Uptake

SAN cells were loaded with X-Rhod-1 AM for 40 minutes at 37°C. They were then plated on cover slips coated with laminin and poly-L-lysine. The cells were initially perfused with 50 μg/ml of Saponin in intracellular solution containing (in mM): 135 KCl, 0 NaCl, 20 HEPES, 5 pyruvate, 2 glutamate, 2 malate, 0.5 KH_2PO_4, 0.5 $MgCl_2$, 15 2,3-butanedione monoxime, 5 EGTA, and 1.86 $CaCl_2$ to yield a free $[Ca^{2+}]_i$ of 100 nM with pH 7.2. The solution was then switched to without Saponin. Mitochondrial Ca^{2+} uptake was monitored by the change in fluorescence intensity, normalized to the baseline fluorescence intensity, after the addition of 1.35 μM Ca^{2+}, 5 μM Ca^{2+}, and 10 μM Ca^{2+}. All measurements were taken at 37°C.

Mitochondrial Membrane Potential

Tetramethylrodamine ester (TMRM; λ_{ex} = 514 nm, λ_{em} = 590 nm) was used to assess the mitochondrial membrane potential [14]. SAN cells were incubated with 5 nM TMRM for 30 minutes at 37°C. Cells were perfused with 5 nM TMRM in intracellular solution at 37°C.

Reactive Oxygen Species (ROS) Production

Intact SAN cells were loaded with 0.5 μM MitoSox Red (λ_{ex} = 488 nm, λ_{em} = 510 nm for 30 minutes at 37°C. ROS generation was monitored under basal conditions and after 1 μM isoproterenol application in intracellular solution at 37°C.

Mitochondrial ATP Generation

ATP changes were monitored using mag-fluo-4 (Invitrogen, ThermoFisher Scientific) as previously described [14]. ATP hydrolysis is coupled to an increase in $[Mg^{2+}]_i$; When there's an increase in ATP hydrolysis, there will be an increase in mag-fluo-4 signal intensity. SAN cells were loaded with 10 μM mag-fluo-4 (λ_{ex} = 488 nm, λ_{em} = 565-605 nm) for 30 minutes at 37°C. To stimulate complex I-mediated respiration, 5 mM pyruvate and 5 mM malate were perfused in intracellular buffer. To stimulate complex II-mediated respiration, 5 mM succinate was supplied. All measurements were taken at 37°C.

Electrophysiology

SAN cells were isolated from WT sham, WT TAC, and control mice. Spontaneous single cell action potentials were recorded in current-clamp mode using the perforated patch configuration at 36 ± 0.5 °C. Amphotericin B (240 μg/ml) was added into the pipette solution to form the perforated patch to record action potentials (AP). Spontaneous APs were recorded in Tyrode's solution with the pipette filled with (in mM): 30 potassium aspartate, 10 NaCl, 10 HEPES, 0.04 $CaCl_2$, 2.0 Mg-ATP, 7.0 phosphocreatine, 0.1 Na-GTP, with pH adjusted to 7.2 with KOH. 1 uM FCCP was applied to WT sham SANCs after the recording is stable.

Western Blot

SAN, atrial, and ventricular tissue from the same heart were flash frozen in liquid nitrogen for western blotting experiments. In order to compare relative protein expression levels in SAN, atrial, and ventricular tissue, samples of all three tissue types were included in each blot, and the same amount of total protein (10 μg) was loaded in each lane. Membranes were blocked in 5% non-fat dry milk (Bio-Rad) in TBS for 1 h (room temperature) and then incubated with primary antibodies 1:1000 COX IV (Santa Cruz), 1:1000 Mitofusin-2 (CST), 1:1000 DRP-1 (Sigma), and 1:10000 GAPDH (Abcam), all in 5% non-fat dry milk in TBS-T overnight at 4°C.

SAN Whole Mount Fluorescent Immunohistochemistry

The SAN whole mount fluorescent immunohistochemistry was done as previously described [18]. Hearts from sham and TAC mice were removed and placed into a dissecting dish containing cold 0.01 M PBS. The left and right atrial walls, appendages, and interatrial septum were separated and pinned on a silicone pad in a dissecting dish for fixation for 25 mins at 4 °C in 4% paraformaldehyde (PFA) solution in 0.01 M phosphate buffer (PB, pH 7.4). To decrease tissue autofluorescence, the flattened tissues were cleared using ethanol with dimethylsulfoxide (20%, DMSO), hydrogen peroxide in ethanol (6%, H_2O_2), and dehydrated through a graded ethanol series. The whole-mount preparations were then rehydrated with 10-minute successive washes through a graded ethanol series and permeabilized in 3 × 10-minute changes of 0.01 M PBS containing 0.5% Triton X-100. Nonspecific binding was blocked for 2 h in PBS containing 5% normal donkey serum and 0.5% Triton X-100. The SAN tissues were incubated in a mixture of anti-HCN4 (rabbit polyclonal, Sigma) and anti-COX IV (goat polyclonal, Santa Cruz) primary antibodies for 48h at 4 °C. Then they were incubated with Alexa Fluor 488 anti-rabbit and Alexa Fluor 555 anti-goat secondary antibodies for 4 h in dark at room temperature. Finally, the SAN

tissues were mounted and STED imaging was done by Olympus microscope system. Z-stack images were taken and then were analyzed by Imaris. The whole-mount preparations were imaged under 10x and then stitched together by Olympus software. Imaris was used to make the whole SAN tissue 3D reconstruction. Zoomed in images were taken under 40x to look at the SAN head, body and tail.

Statistical Analysis

All data are reported as mean ± standard error, unless otherwise stated. Statistical significance was determined using student paired t test. A value of $p<0.05$ was considered statistically significant.

RESULTS

Transverse aortic constriction induced heart failure (HF) in mice

Sinoatrial node dysfunction is well described in patients with HF [3]. To generate the HF model, we used a well-established pressure overload model, where the transverse aorta is constricted to the diameter of approximately 0.4 mm. Validation of constriction was performed by taking the ratio of the common carotid arteries' blood flow velocities as previously described [14]. Mice were randomly assigned to undergo either sham operation, or TAC surgery. After 8 weeks, cardiac function was assessed in both groups. Representative whole heart images from both groups are shown in **Figure 3.1A**. As evident, hearts from TAC mice were significantly larger in size and weight than hearts from sham-operated mice (**Figures 3.1A-B**, **1H,** $p<0.0001$). Moreover, there was pulmonary congestion in the TAC mice (**Figure 3.1C**, $p<0.0001$). There was an increase in cardiac fibrosis in HF mice. Indeed, heart sections stained with both Masson's Trichrome (MT)

and Picrosirius Red (PSR, **Figure 3.1D**) revealed increased collagen deposition in TAC mice (**Figure 3.1E**, p<0.0.001). Functionally, TAC mice showed depressed systolic function, as seen by the representative M-mode images taken at the parasternal short axis (**Figure 3.1F**), and quantitatively by the fractional shortening (**Figure 3.1H**, p<0.0001). At this stage of HF, TAC mice exhibited significant sinus bradycardia compared to sham animals (**Figure 3.1G**, p<0.05). In addition, diastolic function was assessed in these mice. Representative tracings of blood flow velocity through the mitral valve are shown in **Figure 3.1I**. TAC mice showed lower deceleration time (**Figure 3.1J**, p<0.05**)** and elevated E/A ratio (**Figure 3.1K**, p<0.05), suggesting impaired diastolic function. Taken together, these results show that after 8 weeks of TAC, mice developed impaired cardiac function and experienced cardiac structural remodeling.

HF mice exhibit sinus bradycardia *in vivo* and isolated SANCs from HF mice show reduced AP frequency

To examine whether pressure overload HF affected the sinus node function *in vivo*, ambulatory ECG recordings were obtained before surgery and 8 weeks after either sham- or TAC operations. **Figure 3.2A** shows representative ECG tracings of the two groups at baseline conditions, and after 8 weeks of surgery. As manifested in these tracings, abnormal sinus rhythm occurred when the mice developed HF. Summary data for the 24-hour recordings demonstrate a significant reduction in heart rate in the HF mice at almost all time points during the mice's circadian rhythm (**Figure 3.2B**). This decrease in HR was corroborated in the conscious echocardiographic findings (**Figure 3.1G**). Together, the data demonstrate abnormal sinus rhythm in HF, with sinus bradycardia at basal heart rate.

Since heart rates are influenced by both intrinsic sinus node function and input from the autonomic nervous system, we directly determine the spontaneous firing frequency from single isolated SANCs that devoid of autonomic nervous system input. Representative AP tracings of sham and TAC SANCs are shown in **Figure 3.2C**. Single SANCs isolated from HF show a significant decrease in AP frequency (**Figure 3.2D**) as well as a prolongation of the AP duration (APD) at 90% repolarization (APD_{90}, **Figure 3.2E**, $p<0.05$) and 50% repolarization (APD_{50}, **Figure 3.2F**, $p<0.05$). Peak potential (**Figure 3.2G**) and maximum diastolic potential (**Figure 3.2H)** did not change with HF.

Mitochondrial uncoupling results in a decrease firing frequency of SANCs

To directly investigate the effects of observed alterations in structural, functional as well as mitochondria-SR microdomains in HF on SAN function, we took advantage of a known potent uncoupler of oxidative phosphorylation in mitochondria, carbonyl cyanide-p-trifluoromethoxyphenylhydrazone (FCCP). FCCP disrupts the mitochondrial proton gradients resulting in uncoupling of the oxidative phosphorylation and ATP production. **Figure 3.2I** shows representative traces of AP recordings before and after application of FCCP (1 μM). FCCP results in an immediate and significant decrease in the firing frequency of SANCs (**Figure 3.2J**, $p<0.05$). There was a trend towards prolongation of the APD (**Figures 3.2K and 3.2L**), but peak potential (**Figure 3.2M**) was not affected with FCCP application. Maximum diastolic potential (**Figure 3.2N**, $p<0.01$), however, was significantly more hyperpolarized in FCCP-treated SANCs.

HF induced structural alterations to SAN mitochondria

Proper identification and isolation of the SAN tissue and SANCs are important for the success of this study. Isolation of SAN tissue was performed according to Fenske et al [15]. Whole mount of SAN regions from sham- and TAC-operated mice were obtained and visualized using HCN4 as a marker as well as COX IV to label the inner mitochondrial membrane protein. Important landmarks were identified including superior vena cava (SVC), right atrial appendage (RAA), and crista terminalis (CT). We then examined three main regions of the SAN tissue—the SAN head, body, and tail. (**Supplementary Figure 3.S1**)

To assess the SAN mitochondrial morphological changes that occur with HF, we used transmission electron microscopy (TEM). Representative images of mitochondria from sham-operated and TAC-operated mice are seen at x5300, x6700, and x57000 magnifications in **Figure 3.3A**. We analyzed many mitochondrial parameters to acquire the overall structural changes that occur with HF. With HF, there was a significant decrease in mitochondrial area (**Figure 3.3B**, $p<0.001$) and perimeter (**Figure 3.3C**, $p<0.001$). Mitochondria from TAC mice had a significant deviation away from circularity (**Figure 3.3D**, $p<0.05$). In addition, skewness, a measure of asymmetry in distribution, indicated that there was a significant increase in smaller mitochondria in the HF group (**Figure 3.3F**, $p<0.0001$). Indeed, when we plotted the relative frequency distribution, we observed more smaller mitochondria (area < 0.2 μm^2, ~25% of total mitochondria analyzed) in the TAC group versus the sham group (~10%). When we calculated the length-to-width ratio, or the aspect ratio, we did not see a significant difference (**Figure 3.3G**). Feret's diameter, computed as the longest distance between two points on the mitochondria, was significantly lower in the TAC group (**Figure 3.3H**, $p<0.05$). Taken together, the morphology of the mitochondria changed significantly during HF. Our data suggest that there was an increase in the number of smaller

mitochondria. Furthermore, we observed an increase in the number of damaged mitochondria, as evident by representative images seen in **Figure 3.3A**, suggesting that in addition to the accumulation of smaller mitochondria, the normal-sized or larger-sized mitochondria have damaged cristae structures, which may impair the mitochondria's function.

HF reduced mitochondria and SR colocalization

In addition to the structural remodeling that occurred with the SAN mitochondria during HF, we tested whether spatial proximity between the SAN mitochondria and the sarcoplasmic reticulum (SR) was altered, since the close distance between the two organelles is crucial for proper crosstalk. Simultaneous immunolabeling of SANCs with RyR-2 and COX IV disclosed a pattern of close proximity and similar spatial organization between SR and mitochondria under sham-operated conditions (**Figure 3.4A**). However, with HF, no distinct structural organization can be seen. Quantification of immunocolocalization degree by Mander's coefficient analysis revealed a reduction in the fraction of RyR-2 overlapping with COX IV in TAC mice SANCs (**Figure 3.4B**).

Alteration of the mitochondria and SR microdomain in SANCs in HF

We then used the proximity ligation assay (PLA) as an additional analytical tool to examine the association between RyR2 and COX IV, mitofusin-2, or DRP-1. PLA fluorescence puncta are only observed if proteins of interest are 40 nm or less apart, whereas PLA signal was absent when at least one primary antibody was omitted. Robust fluorescent spots were detected in SANCs co-labeled for RyR2 and COX IV, mitofusin-2, or DRP-1 but not in TAC SANCs (**Figure 3.5A**). There were significant reductions in the positive amplification puncta in TAC SANCs compared to sham SANCs (**Figure 3.5B**). Altogether, these results suggest that in the SANCs, the

mitochondria are located within nanometer proximity (<~40 nm) with the SR. However, under HF conditions, the spatial proximity between the mitochondria and SR was greatly diminished.

Mitochondrial function was impaired with HF

The mitochondria are responsible for many vital cellular processes, and their normal functioning is crucial for cell survival. To assess the changes in mitochondrial function, we examined mitochondrial membrane potential, Ca^{2+} uptake, ATP production, and ROS production. Representative images of isolated SAN cells loaded with TMRM, a mitochondrial membrane potential dye, are shown in **Figure 3.6A**. Mitochondrial membrane potential, which is an important determinant of energy production and overall mitochondrial function, was more depolarized in isolated SAN cells from TAC mice (**Figure 3.6B**, $p<0.001$). Moreover, there was a diminished response in mitochondrial Ca^{2+} uptake (**Figures 3.6C-D**) when permeabilized TAC SANCs were challenged with increasing extramitochondrial concentrations of Ca^{2+} (1.35 μM, 5 μM, and 10 μM), relative to SANCs from sham mice, as indicated by the lowered response in X-Rhod-1 fluorescence intensity ($p<0.001$, **Figure 3.6D**). When the isolated SANCs from TAC mice were supplied with complex-I substrates (5 mM glutamate / 5 mM malate, **Figures 3.6E, G**) and complex-II substrate (5 mM succinate, **Figures 3.6F, G**), ATP level was significantly lower than SANCs from sham mice, as indicated by the level of Mag-Fluo-4 intensity ($p<0.001$). Furthermore, the SANCs from TAC mice had an elevated production of superoxide, the predominant ROS, as depicted by the increased level of MitoSox Red fluorescence after perfusion with isoproterenol (**Figures 3.6H-I**), a β-adrenergic receptor agonist. Taken together, our data suggest that overall mitochondrial function declined with HF.

DISCUSSION

The heart requires a substantial amount of energy to sustain itself on a beat-to-beat basis. Hence, it is imperative that cardiomyocytes are populated with a dense network of mitochondria that supply the bulk energy through oxidative phosphorylation [10, 19]. Normal functioning mitochondria are therefore crucial to cardiac cell survival, and dysfunctional mitochondria have been associated with a number of cardiovascular diseases, including ischemia-reperfusion (I/R) injury, hypertension, diabetic cardiomyopathy, cardiac hypertrophy, and HF [20]. Although mitochondrial dysfunction in HF have been well studied in ventricular cardiomyocytes, where the energy starvation hypothesis was first proposed [21], to date, there is a significant gap in our knowledge in the SAN mitochondria during HF. Since SANCs are non-contractile, autorhythmic cells with a high density of mitochondria [10], alterations in the SAN mitochondria can contribute to SAN dysfunction commonly seen with HF [3].

In the present study, the development of HF at 8 weeks corresponded to a decline in heart rate in TAC mice as depicted in not only the conscious echocardiography recordings, but also in the 24-hour ECG recordings. Sinus bradycardia observed *in vivo* was also present *in vitro* in both isolated SANCs and isolated SAN tissue with a significant decrease in AP frequency in SANCs isolated from HF mice. Application of a known potent mitochondrial uncoupler, we observed a significant decrease in LCR, CaT and AP firing frequency, suggesting that functionally impaired mitochondria contributed to a decline in SAN function.

Importantly, we observe that with HF, there is an accumulation of damaged mitochondria in the SAN with reduced ability to uptake Ca^{2+} at increasing extramitochondrial [Ca^{2+}]. This, in

part, contributes to a reduction in energy generation when they are supplied with either complex I (glutamate/malate) or complex II (succinate) substrates. Moreover, the structurally damaged and functionally impaired mitochondria generate significantly more superoxide, the predominant ROS in mitochondria, after β-adrenergic stimulation. Together, our data demonstrate that the mitochondria in SANCs from HF mice were functionally compromised, contributing to the pathogenesis of SAN dysfunction in HF.

Sinus Node Dysfunction During HF

The SAN serves as the primary pacemaking region, generating spontaneous APs that propagate throughout the heart. During HF, however, its automaticity is impaired, contributing towards the increase in morbidity and mortality in HF patients [2, 3, 22]. Various components of the membrane clock and Ca^{2+} clock [23] have been shown to be significantly remodeling during HF. In a rapid-pacing canine model of HF, the slope of enhanced late diastolic Ca^{2+} was significantly lower in the superior SAN, and ectopic pacemaking activity occurred in the lower crista terminalis in the presence and absence of β-adrenergic stimulation [6]. Moreover, expression of HCN channel at both mRNA and protein levels decreased in a similar model of HF [7]. With a volume and pressure overload rabbit HF model, there was a significant increase in the *in vitro* and *in vivo* intrinsic cycle length of the SAN [24]. Verkerk et al. also found an increase in intrinsic cycle length, with a concomitant decrease in diastolic depolarization rate [8]. These investigators also reported a decrease in the pacemaker current, I_f, without alterations in T- and L-type Ca^{2+} currents. In patients with congestive HF, the intrinsic cycle length increased with prolongation of sinoatrial conduction time [3]. Together, these studies reveal that ionic remodeling impairs SAN function. However, the establishment of the electrochemical gradients requires the input of energy. Although remodeling

does indeed occur at the transporter and channel levels, the possible role of the mitochondria in the pathogenesis cannot be ignored, as these organelles are crucial mediators of cell viability.

Mitochondria's Fuel to Sustain SAN Automaticity

The mitochondria partake in the SAN's automaticity, in part, through their involvement in Ca^{2+} handling and energy production. The spontaneous depolarization of the SAN triggers the influx of Ca^{2+} through the L-type Ca^{2+} channels, which subsequently stimulates the release of Ca^{2+} through the ryanodine receptors (RYR2) on the SR [10, 25]. The release of Ca^{2+} from RYR2 results in localized elevation of intracellular Ca^{2+} (Ca^{2+}_i) at microdomains between the mitochondria and SR for localized signaling [26, 27]. Crosstalk between the mitochondria and the SR ensures coupling of energy production with the cell's metabolic needs, which is mediated, in part, by mitochondrial Ca^{2+} [10, 26, 28]. While inside the mitochondrial matrix, Ca^{2+} stimulates mitochondrial enzymes [29], producing more reduced equivalents that can be oxidized for energy production [30].

It has been proposed that the increase in Ca^{2+}_i stimulates the plasma membrane Na^+/Ca^{2+} exchanger, generating a net inward current that contributes to the spontaneous depolarization, termed the Ca^{2+} clock [5]. The periodic rise and fall of Ca^{2+} requires a beat-to-beat reestablishment of the ionic gradient, which is fueled primarily by fatty acid oxidation in cardiomyocytes [31]. With the influx of Ca^{2+}, and the rise in Ca^{2+} through Ca^{2+}-induced Ca^{2+} release, Ca^{2+} acts as a second messenger to match energy production with energy demand, which is especially important during increased sympathetic tone when energy demand is elevated. Thus, although not directly, the mitochondria participate in the SAN's automaticity through their involvement in coupling metabolic supply with demand. As directly demonstrated in this study, application of a known

mitochondrial uncoupler to isolated SANCs *in vitro* results in a significant reduction in LCR, CaT and AP frequency.

Altered Mitochondrial Microdomain with HF

Microdomains that exist between the mitochondria and the SR serve critical roles in spatial, localized signaling, allowing an interface for proper communication[32]. Mitofusin-2, a fusion protein, has been shown to tether the mitochondria with the sarco-endoplasmic reticulum[33, 34]. Ablation of mitofusin-2 produced mitochondrial fragmentation, and impaired normal cardiac function [35]. Moreover, mitofusin-2 deficiency reduces the SR-mitochondrial contact length (increased distance between the two organelles) and decreases mitochondrial Ca^{2+} uptake [36]. With the disruption of the microdomain, the bioenergetic feedback from Ca^{2+}-induced stimulation is diminished.

In the present study, we demonstrate that the mitochondria and SR were situated in close proximity (<40 nm) in isolated SANCs from sham-operated animals, probing for mitofusin-2 (fusion) and COX IV (inner mitochondrial membrane protein) with RYR2 (SR protein). This close proximity suggests the importance of crosstalk between the mitochondria and SR in the autorhythmic cells, even though they lack distinct, organized myofibrils. In contrast, SANCs isolated from TAC mice show a significant increase in the proximity between the SR and mitochondria, suggesting structural remodeling not only within the mitochondria, but also at the subcellular level with the disruption of their microdomains. Finally, we demonstrate that with the reduced microdomains and accumulation of damaged mitochondria, the mitochondrial function was significantly impaired, which contributes, in part, to the abnormal sinus rhythm observed.

Conclusions

Taken together, our results show that sinus bradycardia occurs concurrently with the development of HF in a murine model. The reduced heart rate was not only present *in vivo*, but it was also observed *in vitro* in isolated SANCs and isolated SAN tissue. There is significant structural remodeling of mitochondria with an accumulation of small mitochondria in the SAN HF tissue, with abnormal cristae. Functionally, this translated to diminished mitochondrial membrane potential, depressed mitochondrial energy production, reduced mitochondrial Ca^{2+} uptake, and increased ROS generation. SANCs challenged with a mitochondrial uncoupler exhibit a significant reduction in LCR, CaT and firing frequency, suggesting that uncoupled, or functionally impaired, mitochondria affect beating frequency. These findings collectively support the notion that impaired mitochondria can contribute to sinus bradycardia commonly seen with HF.

ACKNOWLEDGMENTS

This work was supported by a American Heart Association (AHA) Predoctoral Award 18PRE34030199 (LR), Postdoctoral Fellowships from NIH T32 Training Grant in Basic & Translational Cardiovascular Science HL86350 and NIH F32 HL149288 (PNT), NIH R01 HL085727, HL085844, HL137228, and S10 RR033106, Research Award from the Rosenfeld Foundation, VA Merit Review Grant I01 BX000576 and I01 CX001490 (NC). NC is the holder of the Roger Tatarian Endowed Professorship in Cardiovascular Medicine and a part-time staff physician at VA Northern California Health Care System, Mather, CA.

AUTHORS' CONTRIBUTIONS

LR designed the research study, conducted experiments, acquired data, analyzed data, and wrote the manuscript. VT, YL, NG conducted experiments, acquired data, and analyzed data. XD provided advice and technical assistance. LFS provided financial support. PNT designed the research study, conducted experiments, acquired data, analyzed data, and wrote the manuscript. NC designed the research study, provided financial support, and wrote the manuscript.

REFERENCES

1. Metra M and Teerlink JR. Heart failure. *Lancet*. 2017;390:1981-1995.

2. Benjamin EJ, Virani SS, Callaway CW, Chamberlain AM, Chang AR, Cheng S, Chiuve SE, Cushman M, Delling FN, Deo R, de Ferranti SD, Ferguson JF, Fornage M, Gillespie C, Isasi CR, Jimenez MC, Jordan LC, Judd SE, Lackland D, Lichtman JH, Lisabeth L, Liu S, Longenecker CT, Lutsey PL, Mackey JS, Matchar DB, Matsushita K, Mussolino ME, Nasir K, O'Flaherty M, Palaniappan LP, Pandey A, Pandey DK, Reeves MJ, Ritchey MD, Rodriguez CJ, Roth GA, Rosamond WD, Sampson UKA, Satou GM, Shah SH, Spartano NL, Tirschwell DL, Tsao CW, Voeks JH, Willey JZ, Wilkins JT, Wu JH, Alger HM, Wong SS and Muntner P. Heart Disease and Stroke Statistics-2018 Update: A Report From the American Heart Association. *Circulation*. 2018;137:e67-e492.

3. Sanders P, Kistler PM, Morton JB, Spence SJ and Kalman JM. Remodeling of sinus node function in patients with congestive heart failure: reduction in sinus node reserve. *Circulation*. 2004;110:897-903.

4. Mangoni ME and Nargeot J. Genesis and regulation of the heart automaticity. *Physiol Rev*. 2008;88:919-82.

5. Maltsev VA and Lakatta EG. Normal heart rhythm is initiated and regulated by an intracellular calcium clock within pacemaker cells. *Heart Lung Circ*. 2007;16:335-48.

6. Shinohara T, Park HW, Han S, Shen MJ, Maruyama M, Kim D, Chen PS and Lin SF. Ca2+ clock malfunction in a canine model of pacing-induced heart failure. *Am J Physiol Heart Circ Physiol*. 2010;299:H1805-11.

7. Zicha S, Fernandez-Velasco M, Lonardo G, L'Heureux N and Nattel S. Sinus node dysfunction and hyperpolarization-activated (HCN) channel subunit remodeling in a canine heart failure model. *Cardiovasc Res*. 2005;66:472-81.

8. Verkerk AO, Wilders R, Coronel R, Ravesloot JH and Verheijck EE. Ionic remodeling of sinoatrial node cells by heart failure. *Circulation*. 2003;108:760-6.

9. Yanni J, Tellez JO, Maczewski M, Mackiewicz U, Beresewicz A, Billeter R, Dobrzynski H and Boyett MR. Changes in ion channel gene expression underlying heart failure-induced sinoatrial node dysfunction. *Circ Heart Fail*. 2011;4:496-508.

10. Yaniv Y, Juhaszova M, Lyashkov AE, Spurgeon HA, Sollott SJ and Lakatta EG. Ca2+-regulated-cAMP/PKA signaling in cardiac pacemaker cells links ATP supply to demand. *J Mol Cell Cardiol*. 2011;51:740-8.

11. Murphy MP. How mitochondria produce reactive oxygen species. *Biochem J*. 2009;417:1-13.

12. Williams GSB, Boyman L, Chikando AC, Khairallah RJ and Lederer WJ. Mitochondrial calcium uptake. *Proceedings of the National Academy of Sciences*. 2013;110:10479.

13. Wang C and Youle RJ. The role of mitochondria in apoptosis*. *Annu Rev Genet*. 2009;43:95-118.

14. Thai PN, Daugherty DJ, Frederich BJ, Lu X, Deng W, Bers DM, Dedkova EN and Schaefer S. Cardiac-specific Conditional Knockout of the 18-kDa Mitochondrial Translocator Protein Protects from Pressure Overload Induced Heart Failure. *Sci Rep*. 2018;8:16213-16213.

15. Fenske S, Probstle R, Auer F, Hassan S, Marks V, Pauza DH, Biel M and Wahl-Schott C. Comprehensive multilevel in vivo and in vitro analysis of heart rate fluctuations in mice by ECG telemetry and electrophysiology. *Nat Protoc*. 2016;11:61-86.

16. Fredriksson S, Gullberg M, Jarvius J, Olsson C, Pietras K, Gustafsdottir SM, Ostman A and Landegren U. Protein detection using proximity-dependent DNA ligation assays. *Nat Biotechnol*. 2002;20:473-7.

17. Picard M, White K and Turnbull DM. Mitochondrial morphology, topology, and membrane interactions in skeletal muscle: a quantitative three-dimensional electron microscopy study. *J Appl Physiol (1985)*. 2013;114:161-171.

18. Pauza DH, Rysevaite K, Inokaitis H, Jokubauskas M, Pauza AG, Brack KE and Pauziene N. Innervation of sinoatrial nodal cardiomyocytes in mouse. A combined approach using immunofluorescent and electron microscopy. *J Mol Cell Cardiol*. 2014;75:188-97.

19. Ingwall JS and Weiss RG. Is the failing heart energy starved? On using chemical energy to support cardiac function. *Circ Res*. 2004;95:135-45.

20. Siasos G, Tsigkou V, Kosmopoulos M, Theodosiadis D, Simantiris S, Tagkou NM, Tsimpiktsioglou A, Stampouloglou PK, Oikonomou E, Mourouzis K, Philippou A, Vavuranakis M, Stefanadis C, Tousoulis D and Papavassiliou AG. Mitochondria and cardiovascular diseases-from pathophysiology to treatment. *Ann Transl Med*. 2018;6:256.

21. Ventura-Clapier R, Garnier A and Veksler V. Energy metabolism in heart failure. *J Physiol*. 2004;555:1-13.

22. Faggiano P, d'Aloia A, Gualeni A, Gardini A and Giordano A. Mechanisms and immediate outcome of in-hospital cardiac arrest in patients with advanced heart failure secondary to ischemic or idiopathic dilated cardiomyopathy. *Am J Cardiol*. 2001;87:655-7, a10-1.

23. Lakatta EG, Maltsev VA and Vinogradova TM. A coupled SYSTEM of intracellular Ca2+ clocks and surface membrane voltage clocks controls the timekeeping mechanism of the heart's pacemaker. *Circulation research*. 2010;106:659-673.

24. Opthof T, Coronel R, Rademaker HM, Vermeulen JT, Wilms-Schopman FJ and Janse MJ. Changes in sinus node function in a rabbit model of heart failure with ventricular arrhythmias and sudden death. *Circulation*. 2000;101:2975-80.

25. Choudhury M, Boyett MR and Morris GM. Biology of the Sinus Node and its Disease. *Arrhythm Electrophysiol Rev*. 2015;4:28-34.

26. Bers DM. Calcium Cycling and Signaling in Cardiac Myocytes. *Annual Review of Physiology*. 2008;70:23-49.

27. Rizzuto R, Brini M, Murgia M and Pozzan T. Microdomains with high Ca2+ close to IP3-sensitive channels that are sensed by neighboring mitochondria. *Science*. 1993;262:744-7.

28. Kohlhaas M and Maack C. Calcium release microdomains and mitochondria. *Cardiovascular Research*. 2013;98:259-268.

29. Tarasov AI, Griffiths EJ and Rutter GA. Regulation of ATP production by mitochondrial Ca(2+). *Cell Calcium*. 2012;52:28-35.

30. Fink BD, Bai F, Yu L and Sivitz WI. Regulation of ATP production: dependence on calcium concentration and respiratory state. *Am J Physiol Cell Physiol*. 2017;313:C146-c153.

31. Ventura-Clapier R, Garnier A, Veksler V and Joubert F. Bioenergetics of the failing heart. *Biochimica et Biophysica Acta (BBA) - Molecular Cell Research*. 2011;1813:1360-1372.

32. Dorn GW and Maack C. SR and mitochondria: Calcium cross-talk between kissing cousins. *Journal of Molecular and Cellular Cardiology*. 2013;55:42-49.

33. de Brito OM and Scorrano L. Mitofusin 2 tethers endoplasmic reticulum to mitochondria. *Nature*. 2008;456:605-610.

34. Eisner V, Csordás G and Hajnóczky G. Interactions between sarco-endoplasmic reticulum and mitochondria in cardiac and skeletal muscle - pivotal roles in Ca^{2+} and reactive oxygen species signaling. *J Cell Sci*. 2013;126:2965-2978.

35. Chen Y, Liu Y and Dorn GW, 2nd. Mitochondrial fusion is essential for organelle function and cardiac homeostasis. *Circulation research*. 2011;109:1327-1331.

36. Chen Y, Csordas G, Jowdy C, Schneider TG, Csordas N, Wang W, Liu Y, Kohlhaas M, Meiser M, Bergem S, Nerbonne JM, Dorn GW, 2nd and Maack C. Mitofusin 2-containing mitochondrial-reticular microdomains direct rapid cardiomyocyte bioenergetic responses via interorganelle Ca(2+) crosstalk. *Circ Res*. 2012;111:863-75.

FIGURES

Figure 3.1.

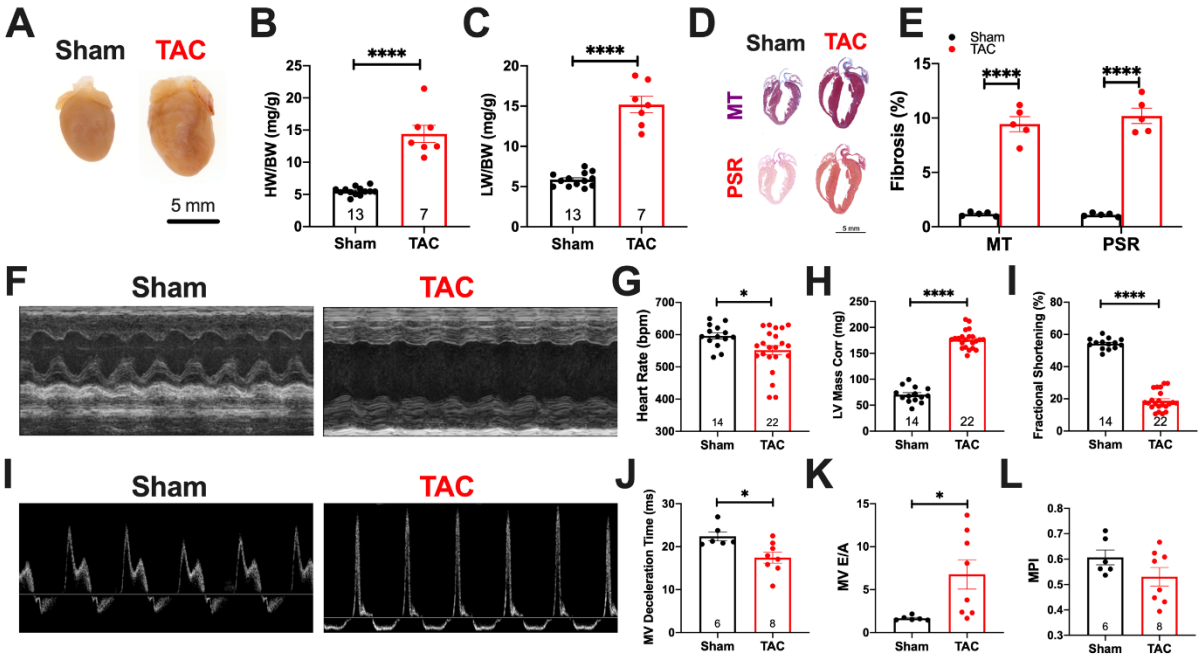

Figure 3.1. Transverse aortic constriction induced heart failure (HF) in mice. A) Representative images of hearts taken at 8 weeks after sham-operation and TAC-operation. **B)** With HF, there was an increase in heart weight to body weight ratio and **C)** lung weight to body weight ratio. **D)** Hearts were sliced into 5 μM sections, and stained with Masson's Trichrome (MT) and Picrosirius Red (PSR) to assess collagen content. **E)** With HF, there was an increase in collagen deposition. Conscious echocardiography was used to determine cardiac structure and function. **F)** Representative images taken at the M-mode parasternal short axis reveal severely dilated left ventricular chamber, thickened left ventricular wall, and significantly depressed ejection fraction in TAC mice. **G)** Heart rate was significantly lower in TAC mice. **H)** HF induced an increase in left ventricular mass, **I)** with a concomitant decrease in fractional shortening. **I)**

Blood flow through the mitral valve was assessed using pulse wave doppler to capture diastolic function, as seen in the representative images. **J**) Quantitatively, mitral valve (MV) deceleration time significantly decreased with TAC, and the **K**) MV E/A ratio increased. **L**) Myocardial performance index did not change. Data are expressed as mean ± SEM. * $p<0.05$, ** $p<0.01$, *** $p<0.001$, **** $p<0.0001$.

Figure 3.2.

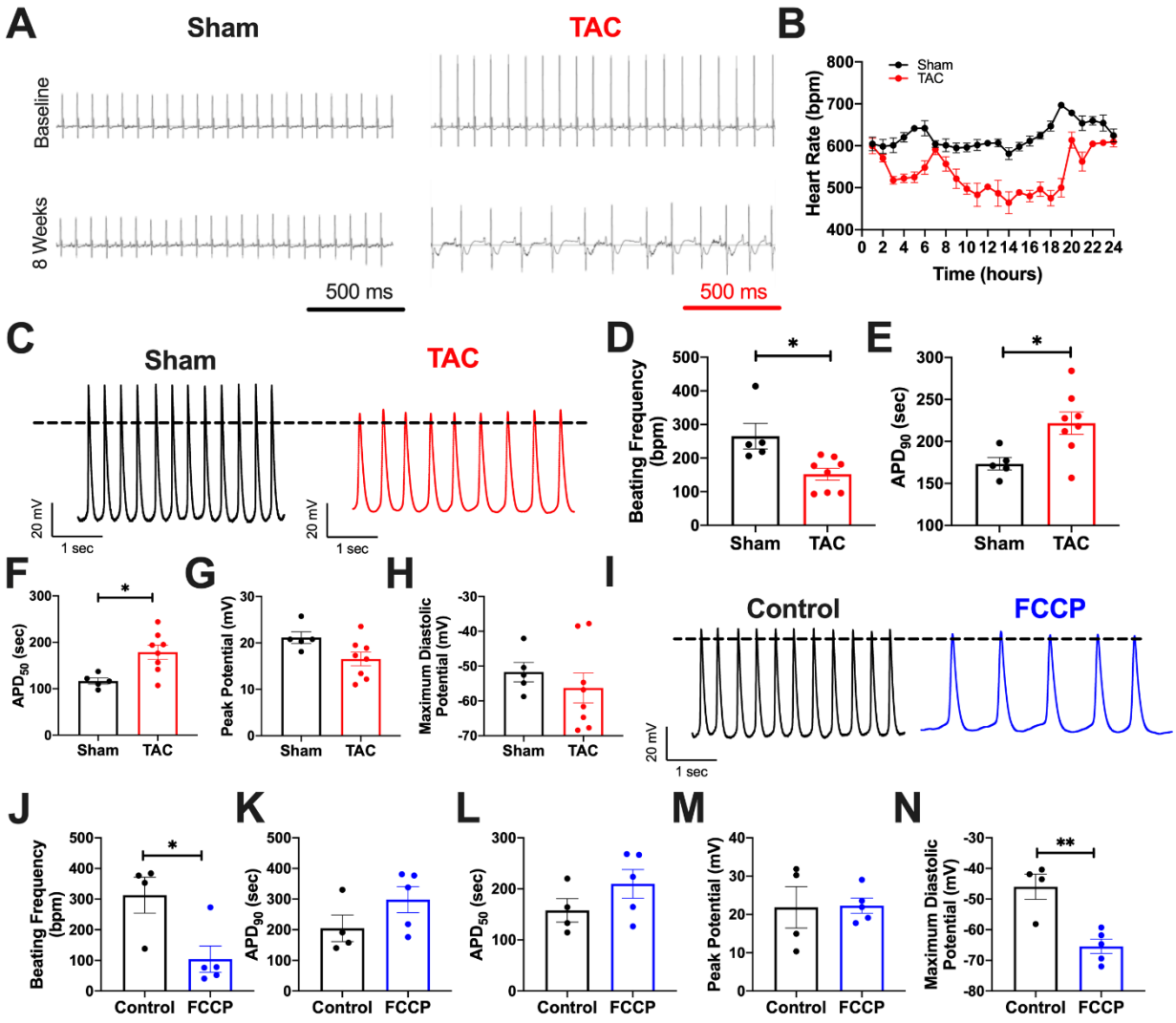

Figure 3.2. HF mice exhibited bradycardia *in vivo* and isolated SANCs from HF mice had reduced AP frequency. A) Representative ECG tracings during the 24-hour recording period at baseline and at 8 weeks for sham-operated and TAC-operated mice. At the 8-week mark in TAC mice, there was evidence of abnormal sinus rhythm. **B**) As manifested by the 24-hour ECG recordings, heart rate was significantly lower in the TAC (n=6) than the sham-operated mice (n=9) during most of the mouse's circadian rhythm. We also examined *in vitro* to determine the changes in APs with HF. **C**) Representative tracings of AP recordings from SAN cells from sham-operated

mice and TAC mice are shown. **D**) TAC SANCs exhibited decreased beating frequency, **E**) prolonged APD_{90}, and **F**) APD_{50}. There was a trend towards a reduced **G**) peak potential and **H**) maximum diastolic potential in TAC SANCs relative sham SANCs. We then tested whether FCCP, a potent mitochondrial uncoupler, had any effect on AP. **I**) Representative tracings show control SANCs and SANCs perfused with 1 μM FCCP. **J**) AP beating frequency decreased with FCCP. **K**) There was a trend towards prolonged APD_{90}, and **L**) APD_{50}. **M**) Peak potential was not affected, and **N**) maximum diastolic potential was more hyperpolarized. Data are expressed as mean ± SEM. n=3 mice for all; n=5 SANCs for sham, n=9 SANCs for TAC, n=4 for control, and n=5 for FCCP. * $p<0.05$, ** $p<0.01$.

Figure 3.3.

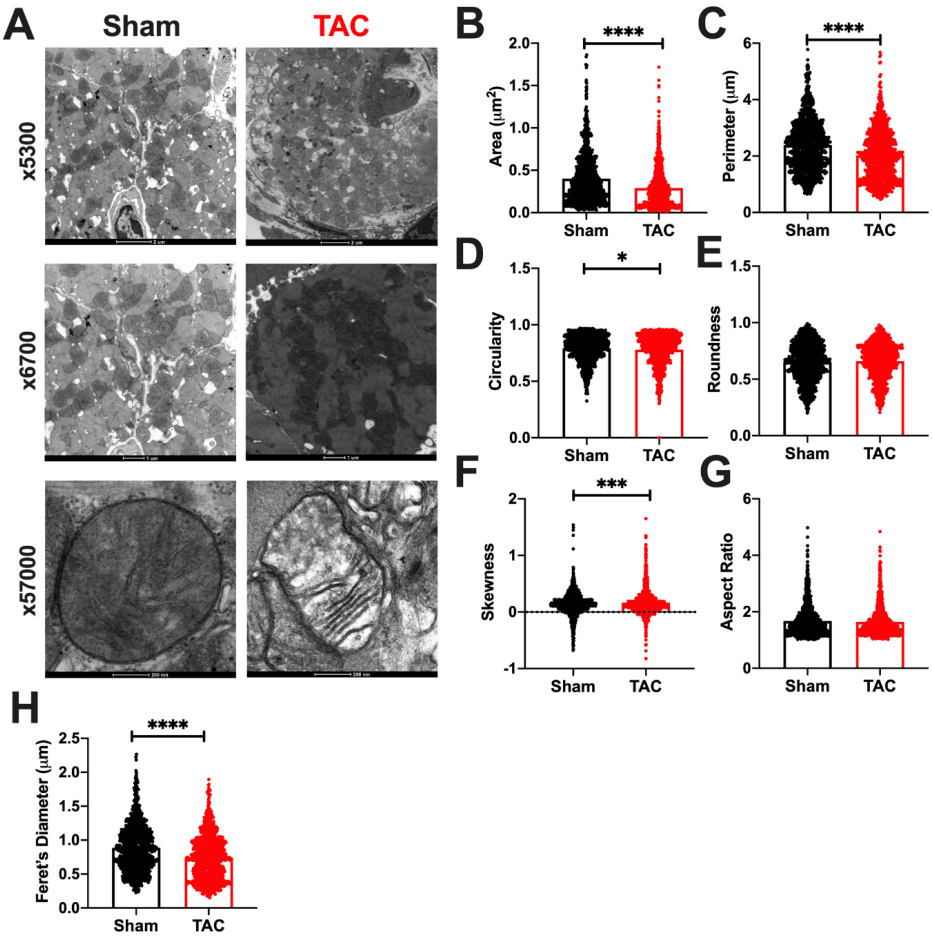

Figure 3.3. HF induced morphological changes to SAN mitochondria. To assess morphological parameters, we examined 100 nm sections of SAN tissues under the electron microscope. **A**) Representative images at x5300, x6700, and 57000 magnifications are seen. As seen in the higher magnifications, mitochondrial internal structural integrity was damaged with HF. Quantification of the different parameters revealed distinct morphological changes to SAN mitochondria during HF. We assessed **B**) area, **C**) perimeter, **D**) circularity, **E**) roundness, **F**) skewness, **G**) aspect ratio, and **H**) Feret's diameter. n = 3 mice for each group, with multiple EM sections from each group; n=1100 mitochondria for the sham group and n=980 mitochondria for the TAC group. Data are expressed as mean ± SEM. * $p<0.05$, *** $p<0.001$, **** $p<0.0001$.

Figure 3.4.

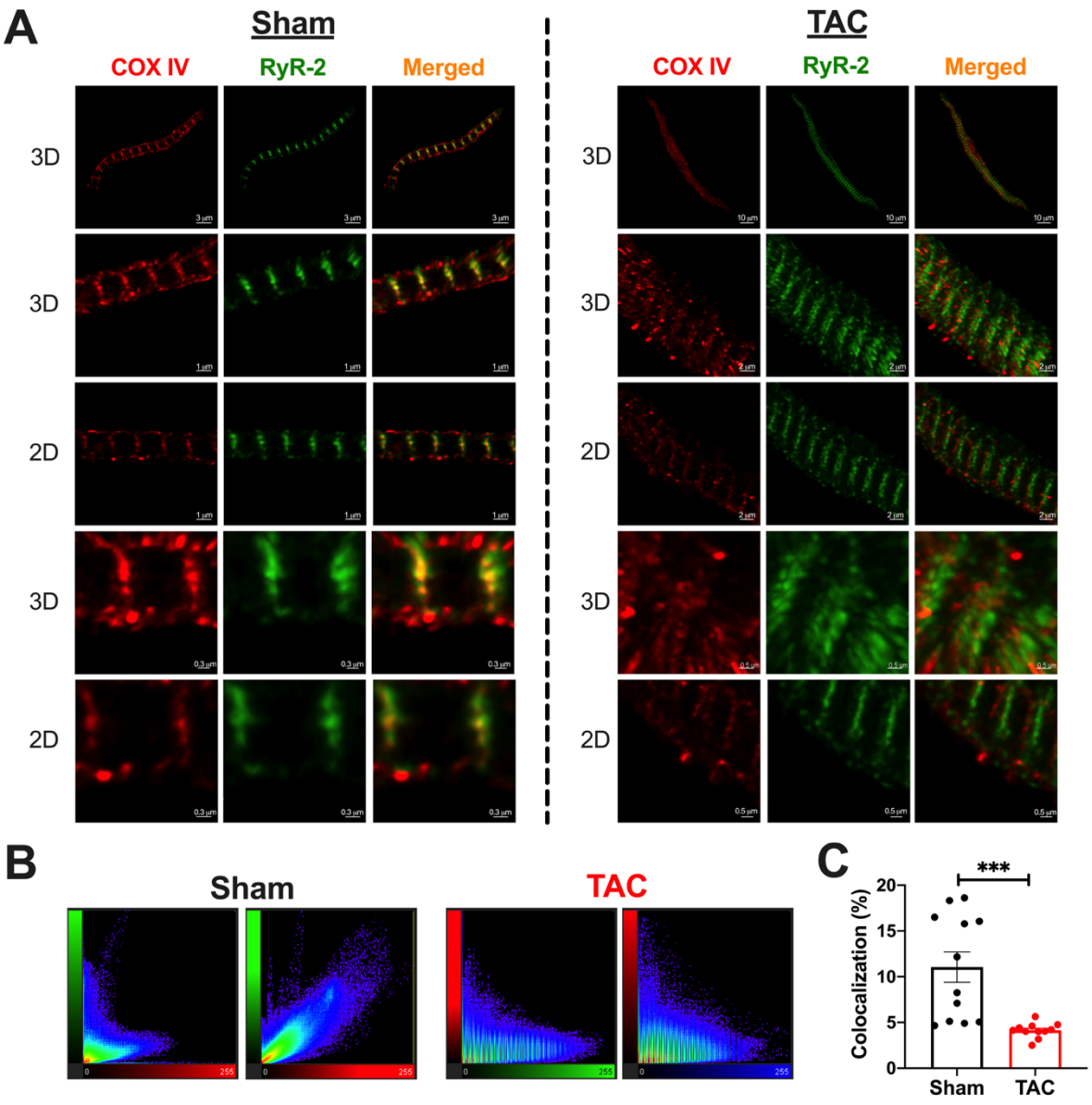

Figure 3.4. HF reduced mitochondria and SR colocalization. A) Representative 2D and 3D STED immunofluorescent images of sham and TAC SANCs simultaneously labeled with RyR-2 (green) and COX IV (red) are shown. As manifested from these images, colocalization of the mitochondria with SR appeared more organized. However, HF disrupted this organization, evident by an apparent reduction in merged signal. 2D and 3D images are shown at different

magnifications. **B**) 2D histograms reveal more colocalization of the mitochondria and SR in the sham SANCs. **C**) Quantification using Mander's coefficient analysis (percentage of RyR-2 that overlaps with COX IV, with respect total RyR-2 fluorescence) showed that colocalization decreased significantly in TAC SANCs. n=3 mice for each group; n=12 SANCs for sham group, and n=11 SANCs for TAC group. Data are represented as mean ± SEM. *** $p<0.001$.

Figure 3.5.

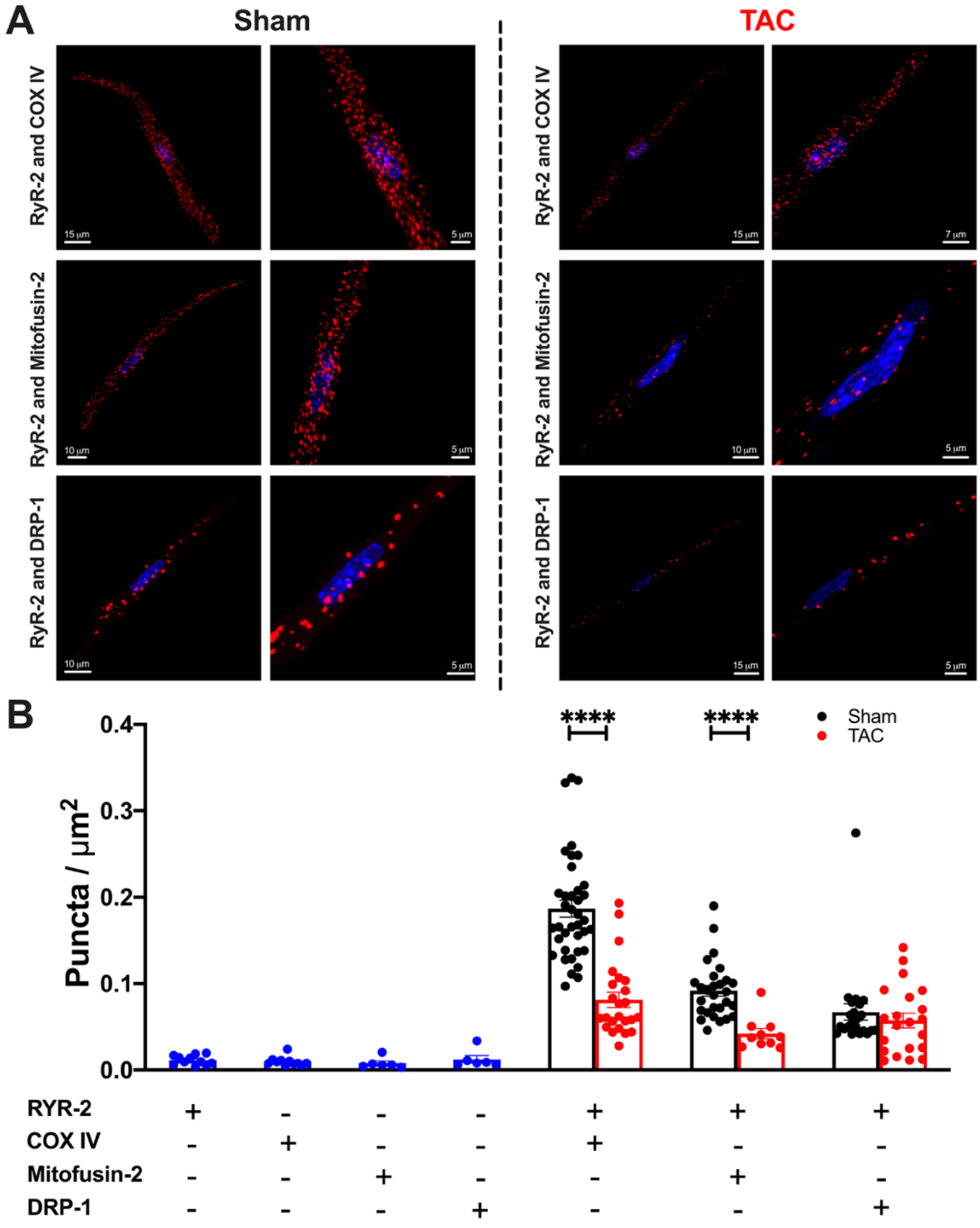
A
Sham
TAC
RyR-2 and COX IV
RyR-2 and Mitofusin-2
RyR-2 and DRP-1
15 µm
5 µm
7 µm
10 µm
B
Puncta / µm2
0.4
0.3
0.2
0.1
0.0
****
****
Sham
TAC
RYR-2 + - - - + + +
COX IV - + - - + - -
Mitofusin-2 - - + - - + -
DRP-1 - - - + - - +

Figure 3.5. HF disrupted the mitochondria and SR microdomain. A) Representative fluorescence 3D PLA (red)/DAPI (blue) images from confocal z-stack of SANCs from sham and TAC mice labeled with RyR-2 + COX IV, RyR-2 + Mitofusin-2, RyR-2 and DRP-1. Positive cross-reactivity, which reflects an intermolecular distance of 40 nm or less, is shown by the red amplification spots (puncta), and the nuclei are depicted in blue. **B**) HF was associated with a significant reduction in the number of puncta, as evident by the decrease in the number of puncta per area. Quantification of PLA fluorescent puncta per cell area (puncta/μm^2) for SANCs labeled with revealed a decrease in spatial proximity between RyR-2 and COX IV (n=38 SANCs for sham, n=24 SANCs for TAC), and RyR-2 and Mitofusin-2 (n=28 SANCs for sham, n=10 SANCs for TAC, but not with DRP-1 (n=24 SANCs for sham, n=21 SANCs for TAC). We used n=3-4 mice for each group. Data are expressed as mean ± SEM. **** $p<0.0001$.

Figure 3.6.

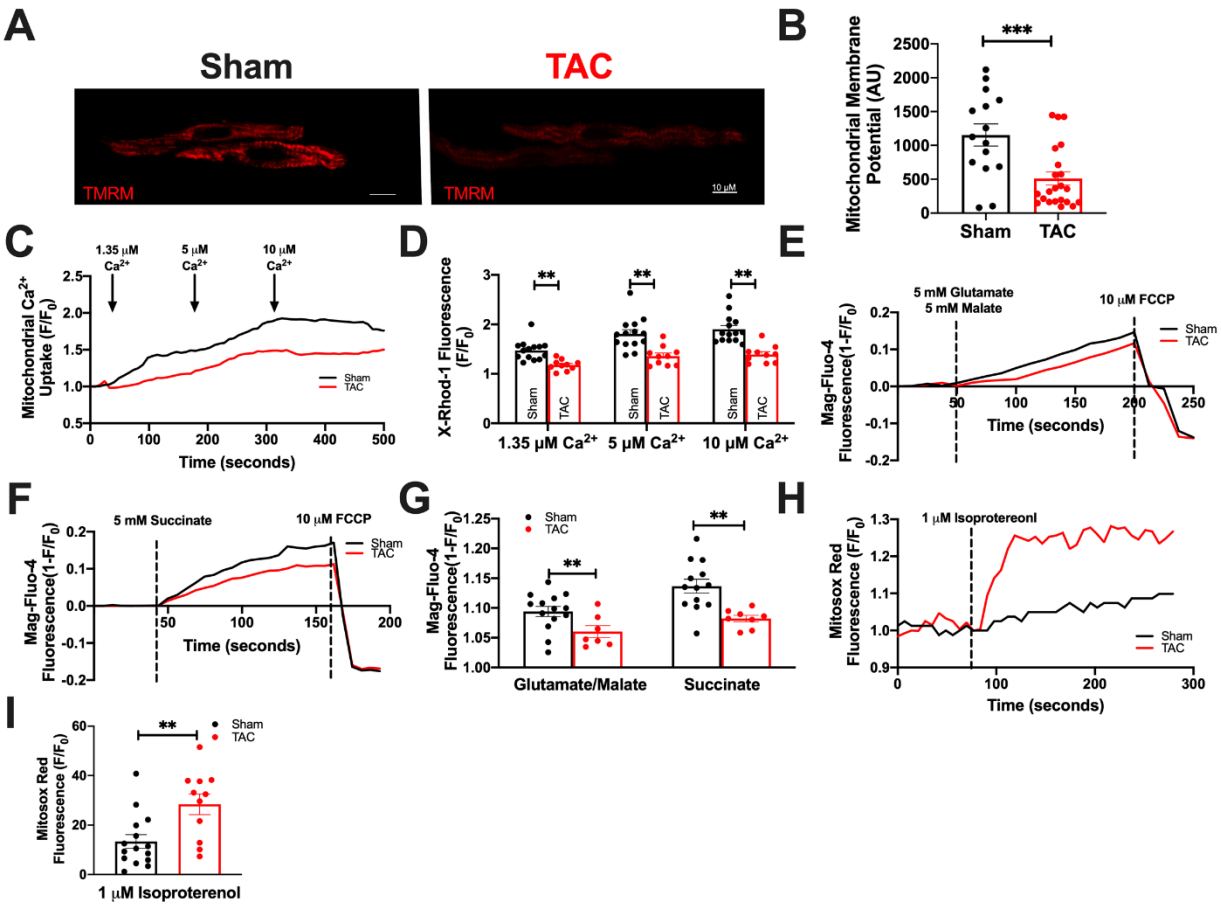

Figure 3.6. Mitochondrial function was impaired with HF. A) Representative images of SANCs from sham and TAC mice loaded with TMRM, a mitochondrial potential dye. TAC SANCs had more depolarized membrane potential, as evident by not only in the representative images, but also **B**) quantitatively. When TAC SANCs were challenged with increasing extramitochondrial [Ca^{2+}], mitochondrial uptake (monitored by X-Rhod-1 fluorescence) was significantly lower in all cases relative to sham SANCs, manifested in **C**) representative tracings and **D**) quantitatively of normalized X-Rhod-1 fluorescence intensity (n=14 sham and n=10 TAC SANCs). **E**) Application of 5 mM of glutamate and 5 mM malate (n=14 sham and n=7 TAC

SANCs), and **F**) 5 mM succinate (n=13 sham and n=8 TAC SANCs) resulted in more ATP concentration, as indicated by Mag-Fluo-4 fluorescence. **G**) The production of ATP was lower in TAC SANCs under both conditions. **H**) Measurement of ROS production using MitoSox Red revealed an increase in ROS production as depicted in the representative tracings. **I**) When MitoSox red signal was normalized to baseline, we found that TAC SANCs had more production of ROS (n=15 sham and n=11 TAC SANCs). Data are expressed as mean ± SEM. ** $p<0.01$, *** $p<0.001$.

Supplementary Figure 3.S1

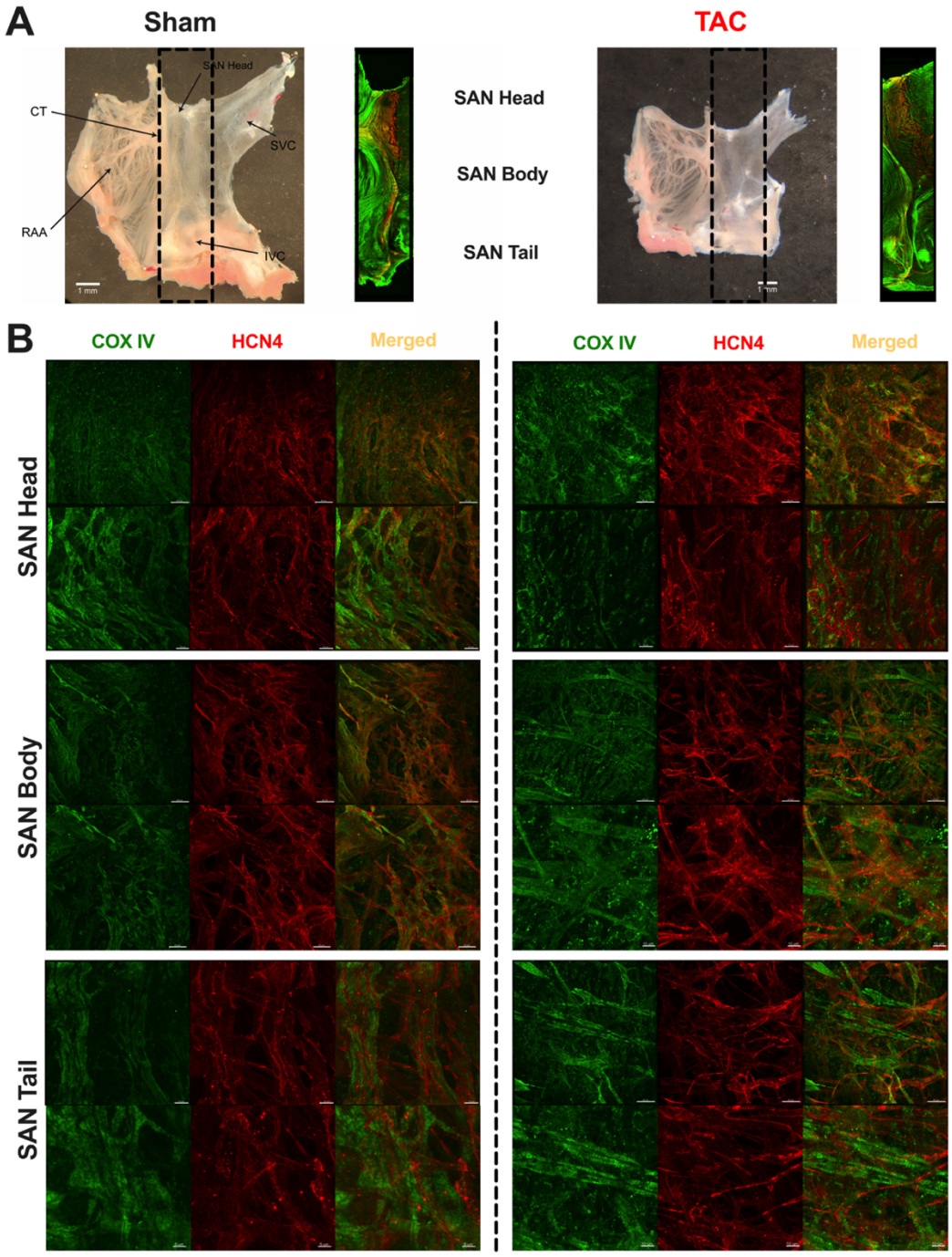

Supplementary Figure 3.S1 Whole mount of SAN regions from sham- and TAC-operated mice were obtained (**A**) and visualized using HCN4 as a marker as well as COX IV to label the inner

mitochondrial membrane protein (**A and B**). Important landmarks were identified including superior vena cava (SVC), right atrial appendage (RAA), and crista terminalis (CT). We then examined three main regions of the SAN tissue—the SAN head, body, and tail (**B**).

CHAPTER 4

Disruption of Protein Quality Control of Human *Ether-à-go-go Related Gene* (hERG) K^+ Channel Results in Profound Long QT Syndrome

Hannah A. Ledford[1*], Lu Ren[1*], Phung N. Thai[1], Seojin Park[1,2], Valeriy Timofeyev[1], Padmini Sirish[1,3], Wilson Xu[1], Aiyana M. Emigh[4], James R. Priest[5], Marco V. Perez[5], Euan A. Ashley[5], Vladimir Yarov-Yarovoy[4], Ebenezer N. Yamoah[2], Xiao-Dong Zhang[1,3], and Nipavan Chiamvimonvat[1,3]

[1]Division of Cardiovascular Medicine, Department of Internal Medicine
University of California, Davis, Davis, CA

[2]Department of Physiology and Cell Biology
University of Nevada, Reno, Reno, NV

[3]Department of Veterans Affairs, Northern California Health Care System, Mather, CA

[4]Department of Physiology and Membrane Biology
University of California, Davis, Davis, CA

[5]Division of Cardiovascular Medicine, Department of Medicine
Stanford University, Stanford, CA

* denotes equal contributions

Running Title: RNF207 Degrades hERG T613M Mutant Channel

To whom correspondence should be address:

Nipavan Chiamvimonvat and Xiao-Dong Zhang
Division of Cardiovascular Medicine
Department of Medicine
University of California, Davis,
451 Health Science Drive, GBSF 6315, Davis, CA 95616,
e-mail: nchiamvimonvat@ucdavis.edu, xdzhang@ucdavis.edu

The authors declare no competing interests.

ABSTRACT

Background: Long QT syndrome (LQTS) is a hereditary disease that predisposes patients to life-threatening cardiac arrhythmias and sudden cardiac death. Our previously study of human *ether-à-go-go related gene* (*hERG*)-encoded K^+ channel ($K_v11.1$) supports an association between hERG and RING Finger Protein 207 (RNF207) variants in aggravating the onset and severity of LQTS, specifically T613M hERG ($hERG_{T613M}$) and RNF207 frameshift ($RNF207_{G603fs}$) mutations. However, the underlying mechanistic underpinning remains unknown.

Objective: The purpose of the current study is to test the role of RNF207 on the function of *hERG*-encoded K^+ channel subunits.

Methods and Results: Here, we demonstrate that RNF207 serves an E3 ubiquitin ligase and targets misfolded $hERG_{T613M}$ proteins for degradation. $RNF207_{G603fs}$ exhibits decreased activity and hinders the normal degradation pathway; this increases the levels of $hERG_{T613M}$ subunits and their dominant-negative effect on the wild-type (WT) subunits, ultimately resulting in decreased current density. Finally, the presence of $RNF207_{G603fs}$ with $hERG_{T613M}$ results in significantly prolonged action potential durations and reduced hERG current in human pluripotent stem cell-derived cardiomyocytes.

Conclusions: Our study establishes RNF207 as an interacting protein serving as a ubiquitin ligase for *hERG*-encoded K^+ channel subunits. Normal function of RNF207 is critical for the quality control of hERG subunits and, consequently, cardiac repolarization. Moreover, our study provides the first evidence for protein quality control as a new paradigm in life-threatening cardiac arrhythmias in LQTS patients.

Keywords: human *ether a-go-go related* gene (*hERG*)-encoded potassium channels, RING Finger Protein 207 (RNF207), ion channel degradation, long QT syndrome, human arrhythmia syndrome

INTRODUCTION

The pore forming α subunit of the $K_v11.1$ channel (also known as human *Ether-à-go-go Related* gene, hERG, encoded by the *KCNH2* gene) underlies the rapid component of the delayed rectifier K^+ current (I_{Kr})[1-3]. The *hERG*-encoded K^+ channel is known to play a critical role in ventricular repolarization. Indeed, loss-of-function mutations in *hERG*-encoded K^+ channels result in decreased I_{Kr}, causing delayed repolarization and the prolonged QT interval characteristic of Long QT Syndrome (LQTS) Type 2[2, 4-6]. The fundamental defect in LQTS is prolonged ventricular repolarization, caused by the imbalance of inward and outward currents, and an increase in occurrences of torsades de pointes polymorphic ventricular tachycardia, ventricular fibrillation, and sudden cardiac death[7-9].

Genetic mutations in cardiac ion channels, known collectively as cardiac ion channelopathies, have been shown to cause a significant percentage of LQTS cases[7, 8, 10-12]. Currently, it is estimated that 1 in 5,000 people carry a LQTS mutation. Defects in *hERG*-encoded K^+ channels are the second leading cause of LQTS. Moreover, *hERG*-encoded K^+ channels represent the most common target for drug-induced LQTS.[2, 4-6, 13-16] With the inclusion of drug-induced or acquired LQTS cases, many of whom have the same genetic ion channel defects as those with the congenital LQTS disease, it is estimated that the true incidence of LQTS may be as high as 1 in 1,000[7, 11, 12].

Previous studies have provided new evidence that LQTS manifests not only from mutations in cardiac ion channels (as in LQT1, LQT2, and LQT3), but also mutations in ion channel interacting proteins (such as calmodulin in LQT14-16)[17-22]. One potential ion channel interacting protein is RING Finger Protein 207 (RNF207), encoded by its gene located on chromosome 1.

RNF207 is a specialized type of zinc finger protein, shown to be associated with prolongation of the QT interval[23-27].

Our previous study revealed RNF207 as a potential modifier of the hERG channel.[28] Specifically, a term female infant presented with perinatal LQTS with recurrent life-threatening ventricular arrhythmias. Using whole-genome sequencing (WGS), a paternally inherited, known pathogenic variant in *KCNH2* leading to a missense mutation (p.T613M, $hERG_{T613M}$) was identified. In addition, WGS revealed a maternally inherited variant of unknown significance in *RNF207* gene (a frameshift mutation, $RNF207_{G603fs}$). The patient was heterozygous for both variants, however, neither parent presented with LQTS. The findings suggest that the patient's presentation of LQTS may result from the simultaneous inheritance of the heterozygous RNF207 variant with the $hERG_{T613M}$ channel (**Fig. 4.1A**).

Previous literature has shown that the T613M hERG mutation ($hERG_{T613M}$, located in the CpG sequence of the pore helix, **Fig. 4.1A**) produces no detectable current and very low surface expression, suggesting a trafficking defect[29]. Co-expression of $hERG_{T613M}$ with wild-type hERG ($hERG_{WT}$) subunits presented very low current density, indicating that $hERG_{T613M}$ may exert a dominant-negative effect when forming heterotetramers with $hERG_{WT}$ subunit[29].

There is evidence for an interaction between the $hERG_{WT}$ and RNF207 proteins *via* RNF207's RING domain[25]. This RING domain, as well as RNF207's structural similarity to tripartite motif-containing proteins (TRIM), suggest a potential function of RNF207 as an E3 ubiquitin ligase and a possible role in facilitating protein degradation[30, 31]. However, the exact molecular mechanisms remain unexplored.

Misfolded hERG proteins are frequently degraded by endoplasmic reticulum (ER)-associated degradation (ERAD)[30, 32-34]. Following polyubiquitination, proteins are dislocated from

the ER and degraded by proteasome within the cytosol. Several quality control proteins targeting *hERG*-encoded K^+ channel subunits have been identified. C-terminus of heat shock cognate protein 70 (HSC70)-Interacting Protein (CHIP), an E3 ubiquitin ligase, has been shown to be involved in ERAD of hERG proteins through polyubiquitination[35-37]. CHIP knockdown, however, fails to completely abolish hERG polyubiquitination, suggesting that other E3 ligase may account for the remaining polyubiquitination[34]. RNF207 has been shown to interact with chaperones heat shock protein 70 (Hsp70), Hsc70, and DJA1, which have also been shown to be involved in the regulation of hERG subunits and CHIP-mediated ERAD.[25, 38, 39] Therefore, RNF207 may play a critical role in ERAD. Through lysosomal degradation, neural precursor cell expressed developmentally down-regulated protein 4-2 (NEDD4-2) also acts as an ubiquitin ligase for hERG subunits, but *via* mono-ubiquitination[32, 33, 40, 41]. Neither CHIP nor NEDD4-2 is thought to act alone, and it is likely that multiple ligases act in concert to coordinate the degradation of mutant hERG subunits.

Here, we demonstrate that RNF207 serves as one of the ubiquitin ligases and targets misfolded $hERG_{T613M}$ proteins for degradation. Mutant RNF207 ($RNF207_{G603fs}$) exhibits decreased activity and hinders the normal degradation pathway; this increases the levels of $hERG_{T613M}$ subunits and their dominant-negative effect on the WT subunits, ultimately resulting in decreased current density. Our study provides novel mechanisms whereby dysfunction in degradation-dependent quality control plays a key role in aggravating the effects of existing LQTS mutations.

MATERIALS AND METHODS

Cell Culture and Transfections

Human embryonic kidney (HEK 293) cells were maintained in Dulbecco's Modified Eagle's Medium (DMEM) with 10% fetal bovine serum and 1% penicillin/ streptomycin, at 37 ºC with 5% CO_2 in a humidified chamber. Cells were transfected at 60-80% confluency, using Lipofectamine 2000 (Thermo Fisher Scientific, Waltham, MA). All experiments were conducted 48-60 hours following transfection, as published electrophysiology data suggests that hERG expression and membrane trafficking are optimal 24-96 hours post transfection[42, 43]. hERG cDNA plasmids included green fluorescent protein (GFP) as a reporter gene using pIRES2-EGFP vector (Takara Bio USA, Inc., Mountain View, CA) to select for transfected cells. The hERG, MiRP1, and RNF207 plasmids were transfected using a 1:2:3 molar ratio (400 ng: 500 ng: 1000 ng). Total transfected DNA was held constant at 1900 ng when $hERG_{T613M}$ and $RNF207_{G603fs}$ were co-transfected (200 ng $hERG_{WT}$: 200 ng $hERG_{T613M}$: 500 ng MiRP1: 500 ng $RNF207_{WT}$: 500 ng $RNF207_{G603fs}$) and in groups expressing hERG alone. Confocal microscopy was used to evaluate the transfection efficiency. Native expression of the hERG and RNF207 proteins was also quantified.

Plasmid Construction

$RNF207_{WT}$ and $RNF207_{G603fs}$ (1807-1811P, GGCCT->GCT frameshift mutation) in pEZ-M14 mammalian expression vector with C-3xFlag were purchased from Genecopoeia (Rockville, MD) and Thermo Fisher Scientific (GeneArt Gene Synthesis), respectively. The pIRES2-EGFP-hERG (NM_172056.2) and pIRES2-EGFP-$hERG_{T613M}$-Myc (C->T, T613M with Myc tag inserted between S1-S2 extracellular loop nt 1273-1350, aa 425-450 in cgi-hERG vector) constructs were purchased from Genecopoeia. The $hERG_{T613M}$ (C->T T613M) construct was generated from the

pIRES-EGFP-hERG plasmid using Quickchange II XL Site-Directed Mutagenesis (Agilent Technologies, Santa Clara, CA). A hemagglutinin (HA) tag was inserted into the extracellular S1-S2 loop of pIRES2-EGFP $hERG_{WT}$ with ClC-5 Cl^- channel D1-D2 loop to increase flexibility,[44] as we have previously described[45]. S1-S2 loop amino acid sequences were changed to TAVFTPYSAAFLSHE**YPYDVPDYA**VTFEERDKCPEWNCLKETEEGPPATE, with inserted sequence underlined and epitope shown in bold. The pIRES2-EGFP-hERG-HA plasmid was used to generate the $hERG_{WT}$-ΔN, 404-1159 aa residues; $hERG_{WT}$-ΔC, 1-654 aa residues; hERG N-terminus, 1-403 aa residues; and hERG C-terminus, 660-1160 aa residues. All constructs were verified by automated sequencing.

Cardiac Myocyte Isolation

Ventricular cardiomyocytes were isolated from New Zealand White rabbits (4 months old) as well as guinea pigs (2-3 months old, Charles River Laboratories, Wilmington, MA), according to our previously established methods[46]. All animal care and use were approved by the University of California, Davis, Institutional Animal Care and Use Committee. Animal use was in accordance with National Institutes of Health and institutional guidelines. All reagents were obtained from Sigma-Aldrich (St. Louis, MO) unless stated otherwise.

Immunofluorescence Confocal Microscopy and Stimulated Emission Depletion (STED) Microscopic Imaging

Immunofluorescence confocal microscopy was performed on isolated guinea pig and rabbit ventricular cardiomyocytes and HEK293 cells. Primary antibodies used include anti-hERG (1:50 dilution, mouse monoclonal antibody, sc-377388, Santa Cruz) and anti-RNF (1:200 dilution, HPA042535, rabbit polyclonal, Sigma-Aldrich, St. Louis, MO) for dual labeling, anti-hERG (1:200 dilution, APC-062, rabbit polyclonal, Alomone Labs, Jerusalem, Israel) or anti-RNF207

(1:200 dilution, HPA042535, rabbit polyclonal, Sigma-Aldrich) for dual labeling with anti-α-actinin2 (1:300 dilution, mouse monoclonal, a7811, Sigma-Aldrich) in guinea pig ventricular myocytes. Additional antibodies used include anti-HA (1:100 non-permeabilized; 1:250 permeabilized, H6908, Sigma), and anti-Myc tag (1:100 non-permeabilized; 1:250 permeabilized, ab18185, Abcam, Cambridge, MA) antibodies.

Cells were fixed in 4% paraformaldehyde, blocked with 1% bovine serum albumin, and incubated with primary antibodies overnight at 4°C. For permeabilized (P) conditions, cells were treated with Triton-X. Secondary antibodies included IgG (H+L) Alexa Fluor 555 and Alexa Fluor 647 (Life Technologies, Carlsbad, CA, 1:500 dilution). Non-permeabilized to permeabilized imaging and quantification was performed as previously described.[47, 48] Anti-HA and anti-Myc tag antibodies were used to test non-permeabilized to permeabilized staining in order to quantify the ratio of hERG channels on the cell membrane over cytosolic hERG channels. Specifically, a 1:100 dilution of anti-HA or anti-Myc tag antibodies were used with Alexa Fluor 555 secondary antibody (Thermo Fisher Scientific) under non-permeabilized condition to target membrane-bound hERG channels, followed by permeabilization and a 1:250 dilution of anti-HA or anti-Myc tag primary antibody and Alexa Fluor 647 secondary antibody (Thermo Fisher Scientific) to target cytosolic hERG channels. The fluorescence ratio of 555/647 was quantified, as previously described, using ImageJ FIJI software[47, 48].

For co-localization experiments in rabbit ventricular myocytes (**Supp. Fig. S4.2**), primary antibodies were tagged with 1:40 anti-rabbit Fab Alexa Fluor 488 (Jackson ImmunoResearch) and 1:100 anti-rabbit F(ab)2 Alexa Fluor 555 (Life Technologies). Rabbit cardiomyocytes were blocked with unlabeled Fab antibody (Jackson ImmunoResearch) prior to the addition of each primary antibody to prevent cross-talk and background labeling of endogenous rabbit antigens

(**Supp. Fig. S4.3**). Additional positive and negative controls were used to demonstrate alternate staining patterns from inaccurate rabbit antibody labeling of endogenous rabbit antigens, as well as to verify complete blocking of these antigens in the presence of unlabeled Fab antibody. Coverslips were mounted onto slides using Prolong Gold Antifade Mountant (P32930, ThermoFisher Scientific) and imaged on an LSM700 Zeiss laser scanning confocal microscope (Carl Zeiss, Oberkochen, Germany). STED microscopy was performed on a Leica STED (TCS SP8 STED 3X) microscope. Deconvolution, using Huygens Professional software, was limited to 15 iterations and a signal to noise ratio of 4 with manual evaluation of background intensity.

Proximity ligation assay

A Duolink In Situ proximity ligation assay (PLA) (Sigma-Aldrich) was used to detect complexes containing *hERG*-encoded K^+ channel subunits, RNF207 and α-actinin2 proteins in freshly isolated guinea pig ventricular myocytes as previously described.[49] Antibodies and dilution used were the same as in immunofluorescence imaging in guinea pig ventricular myocytes described above. For control, cells were incubated with a single primary antibody. Ventricular myocytes were imaged on an LSM700 Zeiss laser scanning confocal microscope and images were acquired at different optical planes (z-axis of 0.5 mm). Imaging and analysis were performed as previously described using NIH ImageJ open software[49].

Co-Immunoprecipitation Assay and Western Blot

Co-immunoprecipitation (co-IP) was performed on protein isolated from transfected HEK 293 cells. Protein from each group was isolated and combined with Pierce Protein A/G Agarose Beads (ThermoFisher Scientific), using 2.5 μg of anti-hERG antibody (APC-062, Alomone). Samples were run on Bio-Rad 8-16% TGX gels at 100 V for 1 hour, transferred to nitrocellulose membranes, blocked with 3% milk, and incubated overnight at 4 ˚C using anti-hERG (1:3000,

Alomone) and anti-FLAG antibodies (1:400, F3040, Sigma-Aldrich) to target the FLAG tag on the RNF207 construct.

The $hERG_{WT}$-ΔN, $hERG_{WT}$-ΔC, hERG N-terminus, and hERG C-terminus (tagged with HA) were co-transfected in HEK 293 cells with $RNF207_{WT}$-FLAG and co-immunoprecipitated using 2.5 μg anti-HA antibody (Sigma-Aldrich).

Electrophysiology

Whole-cell patch-clamp experiments were performed on HEK 293 cells and hiPSC-CMs transfected with $hERG_{WT}$, $hERG_{T613M}$, $RNF207_{WT}$, and $RNF207_{G603fs}$. All cells were co-transfected with the β subunit, MiRP1. All currents were recorded at room temperature using whole-cell patch-clamp techniques. Bath (external) solution contained (in mM): 140 NaCl, 5.4 KCl, 1 $MgCl_2$, 10 HEPES, 10 Glucose, 2 $CaCl_2$ with a pH of 7.4. The pipette (internal) solution contained (in mM): 140 KCl, 1 $MgCl_2$, 10 HEPES, 5 EGTA, 4 MgATP with a pH of 7.3. I_{Kr} was elicited using a holding potential of -80 mV with 10-mV depolarizing steps up to 80 mV followed by a -50 mV step to elicit the tail currents, according to our previously published protocol.[50] E-4031 (1 μM) was used to confirm I_{Kr} recordings in transfected HEK 293 cells (see **Supp. Fig. 4.4**) and hiPSC-CMs (**Fig. 4.8**). Series resistance was compensated at 60-80%. Pipette resistances were between 2-4 MΩ and seal resistances were > 2 GΩ.

Action potentials of hiPSC-CMs were recorded using perforated patch-clamp techniques at room temperature. The patch-pipettes were backfilled with amphotericin (200 μg/ml). The pipette solution contained (in mM): 120 potassium glutamate, 1 $MgCl_2$, 25 KCl, 10 HEPES, 1 $CaCl_2$, pH 7.25, and the extracellular solution contained (in mM): 138 NaCl, 4 KCl, 1 $MgCl_2$, 2 $CaCl_2$, 0.33 NaH_2PO_4, 10 Glucose, 10 HEPES, pH 7.4. All recordings were performed using 3 M KCl agar bridges. Recordings were obtained using an Axopatch 200B amplifier and pClamp 10.2 (Molecular

Devices, Sunnyvale, CA). Currents were filtered at 2 kHz and sampled at 10 kHz and analyzed using OriginPro 8 (OriginLab, Northampton, MA). All current densities were normalized to cell capacitance.

Human induced pluripotent stem cell-derived cardiomyocytes

hiPSC-CMs were obtained from Cellular Dynamics International (CDI, Madison, WI) and maintained according to the manufacturer's protocol. Briefly, the hiPSC-CM vial was immersed in a 37°C water bath for 4 minutes, the contents transferred to a 50 ml sterile tube and plating medium (CDI, Madison, WI) was transferred drop-wise onto the cells. Sample cells were counted using a hemocytometer to determine the viable cell density. The cells were plated onto 6-well cell culture plates (Stemcell Technologies, Vancouver, Canada) pre-coated with 0.1% gelatin (ThermoFisher Scientific) in water at 37°C cell culture incubator for 1 hour. Two days after plating, non-adherent cells were gently washed off and the hiPSC-CMs were maintained in Maintenance media (CDI, Madison, WI), replacing the media every other day. Two weeks after plating, the cells were washed twice with Dulbecco's Phosphate Buffered Saline (D-PBS, Invitrogen), enzymatically digested with 0.1% trypsin (Invitrogen) and plated onto gelatin coated plates as individual cells and utilized for electrophysiology.

Transfection of hiPSCs was conducted using magnetic nanoparticles according to the methods we previously reported [51]. Confocal microscopy was used to evaluate the transfection efficiency. Native expression of the hERG and RNF207 proteins was also quantified.

Molecular Modeling

The *hERG*-encoded K^+ *channel* structure was previously determined at 3.8 Å resolution using cryo-electron microscopy (cryo-EM).[52] We used *Rosetta modeling* software[53-56] and hERG cryo-EM structure[52] as a template to generate the hERG model (**Fig. 4.5**). It is of interest to note

that the T613 residue is positioned in close proximity to an α-helix in the pore loop. Molecular visualization was performed using the University of California, San Francisco Chimera software package[57].

Auto-ubiquitinylation Assay

E3 ubiquitin ligase activity was quantified using an Auto-Ubiquitinylation Kit (BML-UW0970-0001, Enzo Life Sciences, Inc., Farmingdale, NY), according to the manufacturer's recommendations. To isolate protein prior to testing, we used 2.5 μg anti-FLAG antibody to pull down $RNF207_{WT}$-FLAG and $RNF207_{G603fs}$-FLAG and 2.5 μg anti-hERG antibody to pull down $hERG_{WT}$ and $hERG_{T613M}$ from transfected HEK 293 cells.

Degradation Assays

Degradation assays were performed on HEK 293 cells transfected with 1) $hERG_{WT}$: $RNF207_{WT}$, 2) $hERG_{WT}$: $hERG_{T613M}$: $RNF207_{WT}$, 3) $hERG_{WT}$: $hERG_{T613M}$: $RNF207_{WT}$: $RNF207_{G603fs}$, and 4) $hERG_{WT}$: $RNF207_{WT}$: $RNF207_{G603fs}$. All groups were co-transfected with the ß subunit, MiRP1. At 48 hours following transfection, cells were treated with brefeldin A and collected at 0, 3, 6, 12, and 24 hours later. Additional groups were treated either MG132 or bafilomycin A1 in addition to brefeldin A. Brefeldin A, MG132, and cell culture media were purchased from Sigma-Aldrich. Bafilomycin A1 was purchased from Invitrogen (Carlsbad, CA). All immunoblots were quantified using ImageJ FIJI software.

Statistical Analysis

Data are shown as mean ± SEM and analyzed using OriginPro 8.0. One-way analysis of variance was used with Tukey post-hoc analysis and $p < 0.05$ considered significant. Number of technical and biological replicates is based on previously published observations to reached

statistical differences between datasets following a power analysis with power of 0.8 for an alpha value of 0.05. We accounted for variability in sample preparation by performing technical replicates as well as biological replicates. Statistical significance was then determined using appropriate paired or unpaired Student's *t*-test, nonparametric tests or One-way analysis of variance (ANOVA) for multiple comparisons with Brown-Forsythe or Tukey's post hoc analyses. $P < 0.05$ was considered statistically significant (denoted by * in figures).

RESULTS

$hERG_{T613M}$ exerts a dominant-negative effect when co-expressed with $hERG_{WT}$

HEK 293 cells were transfected with hERG and an accessory subunit, KCNE2 (MiRP1).[58, 59] I_{Kr} is known for its signature properties of slow activation, fast inactivation, and rapid recovery from inactivation.[3] In whole-cell voltage-clamp experiments, the $hERG_{T613M}$ mutant failed to conduct I_{Kr} due to membrane trafficking defects, as shown in both our electrophysiology and immunofluorescence data (**Fig. 4.1B&D**, and **Fig. 4.3A&C**). The $hERG_{T613M}$ failed to traffic to the membrane on its own and was confined to the endoplasmic reticulum (**Supp. Fig. 4.1**). Our data are consistent with previous studies on the T613M mutation[29]. Co-expression of $hERG_{WT}$ with $hERG_{T613M}$ only partially rescued I_{Kr} with significantly reduced current density compared to the expression of $hERG_{WT}$ subunits alone (**Fig. 4.1B-D**, $p < 0.05$). Moreover, the $hERG_{WT}$:$hERG_{T613M}$ current exhibited significantly faster time constants for activation and inactivation and significantly slower time constants for deactivation and recovery from inactivation (**Fig. 4.1E-H**, *$p < 0.05$, **$p < 0.01$), suggesting the formation of hetero-tetramers between WT and mutant subunits.

The hERG-encoded K^+ channel subunits co-localize with $RNF207_{WT}$

Immunofluorescence experiments, visualized with confocal microscopy, in guinea pig ventricular cardiomyocytes showed strong co-localization of hERG and RNF207 proteins as well as co-localization of hERG and RNF207 with α-actinin2, used to mark the z lines (**Fig. 4.2A**). Experiments using confocal and high-resolution microscopy were also performed in rabbit ventricular myocytes (**Supp. Fig. 4.2**). Positive and negative controls were used to confirm the localization of both hERG and RNF207 to the z lines and to eliminate contaminating signal from endogenous antigens in rabbit ventricular myocytes (**Supp. Fig. 4.3**). As shown by the co-localization profile, both hERG and RNF207 proteins localized near the z lines (**Fig. 4.2A** and **Fig. S4.2C**). In accordance with previous literature, hERG channels are expressed predominantly along the t-tubules[60, 61]. We further used proximity ligation assay (PLA), which detects whether 2 proteins of interest are ≤ 40 nm apart (**Fig. 4.2B, C**). We have extensively validated this approach in our prior study[49]. Robust PLA signals were observed in guinea pig ventricular myocytes co-labeled with anti-hERG, anti-RNF207, and anti-α-actinin2 antibodies (**Fig. 4.2B**). Three-dimensional (3D) rendering are shown in Online Supplemental Movies. In contrast, PLA signals were completely absent when one of the primary antibodies was omitted (**Fig. 4.2C**). The results further support a close association (≤ 40 nm) between *hERG*-encoded K^+ channel subunits and RNF207. Additionally, the findings further support co-localization of *hERG*-encoded K^+ subunits and RNF207 along the z lines of ventricular myocytes.

$RNF207_{G603fs}$ exhibits decreased E3 ubiquitin ligase activity

Using an auto-ubiquitinylation assay, we demonstrate that RNF207 is, indeed, an E3 ubiquitin ligase (**Fig. 4.2D**). As compared to the known auto-ubiquitin ligase, MDM2, $RNF207_{WT}$ displayed strong auto-ubiquitinylation (**Fig. 4.2D**). When ubiquitin ligase activity was evaluated in the presence of $hERG_{WT}$, we did not observe significant ubiquitination by $RNF207_{WT}$ (**Fig. 4.2E**, lane 2). In contrast, incubation of $RNF207_{WT}$ with $hERG_{T613M}$ resulted in significant ubiquitination of the $hERG_{T613M}$ subunits (**Fig. 4.2E**, lane 3). Importantly, $RNF207_{G603fs}$ failed to tag the $hERG_{T613M}$ mutant subunit with ubiquitin (**Fig. 4.2E**, lane 5). Summary data from ubiquitination assay for RNF207 and hERG wild-type and mutant proteins are shown in **Fig. 4.2F**.

$RNF207_{WT}$ decreases $hERG_{T613M}$ membrane-bound population

Using our previously published methods on non-permeabilized (NP) to permeabilized (P) immunofluorescent staining, an HA tag was inserted into the S1-S2 linker of the $hERG_{WT}$ plasmid in order to quantify the ratio of hERG channels on the membrane *versus* those in the cytosol (**Fig. 4.3A, B**).[47] In addition, we inserted a Myc tag into the S1-S2 linker of $hERG_{T613M}$ to distinguish between WT and mutant hERG subunits on the membrane (**Fig. 4.3B**). $hERG_{T613M}$ subunits failed to show fluorescence in non-permeabilized condition, due to trafficking defects (**Fig. 4.3A**). The $hERG_{WT}$:$hERG_{T613M}$ group, however, showed normal fluorescent levels.

We next tested the roles of $RNF207_{WT}$ and $RNF207_{G603fs}$ on hERG subunit membrane localization. We tested NP to P fluorescence ratios for HA and MYC tag in order to quantify the localization of mutant and WT hERG subunits when $hERG_{WT}$:$hERG_{T613M}$:$RNF207_{WT}$ were co-expressed (**Fig. 4.3A&C**). Our data shows normal fluorescence for $hERG_{WT}$-HA on the membrane, whereas $hERG_{T613M}$-MYC was primarily seen in the cytosol, suggesting a greater population of $hERG_{WT}$ channels on the membrane (**Fig. 4.3A&C**). The addition of $RNF207_{G603fs}$, however,

resulted in an increase in $hERG_{T613M}$ subunits on the membrane, suggesting decreased degradation of $hERG_{T613M}$ by $RNF207_{G603fs}$.

$RNF207_{WT}$ increases degradation of $hERG_{T613M}$ subunits.

Following transfection with hERG and RNF207 WT and mutant proteins, we treated HEK 293 cells with brefeldin A and collected protein lysate at various time points (0, 3, 6, 12, and 24 hours after treatment). Brefeldin A, an inhibitor of ER to Golgi transport, decreased the fully glycosylated 155 kDa form, while the cytosolic core glycosylated 135 kDa form of hERG subunits increased over time (**Fig. 4.4A**). Western blot analyses showed significant accumulation of hERG subunits when $hERG_{WT}$:$hERG_{T613M}$ subunits were co-expressed with $RNF207_{WT}$:$RNF207_{G603fs}$ (closed Δ) compared to the co-expression with $RNF207_{WT}$ (closed O, **Fig. 4.4A&B, *P<0.05**). The differences between these two groups were reduced by the addition of MG 132, a proteasome inhibitor, suggesting that $RNF207_{WT}$ may function through the ubiquitin proteasome system **(Fig. 4.4A&C**). Similar effects were also seen with the addition of bafilomycin A1, a lysosome inhibitor, suggesting additional role of lysosomal degradation (**Fig. 4.4A&D**).

RNF207 interacts with the hERG K^+ channel subunits via the C terminus

Co-immunoprecipitation experiments revealed that $hERG_{WT}$ successfully immunoprecipitated $RNF207_{WT}$, suggesting that the two proteins form multi-protein complexes (**Fig. 4.5A**). $hERG_{T613M}$ also pulled down $RNF207_{WT}$, suggesting an interaction between mutant hERG subunits and the functional RNF207 (**Fig. 4.5A**). The $RNF207_{G603fs}$ showed a weaker interaction with $hERG_{WT}$, but also interacted with $hERG_{T613M}$. Co-immunoprecipitation assays were performed in triplicate to verify the findings.

In order to further elucidate the domain necessary for RNF207's interaction with the hERG K^+ channel, we designed four additional hERG-HA constructs: hERG ΔN (ΔN), hERG ΔC (ΔC), hERG N-terminus (N_{cyt}), and hERG C-terminus (C_{cyt}) (**Fig. 4.5B**). We co-expressed $RNF207_{WT}$-FLAG with the hERG fragments and performed co-immunoprecipitation assays to determine the interaction domain of the hERG channel with RNF207 (**Fig. 4.5C**). The lysate samples are show in Lanes 1-4. The hERG ΔN and hERG C-terminus were able to successfully immunoprecipitate $RNF207_{WT}$ (Lanes 5 and 8, **Fig. 4.5C,** upper panel), while hERG ΔC and hERG N-terminus failed to pull down RNF207 (Lanes 6 and 7, **Fig. 4.5C,** upper panel). The reverse experiments were performed in the lower panel using anti-FLAG and anti-HA antibodies for immunoprecipitation and immunoblotting, respectively. There are some nonspecific bands from the immunoprecipitated samples (**Fig. 4.5C**, lower panel, Lanes 5-8), however, a distinct band of expected size could be discerned in Lane 5, corresponding to $hERG_{WT}$-ΔN, consistent with the findings obtained using anti-HA and anti-FLAG antibodies for immunoprecipitation and immunoblotting, respectively (upper panel). Altogether, the data suggest that the C terminus of $hERG_{WT}$ plays an important role in its interaction with $RNF207_{WT}$.

To determine the mechanistic underpinning of $hERG_{T613M}$ on the alterations in the time-dependent kinetics of the channel (**Fig. 4.1E-H**), we took advantage of the published cryo-EM hERG structure [52] using *Rosetta modeling* software (**Fig. 4.5D**) to further inform the functional analyses. The hERG backbone is shown with rainbow color scheme from the N (blue) to C terminus (red). The T613 residue is seen to position near the extracellular side of the pore, likely plays critical roles in channel activation and inactivation kinetics as demonstrated in **Fig. 4.1E-H**.

$RNF207_{G603fs}$ decreases I_{Kr} density

To directly test our hypothesis that RNF207 plays critical roles in the quality control of hERG subunits, we conducted whole-cell voltage-clamp experiments to functionally test the effects of WT compared to mutant RNF207 on $hERG_{WT}$ and $hERG_{T613M}$ (**Fig. 4.6A**). Expression of $hERG_{WT}$ with $RNF207_{WT}$ exhibited normal hERG current density (**Fig. 4.6A-C**, black traces). Although $hERG_{T613M}$ and $hERG_{WT}$ co-expression produces very low current density with altered kinetics (**Fig. 4.1B-F**), the addition of $RNF207_{WT}$ rescued current density to near $hERG_{WT}$ levels (**Fig. 4.6A-C,** red traces), suggesting the enhanced degradation and subsequent decrease in dominant-negative effects from $hERG_{T613M}$ subunits. Additionally, the time- and voltage-dependent kinetics were restored to near $hERG_{WT}$ levels (**Fig 4.6D-G**) consistent with the notion that the functional channels consist of mostly $hERG_{WT}$ subunits, in the form of homotetramers instead of heterotetramers as in **Fig. 4.1E-H**. In contrast, $RNF207_{G603fs}$ failed to restore the current density, despite the co-expression with $RNF207_{WT}$ (**Fig. 4.6A-C,** blue traces). The rectification, due to the channel's fast inactivation, also decreased (**Fig. 4.6B**). The recovery from inactivation time constant (closed Δ, **Fig. 4.6E**) and slow component of deactivation (open Δ **Fig. 4.6G**) were significantly slower in the presence of $RNF207_{G603fs}$, while the activation time constant was significantly faster (**Fig. 4.6F**). Indeed, alterations in the time-dependent kinetics further support the formation of heterotetrameric channels consistent with findings shown in **Fig. 4.1E-H.**

Co-expression of $hERG_{T613M}$ and $RNF207_{G603fs}$ in hiPSC-CMs results in prolonged action potential durations and E-4031-sensitive currents.

Finally, to test the functional roles of RNF207 under physiological conditions closer to that seen in the patient, we took advantage of human induced pluripotent stem cell-derived cardiomyocytes (hiPSC-CMs, iCell) as a platform. We co-expressed WT and mutant hERG and RNF207 proteins to directly compare the effects of WT and mutant RNF207 on cardiac action

potential durations (APDs). APD at 50% and 90% repolarization (APD_{50} and APD_{90}), mean diastolic potential, and peak action potential (AP) amplitude were quantified (**Fig. 4.7A-F**).

Cells expressing $hERG_{WT}$:$hERG_{T613M}$:$RNF207_{WT}$:$RNF207_{G603fs}$ (denoted as the "mutant" group) showed significantly longer APDs (APD_{50} and APD_{90}) compared to cells expressing $hERG_{WT}$:$RNF207_{WT}$ (wild-type, "WT" group), or non-transfected cells ("non-TF") (**Fig. 4.7A-C**). More importantly, expression of $RNF207_{WT}$ resulted in the "rescue" of the delayed repolarization seen in the mutant group ($hERG_{WT}$:$hERG_{T613M}$:$RNF207_{WT}$ without the mutant RNF207, denoted as the "rescue" group) consistent with the findings from **Fig 4.6**, demonstrating that RNF207 plays critical roles in the quality control of hERG subunits.

Finally, we recorded the E-4031-sensitive currents from the same three groups of hiPSC-CMs as in **Fig. 4.8**. There was a significant decrease in E-4031-sensitive current in hiPSC-CMs expressing $hERG_{WT}$:$hERG_{T613M}$:$RNF207_{WT}$:$RNF207_{G603fs}$ compared to $hERG_{WT}$:$RNF207_{WT}$. Importantly, expression of $RNF207_{WT}$ resulted in the "rescue" of the E4031-sensitive hERG current ($hERG_{WT}$:$hERG_{T613M}$:$RNF207_{WT}$ without the mutant RNF207, denoted as the "rescue" group) consistent with the findings from AP recordings in **Fig. 4.7** as well as data from HEK 293 cells shown in **Fig. 4.6**.

DISCUSSION

While the majority of LQTS cases are attributed to defects in the ion channels responsible for shaping the action potential, previous studies have provided new evidence where mutations in ion channel interacting proteins act as potential culprits in the development of LQTS. Calmodulin's role in LQTS Type 14, 15, and 16 is one such example.[17] Here, we propose that

quality control mechanisms play a key role in either aggravating or appeasing existing ion channel mutations—particularly in cases of variable penetrance or heterozygous inheritance.

Protein quality control as a new paradigm for cardiac arrhythmias in LQTS

In our previously published patient,[28] we observed severe LQTS with early onset. WGS identified that the patient was heterozygous for the $hERG_{T613M}$ and $RNF207_{G603fs}$ variants. The absence of LQTS symptoms in the parents suggests that the combination of these two mutations may be responsible for aggravating the LQTS phenotype. Our current study suggests that quality control mechanisms, including the degradation by ubiquitin ligases like RNF207, are critically important in regulating the impacts of these ion channel mutations. Indeed, we demonstrate that $RNF207_{WT}$ rescued the detrimental effects of $hERG_{T613M}$ co-expression with $hERG_{WT}$, while the addition of $RNF207_{G603fs}$ failed to rescue I_{Kr} and aggravate the LQTS phenotype. Several cardiac ion channels are known to be regulated through ERAD, therefore, our results support the underlying hypothesis that quality control mechanisms are critical regulators of ion channel function, and consequently, disorders like LQTS and sudden cardiac death.

Identification of RNF207 as an E3 ubiquitin ligase

We demonstrate, using confocal and high-resolution microscopy, that RNF207 colocalizes with the hERG channel, near the z lines, in ventricular cardiomyocytes. While RNF207 mainly colocalizes with hERG (**Fig. 4.2A-C**), there is also fluorescence between the t-tubules, in the cytosol. This corroborates with the notion that RNF207, as an E3 ubiquitin ligase, may interact with several different proteins. It has previously been shown that RNF207 also interacts with voltage-dependent anion-selective channel protein 1 (VDAC1) in the outer mitochondrial membrane.[62]

RNF207 displays sequence similarities to tripartite motif-containing proteins (TRIM).[30, 31] In combination with its zinc finger structure, this suggests that it may have ubiquitin ligase activity. We confirmed $RNF207_{WT}$ functions as an E3 ubiquitin ligase for $hERG_{T613M}$, primarily through the ubiquitin proteasome system. Co-immunoprecipitation experiments confirm that RNF207 and hERG reside within the same multi-protein complex, while further analyses using C- and N-terminal fragments of hERG subunits identify the C-terminus of hERG channel as the interacting domain with RNF207. $RNF207_{WT}$ successfully rescues the hERG current density *via* ubiquitination when WT and mutant subunits are co-expressed, whereas $RNF207_{G603fs}$ fails to ubiquitinate and rescue I_{Kr}. In future studies, *de novo* molecular modeling may be used to generate a potential structure for RNF207 and changes to the structure that result from the RNF207 G603fs mutation. Specifically, changes to the domain responsible for ubiquitin ligase activity and docking to the hERG protein would be of particular interest.

Functional roles of T613 residues in the time-dependent kinetics of hERG channels

Previous literature has shown that $hERG_{T613M}$ fails to traffic and produce currents when expressed alone, but exhibits decreased current density when co-expressed with $hERG_{WT}$, consistent with our findings.[30] Additionally, $hERG_{T613M}$, when co-expressed with $hERG_{WT}$, alters the time- and voltage-dependent kinetics. Specifically, the activation and inactivation time constants are significantly faster while the deactivation and recovery from inactivation are significantly slower when $hERG_{T613M}$ and $hERG_{WT}$ are co-expressed. The changes in inactivation are in accordance with our molecular model of $hERG_{T613M}$, as the rectification from the hERG channel's inactivation process has been shown to be similar to C-type inactivation, which takes place near the outer region of the pore helix[63-65].

We measured activation using the envelope of tails protocol and fit to a single exponential function. While this was consistent at range of voltages shown (**Figs. 4.1&4.6**), it was clear that not all voltages fit with single exponential data analysis. Indeed, it has been suggested that the hERG channel has a two-step activation process, consisting of voltage-sensitive and voltage-insensitive steps [65, 66]. The activation gate for the hERG channel is located near the cytosolic region of the S6 helices, although activation kinetics have also been shown to be regulated by the S4-S5 linker and PKA binding domains[67-69]. The enhanced activation in the heterotetrameric channels are observed together with delayed deactivation, consistent with results seen in previous studies[29].

Findings from previous studies

Previous genome-wide association studies have identified single nucleotide polymorphisms within the gene encoding RNF207 and QT interval prolongation[23-27]. Our findings are consistent with a previous study showing that RNF207 and the *hERG*-encoded K^+ channel interact and co-localize[25]. The previous study suggests that RNF207 overexpression significantly increases hERG protein trafficking, membrane expression, and the current density. Our current study provides additional evidence for a novel role of RNF207 as channel interacting partner that serves critical roles in quality control of the proteins.

Future studies

All experiments in our study included the β subunit, MiRP1. However, we limited our analyses to the hERG 1a isoform. The hERG 1b isoform, which lacks the EAG domain, has been shown to significantly contribute to I_{Kr}[70, 71]. Indeed, the inclusion of hERG 1b in this study may show effects on changes to the time- and voltage-dependent kinetics, specifically deactivation. Therefore, both hERG 1a and hERG 1b isoforms will be used in future studies. Additionally, we

recognize that multiple safeguards are in place to maintain quality control for ion channels, such as $K_v11.1$. Indeed, it has been shown that both CHIP and NEDD4-2 also function as ubiquitin ligases for the hERG channel[25, 32, 33, 38-41]. These ubiquitin ligases may act in concert, and thus, further exploration of these interacting proteins will add to our current understanding of cardiac ion channel dynamics and potential clinical applications[34]. Since RNF207 is an E3 ubiquitin ligase, it likely interacts with multiple proteins in cardiac myocytes. The mutant $RNF207_{G603fs}$ protein may have additional functional effects on other ion channels, contributing to the long QT phenotype. Future studies are required to further test the roles of RNF207 in native cells with other intact ubiquitin ligase systems. Investigations taking advantage of patient-specific hiPSCs will also provide additional insights into the roles of quality control on cardiac ion channel function in human arrhythmias.

In summary, knowledge into the intricate and precise regulatory mechanisms of ion channels will provide an enormous opportunity to uncover new therapeutic targets that may serve to "fine tune" ion channel function, instead of "blocking" ion channels directly as in our current forms of anti-arrhythmic drugs, thus, serving as a paradigm shift in our new rationale for development of anti-arrhythmic therapy.

AUTHOR CONTRIBUTIONS

HAL, LR, PNT, SP, PS, AME, WX, VT, XDZ: executed experiments; collected, analyzed and interpreted data. JRP, MVP, EAA, VYY, ENY, and NC: provided reagents and access to equipment, and interpreted data. HAL and NC: conceived and designed experiments, collected, analyzed, interpreted data and wrote the manuscript.

ACKNOWLEDGMENTS

This study was supported in part by Predoctoral Fellowship from NIH/NHLBI Institutional Training Grant in Basic and Translational Cardiovascular Science NIH T32 HL086350, and NIH F31 HL136120 Predoctoral Awards (HAL), American Heart Association (AHA) Predoctoral Fellowship Award (LR), NIH F32 HL149288 (PNT), NIH R56 HL138392 (XDZ), NIH R01 HL085727, NIH R01 HL085844, NIH R01 HL137228 (NC), NIH R01 HL128537 (VYY), VA Merit Review Grant I01 BX000576 and I01 CX001490 (NC), NIH R01 DC016099, NIH P01 AG051443, NIH R01 DC015135 (ENY), AHA Postdoctoral Fellowship Award, California Institute for Regenerative Medicine (CIRM) Training Grant to UC Davis, Harold S. Geneen Charitable Trust Award Program for Coronary Heart Disease Research, AHA Career Development Award (PS). NC is the holder of the Roger Tatarian Endowed Professorship in Cardiovascular Medicine. Molecular graphics and analyses performed with UCSF Chimera, developed by the Resource for Biocomputing, Visualization, and Informatics at the University of California, San Francisco, with support from NIH P41 GM103311.

REFERENCES

1. Sanguinetti MC, Jiang C, Curran ME, Keating MT. A mechanistic link between an inherited and an acquired cardiac arrhythmia: HERG encodes the I_{Kr} potassium channel. Cell Apr 21 1995;81:299-307.

2. Jonsson MK, van der Heyden MA, van Veen TA. Deciphering hERG channels: molecular basis of the rapid component of the delayed rectifier potassium current. J Mol Cell Cardiol Sep 2012;53:369-374.

3. Trudeau MC, Warmke JW, Ganetzky B, Robertson GA. HERG, a human inward rectifier in the voltage-gated potassium channel family. Science (New York, NY) Jul 7 1995;269:92-95.

4. Sanguinetti MC, Tristani-Firouzi M. hERG potassium channels and cardiac arrhythmia. Nature Mar 23 2006;440:463-469.

5. Tseng GN. I_{Kr}: the hERG channel. J Mol Cell Cardiol May 2001;33:835-849.

6. Vandenberg JI, Perry MD, Perrin MJ, Mann SA, Ke Y, Hill AP. hERG K^+ Channels: Structure, Function, and Clinical Significance. Physiological Reviews 2012;92:1393-1478.

7. Ackerman MJ. The Long QT Syndrome: Ion Channel Diseases of the Heart. Mayo Clinic Proceedings 1998;73:250-269.

8. Kass RS, Moss AJ. Long QT syndrome: novel insights into the mechanisms of cardiac arrhythmias. Journal of Clinical Investigation 2003;112:810-815.

9. Roden DM, Lazzara R, Rosen M, Schwartz PJ, Towbin J, Vincent GM, LQTS* ftSFTFo. Multiple Mechanisms in the Long-QT Syndrome: Current Knowledge, Gaps, and Future Directions. Circulation October 15, 1996 1996;94:1996-2012.

10. Schwartz PJ, Ackerman MJ, George AL, Jr., Wilde AA. Impact of genetics on the clinical management of channelopathies. J Am Coll Cardiol Jul 16 2013;62:169-180.

11. Giudicessi JR, Ackerman MJ. Genotype- and phenotype-guided management of congenital long QT syndrome. Curr Probl Cardiol Oct 2013;38:417-455.

12. Schwartz PJ, Ackerman MJ. The long QT syndrome: a transatlantic clinical approach to diagnosis and therapy. Eur Heart J Oct 2013;34:3109-3116.

13. Fitzgerald PT, Ackerman MJ. Drug-induced torsades de pointes: the evolving role of pharmacogenetics. Heart Rhythm Nov 2005;2:S30-37.

14. Perry MD, Ng CA, Mann SA, Sadrieh A, Imtiaz M, Hill AP, Vandenberg JI. Getting to the heart of hERG K^+ channel gating. J Physiol Jun 15 2015;593:2575-2585.

15. Sanguinetti MC, Jiang C, Curran ME, Keating MT. A mechanistic link between an inherited and an acquird cardiac arrthytmia: HERG encodes the I_{Kr} potassium channel. Cell 4/21/ 1995;81:299-307.

16. Curran ME, Splawski I, Timothy KW, Vincent GM, Green ED, Keating MT. A molecular basis for cardiac arrhythmia: HERG mutations cause long QT syndrome. Cell Mar 10 1995;80:795-803.

17. Crotti L, Johnson CN, Graf E, et al. Calmodulin mutations associated with recurrent cardiac arrest in infants. Circulation Mar 5 2013;127:1009-1017.

18. Abriel H. Cardiac sodium channel Nav1.5 and interacting proteins: Physiology and pathophysiology. Journal of Molecular and Cellular Cardiology 1// 2010;48:2-11.

19. Medeiros-Domingo A, Kaku T, Tester DJ, Iturralde-Torres P, Itty A, Ye B, Valdivia C, Ueda K, Canizales-Quinteros S, Tusié-Luna MT, Makielski JC, Ackerman MJ. SCN4B-Encoded Sodium Channel β4 Subunit in Congenital Long-QT Syndrome. Circulation 2007;116:134-142.

20. Limpitikul WB, Dick IE, Joshi-Mukherjee R, Overgaard MT, George Jr AL, Yue DT. Calmodulin mutations associated with long QT syndrome prevent inactivation of cardiac L-type Ca^{2+} currents and promote proarrhythmic behavior in ventricular myocytes. J Molec Cell Cardio 9// 2014;74:115-124.

21. Nakano Y, Shimizu W. Genetics of long-QT syndrome. Journal of human genetics 2015.

22. Crotti L, Spazzolini C, Tester DJ, et al. Calmodulin mutations and life-threatening cardiac arrhythmias: insights from the International Calmodulinopathy Registry. Eur Heart J Sep 14 2019;40:2964-2975.

23. Andreasen L, Nielsen JB, Christophersen IE, Holst AG, Sajadieh A, Tveit A, Haunsø S, Svendsen JH, Schmitt N, Olesen MS. Genetic Modifier of the QTc Interval Associated With Early-Onset Atrial Fibrillation. Canadian J Cardio 10// 2013;29:1234-1240.

24. Han QY, Wang HX, Liu XH, Guo CX, Hua Q, Yu XH, Li N, Yang YZ, Du J, Xia YL, Li HH. Circulating E3 ligases are novel and sensitive biomarkers for diagnosis of acute myocardial infarction. Clin Sci (Lond) Jun 2015;128:751-760.

25. Roder K, Werdich AA, Li W, Liu M, Kim TY, Organ-Darling LE, Moshal KS, Hwang JM, Lu Y, Choi BR, MacRae CA, Koren G. RING finger protein RNF207, a novel regulator of cardiac excitation. J Biol Chem Dec 5 2014;289:33730-33740.

26. Newton-Cheh C, Eijgelsheim M, Rice KM, et al. Common variants at ten loci influence QT interval duration in the QTGEN Study. Nat Genet Apr 2009;41:399-406.

27. Pfeufer A, Sanna S, Arking DE, et al. Common variants at ten loci modulate the QT interval duration in the QTSCD Study. Nat Genet Apr 2009;41:407-414.

28. Priest JR, Ceresnak SR, Dewey FE, Malloy-Walton LE, Dunn K, Grove ME, Perez MV, Maeda K, Dubin AM, Ashley EA. Molecular diagnosis of long QT syndrome at 10 days of life by rapid whole genome sequencing. Heart Rhythm Oct 2014;11:1707-1713.

29. Huang FD, Chen J, Lin M, Keating MT, Sanguinetti MC. Long-QT syndrome-associated missense mutations in the pore helix of the HERG potassium channel. Circulation Aug 28 2001;104:1071-1075.

30. Gong Q, Keeney DR, Molinari M, Zhou Z. Degradation of trafficking-defective long QT syndrome type II mutant channels by the ubiquitin-proteasome pathway. J Biol Chem May 13 2005;280:19419-19425.

31. Marin I. Origin and diversification of TRIM ubiquitin ligases. PLoS One 2012;7:e50030.

32. Cui Z, Zhang S. Regulation of the human ether-a-go-go-related gene (hERG) channel by Rab4 protein through neural precursor cell-expressed developmentally down-regulated protein 4-2 (Nedd4-2). J Biol Chem Jul 26 2013;288:21876-21886.

33. Guo J, Wang T, Li X, Shallow H, Yang T, Li W, Xu J, Fridman MD, Yang X, Zhang S. Cell surface expression of human ether-a-go-go-related gene (hERG) channels is regulated by caveolin-3 protein via the ubiquitin ligase Nedd4-2. J Biol Chem Sep 28 2012;287:33132-33141.

34. Foo B, Williamson B, Young JC, Lukacs G, Shrier A. hERG quality control and the long qt syndrome. J Physiol Dec 31 2015.

35. Iwai C, Li P, Kurata Y, et al. Hsp90 prevents interaction between CHIP and HERG proteins to facilitate maturation of wild-type and mutant HERG proteins. Cardiovasc Res Dec 1 2013;100:520-528.

36. Murata S, Minami Y, Minami M, Chiba T, Tanaka K. CHIP is a chaperone-dependent E3 ligase that ubiquitylates unfolded protein. EMBO reports 2001-12-01 00:00:00 2001;2:1133-1138.

37. Willis MS, Patterson C. Into the heart: the emerging role of the ubiquitin-proteasome system. J Mol Cell Cardiol Oct 2006;41:567-579.

38. Ficker E, Dennis AT, Wang L, Brown AM. Role of the cytosolic chaperones Hsp70 and Hsp90 in maturation of the cardiac potassium channel HERG. Circ Res Jun 27 2003;92:e87-100.

39. Walker VE, Wong MJ, Atanasiu R, Hantouche C, Young JC, Shrier A. Hsp40 chaperones promote degradation of the HERG potassium channel. J Biol Chem Jan 29 2010;285:3319-3329.

40. Lamothe SM, Zhang S. The serum- and glucocorticoid-inducible kinases SGK1 and SGK3 regulate hERG channel expression via ubiquitin ligase Nedd4-2 and GTPase Rab11. J Biol Chem May 24 2013;288:15075-15084.

41. Kang Y, Guo J, Yang T, Li W, Zhang S. Regulation of the human ether-a-go-go-related gene (hERG) potassium channel by Nedd4 family interacting proteins (NDFIPS). Biochem J 2015;472:71-82.

42. Zhou Z, Gong Q, Epstein ML, January CT. HERG channel dysfunction in human long QT syndrome. Intracellular transport and functional defects. J Biol Chem Aug 14 1998;273:21061-21066.

43. Zhou Z, Gong Q, Ye B, Fan Z, Makielski JC, Robertson GA, January CT. Properties of HERG channels stably expressed in HEK 293 cells studied at physiological temperature. Biophys J Jan 1998;74:230-241.

44. Schwake M, Pusch M, Kharkovets T, Jentsch TJ. Surface expression and single channel properties of KCNQ2/KCNQ3, M-type K^+ channels involved in epilepsy. Journal of Biological Chemistry 2000;275:13343-13348.

45. Sihn CR, Kim HJ, Woltz RL, Yarov-Yarovoy V, Yang PC, Xu J, Clancy CE, Zhang XD, Chiamvimonvat N, Yamoah EN. Mechanisms of Calmodulin Regulation of Different Isoforms of $K_v7.4$ K^+ Channels. J Biol Chem Jan 29 2016;291:2499-2509.

46. Li N, Timofeyev V, Tuteja D, et al. Ablation of a Ca^{2+}-activated K^+ channel (SK2 channel) results in action potential prolongation in atrial myocytes and atrial fibrillation. J Physiol Mar 1 2009;587:1087-1100.

47. Rafizadeh S, Zhang Z, Woltz RL, et al. Functional interaction with filamin A and intracellular Ca^{2+} enhance the surface membrane expression of a small-conductance Ca^{2+}-activated K^+ (SK2) channel. Proceedings of the National Academy of Sciences of the United States of America Jul 8 2014;111:9989-9994.

48. Zhang Z, Ledford HA, Park S, et al. Distinct subcellular mechanisms for the enhancement of the surface membrane expression of SK2 channel by its interacting proteins, α-actinin2 and filamin A. J Physiol Apr 01 2017;595:2271-2284.

49. Syed AU, Reddy GR, Ghosh D, et al. Adenylyl cyclase 5-generated cAMP controls cerebral vascular reactivity during diabetic hyperglycemia. J Clin Invest Jun 4 2019;129:3140-3152.

50. Sharma D, Glatter KA, Timofeyev V, Tuteja D, Zhang Z, Rodriguez J, Tester DJ, Low R, Scheinman MM, Ackerman MJ, Chiamvimonvat N. Characterization of a KCNQ1/KVLQT1 polymorphism in Asian families with LQT2: implications for genetic testing. J Mol Cell Cardiol Jul 2004;37:79-89.

51. Yamoah MA, Moshref M, Sharma J, Chen WC, Ledford HA, Lee JH, Chavez KS, Wang W, Lopez JE, Lieu DK, Sirish P, Zhang XD. Highly efficient transfection of human induced pluripotent stem cells using magnetic nanoparticles. Int J Nanomedicine 2018;13:6073-6078.

52. Wang W, MacKinnon R. Cryo-EM Structure of the Open Human Ether-à-go-go-Related K+ Channel hERG. Cell 2017/04/20/ 2017;169:422-430.e410.

53. Rohl CA, Strauss CE, Misura KM, Baker D. Protein structure prediction using Rosetta. Methods Enzymol 2004;383:66-93.

54. Yarov-Yarovoy V, Schonbrun J, Baker D. Multipass membrane protein structure prediction using Rosetta. Proteins Mar 1 2006;62:1010-1025.

55. Yarov-Yarovoy V, DeCaen PG, Westenbroek RE, Pan CY, Scheuer T, Baker D, Catterall WA. Structural basis for gating charge movement in the voltage sensor of a sodium channel. Proceedings of the National Academy of Sciences of the United States of America Jan 10 2012;109:E93-102.

56. Wang RY, Song Y, Barad BA, Cheng Y, Fraser JS, DiMaio F. Automated structure refinement of macromolecular assemblies from cryo-EM maps using Rosetta. Elife Sep 26 2016;5.

57. Pettersen EF, Goddard TD, Huang CC, Couch GS, Greenblatt DM, Meng EC, Ferrin TE. UCSF Chimera--a visualization system for exploratory research and analysis. Journal of computational chemistry Oct 2004;25:1605-1612.

58. Abbott GW. The KCNE2 K^+ channel regulatory subunit: Ubiquitous influence, complex pathobiology. Gene Sep 15 2015;569:162-172.

59. Liu L, Tian J, Lu C, Chen X, Fu Y, Xu B, Zhu C, Sun Y, Zhang Y, Zhao Y, Li Y. Electrophysiological Characteristics of the LQT2 Syndrome Mutation KCNH2-G572S and Regulation by Accessory Protein KCNE2. Front Physiol 2016;7:650.

60. Pond AL, Scheve BK, Benedict AT, Petrecca K, Van Wagoner DR, Shrier A, Nerbonne JM. Expression of distinct ERG proteins in rat, mouse, and human heart. Relation to functional I(Kr) channels. J Biol Chem Feb 25 2000;275:5997-6006.

61. Roti ECR, Myers CD, Ayers RA, Boatman DE, Delfosse SA, Chan EKL, Ackerman MJ, January CT, Robertson GA. Interaction with GM130 during HERG Ion Channel

Trafficking: Disruption by type 2 congenital long QT syndrome mutations. J Biol Chem December 6, 2002 2002;277:47779-47785.

62. Mizushima W, Takahashi H, Watanabe M, et al. The novel heart-specific RING finger protein 207 is involved in energy metabolism in cardiomyocytes. J Mol Cell Cardiol Nov 2016;100:43-53.

63. Spector PS, Curran ME, Zou A, Keating MT, Sanguinetti MC. Fast inactivation causes rectification of the IKr channel. J Gen Physiol May 1996;107:611-619.

64. Smith PL, Baukrowitz T, Yellen G. The inward rectification mechanism of the HERG cardiac potassium channel. Nature Feb 29 1996;379:833-836.

65. Wang S, Liu S, Morales MJ, Strauss HC, Rasmusson RL. A quantitative analysis of the activation and inactivation kinetics of HERG expressed in Xenopus oocytes. The Journal of Physiology 1997;502:45-60.

66. Zhou Q, Bett GC. Regulation of the voltage-insensitive step of HERG activation by extracellular pH. American Journal of Physiology-Heart and Circulatory Physiology 2010;298:H1710-H1718.

67. Ng CA, Perry MD, Tan PS, Hill AP, Kuchel PW, Vandenberg JI. The S4-S5 linker acts as a signal integrator for HERG K+ channel activation and deactivation gating. PLoS One 2012;7:e31640.

68. Perrin MJ, Subbiah RN, Vandenberg JI, Hill AP. Human ether-a-go-go related gene (hERG) K+ channels: function and dysfunction. Progress in biophysics and molecular biology 2008;98:137-148.

69. Thomas D, Zhang W, Karle CA, Kathöfer S, Schöls W, Kübler W, Kiehn J. Deletion of Protein Kinase A Phosphorylation Sites in the HERG Potassium Channel Inhibits Activation Shift by Protein Kinase A. Journal of Biological Chemistry September 24, 1999 1999;274:27457-27462.

70. Jones DK, Liu F, Vaidyanathan R, Eckhardt LL, Trudeau MC, Robertson GA. hERG 1b is critical for human cardiac repolarization. Proceedings of the National Academy of Sciences of the United States of America Dec 16 2014;111:18073-18077.

71. Jones EM, Roti Roti EC, Wang J, Delfosse SA, Robertson GA. Cardiac IKr channels minimally comprise hERG 1a and 1b subunits. J Biol Chem Oct 22 2004;279:44690-44694.

Figure 4.1

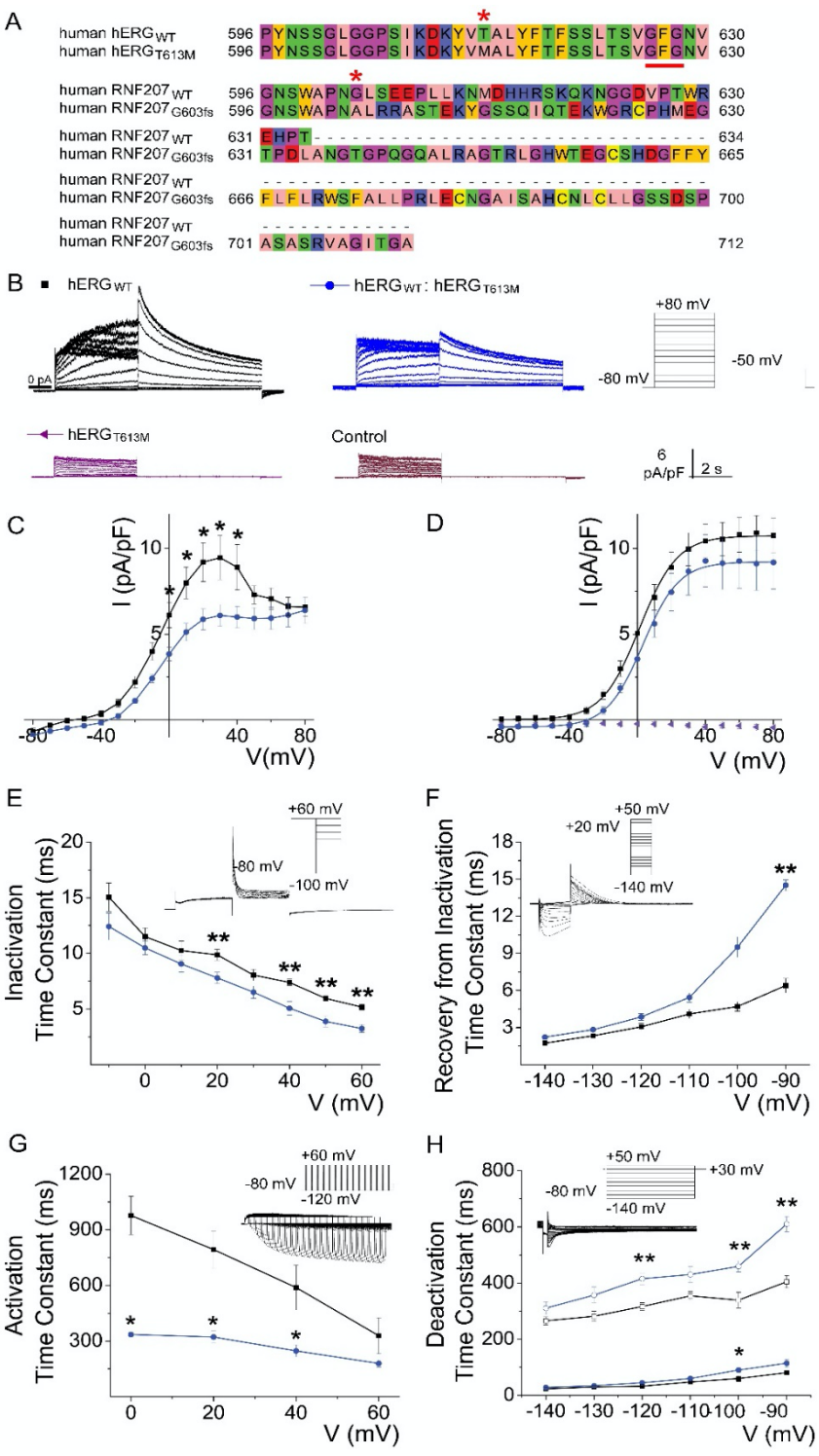
A
human hERG WT 596 PYNSSGLGGPSIKDKYVTALYFTFSSLTSVGFGNV 630
human hERG T613M 596 PYNSSGLGGPSIKDKYVMALYFTFSSLTSVGFGNV 630
human RNF207 WT 596 GNSWAPNGLSEEPLLKNMDHHRSKQKNGGDVPTWR 630
human RNF207 G603fs 596 GNSWAPNALRRASTEKYGSSQIQTEKWGRCPHMEG 630
human RNF207 WT 631 EHPT 634
human RNF207 G603fs 631 TPDLANGTGPQGQALRAGTRLGHWTEGCSHDGFFY 665
human RNF207 WT
human RNF207 G603fs 666 FLFLRWSFALLPRLECNGAISAHCNLCLLGSSDSP 700
human RNF207 WT
human RNF207 G603fs 701 ASASRVAGITGA 712
B
hERG WT
hERG WT : hERG T613M
+80 mV
-80 mV
-50 mV
0 pA
hERG T613M
Control
6 pA/pF
2 s
C
I (pA/pF)
V(mV)
D
I (pA/pF)
V (mV)
E
Inactivation Time Constant (ms)
+60 mV
-80 mV
-100 mV
V (mV)
F
Recovery from Inactivation Time Constant (ms)
+50 mV
+20 mV
-140 mV
V (mV)
G
Activation Time Constant (ms)
+60 mV
-80 mV
-120 mV
V (mV)
H
Deactivation Time Constant (ms)
+50 mV
+30 mV
-80 mV
-140 mV
V (mV)

Figure 4.1. Dominant-negative effect and altered channel gating kinetics by $hERG_{T613M}$. A. Upper panel shows amino acid sequence alignments for $hERG_{WT}$ and $hERG_{T613M}$ (residues 596-630). The conserved selectivity filter of the hERG subunit, GFG, is underlined. Lower panels show amino acid sequence alignments for $RNF207_{WT}$ and $RNF207_{G603fs}$ starting from residue 596 to the end of the polypeptide. * is shown for mutated residues (613 in hERG sequence, 603 in RNF207 sequence). **B.** Representative whole-cell voltage-clamp recordings from HEK 293 cells expressing $hERG_{WT}$ alone (black traces), $hERG_{WT}$:$hERG_{T613M}$ (blue traces), $hERG_{T613M}$ alone (purple traces), or non-transfected cells (red traces). **C.** Summary data for current densities for $hERG_{WT}$ alone (black traces) compared to $hERG_{WT}$:$hERG_{T613M}$ (blue traces) (n= 20-30 cells, $*P<0.05$). **D.** Summary data for voltage-dependent activation using the peak tail current density fitted using Boltzmann function with $V_{1/2}$ = -3.28 ± 1.53 for $hERG_{WT}$; 1.55 ± 2.36 for $hERG_{WT}$: $hERG_{T613M}$ and slope constants = 8.67 ± 0.22 for $hERG_{WT}$; 8.50 ± 0.48 for $hERG_{WT}$: $hERG_{T613M}$. **E & F.** Time constants of inactivation and recovery from inactivation from $hERG_{WT}$ alone (black traces) compared to $hERG_{WT}$:$hERG_{T613M}$ (blue traces). **G & H.** Time constants of activation and deactivation from $hERG_{WT}$ alone (black traces) compared to $hERG_{WT}$:$hERG_{T613M}$ (blue traces). The insets show voltage-clamp protocols and representative current traces (n= 6-11, inactivation; n= 9-11, recovery from inactivation; n = 3, activation; n= 5-10, deactivation). $*P<0.05$, $**P<0.01$. Data shown are mean ± S.E.M. Analyses were performed using Student's t-test.

Figure 4.2

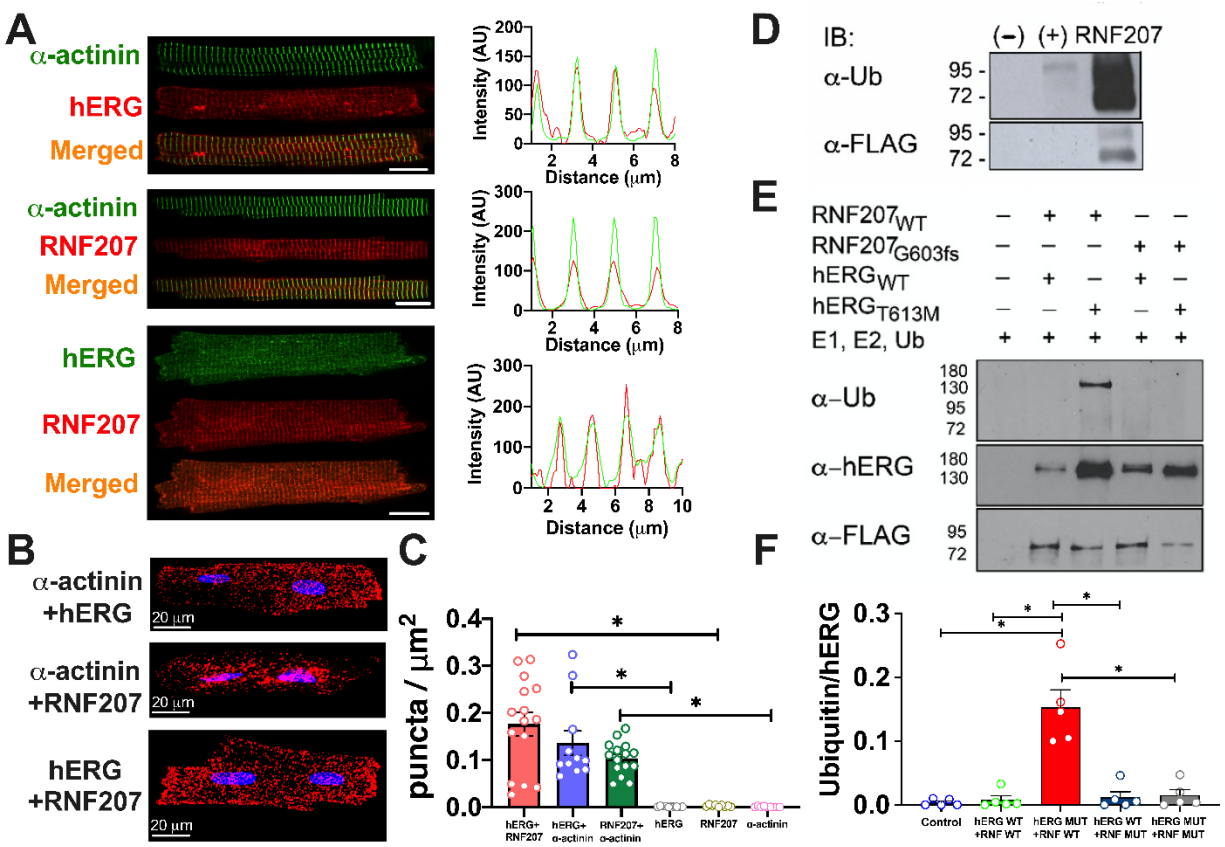

Figure 4.2. Colocalization of hERG and RNF207 in guinea pig ventricular cardiomyocytes.

A. Confocal images showing colocalization of α-actinin2 (Alexa Fluor 488)and hERG K^+ channel subunits (Alexa Fluor 555), α-actinin2 (Alexa Fluor 488) and RNF207 (Alexa Fluor 555), and hERG K^+ channel subunits (Alexa Fluor 488) and RNF207 (Alexa Fluor 555). The merged images are shown in the corresponding lower panels. Right panels show the corresponding fluorescence intensity profiles perpendicular to the Z lines, demonstrating the colocalization of hERG K^+ channel subunits with α-actinin2, RNF207 with α-actinin2, and hERG K^+ channel subunits with

RNF207, respectively. Scale bar represents 10 μm. **B**. Proximity ligation assay (PLA) for α-actinin2 and hERG K^+ channel subunits, α-actinin2 and RNF207, and hERG K^+ channel subunits and RNF207. **C.** Quantification of PLA puncta/μm^2 cell area (*p<0.05, n = 15, 11, 15, 10, 9, and 9 cells from left to right bars). **D.** Auto-ubiquitinylation assay for $RNF207_{WT}$ (lane 3, right) *vs.* negative control (lane 1, left) and MDM2, a known E3 ubiquitin ligase (positive control, lane 2). Transfected HEK 293 cells were immunoprecipitated (IP) for RNF207-FLAG. An auto-ubiquitinylation assay (Enzo Life Sciences) was conducted on isolated protein, followed by SDS-PAGE and western Blot analysis (IB). Proteins were incubated in the presence of E1 and E2 ubiquitin enzymes, ubiquitin, and ATP. **E.** Ubiquitination assay for RNF207 and hERG wild-type and mutant subunits. Ubiquitinated proteins were absent in the negative control (without RNF207 or hERG, lane 1). The E3-ubiquitin band appeared for $hERG_{T613M}$ incubation with $RNF207_{WT}$ (lane 3), but not in the presence of $RNF207_{G603fs}$ (lane 5) or with $hERG_{WT}$ subunits (either with $RNF207_{WT}$ (lane 2) or with $RNF207_{G603fs}$ (lane 4). Anti-ubiquitin and anti-hERG antibodies were performed on separate membranes. **F,** Quantification of the data from **E** (*P<0.05, n = 5 independent experiments for each group). Data shown are mean ± S.E.M. Analyses were performed using one-way analysis of variance (ANOVA) for multiple comparisons with Brown-Forsythe post hoc analyses.

Figure 4.3

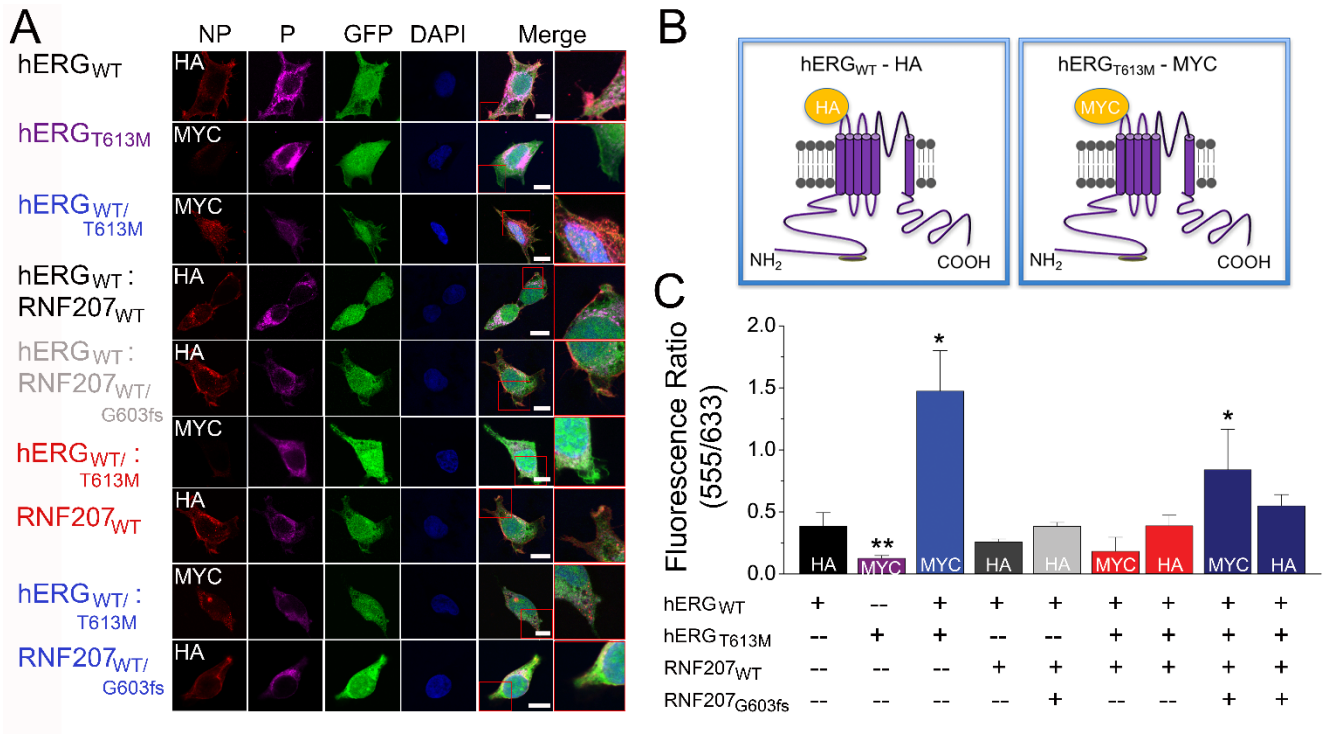

Figure 4.3. Surface membrane and cytosol expression of hERG K^+ channel subunits after co-expression with $RNF207_{WT}$ vs. $RNF207_{G603fs}$. **A.** Immunofluorescence confocal microscopic imaging of HEK 293 cells transfected with different combinations of $hERG_{WT}$, $hERG_{T613M}$, $RNF207_{WT}$, and $RNF207_{G603fs}$. Cells were immunostained using anti-HA (or anti-Myc) antibody followed by chicken anti-mouse Alexa Fluor 555 secondary antibody with no permeabilization (NP). Cells were then permeabilized (P) and immunostained using anti-HA (or anti-Myc) antibody followed by rabbit anti-mouse Alexa Fluor 633 secondary antibody. Scale bar = 10 μm. The last panel in each row represents a higher magnification image from the merged image as outlined in a red box. **B.** schematic diagrams of $hERG_{WT}$-HA and $hERG_{T613M}$-Myc fusion constructs used for the experiments. **C.** Summary data of the fluorescence ratios (555 nm/633 nm) from the different

groups of cells (*P<0.05, **P<0.01, n = 6-10 cells). Data shown are mean ± S.E.M. Analyses were performed using one-way analysis of variance (ANOVA) for multiple comparisons with Tukey's post hoc analyses.

Figure 4.4

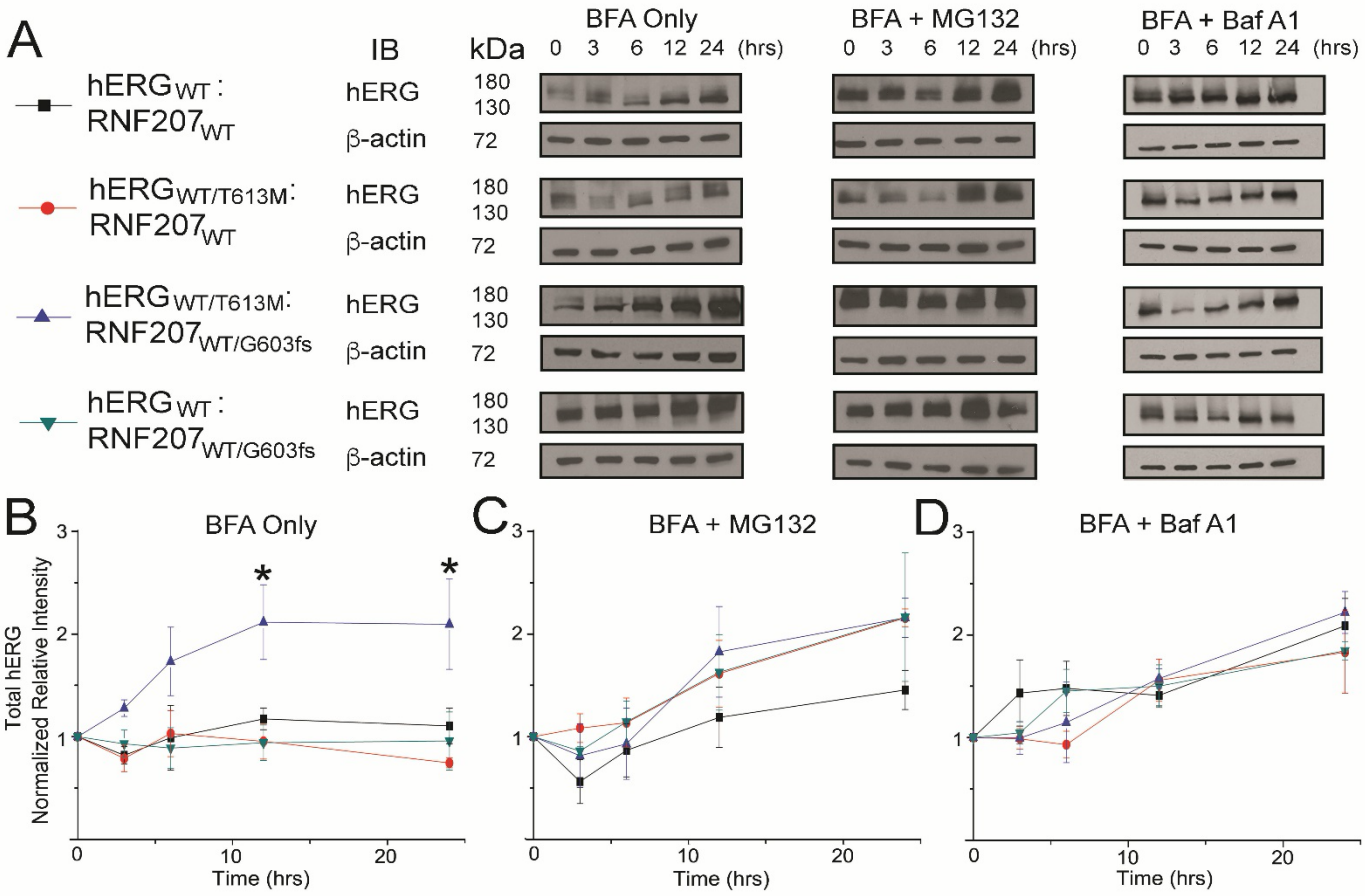

Figure 4.4. Distinct effects of RNF$_{WT}$ *vs.* RNF$_{G603fs}$ on the degradation of hERG K$^+$ channel subunits. A. Degradation assay for HEK 293 cells collected before brefeldin a (BFA) treatment (time=0) *vs.* 3, 6, 12, and 24 hours following treatment. Groups included 1) hERG$_{WT}$:RNF207$_{WT}$, 2) hERG$_{WT}$:hERG$_{T613M}$:RNF207$_{WT}$, 3) hERG$_{WT}$:hERG$_{T613M}$:RNF207$_{WT}$:RNF207$_{G603fs}$, and 4) hERG$_{WT}$:RNF207$_{WT}$:RNF207$_{G603fs}$. Cells were treated with brefeldin A (left panel), brefeldin A + MG 132 (middle panel), or brefeldin A + bafilomycin A1 (right panel). **B.** Quantification of BFA treated groups ($p < 0.05$). Total protein content was also quantified for groups treated with proteasome inhibitor, MG132 (**C**) and lysosome inhibitor, bafilomycin A1 (**D**). Data shown are

mean ± S.E.M. *P<0.05, n = 5 different independent experiments. Analyses were performed using one-way analysis of variance (ANOVA) for multiple comparisons with Tukey's post hoc analyses.

Figure 4.5

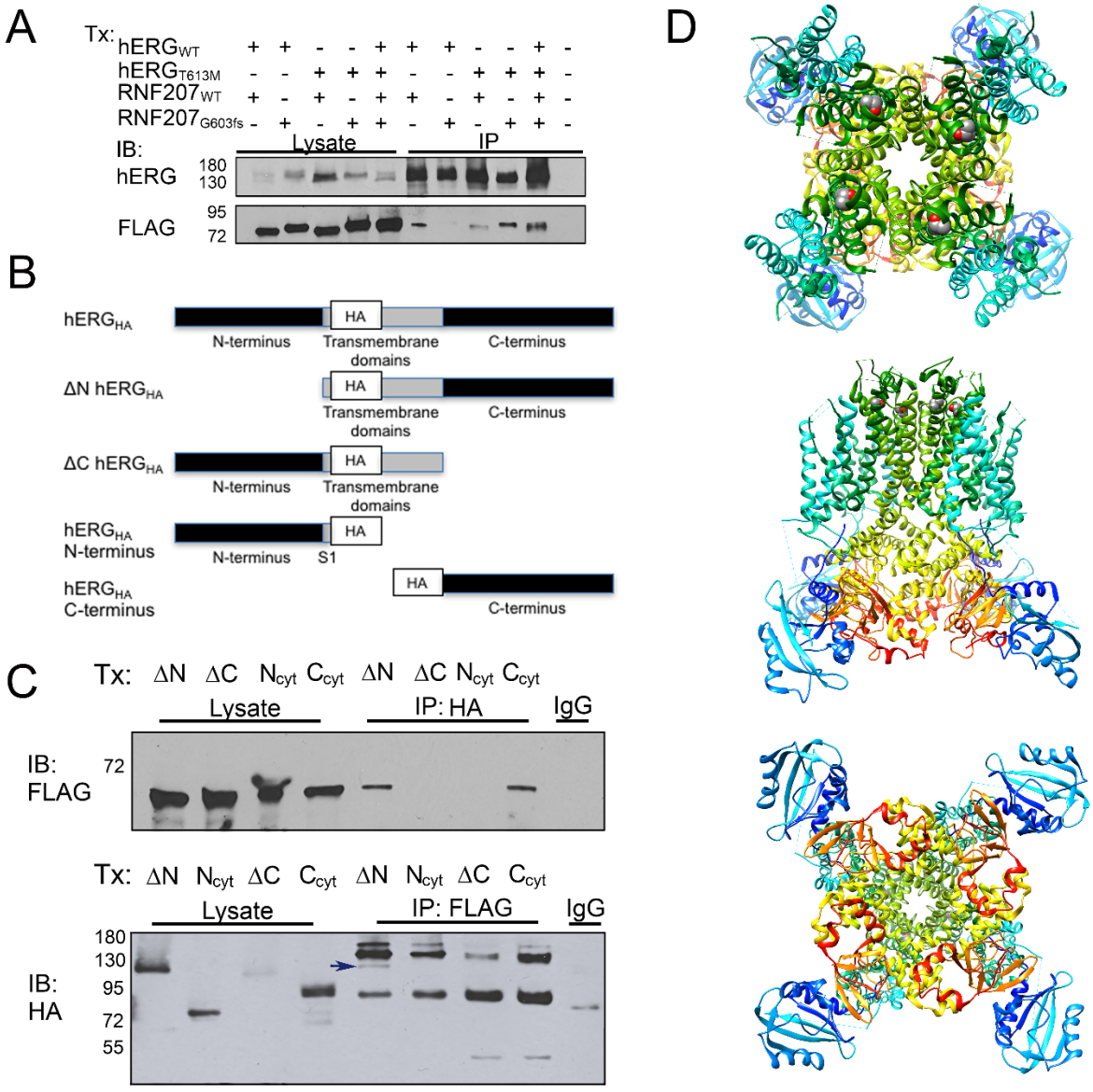

Figure 4.5. Multi-protein complexes formed by hERG K^+ channel subunits and RNF207. A. Co-immunoprecipitation of hERG and RNF207. Transfected (T_x) HEK 293 cells were immunoprecipitated (IP) using anti-hERG antibody and western blot analysis (IB) was performed

using anti-hERG and anti-FLAG antibodies to target the RNF207-FLAG fusion protein. Western blot analyses from lysates and IP are shown in lanes 1-5 and lanes 6-10, respectively. Negative control using IgG for IP is shown in lane 11. **B.** Schematic of $hERG_{WT}$-ΔN, $hERG_{WT}$-ΔC, hERG N-terminus, and hERG C-terminus constructs (tagged with HA). **C.** Co-immunoprecipitation of hERG-HA fragments that were co-transfected (Tx) in HEK 293 cells with $RNF207_{WT}$-FLAG. Immunoprecipitation followed by immunoblotting were performed using anti-HA (IP:HA, upper panel) and anti-FLAG antibodies (IP:FLAG, uper panel), respectively. The reverse experiments were performed as shown in the lower panel. Lanes 1-4 are lyste samples (20 μg each) and lanes 5-8 show immunoprecipitated samples transfected with $hERG_{WT}$-ΔN, $hERG_{WT}$-ΔC, hERG N-terminus, hERG C-terminus, and IgG negative control. Some nonspecific bands are seen in lanes 5-8 in the lower panel. The blue arrow in Lane 5 in the lower panel shows a band of expected size for $hERG_{WT}$-ΔN. **D**. *Rosetta* model of hERG, from top to bottom: 1) view from the extracellular side of the membrane, 2) view from the transmembrane side, and 3) view from the intracellular side of the membrane. Backbone is shown in ribbon representation and colored by rainbow color scheme from the N-terminus region (blue) to C-terminus region (red). Sidechain of T613 residue in each subunit is shown using a space filling representation.

Figure 4.6

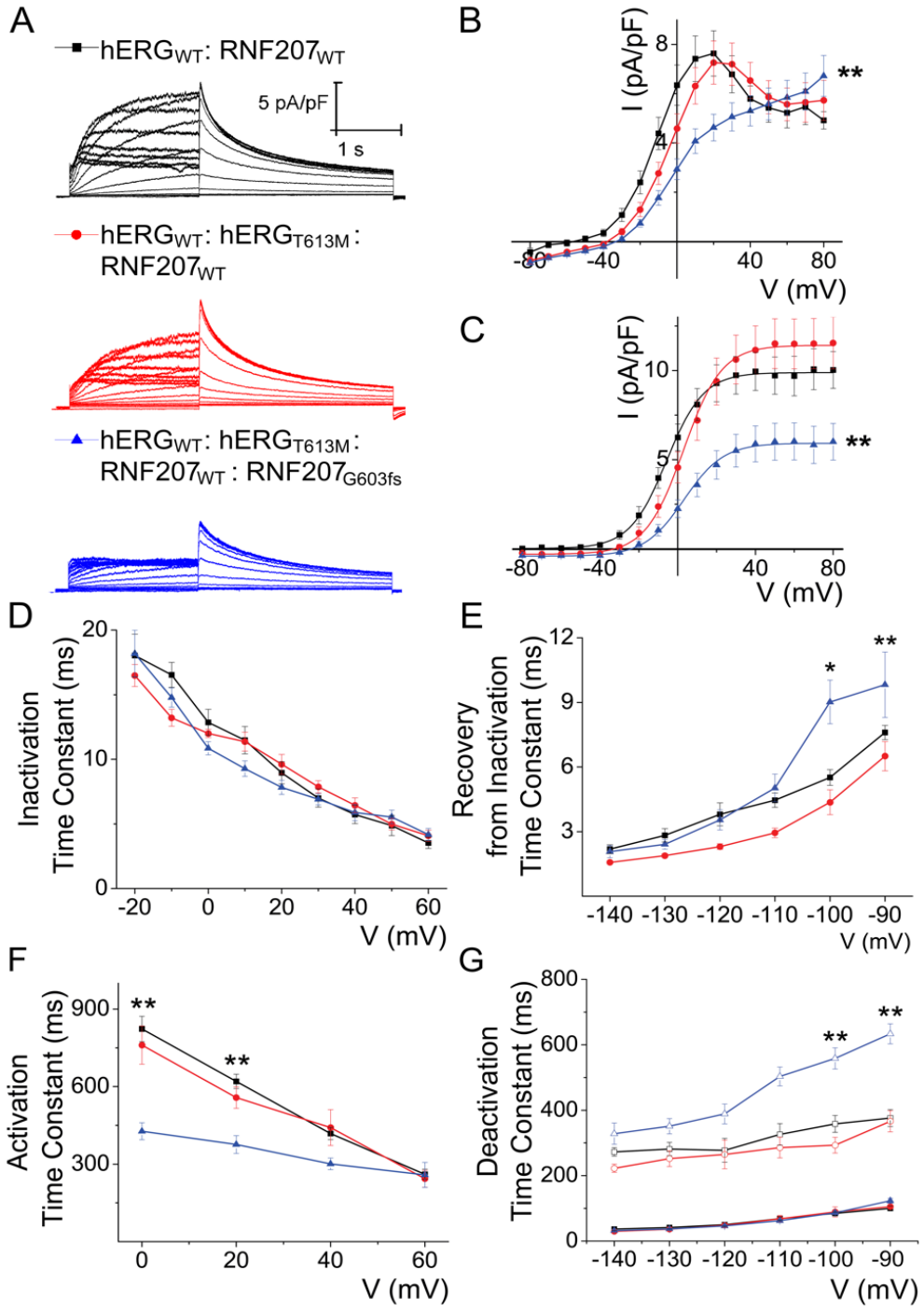
A
hERGWT: RNF207WT
5 pA/pF
1 s
hERGWT: hERGT613M: RNF207WT
hERGWT: hERGT613M: RNF207WT : RNF207G603fs
B
I (pA/pF)
V (mV)
**
C
I (pA/pF)
V (mV)
**
D
Inactivation Time Constant (ms)
V (mV)
E
Recovery from Inactivation Time Constant (ms)
V (mV)
*
**
F
Activation Time Constant (ms)
V (mV)
**
**
G
Deactivation Time Constant (ms)
V (mV)
**
**

Figure 4.6. Differential effects of RNF_{WT} vs RNF_{G603fs} on hERG current. A. Representative whole-cell voltage-clamp recordings from HEK 293 cells expressing $hERG_{WT}$:$RNF207_{WT}$ (black traces), $hERG_{WT}$:$hERG_{T613M}$:$RNF207_{WT}$ (red traces), or $hERG_{WT}$:$hERG_{T613M}$:$RNF207_{WT}$:$RNF207_{G603fs}$ (blue traces). **B.** Summary data for current density for $hERG_{WT}$:$RNF207_{WT}$ (black traces) compared to $hERG_{WT}$:$hERG_{T613M}$:$RNF207_{WT}$ (red traces) and $hERG_{WT}$:$hERG_{T613M}$:$RNF207_{WT}$:$RNF207_{G603fs}$ (blue traces) (n= 14-19). **C.** Summary data for voltage-dependent activation using the peak tail current density fitted using Boltzmann function with $V_{1/2}$ = -6.13 ± 2.99 for $hERG_{WT}$:$RNF207_{WT}$; 3.01 ± 2.10 for $hERG_{WT}$:$hERG_{T613M}$:$RNF207_{WT}$; and 3.78 ± 2.10 for $hERG_{WT}$:$hERG_{T613M}$:$RNF207_{WT}$:$RNF207_{G603fs}$ and slope constants = 8.99 ± 0.47 for $hERG_{WT}$:$RNF207_{WT}$; 9.55 ± 0.49 for $hERG_{WT}$:$hERG_{T613M}$:$RNF207_{WT}$; and 9.80 ± 0.37 for $hERG_{WT}$:$hERG_{T613M}$:$RNF207_{WT}$:$RNF207_{G603fs}$. **D&E.** Time constants of inactivation and recovery from inactivation for $hERG_{WT}$:$RNF207_{WT}$ (black traces) compared to $hERG_{WT}$:$hERG_{T613M}$:$RNF207_{WT}$ (red traces) and $hERG_{WT}$:$hERG_{T613M}$:$RNF207_{WT}$:$RNF207_{G603fs}$ (blue traces). **F&G** Time constants for activation and deactivation, where closed Δ, □, and O represent the fast component and open Δ, □, and O represent the slow component of deactivation. n= 5-10 for inactivation; n= 6-12 for recovery from inactivation; n = 3-5 for activation; n= 5-10 for deactivation. **P*<0.05, ***P*<0.01. In panels **B** and **C**, ***P*<0.01 for $hERG_{WT}$:$hERG_{T613M}$:$RNF207_{WT}$:$RNF207_{G603fs}$ compared to $hERG_{WT}$:$RNF207_{WT}$ and $hERG_{WT}$:$hERG_{T613M}$:$RNF207_{WT}$ throughout positive voltages and was shown only at the end of the curves for clarity. Data shown are mean ± S.E.M. Analyses were performed using one-way analysis of variance (ANOVA) for multiple comparisons with Tukey's post hoc analyses.

Figure 4.7

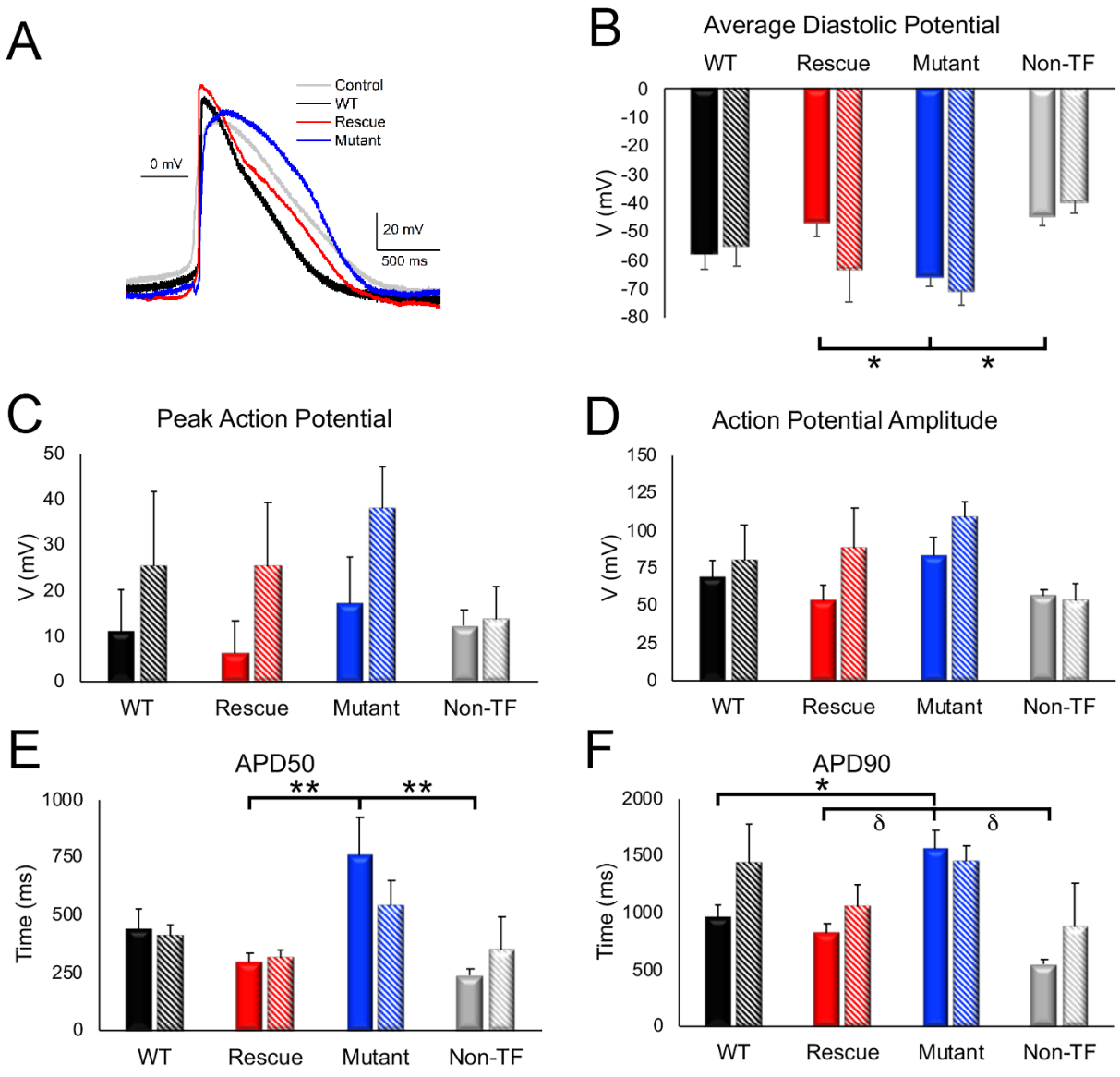

Figure 4.7. Regulation of APDs of hiPSC-CMs by RNF207. A. Representative action potential recordings (hiCell, Cellular Dynamics) in cells expressing $hERG_{WT}$:$RNF207_{WT}$ (black trace), $hERG_{WT}$:$hERG_{T613M}$:$RNF207_{WT}$ (red trace), and $hERG_{WT}$:$hERG_{T613M}$:$RNF207_{WT}$:$RNF207_{G603fs}$ (blue trace) as well as a non transfected cell (grey trace). **B-F.** Summary data for action potential recordings in non-transfected cells (labeled "Non-TF", grey bar) compared to $hERG_{WT}$:$RNF207_{WT}$

(labeled “WT”, black bar), $hERG_{WT}$:$hERG_{T613M}$:$RNF207_{WT}$ (labeled “Rescue”, red bar) and $hERG_{WT}$:$hERG_{T613M}$:$RNF207_{WT}$:$RNF207_{G603fs}$ (labeled “Mutant”, blue bar) at baseline (solid bars) versus 1 μM E-4031(striped bars). Data is shown for average diastolic potential (**B**), peak action potential (**C**), action potential amplitude (**D**), action potential duration at 50% repolarization or APD50 (**E**), and action potential duration at 90% repolarization or APD_{90} (**F**). Data shown represents the average of 5 action potentials per cell, with n= 6-9 cells for baseline recordings and n= 3-5 cells for E-4031 recordings; **P*<0.05, ***P*<0.01, $^{\delta}P$< 0.001. Data shown are mean ± S.E.M. **P*<0.05. Analyses were performed using one-way analysis of variance (ANOVA) for multiple comparisons with Tukey’s post hoc analyses.

Figure 4.8

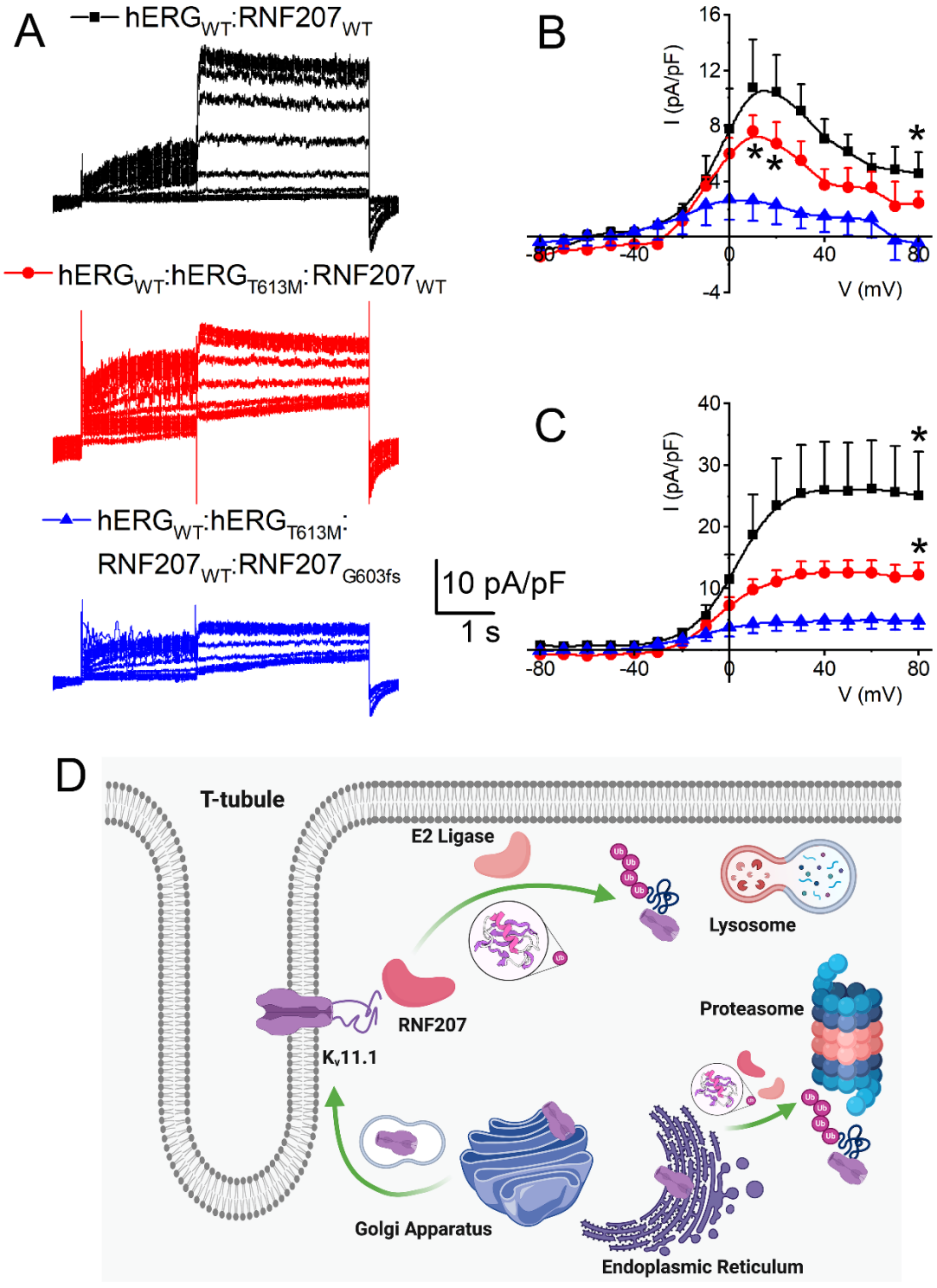
A
hERG$_{WT}$:RNF207$_{WT}$
hERG$_{WT}$:hERG$_{T613M}$:RNF207$_{WT}$
hERG$_{WT}$:hERG$_{T613M}$:
RNF207$_{WT}$:RNF207$_{G603fs}$
10 pA/pF
1 s
B
I (pA/pF)
V (mV)
C
I (pA/pF)
V (mV)
D
T-tubule
E2 Ligase
Lysosome
RNF207
Proteasome
K$_v$11.1
Golgi Apparatus
Endoplasmic Reticulum

Figure 4.8. Regulation of hERG currents by RNF207 in hiPSC-CMs. A. Representative whole-cell currents recorded from hiPSC-CMs expressing $hERG_{WT}$:$RNF207_{WT}$ (black traces), $hERG_{WT}$:$hERG_{T613M}$:$RNF207_{WT}$ (red traces), and $hERG_{WT}$:$hERG_{T613M}$:$RNF207_{WT}$: $RNF207_{G603fs}$ (blue traces). **B.** Summary data for current density for the three groups of cells (n= 5-6). **C.** Summary data for voltage-dependent activation using the peak tail current density fitted using Boltzmann function with $V_{1/2}$ = 2.73 ± 2.55 for $hERG_{WT}$:$RNF207_{WT}$; -3.06 ± 2.47 for $hERG_{WT}$:$hERG_{T613M}$:$RNF207_{WT}$; and -15.85 ± 4.19 for $hERG_{WT}$:$hERG_{T613M}$:$RNF207_{WT}$: $RNF207_{G603fs}$ and slope constants = 8.30 ± 0.72 for $hERG_{WT}$:$RNF207_{WT}$; 9.13 ± 0.39 for $hERG_{WT}$:$hERG_{T613M}$:$RNF207_{WT}$; and 9.97 ± 1.33 for $hERG_{WT}$:$hERG_{T613M}$:$RNF207_{WT}$: $RNF207_{G603fs}$ (n=5-6). In panel **B**, $*P<0.05$ for $hERG_{WT}$:$RNF207_{WT}$ compared to $hERG_{WT}$:$hERG_{T613M}$: $RNF207_{WT}$:$RNF207_{G603fs}$ throughout positive voltages and was shown only at the end of the curve for clarity. In panel **C**, $*P<0.05$ for $hERG_{WT}$:$RNF207_{WT}$ and $hERG_{WT}$:$hERG_{T613M}$:$RNF207_{WT}$ compared to $hERG_{WT}$:$hERG_{T613M}$:$RNF207_{WT}$:$RNF207_{G603fs}$ throughout positive voltages and was shown only at the end of the curves for clarity. Analyses were performed using one-way analysis of variance (ANOVA) for multiple comparisons with Tukey's post hoc analyses. **D.** Schematic diagram of RNF207 interaction with hERG-encoded K^+ channels ($K_v11.1$) with trafficking and degradation pathways (generated using BioRender).

SUPPLEMENTAL FIGURES

Supplemental Figure 4.1

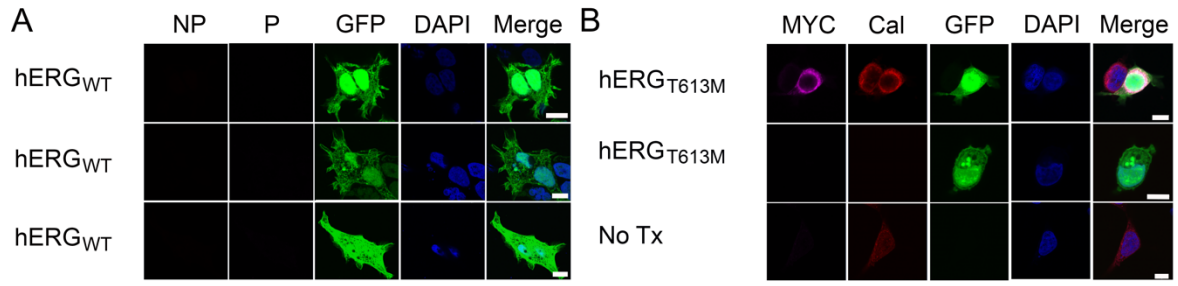

Supplemental Figure 4.1. Control experiments for immunofluorescence microscopy. A. Secondary only controls for immunofluorescence confocal microscopic imaging of HEK 293 cells transfected with hERG$_{WT}$. Controls shown are (from top to bottom) Alexa Fluor 555 only, Alexa Fluor 633 only, and Alexa Fluor 555 with Alexa Fluor 633. Cells were immunostained using a NP to P protocol identical to that used for Figure 3, except anti-HA and anti-Myc primary antibodies were not used. Scale bar = 10 μm. **B.** Immunofluorescence confocal imaging of hERG$_{T613M}$-Myc with calreticulin, an endoplasmic reticulum (ER) resident protein. Middle panel shows secondary only control and lower panel represents immunofluorescence staining with anti-MYC and anti-calreticulin in non-transfected HEK293.

Supplemental Figure 4.2

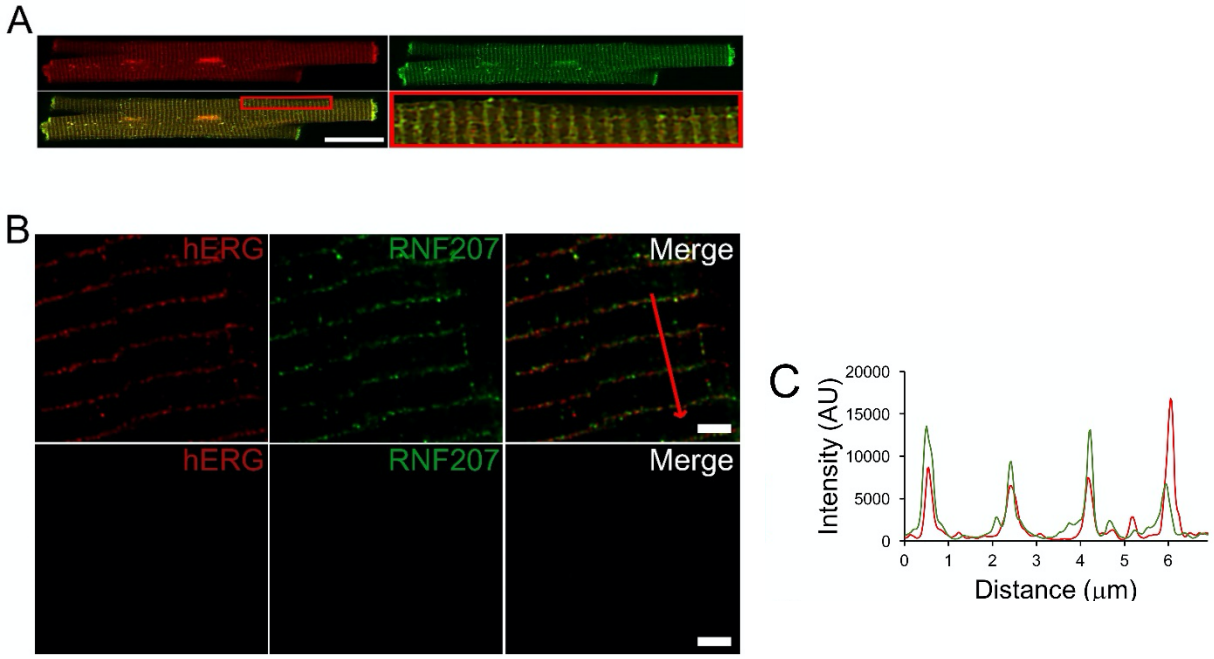

Supplementary Figure 4.2. Colocalization of hERG and RNF207 in rabbit ventricular cardiomyocytes. A. Confocal images showing the expression of hERG (Alexa Fluor 555 F(ab)2), RNF207 (Alexa Fluor 488 Fab); the merged image and enlarged section in the red frame were also shown. Scale bar represents 10 μm. **B**. STED images where the upper panel depicts the same cell shown in panel A, with hERG (AF 555), RNF207 (AF 488), and the merged image. Lower panel shows secondary only negative control. Scale bar represents 2 μm. **C.** Plot profile of hERG (red) and RNF207 (green) localization from STED images in panel B (red line).

Supplemental Figure 4.3

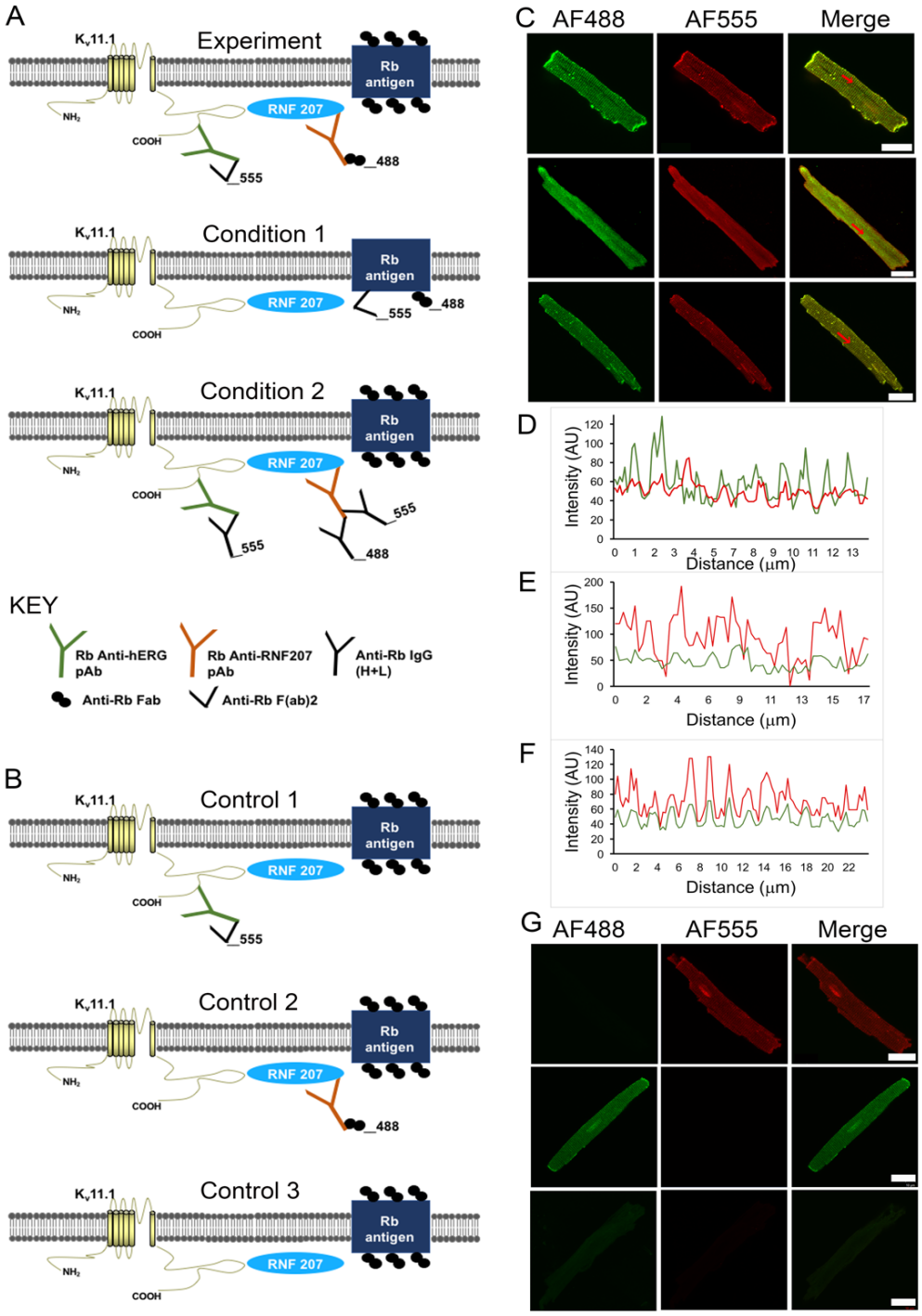

Supplemental Figure 4.3: Fab antibodies reduce antibody cross-talk and nonspecific binding to endogenous antigens. Adult rabbit ventricular cardiomyocytes were used for immunofluorescence colocalization experiments in **Supplementary Figure 2**. Since both primary antibodies were raised in rabbit, multiple controls were necessary to verify colocalization of the hERG and RNF207 proteins. **A)** Schematic diagrams of antibody binding depict (from top to bottom): 1) Experimental condition used in Figure 2 using Fab block, Fab-AF488 secondary antibody, and F(ab)2-555 secondary antibody, 2) Condition 1 without Fab blocking of endogenous rabbit antigens, and 3) Condition 2 with Fab block, AF488 IgG (H+L), and AF555 IgG (H+L) secondary antibodies. **B)** Schematic diagrams of antibody binding for experimental controls. From top to bottom: 1) Control 1 with Fab block and 1:40 rabbit anti-hERG primary antibody and 1:100 F(ab)2-AF555 anti-rabbit secondary antibody, 2) Control 2 with Fab block and 1:40 rabbit anti-RNF207 primary antibody and 1:40 Fab-AF488 anti-rabbit secondary antibody, and 3) Control 3 with Fab block and secondary antibodies only (anti-rabbit AF488-Fab and AF555-F(ab)2). **C)** Immunofluorescence confocal images corresponding to (from top to bottom): 1) Experimental condition, 2) Condition 1, and 3) Condition 2 from panel A. Images from condition 1 (middle panels) were taken with 10% higher gain to emphasize alternate staining pattern. **D)** Line profile from image taken under experimental conditions shows colocalization. Colocalization factor was 0.902. **E)** Line profile from condition 1. **F)** Line profile from image taken under condition 2 shows complete overlap of AF555 intensity with AF488 intensity. Colocalization factor was 1.000. **G)** Immunofluorescence confocal images corresponding to (from top to bottom): 1) Control 1, 2) Control 2, and 3) Control 3 from panel B. The bottom panel shows mild autofluorescence in the 488 channel. Scale bar denotes 10 μm.

Supplemental Figure 4.4

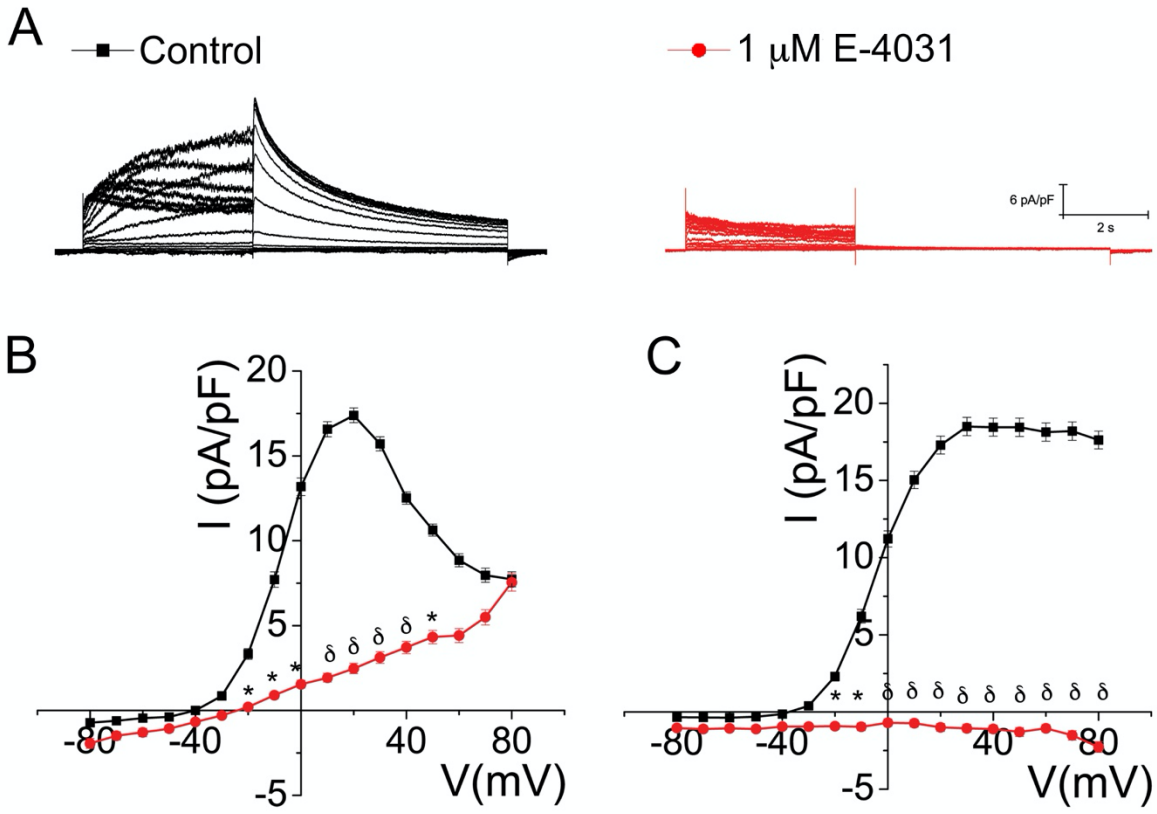

Supplemental Figure 4.4. Inhibitory effects of E-4031 on I_{Kr}. A. HEK 293 cells were transfected with $hERG_{WT}$: MiRP1 and whole-cell voltage-clamp recordings were performed before and after application of 1 μM E-4031, following the same protocol shown in **Figure 1**. Current density at the end of the pre-pulse (**B**) and peak tail current density (**C**) are shown, where * denotes $p < 0.05$ and $^{\delta}$ denotes $p < 0.01$.

Journal of General Physiology 2020 Vol. 152 No. 12 e202012667

CHAPTER 5

Different Arrhythmia-associated Calmodulin Mutations have distinct effects on Cardiac SK channel regulation

Hannah A. Ledford,[1] Seojin Park,[2] Duncan Muir,[1] Ryan L. Woltz,[1] Lu Ren,[1] Phuong T. Nguyen,[3] Padmini Sirish,[1] Wenying Wang,[2] Choong-Ryoul Sihn,[2] Alfred L. George Jr.,[4] Björn C. Knollmann,[5] Ebenezer N. Yamoah,[2] Vladimir Yarov-Yarovoy,[3] Xiao-Dong Zhang[1,6]*, and Nipavan Chiamvimonvat[1,6]*

[1]Division of Cardiovascular Medicine, Department of Internal Medicine, School of Medicine, University of California, Davis, Davis, CA 95616
[2]Department of Physiology and Cell Biology, University of Nevada, Reno, Reno, NV 89557
[3]Department of Physiology and Membrane Biology, School of Medicine, University of California, Davis, Davis, CA 95616
[4]Department of Pharmacology, Northwestern University Feinberg School of Medicine, Chicago, IL 60611
[5]Vanderbilt Center for Arrhythmia Research and Therapeutics, Department of Medicine, School of Medicine, Vanderbilt University, Nashville, TN 37232
[6]Department of Veterans Affairs, Northern California Health Care System Mather, CA 95655

Running title: Mechanisms of human mutant calmodulin on SK channel function

*To whom correspondence should be addressed: Division of Cardiovascular Medicine, Department of Internal Medicine, University of California, Davis, One Shields Avenue, GBSF 6315, Davis, CA 95616 & Department of Veterans Affairs, Northern California Health Care System, 10535 Hospital Way Mather, CA 95655. Email: nchiamvimonvat@ucdavis.edu and xdzhang@ucdavis.edu

Summary

Cardiac small-conductance Ca^{2+}-activated K^+ (SK) channels are gated solely by beat-to-beat changes in intracellular Ca^{2+}. Ledford et al. show distinct mechanisms by which human calmodulin mutants linked to sudden cardiac death regulate SK channels.

Abstract

Calmodulin (CaM) plays a critical role in intracellular signaling and regulation of Ca^{2+}- dependent proteins and ion channels. Mutations in CaM cause life-threatening cardiac arrhythmias. Among the known CaM targets, small-conductance Ca^{2+}-activated K^+ (SK) channels are unique, since they are gated solely by beat-to-beat changes in intracellular Ca^{2+}. However, the molecular mechanisms of how CaM mutations may affect the function of SK channels remain incompletely understood. To address the structural and functional effects of these mutations, we introduced prototypical human CaM mutations in human induced pluripotent stem cell-derived cardiomyocyte-like cells (hiPSC-CMs). Using structural modeling and molecular dynamics simulation, we demonstrate that human calmodulinopathy-associated CaM mutations disrupt cardiac SK channel function via distinct mechanisms. CaM_{D96V} and CaM_{D130G} mutants reduce SK currents through a dominant-negative fashion. By contrast, specific mutations replacing phenylalanine with leucine result in conformational changes that affect helix packing in the C- lobe, which disengage the interactions between apo-CaM and the CaM binding domain of SK channels. Distinct mutant CaMs may result in a significant reduction in the activation of the SK channels, leading to a decrease of the key Ca^{2+}-dependent repolarization currents these channels mediate. The findings in this study may be generalizable to other interactions of mutant CaMs with Ca^{2+}-dependent proteins within cardiac myocytes.

Introduction

Calmodulin (CaM) is a multifunctional Ca^{2+} binding protein that orchestrates a wide range of intracellular signaling and critical cellular processes [1, 2]. CaM, a 17 kDa protein, is encoded by 3 distinct genes in human, namely *CALM1, CALM2, and CALM3*, each of which encodes for an identical CaM protein. CaM is comprised of N- and C-terminal lobes linked by a flexible helix [3, 4]. Each lobe contains two EF hands, canonical Ca^{2+} binding motifs, with the N-lobe having slightly lower Ca^{2+} binding affinity [5-7]. Ca^{2+} binding to the EF hands results in structural and functional changes of target molecules [8].

Recent studies have provided genetic links between human heritable CaM mutations and several types of cardiac arrhythmia syndrome leading to sudden cardiac death, including long QT syndrome (LQTS) [9-11], catecholaminergic polymorphic ventricular tachycardia (CPVT) [12], and familial idiopathic ventricular fibrillation (IVF) [13]. N54I and N98S mutations in CaM are associated with cases of CPVT with altered CaM-ryanodine receptor 2 (RyR2) function; F90L has been shown to be linked to IVF; and D96V, D130G, and F142L are associated with LQTS.

LQTS mutations of CaM have been shown to reside at or near Ca^{2+} coordinating sites within the EF hands of the C-lobe of CaM [14, 15]. *CALM1*-D130G and *CALM2*-D96V mutations alter highly conserved aspartic acid residues that bind Ca^{2+} ions in EF-hand domains IV and III, respectively. The *CALM1*-F142L mutation results in an alteration of the energetic coupling of Ca^{2+} binding and the conformational change associated with CaM activation [9]. All 3 LQTS-associated mutations show reduced Ca^{2+} affinity in the C-lobe by 5-, 13-, and 53-fold for F142L, D96V, and D130G, respectively [9]. These mutations in CaM result in a significant reduction in Ca^{2+}-dependent inactivation (CDI) of $Ca_v1.2$ LTCC [16-18]. In contrast, CPVT mutations in CaM impart little-to-mild reduction of Ca^{2+} binding affinity [12].

Clearly, CaM exerts its function on a number of targets in cardiomyocytes including RyR2 [13, 19-22], K_v7.1 (or KCNQ1) [23-25], L-type Ca^{2+} channels (Ca_v1.2, Ca_v1.3) [26-28] and small-conductance Ca^{2+}-activated K^+ (SK) channels [29, 30]. Among the CaM-targets, SK channels are unique because the channels are voltage-independent and are gated solely by beat-to-beat changes in intracellular Ca^{2+} (Ca^{2+}_i). SK channels harbor a highly conserved CaM-binding domain (CaMBD); the gating of the channels is controlled by Ca^{2+} binding and unbinding to CaM associated with SK channels [29]. Thus, CaM serves as the high affinity Ca^{2+} sensor for SK channels. Studies on human calmodulinopathy have provided evidence for the critical roles of CaM in the functional regulation of SK channels [31, 32]. However, the mechanistic effects on SK channels by mutations in CaM remain incompletely understood.

Ca^{2+}-activated K^+ channels (K_{Ca}) can be divided into three main subfamilies based on their electrophysiological, pharmacological, and molecular phenotypes. These include large-conductance Ca^{2+}- and voltage-activated K^+ channels (BK), the intermediate-conductance K_{Ca} channels (IK or SK4), and the small conductance K_{Ca} channels (SK1, 2, and 3) [33-36]. SK4 channels have intermediate single-channel conductance and are sensitive to charybdotoxin. In contrast, SK channels have small single-channel conductance and are sensitive to apamin. Recent cryo-electron microscopy (cryo-EM) structure of the SK4 channel-CaM complex [37] reveals atomic details of the SK channel C-terminus interaction with the C-lobe of CaM, demonstrating that the C-lobe binds to the channel constitutively, while the N-lobe interacts with the S4-S5 linker in a Ca^{2+}-dependent manner. The S4-S5 linker undergoes conformational changes upon CaM binding to open the channel pore [37]. CaM opens SK channels with median effective intracellular concentration of Ca^{2+} of ~100-400 nM [29, 33].

Here, we take advantage of the SK4 channel-CaM complex structure as a template for *Rosetta* molecular modeling, combined with molecular dynamics simulation, biochemical and functional analyses to test the effects of the known CaM mutations on cardiac SK2 channel functions. Specifically, we tested the hypothesis that human CaM mutations linked to sudden cardiac death disrupt SK channel function by distinct mechanisms. Mutations in the Ca^{2+}-binding domain of CaM (*CALM1* D130G, *CALM2* D96V) result in a dominant-negative (DN) effect while specific mutations with phenylalanine to leucine (*CALM1* F90L and F142L) disrupt the interactions between apo-CaM with the CaMBD of SK channels. SK currents have been shown to be prominently expressed not only in atrial myocytes [38, 39] but also in cardiac Purkinje cells [40]. Indeed, Purkinje cells have been shown to be the probable site of origin of cardiac arrhythmias, including in patients with heritable arrhythmia syndrome [41, 42]. Additionally, SK channels have been shown to be expressed and play important roles in pacemaking cells including sinoatrial and atrioventricular nodes [43, 44]. Distinct mutant CaMs may result in a significant reduction in the activation of the SK channels leading to a decrease of the key Ca^{2+}-dependent repolarization currents mediated by SK channels, exacerbating the effects of CaM mutations in LQTS or IVF.

Materials and Methods

Plasmid construction

Human filamin A (FLNA) in pREP4 vector (Life Technologies, Carlsbad, CA) was a kind gift from Dr. Paramita M. Ghosh (UC Davis, Davis, CA). α-Actinin2 cDNA in pcDNA3 vector was a kind gift from Dr. David Fedida (University of British Columbia, Canada) [45]. Construction of SK2 expression plasmids for heterologous expression in human embryonic kidney cells (HEK 293) was as follows: full-length human cardiac SK2 cDNA was subcloned into pIRES2-EGFP

(Takara Bio USA, Inc., Mountain View, CA) to obtain pSK2-IRES-EGFP plasmid. SK2 channel fusion constructs were generated harboring CaM_{WT} (hSK2-G_4-CaM_{WT}) or mutant CaMs (hSK2-G_4-mutant CaM) to specifically occupy the CaMBD of SK2 channels with CaM_{WT} or mutant CaMs using flexible linkers (glycine linkers) as previously described by Mori *et al*. [46].

To study the subcellular localization of SK2 channel subunit, modified human influenza hemagglutinin (HA) tag was inserted into the extracellular S1-S2 loop of the channel. Specifically, modified HA epitope was flanked with the ClC-5 chloride channel D1-D2 loop to increase accessibility and inserted in the end of the S1-S2 loop of SK2 channel subunit as we have described previously [47]. The inserted amino acid sequence was NSEHYPYDVPDYAVTFEERDKCPEWNC. The epitope is underlined. Epitope tags were generated by recombination polymerase chain reaction and verified by automated sequencing.

Human embryonic kidney (HEK) 293 cells and plasmid transfection

HEK 293 cells were maintained in Dulbecco's modified Eagle's medium supplemented with 10% fetal bovine serum. Cell lines were maintained at 37 °C in a humidified atmosphere containing 5% CO_2. All cell culture reagents were purchased from Life Technologies. HEK293 cells were transfected using the following plasmid compositions: pSK2-IRES-EGFP, in combination with pREP4-FLNA and pcDNA3-α-actinin2, with wild-type (CaM_{WT}) or mutant CaM (1 μg for each plasmid), using Lipofectamine™ 2000 (Life Technologies) according to the manufacturer's protocol. The 1:1 ratio of the plasmids was determined to be most optimal for SK2 current expression in our prior published studies [48].

Patch-clamp recordings

Whole-cell $I_{K,Ca}$ was recorded from transfected HEK293 cells and human induced pluripotent stem cell (hiPSC)-derived cardiomyocyte-like cells (hiPSC-CMs) at room temperature using conventional patch-clamp techniques, as previously described [38]. For current recordings, the extracellular solution contained (in mmol/liter (mM)): *N*-methylglucamine (NMG) 140, KCl 4, $MgCl_2$ 1, glucose 5, and HEPES 10, pH 7.4 with HCl. The internal solution contained (in mM): potassium gluconate 144, $MgCl_2$ 1.15, EGTA 5, HEPES 10, and $CaCl_2$ yielding a free cytosol Ca^{2+} concentration of 500 nM, using the software by C. Patton of Stanford University (http://maxchelator.stanford.edu/). The pH was adjusted to 7.25 using KOH. To isolate apamin-sensitive SK currents, extracellular solution containing apamin (10 nM) was applied during the recordings, and the difference currents between the control and the apamin-containing solution were calculated to be the apamin-sensitive currents. The current was elicited from a holding potential of -55 mV using a ramp voltage-clamp protocol ranging from -120 to +60 mV with a 2 second duration.

For hiPSC-CM recordings, 0.006 mM WT CaM or mutant CaM peptides were added to the intracellular solution and the recordings were performed 3 minutes after forming whole-cell recording for compete dialysis of the peptides. Action potentials were recorded using perforated patch-clamp techniques at room temperature. The patch-pipettes were backfilled with amphotericin (200 μg/ml). The pipette solution contained (in mM): 120 potassium glutamate, 1 $MgCl_2$, 25 KCl, 10 HEPES, 1 $CaCl_2$, pH 7.25, and the extracellular solution contained (in mM): 138 NaCl, 4 KCl, 1 $MgCl_2$, 2 $CaCl_2$, 0.33 NaH_2PO_4, 10 Glucose, 10 HEPES, pH 7.4.

All recordings were performed using 3 M KCl agar bridges. Cell capacitance was calculated as the ratio of total charge (the integrated area under the current transient) to the magnitude of the pulse (20 mV). Currents were normalized to cell capacitance to obtain the current density. The series resistance was compensated electronically. In all experiments, a series

resistance compensation of ≥90% was obtained. The currents and membrane potentials were recorded using Axopatch 200A amplifier (Molecular Devices, LLC., Sunnyvale, CA, USA), filtered at 1 kHz using a 4-pole Bessel filter and digitized at a sampling frequency of 5 kHz. Data acquisition and analysis were carried out using pClamp 10 software (Molecular Devices) and Origin software (OriginLab, Northampton, MA, USA).

Immunofluorescence confocal laser scanning microscopy of HEK 293 cells

HEK293 cells were co-transfected with human cardiac SK2-HA channel together with α-actinin and FLNA, using lipofectamine (Life Technologies, Catalog #11668-019), with CaM_{WT} or mutant CaM as we have previously described [48]. After blocking with 1% Bovine Serum Albumin (BSA, Sigma, Catalog #A7030) and no permeabilization (NP), SK2 channels localized on the cell membrane were labeled with monoclonal anti-HA antibody (Covance, catalog #MMS-101P, 1:100 dilution), by incubating overnight in the humidified chamber (4 °C), followed by treatment with chicken anti-mouse Alexa Fluor 555 secondary antibody (Life Technologies, Catalog #A-21200, 1:500 dilution) for 1 hour at room temperature. Cells were then permeabilized (P) with 0.01% Triton X (Fisher) and blocked with 1% BSA again, and intracellular SK2 channels were labeled with anti-HA antibody (Covance, 1:250 dilution) at 4 °C overnight and a rabbit anti-mouse Alexa Fluor 633 secondary antibody (Life Technologies, Catalog #21427, 1:500 dilution). Coverslips were mounted using mounting medium containing 4′,6-diamidino-2-phenylindole (DAPI, VectaMount, catalog #H-5000, Vector Laboratories, Inc.) and imaged under Zeiss LSM 700 confocal laser scanning microscope.

Specifically, to quantify the 555/633 fluorescence ratio, anti-HA antibody and Alexa Fluor 555 secondary antibody were used to label SK2 channel with extracellular hemagglutinin (HA) tag (SK2-HA) prior to permeabilization. The cells were then permeabilized using Triton-X and

intracellular SK2 channels were labeled with anti-HA antibody and Alexa Fluor 633 secondary antibody. Fluorescence ratio of 555/633 then represents the ratio of SK2 channel numbers on cell membrane over those inside the cells as we have previously described [48]. Cells co-transfected with CaM_{WT} or mutant forms of CaM were immunolabeled in parallel and all the microscopic settings were kept the same for all groups. Blind analysis was performed on unaltered images using Fiji ImageJ.

Human induced pluripotent stem cell (hiPSC)-derived cardiomyocyte-like cells (hiPSC-CMs)

Feeder-free hiPSCs (iPS-D19-9-T7, WiCell, Madison, WI, USA) were cultured with mTeSR on hiPSC-qualified matrigel. HiPSCs were differentiated into hiPSC-CMs following the protocols we previously reported [49, 50]. We have observed ~80-90% cardiomyocyte as shown previously [49]. HiPSC-CMs at day 40 (maturing cardiomyocytes) were used for experiments. CaM_{WT} and mutant CaM peptide were used to test the functional changes of endogenous SK currents in hiPSC-CMs. The effects of WT compared to mutant CaMs were tested on the apamin-sensitive currents.

Generation of recombinant CaM proteins

WT and mutant CaM proteins were prepared as previously described [13]. Briefly, the recombinant CaM cDNA sub-cloned into a pET15b vector was mutated using QuikChange site directed mutagenesis (Agilent Technologies, Santa Clara, CA). Proteins were expressed in E. coli BL21 (DE3) cells and purified by hydrophobic chromatography using a phenyl sepharose column. Purified protein was dialyzed overnight at 4°C twice in 50 mM HEPES at pH 7.4, 100 mM KCl, and 5 mM EGTA, and twice more with the same buffer except EGTA was lowered to 0.05 mM to

remove Ca^{2+}. The molecular mass of all proteins was confirmed using negative electrospray mass spectroscopy.

Structural modeling of CaM, CaM mutants, and hSK2 channel

Structural modeling of CaM_{WT}, CaM_{F90L}, CaM_{F93L}, and CaM_{F142L} and the human SK2 (hSK2) channel was performed using Rosetta loop modeling and relax applications [51-57] based on the hSK4 bound to apo-CaM cryo-EM structure (PDB: 6CNM) [37] as a template.

First, we directly compared the sequence between hSK2 (UniProt ID: Q9H2S1) with the cyo-EM structure of hSK4 (PDB ID: 6CNM) that was used as the template for molecular modeling. The sequence identity between the two structures is 46%, while the sequence similarity is 63%. We further compared the sequence for the CaMBD (amino acid residues 412-488 in hSK2, DTQLTKRVKNAAANVLRETWLIYKNTKLVKKIDHAKVRKHQRKFLQAIHQLRSVKME QRKLNDQANTLVDLAKTQNI). The sequence identity between the two CaMBDs is 47% with sequence identity of 68%.

HSK2 channel sequence was threaded onto the hSK4 structure. One thousand models of hSK2 channel were generated using the Rosetta relax application, then clustered; the top model after clustering was selected as the best hSK2 model. The hSK2 model was used to replace the hSK4 peptide in the CaMBD based on hSK4-CaM complex structure [37]. One thousand models of the hSK2-CaM complex were generated using the Rosetta relax application, then clustered and the top model after clustering was selected as the best hSK2-CaM complex model, shown in **Fig. 5.6**. To determine the structure of the C-lobe of apo-CaM, CaM was taken from the 6CNM structure, mutated for the mutant models, relaxed, and finally clustered with the top models shown in **Fig. 5.6**. The mutant CaM models were created by mutating the CaM_{WT} and then using the Rosetta relax application to model potential conformational changes, induced by specific CaM mutations.

Ten thousand models were generated, the 1,000 lowest energy models were clustered, and the top models after clustering for each CaM mutant were selected as the best model. Molecular graphics and analyses were performed with the UCSF Chimera package [58].

Molecular dynamics (MD) simulations of WT and mutant CaM

Structures representing WT and mutant apo-CaM were obtained from Rosetta modeling as described above. The webserver CHARMM-GUI was used to prepare apo-CaM and create the solvent box [59-61]. The protein was immersed in a TIP3 water box with dimensions of 9 nm on all sides. Na and Cl ions were added to a final concentration of 150 mM to neutralize charge. In total, the system was composed of ~15,000 (± 1,000) atoms [59-61]. Periodic boundary conditions with dimensions equivalent to the water box were used [62].

Equilibration and production runs were performed using NAMD 2.13 [62] on a local GPU cluster using CHARMM36m force fields [63, 64]. After 100,000 steps of steepest descent minimization, MD simulations started with a time step of 1 fs with harmonic restraints initially applied to protein heavy atoms. These restraints were slowly released over 0.5 ns. These systems were equilibrated further for 0.2 ns with a time step of 2 fs. In order to use a 2 fs time step, all bonds to H atoms were constrained using the SHAKE algorithm. All simulations were performed in NPT ensemble. Temperature is maintained at 303.15 K using Langevin thermostat and constant pressure at 1 atm is maintained using Nosé-Hoover barostat.

Electrostatic interactions were computed using Particle Mesh Ewald (PME) method [65]. Non-bonded pair lists were updated every 10 steps with a list cutoff distance of 16 Å and a real space cutoff of 12 Å with energy switching starting at 10 Å. After equilibration of 1 ns, the simulation was continued for 1 μs. The full trajectory, including the equilibration and production steps, was used to calculate the root mean square deviation (RMSD). The 1 μs trajectory of the

simulation during the production step was saved every 0.2 ns. This trajectory was then used for analysis.

Root mean square deviation (RMSD)

All measurements and renderings were performed using Visual Molecular Dynamics (VMD) [66]. RMSD was calculated every 0.2 ns over the equilibration and production steps aligned to the first frame in the equilibration step. Specifically, for every 0.2 ns of the production simulation, the RMSD is calculated for apo-CaM_{WT} and the mutant CaMs. The structures are clustered and the cluster with the most decoys is selected as the most probable with the center of the cluster being used as the representative model. Each mutant CaM structure is aligned individually to the WT CaM representative model using the matchmaker tool in UCSF chimera and the distance between the C-alpha of each residue is calculated. The averaged distance and the standard deviation (S.D.) for each comparison for the full C-terminal domain (residues 81-145) and for Ca^{2+} binding site 4 (residues 131-138) was quantified (Tables 1-2 in Online Supplemental Data).

Root mean square fluctuation (RMSF)

Per residue root mean square fluctuation (RMSF) was calculated over a sliding average window of 1 ns time and averaged over the 1 μs trajectory. The per residue RMSF is presented as mean ± standard deviations (S.D.).

Ensembles were generated by clustering the MD run as described in structural modeling section. The top 10 models displayed and aligned with the top cluster model.

Data analysis

Data analysis from patch-clamp recordings was performed by using Origin software (MicroCal Inc). Current density obtained from cells expressing SK2 with CaM_{WT} or mutant CaM

was compared by normalizing the currents with cell capacitance. Where appropriate, pooled data are presented as means ± S.E.M. Statistical comparisons were performed using one-way and two-way analysis of variance combined with Tukey's post hoc analyses. One-way analysis of variance (ANOVA) was used to determine statistically significant differences among three or more groups in **Figs. 5.1, 5.2, 5.4 and 5.5**. Two-way analysis of variance (ANOVA) was used to determine statistically significant differences with two independent variables among three or more groups in **Fig. 5.3**. Post hoc analyses were performed using Tukey's test. Statistical analyses were performed using GraphPad Prism (San Diego, CA) and Origin Software.

Online supplemental material

Fig. S5.1 shows summary data for fluorescence intensity under non-permeabilized (NP, left bars) and permeabilized (P, right bars) conditions for HEK 293 cells expressing SK2 fusion protein with HA tag co-expressed with CaM_{WT} or mutant CaMs (N54I, F90L, D96V, N98S, and D130G). **Fig. S5.2** shows RMSD graphs that include the equilibration and production stages. **Fig. S5.3** shows top ten clustered models of apo-CaM_{F90L}, apo-CaM_{F93L}, and apo-CaM_{F142L} aligned to represent an ensemble of possible states, illustrating the compact distribution of Helix 3 and Ca^{2+} binding site 4 regions. **Fig S5.4** shows graphical comparisons from MD simulations of the C-lobe of apo-CaMs showing hydrogen bond in the apo-CaM_{WT}. The side chain of Asn^{112} on the helix 2 in apo-CaM_{WT} maintains a stable hydrogen bond with the carboxyl oxygen of Ala^{89} residue on the helix 1 during the simulations of the apo-CaM_{WT}, which is not observed in the simulations of the CaM mutants. **Fig. S5.5** shows comparison of RMSF of Ca^{2+}-CaM_{F142L} from MD simulations (A) and N-H heteronuclear NOE saturated/unsaturated ratio (B, BMRB: 34262) [67]. There is similar flexibility including identification of the most flexible amino acid being Lys^{116} residue. **Table 5.1** shows quantification of RMSD calculated from the production portion of MD, presented in **Fig.**

S5.2. Table 2 shows quantification of the differences in RMSD among WT and mutant CaMs, derived from the C terminal domain (residues 81-145) and Ca^{2+} binding site 4 (residues 131-138), presented in **Fig. 5.8**. Movies S1-S3 show morph videos from the top Rosetta model of the C-lobe of apo-CaM_{WT} to the top Rosetta models of apo-CaM_{F90L}, apo-CaM_{F93L}, and apo-CaM_{F142L}, respectively. Movies S4-S6 show morph videos from the top MD model of the C-lobe of apo-CaM_{WT} to the top MD models of apo-CaM_{F90L}, apo-CaM_{F93L}, and apo-CaM_{F142L}, respectively.

Results

Inhibitory effects of human CaM mutations on SK channels

We first co-express human cardiac SK2 channels with different human mutant CaMs compared to wild-type CaM (CaM_{WT}) in HEK293 cells. Our previous studies have shown that cytoskeletal proteins are critical for the proper membrane localization of SK2 channels, therefore, α-actinin2 and filamin A (FLNA) are also used for co-expression in all groups [48, 68, 69].

As positive controls, we test the roles of the N- and C-lobe mutant CaMs in the regulation of SK2 currents using $CaM_{1,2}$ and $CaM_{3,4}$ where the two Ca^{2+}-binding sites in the N- and C-lobe are mutated, respectively, as well as a mutant CaM ($CaM_{1,2,3,4}$) that abolishes the four high affinity Ca^{2+} binding sites [29]. Apamin-sensitive Ca^{2+}-activated K^+ current ($I_{K,Ca}$) is recorded at baseline (before apamin application, black traces) and after apamin application (10 nM, red traces). Both EF hands in the N- and C-lobe of CaM play critical roles in activation of the apamin-sensitive current (**Fig. 5.1A**). Moreover, $CaM_{1,2,3,4}$ results in the most significant inhibition on the apamin-sensitive current compared to $CaM_{1,2}$ and $CaM_{3,4}$ (**Fig. 5.1A**). Summary data for the density of apamin-sensitive currents at the test potentials of -120 and +60 mV are shown in **Fig. 5.1B**. The results are distinct from previously reported demonstrating the critical roles of Ca^{2+} binding to the N- but not the C-lobe of CaM in SK channel gating in oocytes [70]. However, our experiments were

performed in a mammalian expression system with co-expression with α-actinin2 and FLNA. Furthermore, our previous study has documented binding of α-actinin2 to the CaMBD of SK2 channels [48, 68, 71].

Next, we test the effects of LQTS (CaM_{D96V}, CaM_{D130G}), CPVT (CaM_{N54I}, CaM_{N98S}), and IVF (CaM_{F90L}) CaM mutants compared to CaM_{WT}. **Fig. 5.1C** shows the most prominent inhibitory effects on the density of apamin-sensitive currents by the two LQTS mutations (CaM_{D96V} and CaM_{D130G}). CaM_{F90L} results in the least inhibitory effects. The current densities at -120 mV and +60 mV are shown in **Fig. 5.1D**.

No significant alteration in SK2 channel trafficking by human mutant CaMs

The effects of CaM mutations on SK2 current may result from a decrease in the channel activation or trafficking to the cell membrane. We, therefore, test if the reduction in the SK2 current density from co-expression of mutant CaMs results from a decrease in membrane trafficking. Immunofluorescence confocal microscopy is performed using SK2 channels harboring an HA tag in the extracellular S1-S2 loop (SK2-HA) by employing non-permeabilized (NP) compared to permeabilized (P) conditions as we have previously described (**Fig. 5.2** and **Supplemental Figure S5.1**) [48]. Our data suggest that the mutant CaM does not alter SK channel trafficking.

Similar effects of mutant CaMs on SK2 channels revealed by SK2 fusion protein harboring CaM_{WT} or mutant CaMs *via* a flexible glycine linker (G_n)

There are some possible caveats inherent in the experiments presented in **Fig. 5.1** since mutations in CaMs may alter the efficiency of CaM expression in HEK293 cells. To circumvent these possible confounding factors, we generate SK2 channel fusion constructs harboring CaM_{WT} (hSK2-G_4-CaM_{WT}) or mutant CaMs (hSK2-G_4-mutant CaM) to specifically occupy the CaMBD

of SK2 channels with CaM_{WT} or mutant CaMs using flexible linkers (G_n linker, **Fig. 5.3A**), as previously described by Mori *et al*.[46]. This experimental paradigm enables us to selectively test the contribution of the mutant CaMs compared to CaM_{WT} on SK2 channels (**Fig. 5.3A**).

We first demonstrate that the fusion proteins behave as expected by directly comparing apamin-sensitive $I_{K,Ca}$ recorded from HEK293 cells expressing hSK2-G4-CaM_{WT} *vs*. hSK2 co-expressed with CaM_{WT} (**Fig. 5.3B**). Furthermore, co-expression of DN CaM ($CaM_{1,2,3,4}$) with hSK2-G_4-CaM_{WT} fails to knockdown apamin-sensitive current (**Fig. 5.3B**) in contrast to hSK2 co-expressed with $CaM_{1,2,3,4}$ as shown in **Fig. 5.1A**.

Having determined that the fusion proteins function as expected, we compare the density of apamin-sensitive currents between hSK2-G_4-mutant CaM and co-expression of SK2 channel and mutant CaMs (**Fig. 5.3C**). The density is comparable with the most significant inhibitory effects on $I_{K,Ca}$ by the two LQTS mutations tested (CaM_{D96V} and CaM_{D130G}) consistent with a DN effect from these mutations (**Fig. 5.3D-E**). We further test the effects of two additional mutant CaMs (F93L and F142L). CaM_{F142L} is shown to be linked to LQTS while F93 residue is predicted from our molecular model to interact with CaMBD of SK2 channels (described in a later section). These two mutations produce intermediate effects on $I_{K,Ca}$ (**Fig. 5.3D-E**).

Functional effects of mutant CaMs on SK currents in hiPSC-CMs

The experiments, thus far, have relied on a heterologous expression system. We further take advantage of human induced pluripotent stem cells-derived cardiomyocyte-like cells (hiPSC-CMs). The rationale is to determine the functional effects of mutant CaMs on endogenous SK currents with accompanying ion channel interacting proteins within a human cardiomyocyte-like cell. Even though hiPSC-CMs are relatively immature, we demonstrate the expression of SK2 channels in hiPSC-CMs using immunofluorescence confocal microscopy (**Fig. 5.4A**). **Fig. 5.4B**

shows apamin-sensitive current in hiPSC-CMs when the cells were dialyzed by WT or mutant CaM proteins. Dialysis of mutant CaM_{D96V} proteins results in the most prominent knockdown of apamin-sensitive currents in hiPSC-CMs, consistent with its DN effects compared to CaM_{F90L} (**Fig. 5.4C-D**).

Altered interaction between SK2 channel and mutant CaMs

Co-IP was performed as we have previously described [71] between SK2-HA channels (**Fig. 5.5A**) and different mutant CaMs compared to CaM_{WT}. Since native cells contain a large amount of CaM, we constructed fusion protein of CaM with FLAG-tag (DYKDDDDK, CaM_{FLAG}) to enable identification of transfected mutant CaMs *versus* endogenous CaM_{WT} (**Fig. 5.5B**). There is a significant decrease in SK2 channels complexed with mutant CaM_{F90L}, in the absence of Ca^{2+} with EGTA (**Fig. 5.5C**). Negative control experiments are performed using non-transfected (NT) cells and cells transfected with SK2-HA alone, without CaM_{FLAG}. The data suggest a significant reduction in SK2 channel complexed with apo-CaM_{F90L} compared to other CaM mutants, supporting the lack of DN effects with relatively modest inhibition of CaM_{F90L} on SK2 currents.

Structural modeling of CaM_{F90L}, CaM_{F93L}, and CaM_{F142L} mutants and their interactions with SK2 channels

To explore the potential structural changes induced by CaM mutations, we generated structural models of the C-lobe of apo-CaM_{WT}, apo-$CaM_{F90L,}$ apo-$CaM_{F93L,}$ and apo-CaM_{F142L} using *Rosetta* structural modeling. The models of CaM reveal that the Phe→Leu mutations result in conformational changes that affect helix packing in the C-lobe due to the substitution of a relatively large phenylalanine side chain to a smaller leucine side chain (**Fig. 5.6B-D**). Phe^{90} side chain is surrounded by the following residues in the apo-CaM_{WT}: Arg^{87} in helix 1, Ile^{101} in loop 1-2, Val^{137} in loop 3-4, and Tyr^{139} and Phe^{142} in helix 4. Phe^{93} side chain is surrounded by the

following residues in the apo-CaM_{WT}: Ile^{101} in loop 1-2, Leu^{106} and Val^{109} in helix 2, and Phe^{142}, Met^{145}, and Met^{146} in helix 4. Phe^{142} side chain is surrounded by the following residues in the apo-CaM_{WT}: Ile^{86}, Phe^{90}, and Phe^{93} in helix 1, Ile^{101} in loop 1-2, Leu^{106} in helix 2, Val^{137} in loop 3-4, and Tyr^{139}, Met^{145}, and Met^{146} in helix 4. Notably, Phe^{90}, Phe^{93}, and Phe^{142} are interacting with each other in the apo-CaM_{WT}. The conformational effects of the Phe→Leu mutations are further explored in more detail using molecular dynamics (MD) simulations.

Additionally, we generated a structural model of apo-CaM_{WT} in complex with CaMBD from SK2 channel based on the cryo-EM structure of SK4 channel in complex with apo-CaM (PDB: 6CNM)[37]. The three phenylalanine residues (Phe^{90}, Phe^{93}, and Phe^{142}) from the C-lobe of CaM can be seen interacting with hydrophobic residues from the CaMBD of SK2 channels (**Fig. 5.6E-F**). Consistent with our hypothesis, we predict that substitution of the phenylalanine side chain may result in a significant decrease in the interaction of apo-CaM and SK2 CaMBD. Even though CaM_{F90L} and CaM_{F142L} have previously been described to be linked to human arrhythmias, CaM_{F93L} has not been described in patients. Our molecular modeling predicts Phe^{93} residue to intimately interact with SK2 CaMBD. Indeed, CaM_{F93L} results in a significant decrease in SK2 current, supported by our functional analyses (**Fig. 5.3D-E**).

Molecular Dynamics simulations provide insights into the conformational changes of CaM_{F90L}, CaM_{F93L}, and CaM_{F142L}

To further explore potential conformational changes induced by the Phe→Leu mutations in CaM, we perform molecular dynamics (MD) simulations on the WT and the 3 CaM mutants: F90L, F93L and F142L. Each simulation was performed for 1 μs after equilibration. The simulations for apo-CaM_{WT} was performed twice. Root mean square deviations (RMSD)

demonstrated that the system equilibrated rapidly and the RMSD had plateaued for the entire runs (**Supplemental Fig. 5.2** and **Table 5.1**).

Analyses of the root mean square fluctuation (RMSF) show remarkable findings that the three Phe→Leu mutants affect the per residue structure in similar manners (**Fig. 5.7**) even though the mutants are located in different helices of the C lobe of CaM (helix 1 contains Phe^{90} and Phe^{93} and helix 4 contains Phe^{142}). Compared to apo-CaM_{WT} from the first simulation, all three CaM mutants exhibit more flexibility towards the C-terminal end of helix 2 while the C-terminal end of helix 3 and the Ca^{2+} binding site 4 are less flexible. The largest shifts in RMSF are observed where the side chains of Phe^{90}, Phe^{93}, and Phe^{142} are contacting helices 2 and 3. This agrees with the notion that the Phe→Leu mutation creates a void volume, allowing helices 2 and 3 to repack their side chains and readjust their backbone positions (**Fig. 5.8**, Supplemental **Fig. 5.3**, see also Morph Videos in the Supplemental Data). Differences in the RMSD between an equilibrated apo-CaM_{WT} and mutant CaMs shown in **Fig. 5.8** are quantified for the C terminal domains as well as for Ca^{2+} binding site 4 (**Table 5.2** in Online Supplemental Data).

The RMSD from Simulation 2 of the apo-CaM_{WT} exhibited a transient increase before returning to the baseline towards the end of the simulation (**Supplemental Fig. 5.2**). Closer examinations revealed that the major contributing regions of apo-CaM_{WT} towards the transient increase in the RMSD in Simulation 2 are in helix 3, just proximal to the Ca^{2+} binding site 4, similar to the conformational changes we observed in Simulation 1, but to a larger magnitude. Additionally, Simulation 2 of apo-CaM_{WT} exhibited a similar per residue RMSF pattern to Simulation 1, albeit less in magnitude as demonstrated in **Fig. 5.7**. This is consistent with the lower value of RMSD for Simulation 2 compared to Simulation 1 for the majority of the run. Finally,

there was a return to the average RMSD after the transient increase, supporting the equilibration of the simulations.

Consistent with our observation, the side chain of Asn^{112} on the helix 2 in apo-CaM_{WT} maintains a stable hydrogen bond with the carboxyl oxygen of Ala^{89} residue on the helix 1 during the simulations of the apo-CaM_{WT}, which is not observed in the simulations of the CaM mutants (**Supplemental Fig. 5.4**). This may also, in part, influence the flexibility towards the C-terminal end of helix 2 of the three mutant CaM as discussed above. We suggest that these observed changes may result in a decrease in the interaction of apo-CaM and SK2 CaMBD. Finally, to validate the MD simulations, we directly compare RMSF of Ca^{2+}-CaM_{F142L} from MD simulation with the publicly available N-H heteronuclear NOE saturated/unsaturated ratio from previously published NMR structure (BMRB: 34262) [67]. Indeed, there is significant similarity in the flexibility including identification of the most flexible amino acid residue being Lys^{116} (**Supplemental Fig. 5.5**).

Discussion

The gating of SK channels relies on Ca^{2+} binding to CaM. Mutations on CaM in human calmodulinopathy are predicted to have significant effects on SK channel function. In the current study, we demonstrate a significant reduction in SK currents in the presence of the LQTS CaM mutants, CaM_{D96V} and CaM_{D130G}. The marked reduction in SK currents in the presence of LQTS CaM mutants is consistent with their DN effects. Immunofluorescence staining do not show significant changes in membrane-bound SK2 channels in the presence of wild-type or mutant CaM, suggesting the effects of these CaM mutants are primarily on the Ca^{2+}-CaM-dependent activation of the channels. The DN effect is predicted to result in a reduction in repolarization reserve. We confirmed these results using tandem SK2-CaM constructs to circumvent potential

caveats from endogenous CaM in HEK293 cells and/or changes in CaM expression from mutant constructs.

In contrast to the marked DN effects of CaM_{D96V} and CaM_{D130G}, CaM_{F90L} results in only modest reduction in $I_{K,Ca}$ suggesting a distinct mechanism by disrupting the interaction between apo-CaM and SK channel without the DN effects. Structural modeling and molecular dynamics simulations reveal the atomistic mechanisms in conformational changes caused by the phenylalanine to leucine mutation, which affect helix packing in the C-lobe, disrupting the interactions between apo-CaM with CaMBD of SK channels.

In **Fig. 5.1**, we show that CaM_{D96V} exhibits the most prominent inhibitory effect while CaM_{F90L} exerts only a mild inhibitory effect on apamin-sensitive current. Consistently, dialysis of mutant CaM_{D96V} proteins in hiPSC-CMs results in the most prominent knockdown of apamin-sensitive currents in hiPSC-CMs, compared to CaM_{F90L} (**Fig. 5.4**). As expected, the endogenous SK currents in hiPSC-CMs (**Fig. 5.4**) are much smaller than the overexpressed SK currents in HEK 293 cells (**Fig. 5.1**). Therefore, the two systems were used as complementary studies to evaluate the effects of CaM mutants on the SK currents.

There are six CaM alleles and a mutation in one allele is expected to have only a partial effect on the overall CaM pool within the cell. Therefore, other possible mechanisms may play a role including cell-specific differential expression of the different alleles.

Mechanisms of human calmodulinopathy

CaM serves as a Ca^{2+} sensor for many ion channels and transporters, and consequently, has been shown to play key roles in the regulation of cardiac function; mutations in CaM have been linked to LQTS, CPVT, and IVF [9-11, 72]. Studies on calmodulinopathy have provided evidence for

the critical roles of CaM in the functional regulation of $Ca_v1.2$, RyR2, $K_v7.1$, and SK channels, among others [9, 12, 13, 20, 22, 31, 72].

CaM_{D96V} and CaM_{D130G} occur in highly conserved aspartic acid residues responsible for chelating Ca^{2+} ions in the C-lobe [9]. Consequently, CaM_{D130G} has been shown to have markedly decreased Ca^{2+} binding affinity [13, 22]. In addition, CaM_{D130G} was reported to have a decreased interaction with RyR2, possibly through a DN effect. CaM_{D96V} was previously shown to exhibit an increased K_d for Ca^{2+} binding when compared with CaM_{WT}, although to a lesser extent than that seen in CaM_{D130G} [22]. LQTS mutants (D96V, D130G, and F142L) have been reported to exhibit reduced Ca^{2+} affinity compared to that of CaM_{WT} and CPVT (N54I, N98S) mutants [13]. In addition, the LQTS associated mutants have been shown to suppress Ca^{2+}-dependent inactivation (CDI) of L-type Ca^{2+} currents [14].

Potential roles of cardiac SK channels in calmodulinopathy

We have previously identified the expression of SK channels (SK1, SK2, and SK3) in the heart and demonstrated the critical roles of the channels in mediating action potential repolarization in human atrial myocytes [38]. SK2 channels physically coupled to α-actinin2, allowing a close association with LTCCs [38, 71]. The subcellular localization of SK channels in close proximity to LTCC and RyR2 provides immediate Ca^{2+} source [73], which, through binding of Ca^{2+} to CaM, triggers conformational changes to activate SK channels. SK channels may also play important roles on the feedback mechanism to regulate the activities of LTCCs and RyR2 to influence the local and global Ca^{2+} signaling.

The roles of SK channels in the heart have been extensively studied in the past decade [39]. Single nucleotide polymorphisms of *KCNN* genes encoding for SK channels have been shown to be linked human atrial fibrillation (AF) [74] and SK channels may represent a potential novel

therapeutic target against atrial arrhythmias [75]. Importantly, SK channels participate in the electrical remodeling in AF and heart failure. SK channels are significantly upregulated in AF animal models [76, 77] and failing ventricular myocytes [78, 79]. However, the mechanisms underlying SK channel remodeling in diseased heart remain unclear.

SK channels are unique because the channels are solely gated by intracellular Ca^{2+} through a highly conserved CaMBD. Our data demonstrated the functional effects, structural basis and molecular mechanisms of the disease-causing CaM mutants in the regulation of cardiac SK2 channels, highlighting the potential contribution of cardiac SK channels to human calmodulinopathy. LQTS-associated D96V, D130G, and F142L mutants of CaM have been reported to reduce the Ca^{2+} affinity in the C-lobe of CaM and result in a significant reduction in Ca^{2+}-dependent inactivation of LTCC causing the prolongation of QT intervals and early after depolarization [9]. Even though SK currents are more prominently expressed in atrial compared to ventricular myocytes [38, 39], SK currents are known to be upregulated in failing ventricular myocytes [78, 79] and during hypokalemia [80]. Recent studies have supported their critical roles in cardiac Purkinje cells [40], which are known to be the potential site of origin of cardiac arrhythmias, including patients with heritable arrhythmia syndrome [41, 42]. Moreover, SK channels play critical roles in the pacemaker activity of sinoatrial and atrioventricular nodes [43, 44]. Therefore, mutations in CaMs may result in a significant reduction in the key Ca^{2+}-dependent repolarization currents mediated by SK channels. Even though no SK channel variants have been reported to be associated with an inherited arrhythmia syndrome to date, there is a recent study that reports a rare variant, c.1509C>G (p.F503L), in one *KCNN2* allele in a patient who developed drug induced LQTS [81]. Indeed, this is a rapidly expanding area of research.

Additionally, we have previously shown that SK2 channels co-localized within microdomains of LTCC and RyR2, that serves as the Ca^{2+} source for the activation of SK channels [73]. Conversely, activation of SK2 channels provides a direct link between beat-to-beat changes in intracellular Ca^{2+} and membrane potentials and thus, may serve as the feedback mechanisms to regulate the activities of the LTCC and RyR2 channels. Functional effects of CaM mutations on SK channel activation may indirectly disrupt this possible feedback mechanism on LTCC and RyR2 channels.

Recent studies have evaluated the effects of arrhythmogenic CaM mutations on SK2 and SK3 channel function in HEK293 cells [31, 32]. They similarly observed effects independent of SK2 expression and trafficking, however our study provides new insights by taking advantage of computational analyses of phenylalanine mutations, F93L and F142L, and the context of native-like cells, through our use of hiPSC-CMs as a system. Although the strength of hiPSC-CMs lies in the study of protein mutations in native-like environments through patient-specific cells, our study was able to harness hiPSC-CMs to further understand WT and mutant CaM dynamics within a system that presumably has more cardiac-specific interacting partners for CaM than is found in HEK 293 cells.

The roles of phenylalanine in the C-lobe of CaM

Apo-CaM binding to the CaMBD of SK channels requires the C-lobe, while binding of Ca^{2+} to the N-lobe is involved in SK channel gating [70]. Several human CaM mutations affect the activation of SK channels [31]. However, the exact mechanisms among the different CaM mutations remain incompletely understood. Our study shows a significant reduction of cardiac SK currents

by CaM_{D96V} and CaM_{D130G}, not only in hetero-expression system but also in endogenous SK currents in hiPSC-CMs, consistent with DN effects on the channel function.

In contrast, phenylalanine mutations in CaM disrupt the interaction between apo-CaM and SK channel without the DN effects. *Rosetta* molecular modeling is used by taking advantage of the recently published cryo-EM structure of the SK4-apo-CaM complex [37]. We identify the interactions of three key phenylalanine residues (Phe^{90}, Phe^{93}, and Phe^{142}) within the C-lobe of apo-CaM with hydrophobic amino acids in the CaMBD within the C terminus of SK2 channel. Consistently, CaM_{F142L} shows less reduction in Ca^{2+} affinity compared to other LQTS mutations (D130G & D96V) [9]. In addition, previous studies have shown reduced binding affinity to RyR2 by CaM_{F90L}. Circular dichroism experiments in the same study suggest C-lobe destabilization and decreased Ca^{2+} binding affinity [21]. Our molecular modeling of the CaM_{F90L} mutant shows a significant deviation from CaM_{WT} in C-lobe structure in the Ca^{2+}-free state (**Fig. 5.6**). Taken together with biochemical and functional analyses, the results suggest that the Phe mutations primarily disrupt apo-CaM interactions with the SK2 CaMBD. Indeed, despite significant conformational changes, there was only modest inhibitory effects on apamin-sensitive currents (**Fig. 5.3**) consistent with a lack of DN effects; in contrast to CaM_{D96V} and CaM_{D130G} mutants. These critical insights into the distinct mechanisms whereby these CaM mutations exert their effects on Ca^{2+}-dependent ion channels and cardiac action potential repolarization help to pave the way for understanding the genotype-phenotype correlations of human calmodulinopathy.

Advancing the atomistic understanding of CaM and SK2 interaction by structural modeling and MD simulations

The structural modeling and MD simulations provide critical insights into the atomistic mechanisms of the CaM mutants in human calmodulinopathy. Our findings suggest that all three

Phe mutations in CaM result in similar conformational changes, including an increase in flexibility of the C-terminal end of helix 2, decrease in flexibility of the C-terminal end of helix 3, and a decrease in the flexibility of the Ca^{2+} binding site 4 (**Fig. 5.7**). The findings support our conclusion that the three Phe→Leu mutations exhibit a similar mechanism in altering the regulation of the hSK2 channel, likely through a reduction in the interaction between apo-CaM and CaMBD in SK2 channel.

Limitations and future directions

RMSD as a metric is circumstantial to derive conclusions on the thermodynamic stability of the WT and mutant CaMs. Nonetheless, we have provided additional analyses of RMSF in the current study. Future studies are needed to derive free-energy calculations of the mutations compared to the CaM_{WT}. The alteration in flexibility and the possible effects of the mutations on Ca^{2+} binding site 4 and their cooperativity with other Ca^{2+} binding sites require further studies as an underlying mechanism affecting hSK2 regulation. Our findings suggest that all three Phe→Leu mutations decrease affinity for hSK2. Future studies are needed to test the possible roles of the hydrogen bonds between side chain of Asn^{112} with the carboxyl oxygen of Ala^{89} residue in apo-CaM_{WT}, which is lost in all three Phe→Leu mutations based on MD simulations.

Additionally, studies evaluating the effects of CaM mutants in native cells would be ideal, however, the study of mutant proteins within endogenous cells is not without its difficulties. In order to circumvent these issues, the study of CaM mutants in cardiomyocyte-like cells may yet yield valuable information. Consequently, patient specific hiPSC-CMs may provide additional insights into the effects of CaM mutants on SK channels and action potential profiles. Finally, future studies using CRISPR/Cas9 gene editing would help to further elucidate the effects of CaM mutations on SK channel function.

Acknowledgments

This work is funded in part by American Heart Association (AHA) Beginning Grant-in-Aid 14BGIA18870087 and NIH R56 HL138392 (XDZ), NIH R01 HL085727, NIH R01 HL085844, and NIH R01 HL137228 (NC), VA Merit Review Grant I01 BX000576 and I01 CX001490 (NC), NIH R01 HL083374 (ALG), NIH R35 HL144980 (BCK), NIH R01 DC015135, NIH R01 DC015252, and NIH P01 AG051443 (EY). HAL received Predoctoral Fellowship from NIH/NHLBI Institutional Training Grant in Basic and Translational Cardiovascular Science (NIH T32 HL086350) and NIH F31 HL136120. PS received Postdoctoral Fellowship from California Institute for Regenerative Medicine (CIRM) Training Grant to UC Davis, NIH/NHLBI Institutional Training Grant in Basic and Translational Cardiovascular Science (NIH T32 HL086350), AHA Career Development Award and Harold S. Geneen Charitable Trust Award (PS). NC is the holder of the Roger Tatarian Endowed Professorship in Cardiovascular Medicine.

Author Contributions

H.A.L., W.W., and X.D.Z. performed the electrophysiological experiments, analyzed and interpreted the data. H.A.L., S.P., L.R. and C.R.S. performed the molecular cloning and biochemical experiments. R.L.W., D.M., P.T.N. and V.Y.Y performed the structural modeling and molecular dynamics simulations. H.A.L. performed immunofluorescence imaging. P.S. performed stem cell differentiation. H.A.L., X.D.Z., P.T.N., E.N.Y., V.Y.Y. and N.C. wrote the manuscript.

A.L.G. and B.C.K. provided critical reagents for the study. H.A.L., E.N.Y., X.D.Z. and N.C. conceived the project, designed the experiments, interpreted the data and wrote the manuscript.

Competing interests

None.

References

1. Crivici A and Ikura M. Molecular and structural basis of target recognition by calmodulin. *Annu Rev Biophys Biomol Struct*. 1995;24:85-116.

2. Chin D and Means AR. Calmodulin: a prototypical calcium sensor. *Trends Cell Biol*. 2000;10:322-8.

3. Babu YS, Sack JS, Greenhough TJ, Bugg CE, Means AR and Cook WJ. Three-dimensional structure of calmodulin. *Nature*. 1985;315:37-40.

4. Heidorn DB and Trewhella J. Comparison of the crystal and solution structures of calmodulin and troponin C. *Biochemistry*. 1988;27:909-15.

5. Klevit RE, Dalgarno DC, Levine BA and Williams RJ. 1H-NMR studies of calmodulin. The nature of the Ca2+-dependent conformational change. *Eur J Biochem*. 1984;139:109-14.

6. Watterson DM, Sharief F and Vanaman TC. The complete amino acid sequence of the Ca2+-dependent modulator protein (calmodulin) of bovine brain. *J Biol Chem*. 1980;255:962-75.

7. Thulin E, Andersson A, Drakenberg T, Forsen S and Vogel HJ. Metal ion and drug binding to proteolytic fragments of calmodulin: proteolytic, cadmium-113, and proton nuclear magnetic resonance studies. *Biochemistry*. 1984;23:1862-70.

8. Saimi Y and Kung C. Calmodulin as an ion channel subunit. *Annu Rev Physiol*. 2002;64:289-311.

9. Crotti L, Johnson CN, Graf E, De Ferrari GM, Cuneo BF, Ovadia M, Papagiannis J, Feldkamp MD, Rathi SG, Kunic JD, Pedrazzini M, Wieland T, Lichtner P, Beckmann BM, Clark T, Shaffer C, Benson DW, Kaab S, Meitinger T, Strom TM, Chazin WJ, Schwartz PJ and George AL, Jr. Calmodulin mutations associated with recurrent cardiac arrest in infants. *Circulation*. 2013;127:1009-17.

10. Boczek NJ, Gomez-Hurtado N, Ye D, Calvert ML, Tester DJ, Kryshtal D, Hwang HS, Johnson CN, Chazin WJ, Loporcaro CG, Shah M, Papez AL, Lau YR, Kanter R, Knollmann BC and Ackerman MJ. Spectrum and Prevalence of CALM1-, CALM2-, and CALM3-Encoded Calmodulin Variants in Long QT Syndrome and Functional Characterization of a Novel Long QT Syndrome-Associated Calmodulin Missense Variant, E141G. *Circulation Cardiovascular genetics*. 2016;9:136-146.

11. Reed GJ, Boczek NJ, Etheridge SP and Ackerman MJ. CALM3 mutation associated with long QT syndrome. *Heart rhythm : the official journal of the Heart Rhythm Society*. 2015;12:419-22.

12. Nyegaard M, Overgaard MT, Sondergaard MT, Vranas M, Behr ER, Hildebrandt LL, Lund J, Hedley PL, Camm AJ, Wettrell G, Fosdal I, Christiansen M and Borglum AD. Mutations in calmodulin cause ventricular tachycardia and sudden cardiac death. *American journal of human genetics*. 2012;91:703-12.

13. Hwang HS, Nitu FR, Yang Y, Walweel K, Pereira L, Johnson CN, Faggioni M, Chazin WJ, Laver D, George AL, Jr., Cornea RL, Bers DM and Knollmann BC. Divergent regulation of ryanodine receptor 2 calcium release channels by arrhythmogenic human calmodulin missense mutants. *Circulation research*. 2014;114:1114-24.

14. Limpitikul WB, Dick IE, Joshi-Mukherjee R, Overgaard MT, George AL, Jr. and Yue DT. Calmodulin mutations associated with long QT syndrome prevent inactivation of cardiac L-type Ca^{2+} currents and promote proarrhythmic behavior in ventricular myocytes. *J Mol Cell Cardiol*. 2014;74:115-24.

15. Jensen HH, Brohus M, Nyegaard M and Overgaard MT. Human Calmodulin Mutations. *Front Mol Neurosci*. 2018;11:396.

16. Peterson BZ, DeMaria CD, Adelman JP and Yue DT. Calmodulin is the Ca^{2+} sensor for Ca^{2+} -dependent inactivation of L-type calcium channels. *Neuron*. 1999;22:549-58.

17. Zuhlke RD, Pitt GS, Deisseroth K, Tsien RW and Reuter H. Calmodulin supports both inactivation and facilitation of L-type calcium channels. *Nature*. 1999;399:159-62.

18. Zuhlke RD, Pitt GS, Tsien RW and Reuter H. Ca^{2+}-sensitive inactivation and facilitation of L-type Ca^{2+} channels both depend on specific amino acid residues in a consensus calmodulin-binding motif in the α1C subunit. *J Biol Chem*. 2000;275:21121-9.

19. Meissner G. Ryanodine activation and inhibition of the Ca^{2+} release channel of sarcoplasmic reticulum. *J Biol Chem*. 1986;261:6300-6.

20. Fukuda M, Yamamoto T, Nishimura S, Kato T, Murakami W, Hino A, Ono M, Tateishi H, Oda T, Okuda S, Kobayashi S, Koseki N, Kyushiki H and Yano M. Enhanced binding of calmodulin to RyR2 corrects arrhythmogenic channel disorder in CPVT-associated myocytes. *Biochemical and biophysical research communications*. 2014;448:1-7.

21. Nomikos M, Thanassoulas A, Beck K, Vassilakopoulou V, Hu H, Calver BL, Theodoridou M, Kashir J, Blayney L, Livaniou E, Rizkallah P, Nounesis G and Lai FA. Altered RyR2 regulation by the calmodulin F90L mutation associated with idiopathic ventricular fibrillation and early sudden cardiac death. *FEBS Lett*. 2014;588:2898-902.

22. Vassilakopoulou V, Calver BL, Thanassoulas A, Beck K, Hu H, Buntwal L, Smith A, Theodoridou M, Kashir J, Blayney L, Livaniou E, Nounesis G, Lai FA and Nomikos M. Distinctive malfunctions of calmodulin mutations associated with heart RyR2-mediated arrhythmic disease. *Biochim Biophys Acta*. 2015;1850:2168-76.

23. Shamgar L, Ma L, Schmitt N, Haitin Y, Peretz A, Wiener R, Hirsch J, Pongs O and Attali B. Calmodulin is essential for cardiac I_{KS} channel gating and assembly: impaired function in long-QT mutations. *Circulation research*. 2006;98:1055-63.

24. Sun J and MacKinnon R. Cryo-EM Structure of a KCNQ1/CaM Complex Reveals Insights into Congenital Long QT Syndrome. *Cell*. 2017;169:1042-1050 e9.

25. Sachyani D, Dvir M, Strulovich R, Tria G, Tobelaim W, Peretz A, Pongs O, Svergun D, Attali B and Hirsch JA. Structural basis of a $K_V7.1$ potassium channel gating module: studies of the intracellular c-terminal domain in complex with calmodulin. *Structure*. 2014;22:1582-94.

26. Halling DB, Aracena-Parks P and Hamilton SL. Regulation of voltage-gated Ca^{2+} channels by calmodulin. *Sci STKE*. 2006;2006:er1.

27. Liang H, DeMaria CD, Erickson MG, Mori MX, Alseikhan BA and Yue DT. Unified mechanisms of Ca2+ regulation across the Ca^{2+} channel family. *Neuron*. 2003;39:951-60.

28. Minor DL, Jr. and Findeisen F. Progress in the structural understanding of voltage-gated calcium channel (CaV) function and modulation. *Channels (Austin)*. 2010;4:459-74.

29. Xia X-M, Fakler B, Rivard A, Wayman G, Johnson-Pais T, Keen J, Ishii T, Hirschberg B, Bond C and Lutsenko S. Mechanism of calcium gating in small-conductance calcium-activated potassium channels. *Nature*. 1998;395:503-507.

30. Schumacher MA, Rivard AF, Bachinger HP and Adelman JP. Structure of the gating domain of a Ca2+-activated K+ channel complexed with Ca2+/calmodulin. *Nature*. 2001;410:1120-4.

31. Yu CC, Ko JS, Ai T, Tsai WC, Chen Z, Rubart M, Vatta M, Everett THt, George AL, Jr. and Chen PS. Arrhythmogenic calmodulin mutations impede activation of small-conductance calcium-activated potassium current. *Heart rhythm : the official journal of the Heart Rhythm Society*. 2016;13:1716-23.

32. Saljic A, Muthukumarasamy KM, la Cour JM, Boddum K, Grunnet M, Berchtold MW and Jespersen T. Impact of arrhythmogenic calmodulin variants on small conductance Ca^{2+}-activated K^+ (SK3) channels. *Physiol Rep*. 2019;7:e14210.

33. Kohler M, Hirschberg B, Bond CT, Kinzie JM, Marrion NV, Maylie J and Adelman JP. Small-conductance, calcium-activated potassium channels from mammalian brain. *Science*. 1996;273:1709-14.

34. Ishii TM, Silvia C, Hirschberg B, Bond CT, Adelman JP and Maylie J. A human intermediate conductance calcium-activated potassium channel. *Proceedings of the National Academy of Sciences of the United States of America*. 1997;94:11651-6.

35. Joiner WJ, Wang LY, Tang MD and Kaczmarek LK. hSK4, a member of a novel subfamily of calcium-activated potassium channels. *Proceedings of the National Academy of Sciences of the United States of America*. 1997;94:11013-8.

36. Vergara C, Latorre R, Marrion NV and Adelman JP. Calcium-activated potassium channels. *Curr Opin Neurobiol*. 1998;8:321-9.

37. Lee CH and MacKinnon R. Activation mechanism of a human SK-calmodulin channel complex elucidated by cryo-EM structures. *Science*. 2018;360:508-513.

38. Xu Y, Tuteja D, Zhang Z, Xu D, Zhang Y, Rodriguez J, Nie L, Tuxson HR, Young JN, Glatter KA, Vazquez AE, Yamoah EN and Chiamvimonvat N. Molecular identification and functional roles of a Ca^{2+}-activated K^+ channel in human and mouse hearts. *J Biol Chem*. 2003;278:49085-94.

39. Zhang XD, Lieu DK and Chiamvimonvat N. Small-conductance Ca^{2+}-activated K^+ channels and cardiac arrhythmias. *Heart Rhythm*. 2015;12:1845-51.

40. Reher TA, Wang Z, Hsueh CH, Chang PC, Pan Z, Kumar M, Patel J, Tan J, Shen C, Chen Z, Fishbein MC, Rubart M, Boyden P and Chen PS. Small-Conductance Calcium-Activated Potassium Current in Normal Rabbit Cardiac Purkinje Cells. *J Am Heart Assoc*. 2017;6.

41. Wilde AAM, Garan H and Boyden PA. Role of the Purkinje system in heritable arrhythmias. *Heart Rhythm*. 2019;16:1121-1126.

42. Haissaguerre M, Shah DC, Jais P, Shoda M, Kautzner J, Arentz T, Kalushe D, Kadish A, Griffith M, Gaita F, Yamane T, Garrigue S, Hocini M and Clementy J. Role of Purkinje conducting system in triggering of idiopathic ventricular fibrillation. *Lancet*. 2002;359:677-8.

43. Zhang Q, Timofeyev V, Lu L, Li N, Singapuri A, Long MK, Bond CT, Adelman JP and Chiamvimonvat N. Functional roles of a Ca^{2+}-activated K^+ channel in atrioventricular nodes. *Circulation research*. 2008;102:465-71.

44. Torrente AG, Zhang R, Wang H, Zaini A, Kim B, Yue X, Philipson KD and Goldhaber JI. Contribution of small conductance K^+ channels to sinoatrial node pacemaker activity: insights from atrial-specific Na^+ /Ca^{2+} exchange knockout mice. *J Physiol*. 2017;595:3847-3865.

45. Cukovic D, Lu GW, Wible B, Steele DF and Fedida D. A discrete amino terminal domain of Kv1.5 and Kv1.4 potassium channels interacts with the spectrin repeats of alpha-actinin-2. *FEBS Lett*. 2001;498:87-92.

46. Mori MX, Erickson MG and Yue DT. Functional stoichiometry and local enrichment of calmodulin interacting with Ca2+ channels. *Science*. 2004;304:432-5.

47. Kim HJ, Lv P, Sihn CR and Yamoah EN. Cellular and molecular mechanisms of autosomal dominant form of progressive hearing loss, *DFNA2*. *J Biol Chem*. 2011;286:1517-27.

48. Rafizadeh S, Zhang Z, Woltz RL, Kim HJ, Myers RE, Lu L, Tuteja D, Singapuri A, Bigdeli AA, Harchache SB, Knowlton AA, Yarov-Yarovoy V, Yamoah EN and Chiamvimonvat N. Functional interaction with filamin A and intracellular Ca^{2+} enhance the surface membrane expression of a small-conductance Ca^{2+}-activated K^{+} (SK2) channel. *Proceedings of the National Academy of Sciences of the United States of America*. 2014;111:9989-94.

49. Yamoah MA, Moshref M, Sharma J, Chen WC, Ledford HA, Lee JH, Chavez KS, Wang W, Lopez JE, Lieu DK, Sirish P and Zhang XD. Highly efficient transfection of human induced pluripotent stem cells using magnetic nanoparticles. *Int J Nanomedicine*. 2018;13:6073-6078.

50. Sirish P, Li N, Timofeyev V, Zhang XD, Wang L, Yang J, Lee KS, Bettaieb A, Ma SM, Lee JH, Su D, Lau VC, Myers RE, Lieu DK, Lopez JE, Young JN, Yamoah EN, Haj F, Ripplinger CM, Hammock BD and Chiamvimonvat N. Molecular Mechanisms and New Treatment Paradigm for Atrial Fibrillation. *Circ Arrhythm Electrophysiol*. 2016;9:pii: e003721.

51. Rohl CA, Strauss CE, Misura KM and Baker D. Protein structure prediction using Rosetta. *Methods Enzymol*. 2004;383:66-93.

52. Bonneau R, Strauss CE and Baker D. Improving the performance of Rosetta using multiple sequence alignment information and global measures of hydrophobic core formation. *Proteins*. 2001;43:1-11.

53. Wang C, Bradley P and Baker D. Protein-protein docking with backbone flexibility. *Journal of molecular biology*. 2007;373:503-19.

54. Yarov-Yarovoy V, Schonbrun J and Baker D. Multipass membrane protein structure prediction using Rosetta. *Proteins*. 2006;62:1010-1025.

55. Yarov-Yarovoy V, Decaen PG, Westenbroek RE, Pan CY, Scheuer T, Baker D and Catterall WA. Structural basis for gating charge movement in the voltage sensor of a sodium channel. *Proceedings of the National Academy of Sciences of the United States of America*. 2012;109:E93-E102.

56. Bender BJ, Cisneros A, 3rd, Duran AM, Finn JA, Fu D, Lokits AD, Mueller BK, Sangha AK, Sauer MF, Sevy AM, Sliwoski G, Sheehan JH, DiMaio F, Meiler J and Moretti R. Protocols for Molecular Modeling with Rosetta3 and RosettaScripts. *Biochemistry*. 2016;55:4748-63.

57. Alford RF, Leaver-Fay A, Jeliazkov JR, O'Meara MJ, DiMaio FP, Park H, Shapovalov MV, Renfrew PD, Mulligan VK, Kappel K, Labonte JW, Pacella MS, Bonneau R, Bradley P, Dunbrack RL, Jr., Das R, Baker D, Kuhlman B, Kortemme T and Gray JJ. The Rosetta All-Atom Energy Function for Macromolecular Modeling and Design. *J Chem Theory Comput*. 2017;13:3031-3048.

58. Pettersen EF, Goddard TD, Huang CC, Couch GS, Greenblatt DM, Meng EC and Ferrin TE. UCSF Chimera--a visualization system for exploratory research and analysis. *J Comput Chem*. 2004;25:1605-12.

59. Jo S, Kim T, Iyer VG and Im W. CHARMM-GUI: a web-based graphical user interface for CHARMM. *J Comput Chem*. 2008;29:1859-65.

60. Brooks BR, Brooks CL, 3rd, Mackerell AD, Jr., Nilsson L, Petrella RJ, Roux B, Won Y, Archontis G, Bartels C, Boresch S, Caflisch A, Caves L, Cui Q, Dinner AR, Feig M, Fischer S, Gao J, Hodoscek M, Im W, Kuczera K, Lazaridis T, Ma J, Ovchinnikov V, Paci E, Pastor RW, Post CB, Pu JZ, Schaefer M, Tidor B, Venable RM, Woodcock HL, Wu X, Yang W, York DM and Karplus M. CHARMM: the biomolecular simulation program. *J Comput Chem*. 2009;30:1545-614.

61. Lee J, Cheng X, Swails JM, Yeom MS, Eastman PK, Lemkul JA, Wei S, Buckner J, Jeong JC, Qi Y, Jo S, Pande VS, Case DA, Brooks CL, 3rd, MacKerell AD, Jr., Klauda JB and Im W. CHARMM-GUI Input Generator for NAMD, GROMACS, AMBER, OpenMM, and CHARMM/OpenMM Simulations Using the CHARMM36 Additive Force Field. *J Chem Theory Comput*. 2016;12:405-13.

62. Phillips JC, Braun R, Wang W, Gumbart J, Tajkhorshid E, Villa E, Chipot C, Skeel RD, Kale L and Schulten K. Scalable molecular dynamics with NAMD. *J Comput Chem*. 2005;26:1781-802.

63. Vanommeslaeghe K, Hatcher E, Acharya C, Kundu S, Zhong S, Shim J, Darian E, Guvench O, Lopes P, Vorobyov I and Mackerell AD, Jr. CHARMM general force field: A force field for drug-like molecules compatible with the CHARMM all-atom additive biological force fields. *J Comput Chem*. 2010;31:671-90.

64. Huang J, Rauscher S, Nawrocki G, Ran T, Feig M, de Groot BL, Grubmuller H and MacKerell AD, Jr. CHARMM36m: an improved force field for folded and intrinsically disordered proteins. *Nat Methods*. 2017;14:71-73.

65. Darden T, York D and Pedersen L. Particle mesh Ewald: An N ·log(N) method for Ewald sums in large systems. *J Chem Phys*. 1993;98:10089-10092.

66. Humphrey W, Dalke A and Schulten K. VMD: visual molecular dynamics. *J Mol Graph*. 1996;14:33-8, 27-8.

67. Wang K, Holt C, Lu J, Brohus M, Larsen KT, Overgaard MT, Wimmer R and Van Petegem F. Arrhythmia mutations in calmodulin cause conformational changes that affect interactions with the cardiac voltage-gated calcium channel. *Proceedings of the National Academy of Sciences of the United States of America*. 2018;115:E10556-E10565.

68. Lu L, Timofeyev V, Li N, Rafizadeh S, Singapuri A, Harris TR and Chiamvimonvat N. Alpha-actinin2 cytoskeletal protein is required for the functional membrane localization of a

Ca2+-activated K+ channel (SK2 channel). *Proceedings of the National Academy of Sciences of the United States of America*. 2009;106:18402-7.

69. Zhang Z, Ledford HA, Park S, Wang W, Rafizadeh S, Kim HJ, Xu W, Lu L, Lau VC, Knowlton AA, Zhang X-D, Yamoah EN and Chiamvimonvat N. Distinct subcellular mechanisms for the enhancement of the surface membrane expression of SK2 channel by its interacting proteins, α-actinin2 and filamin A. *The Journal of Physiology*. 2017;595:2271-2284.

70. Keen JE, Khawaled R, Farrens DL, Neelands T, Rivard A, Bond CT, Janowsky A, Fakler B, Adelman JP and Maylie J. Domains responsible for constitutive and Ca^{2+}-dependent interactions between calmodulin and small conductance Ca^{2+}-activated potassium channels. *The Journal of neuroscience : the official journal of the Society for Neuroscience*. 1999;19:8830-8.

71. Lu L, Zhang Q, Timofeyev V, Zhang Z, Young JN, Shin HS, Knowlton AA and Chiamvimonvat N. Molecular coupling of a Ca2+-activated K+ channel to L-type Ca2+ channels via alpha-actinin2. *Circulation research*. 2007;100:112-20.

72. George AL. Calmodulinopathy: A genetic trilogy. *Heart rhythm : the official journal of the Heart Rhythm Society*. 2015;12:423-424.

73. Zhang XD, Coulibaly ZA, Chen WC, Ledford HA, Lee JH, Sirish P, Dai G, Jian Z, Chuang F, Brust-Mascher I, Yamoah EN, Chen-Izu Y, Izu LT and Chiamvimonvat N. Coupling of SK channels, L-type Ca^{2+} channels, and ryanodine receptors in cardiomyocytes. *Sci Rep*. 2018;8:4670.

74. Roselli C, Chaffin MD, Weng LC, Aeschbacher S, Ahlberg G, Albert CM, Almgren P, Alonso A, Anderson CD, Aragam KG, Arking DE, Barnard J, Bartz TM, Benjamin EJ, Bihlmeyer NA, Bis JC, Bloom HL, Boerwinkle E, Bottinger EB, Brody JA, Calkins H, Campbell A, Cappola TP, Carlquist J, Chasman DI, Chen LY, Chen YI, Choi EK, Choi SH, Christophersen IE, Chung MK, Cole JW, Conen D, Cook J, Crijns HJ, Cutler MJ, Damrauer SM, Daniels BR, Darbar D, Delgado G, Denny JC, Dichgans M, Dorr M, Dudink EA, Dudley SC, Esa N, Esko T, Eskola M, Fatkin D, Felix SB, Ford I, Franco OH, Geelhoed B, Grewal RP, Gudnason V, Guo X, Gupta N, Gustafsson S, Gutmann R, Hamsten A, Harris TB, Hayward C, Heckbert SR, Hernesniemi J, Hocking LJ, Hofman A, Horimoto A, Huang J, Huang PL, Huffman J, Ingelsson E, Ipek EG, Ito K, Jimenez-Conde J, Johnson R, Jukema JW, Kaab S, Kahonen M, Kamatani Y, Kane JP, Kastrati A, Kathiresan S, Katschnig-Winter P, Kavousi M, Kessler T, Kietselaer BL, Kirchhof P, Kleber ME, Knight S, Krieger JE, Kubo M, Launer LJ, Laurikka J, Lehtimaki T, Leineweber K, Lemaitre RN, Li M, Lim HE, Lin HJ, Lin H, Lind L, Lindgren CM, Lokki ML, London B, Loos RJF, Low SK, Lu Y, Lyytikainen LP, Macfarlane PW, Magnusson PK, Mahajan A, Malik R, Mansur AJ, Marcus GM, Margolin L, Margulies KB, Marz W, McManus DD, Melander O, Mohanty S, Montgomery JA, Morley MP, Morris AP, Muller-Nurasyid M, Natale A, Nazarian S, Neumann B, Newton-Cheh C, Niemeijer MN, Nikus K, Nilsson P, Noordam R, Oellers H, Olesen MS, Orho-Melander M, Padmanabhan S, Pak HN, Pare G, Pedersen NL, Pera J, Pereira A, Porteous D, Psaty BM, Pulit SL, Pullinger CR, Rader DJ, Refsgaard L, Ribases M, Ridker PM, Rienstra M, Risch L, Roden DM, Rosand J, Rosenberg MA, Rost N, Rotter JI, Saba S, Sandhu RK, Schnabel RB, Schramm K, Schunkert H, Schurman

C, Scott SA, Seppala I, Shaffer C, Shah S, Shalaby AA, Shim J, Shoemaker MB, Siland JE, Sinisalo J, Sinner MF, Slowik A, Smith AV, Smith BH, Smith JG, Smith JD, Smith NL, Soliman EZ, Sotoodehnia N, Stricker BH, Sun A, Sun H, Svendsen JH, Tanaka T, Tanriverdi K, Taylor KD, Teder-Laving M, Teumer A, Theriault S, Trompet S, Tucker NR, Tveit A, Uitterlinden AG, Van Der Harst P, Van Gelder IC, Van Wagoner DR, Verweij N, Vlachopoulou E, Volker U, Wang B, Weeke PE, Weijs B, Weiss R, Weiss S, Wells QS, Wiggins KL, Wong JA, Woo D, Worrall BB, Yang PS, Yao J, Yoneda ZT, Zeller T, Zeng L, Lubitz SA, Lunetta KL and Ellinor PT. Multi-ethnic genome-wide association study for atrial fibrillation. *Nat Genet*. 2018;50:1225-1233.

75. Diness JG, Bentzen BH, Sorensen US and Grunnet M. Role of Calcium-activated Potassium Channels in Atrial Fibrillation Pathophysiology and Therapy. *Journal of cardiovascular pharmacology*. 2015;66:441-8.

76. Qi XY, Diness JG, Brundel BJ, Zhou XB, Naud P, Wu CT, Huang H, Harada M, Aflaki M, Dobrev D, Grunnet M and Nattel S. Role of small-conductance calcium-activated potassium channels in atrial electrophysiology and fibrillation in the dog. *Circulation*. 2014;129:430-40.

77. Ozgen N, Dun W, Sosunov EA, Anyukhovsky EP, Hirose M, Duffy HS, Boyden PA and Rosen MR. Early electrical remodeling in rabbit pulmonary vein results from trafficking of intracellular SK2 channels to membrane sites. *Cardiovasc Res*. 2007;75:758-69.

78. Chua SK, Chang PC, Maruyama M, Turker I, Shinohara T, Shen MJ, Chen Z, Shen C, Rubart-von der Lohe M, Lopshire JC, Ogawa M, Weiss JN, Lin SF, Ai T and Chen PS. Small-conductance calcium-activated potassium channel and recurrent ventricular fibrillation in failing rabbit ventricles. *Circulation research*. 2011;108:971-9.

79. Chang PC, Turker I, Lopshire JC, Masroor S, Nguyen BL, Tao W, Rubart M, Chen PS, Chen Z and Ai T. Heterogeneous upregulation of apamin-sensitive potassium currents in failing human ventricles. *J Am Heart Assoc*. 2013;2:e004713.

80. Chan YH, Tsai WC, Ko JS, Yin D, Chang PC, Rubart M, Weiss JN, Everett THt, Lin SF and Chen PS. Small-Conductance Calcium-Activated Potassium Current Is Activated During Hypokalemia and Masks Short-Term Cardiac Memory Induced by Ventricular Pacing. *Circulation*. 2015;132:1377-86.

81. Ko JS, Guo S, Hassel J, Celestino-Soper P, Lynnes TC, Tisdale JE, Zheng JJ, Taylor SE, Foroud T, Murray MD, Kovacs RJ, Li X, Lin SF, Chen Z, Vatta M, Chen PS and Rubart M. Ondansetron blocks wild-type and p.F503L variant small-conductance Ca^{2+}-activated K^{+} channels. *Am J Physiol Heart Circ Physiol*. 2018;315:H375-H388.

Figure 5.1

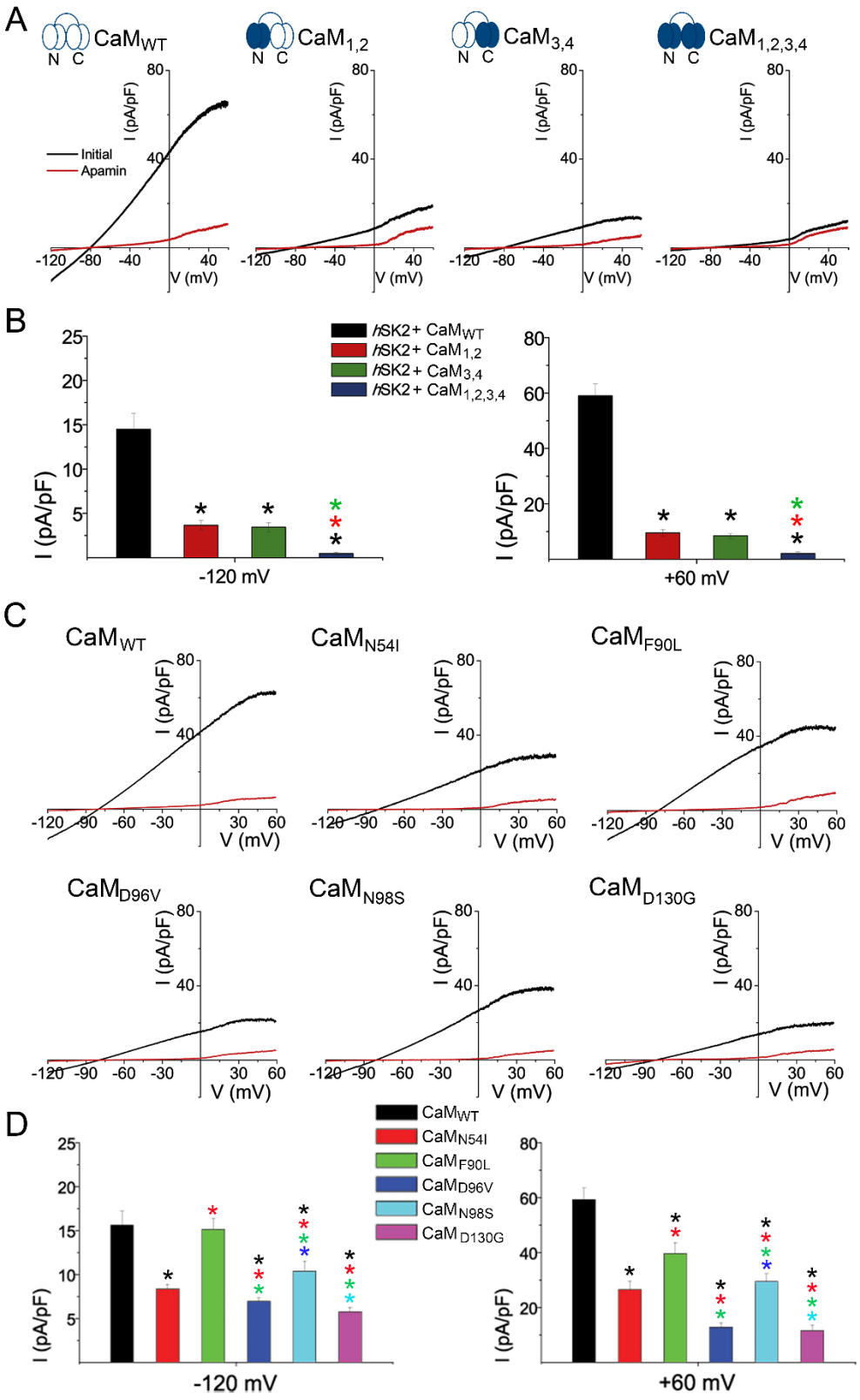
A
CaMWT
CaM1,2
CaM3,4
CaM1,2,3,4
N C
I (pA/pF)
V (mV)
Initial
Apamin
B
hSK2+ CaMWT
hSK2+ CaM1,2
hSK2+ CaM3,4
hSK2+ CaM1,2,3,4
-120 mV
+60 mV
C
CaMWT
CaMN54I
CaMF90L
CaMD96V
CaMN98S
CaMD130G
D
CaMWT
CaMN54I
CaMF90L
CaMD96V
CaMN98S
CaMD130G
-120 mV
+60 mV

Figure 5.1. Mutations in N-Lobe and C-lobe of CaM affect the currents of human SK channels (*h*SK2) expressed in HEK 293 cells. **A.** *h*SK2 channels were co-expressed with CaM_{WT} or mutant CaMs ($CaM_{1,2}$, $CaM_{3,4}$, or $CaM_{1,2,3,4}$). **B.** Summary data at +60 and -120 mV indicating significant reduction of the SK currents by mutant CaMs (n=12 cells, *p <0.05). **C.** *h*SK2 channels were co-expressed with CaM_{WT} (black bars), CaM_{N54I} (red bars), CaM_{F90L} (green bars), CaM_{D96V} (blue bars), CaM_{N98S} (cyan bars), and CaM_{D130G} (magenta bars). Current was recorded before (black trace) and after (red trace) application of apamin (10 nM). **D.** Summary data at -120 mV and +60 mV (n=10-13 cells, *P <0.05). For panels B and D, the colors of the stars (*) denote comparisons with the corresponding bar graphs of the same colors, using one-way analysis of variance combined with Tukey's test (At -120 mV, P=0.00001 for all pairwise comparisons except P=0.04 for CaM_{N54I} *vs* CaM_{D96V}, and P=*NS* for CaM_{D96V} *vs* CaM_{D130G}, and CaM_{WT} *vs* CaM_{F90L}. At +60 mV, P=0.00001 for all pairwise comparisons except P=*NS* for CaM_{D96V} *vs* CaM_{D130G}).

Figure 5.2

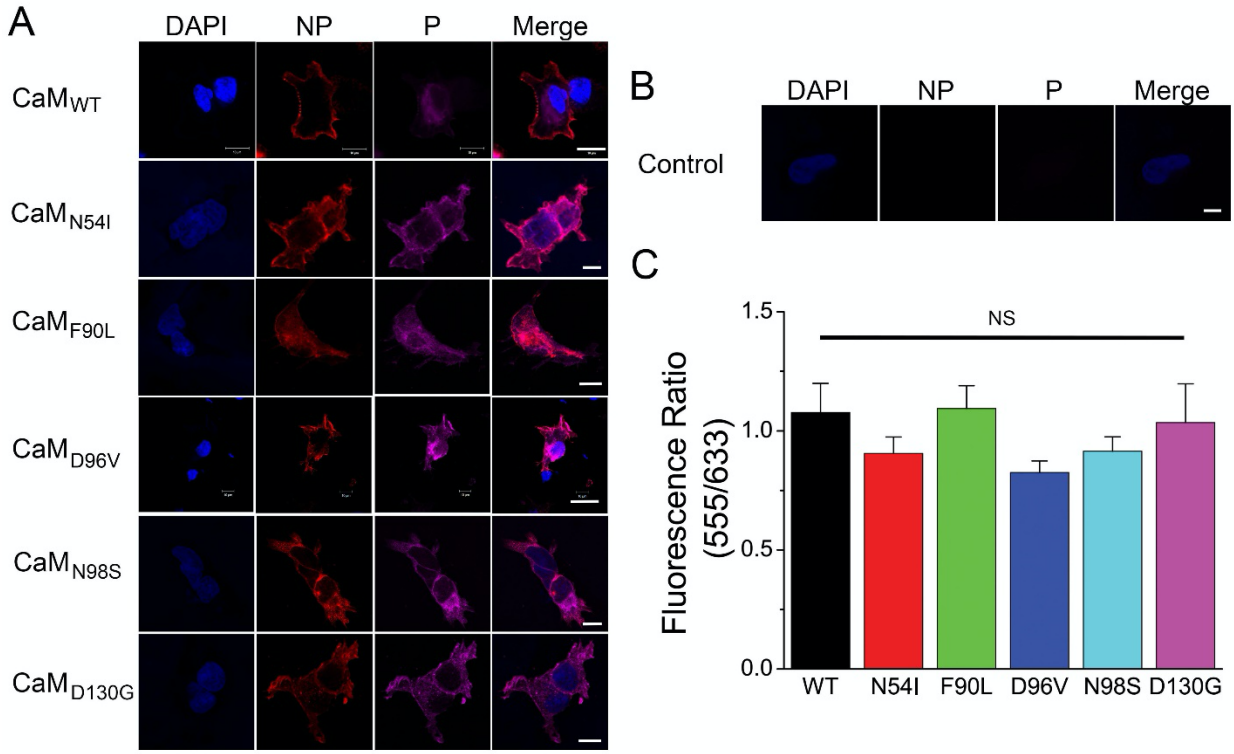

Figure 5.2. Trafficking of hSK2 channels after co-expression with CaM$_{WT}$ or mutant CaMs

A. HEK 293 cells expressing SK2 fusion protein with HA tag co-expressed with CaM$_{WT}$ or mutant CaMs (N54I, F90L, D96V, N98S, and D130G) using non-permeabilized (NP) and permeabilized (P) conditions. **B.** Control represents incubation with secondary antibody alone. Scale bars are 10 μm. **C.** Summary data showing fluorescence intensity under NP/P conditions (555/633 fluorescent intensity). Data shown represent mean ± s.e.m. Statistical analyses were performed using one way analysis of variance combined with Tukey's test. n = 15-20 cells, *P=NS* (not significant).

Figure 5.3

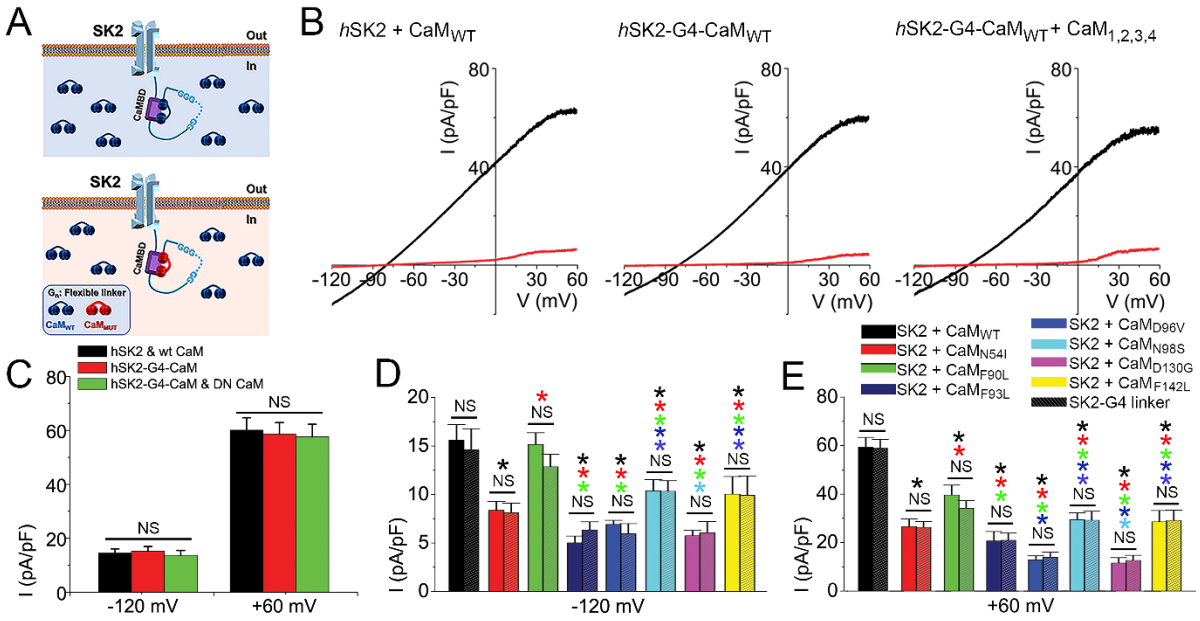

Figure 5.3. hSK2-CaM fusion proteins have similar function as that of co-expressed hSK2& CaM channels. A. Diagram illustrating experimental paradigms using SK2 fusion proteins with flexible glycine linker (G_n linker) fused to CaM_{WT} (upper panel) compared to mutant CaMs (lower panel). **B.** Current recordings before (black trace) and after (red trace) apamin application (10 nM) for *h*SK2 expressed with CaM_{WT} *vs*. *h*SK2-G4-CaM_{WT} *vs*. SK2-G4-CaM_{WT} expressed with DN $CaM_{1,2,3,4}$. **C.** Summary data at -120 mV and +60 mV. **D, E.** Summary data for apamin-sensitive current density in HEK 293 cells co-expressing *h*SK2 with CaM_{WT} or mutant CaM constructs (left bars) compared to SK2-G4-CaM_{WT} or SK2-G4-CaM_{MUT} (hashed bars on the right) where CaM_{MUT} refer to CaM_{N54I} (red bars), CaM_{F90L} (green bars), CaM_{F93L} (purple bars), CaM_{D96V} (blue bars), CaM_{N98S} (cyan bars), CaM_{D130G} (magenta bars), and CaM_{F142L} (yellow bars) at -120 mV (panel **D**) and +60 mV (panel **E**, n = 10-13 cells). Data represent mean ± s.e.m. Statistical analysis was performed using 2-way analysis of variance combined with Tukey's test. The colors of the stars

(*) denote comparisons with the corresponding bar graphs of the same colors. *P<0.05. At -120 mV, P=0.00001 for all pairwise comparisons except P=0.04 for CaM_{N54I} *vs* CaM_{F93L} and CaM_{N54I} *vs* CaM_{D96V}, and P=*NS* for CaM_{WT} *vs* CaM_{F90L}, CaM_{F93L} *vs* CaM_{D96V}, CaM_{F93L} *vs* CaM_{D130G}, CaM_{D96V} *vs* CaM_{D130G}, and CaM_{N98S} *vs.* CaM_{F142L}. At +60 mV, P=0.00001 for all pairwise comparisons except P=*NS* for CaM_{D96V} *vs* CaM_{D130G}, and CaM_{N98S} *vs.* CaM_{F142L}. There were no significant differences between *h*SK2 co-expression with CaM compared to *h*SK2-G4-CaM for WT or mutant CaMs (P=NS).

Figure 5.4

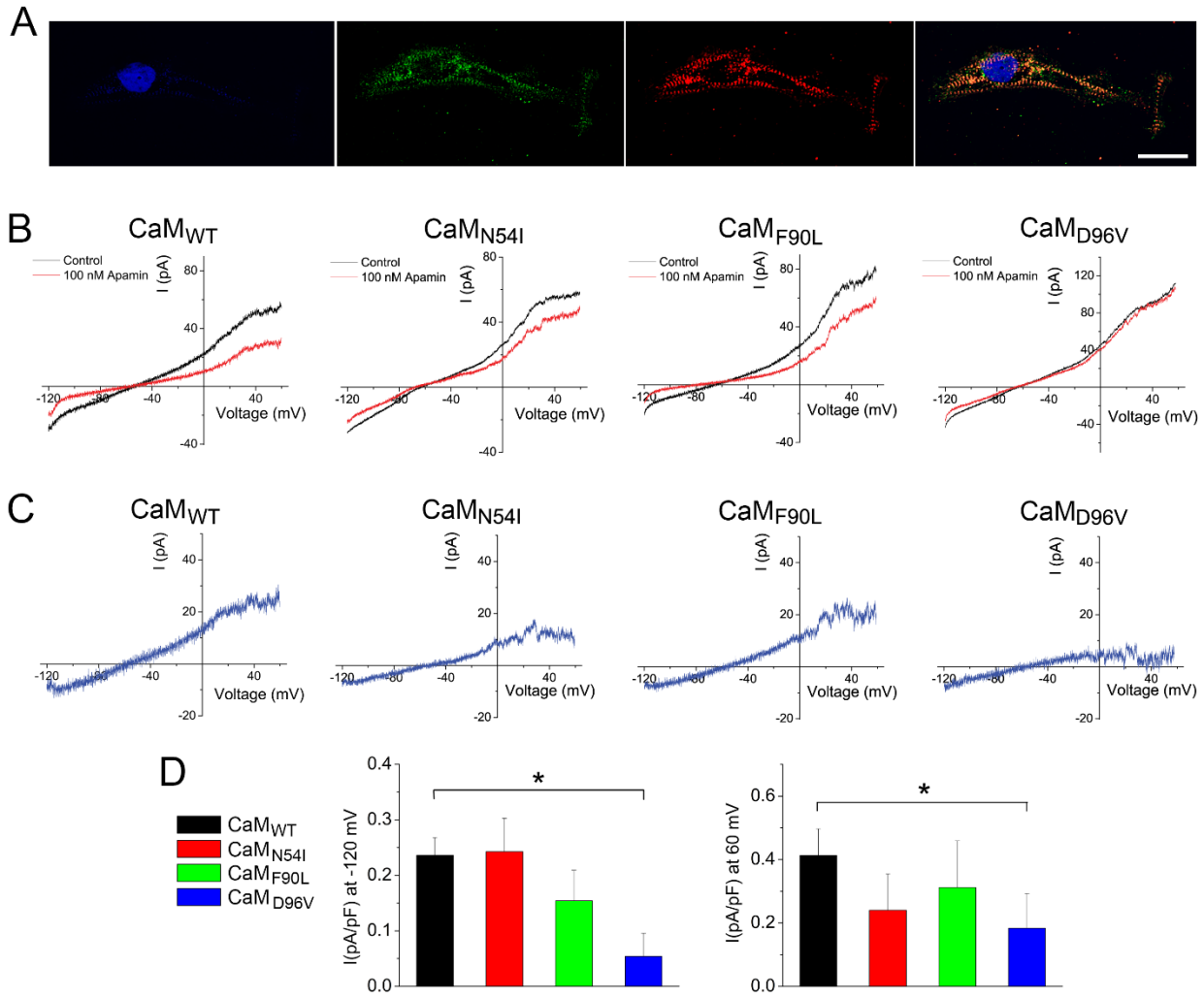

Figure 5.4. Regulation of endogenous SK currents in hiPSC-CMs by intracellular CaM peptides. A. hiPSC-CMs expressing SK2 channels (green) and □-actinin2 (red). DAPI stain is shown in blue. **B.** Effects of mutant CaM peptides (CaM_{N54I}, CaM_{F90L}, and CaM_{D96V}) compared to CaM_{WT} peptide on apamin-sensitive SK currents in hiPSC-CMs. The current was recorded before (black trace) and after (red trace) apamin application (10 nM). **C.** Subtracted apamin-sensitive SK currents in the presence of CaM_{WT} and mutant CaM peptides. **D.** Comparisons of the apamin-sensitive current densities at -120 mV and +60 mV (n = 8-10 cells). Data represent mean ± s.e.m.

Statistical analyses were performed using one-way analysis of variance combined with Tukey's test, *P =0.012 at -120 mV and *P=0.037 at +60 mV.

.

Figure 5.5

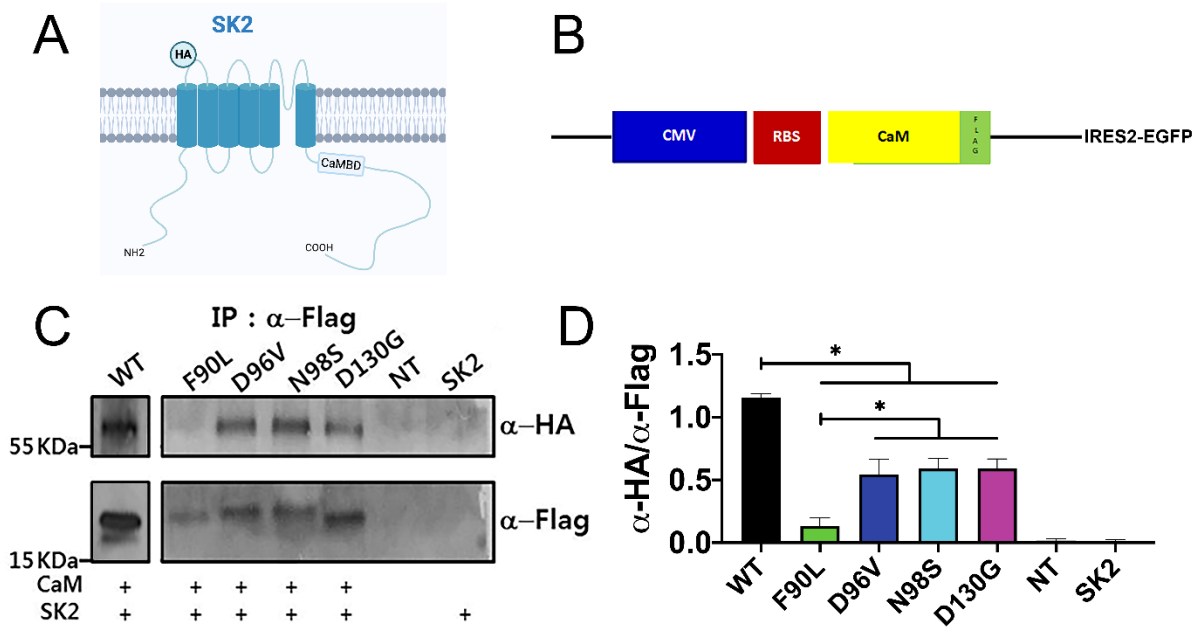

Figure 5.5. Interactions of mutant CaMs with SK2 channels revealed by co-immunoprecipitation assay. A, B. Diagrams depicting SK2 channel subunit with an HA tag in the S1-S2 extracellular loop and CaM with a FLAG tag in the C terminus under the CMV promoter (RBS, ribosome-binding site). **C**, Co-IP using anti-Flag antibody (α-Flag) to pull down SK2 channels identified using anti-HA antibody (α-HA) in the presence of 2 mM EGTA. The right 2 lanes showed the results from non-transfected HEK 293 cells (NT) and cells transfected with SK2 channels only (SK2) as negative controls. **D,** Summary data of the findings in **C**. The background subtracted intensity for SK2 bands using anti-HA antibody was normalized to CaM bands using anti-Flag antibody (NIH ImageJ). Data shown represent mean ± s.e.m (n=3). Statistical analyses were performed using one-way analysis of variance combined with Tukey's test, **P*<0.05 for CaM_{WT} compared to CaM_{F90L}, CaM_{D96V}, CaM_{F98S}, and $CaM_{D130G,}$ and **P*<0.05 for CaM_{F90L} compared to CaM_{D96V}, CaM_{F98S}, and CaM_{D130G} (the *P* values are as follows: CaM_{WT} *vs.* CaM_{F90L},

0.00003; CaM_{WT} *vs.* CaM_{D96V}, 0.002; CaM_{WT} *vs.* CaM_{N98S}, 0.004; CaM_{WT} *vs.* CaM_{D130G}, 0.004; CaM_{F90L} *vs.* CaM_{D96V}, 0.03; CaM_{F90L} *vs.* CaM_{N98S}, 0.02; and CaM_{F90L} *vs.* CaM_{D130G}, 0.02).

Figure 5.6

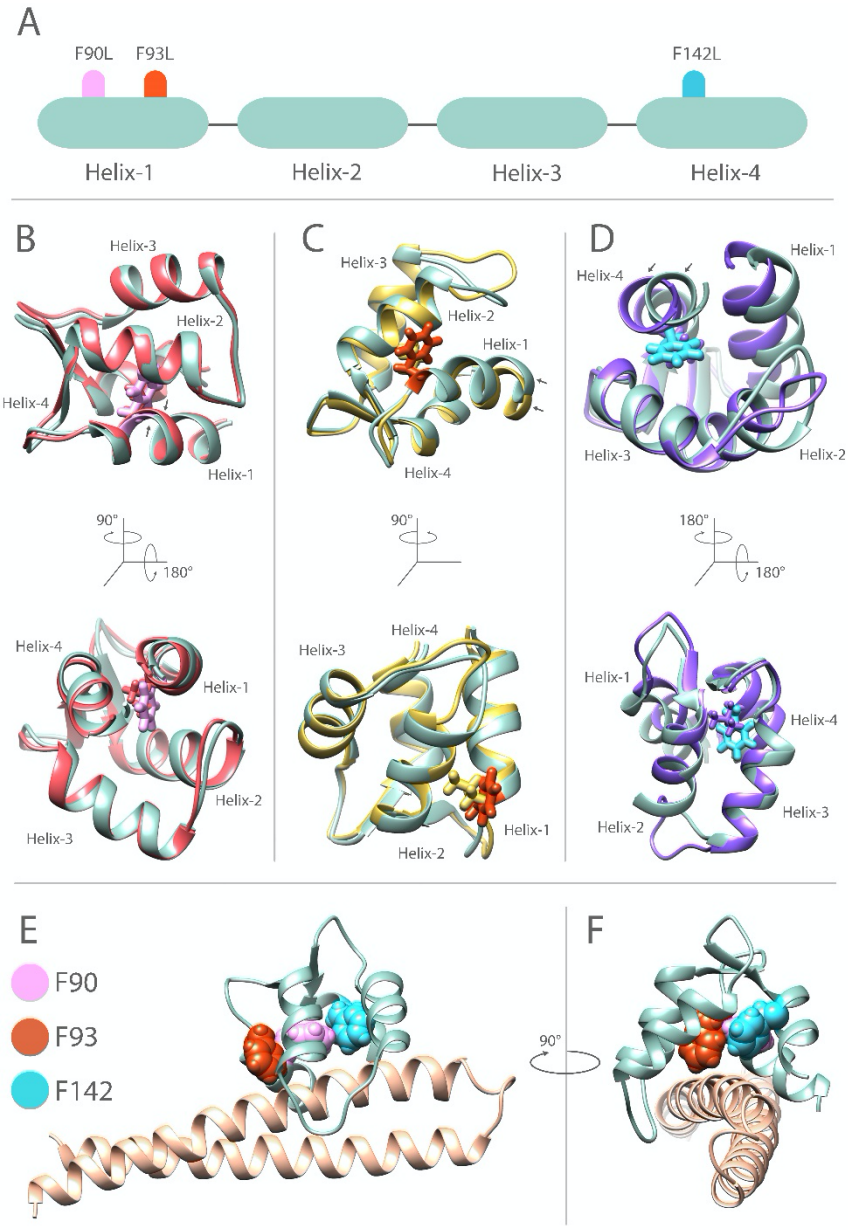

Figure 5.6. Structural modeling of the interactions between CaM mutants and SK2 CaMBD. **A.** Schematic of the 4 α-helices within the C-lobe of CaM. Location of mutations are shown by labels and colored markers. **B-D.** Comparisons of CaM_{WT} (green) and CaM_{F90L} (red, **B**), CaM_{F93L} (yellow, **C**), and CaM_{F142L} (purple, **D**). Side chains of key amino acid residues are shown in stick representation using color scheme shown in panel **A**. Conformational changes due to CaM

mutation are indicated by black arrows in each panel. **E.** C-lobe of apo-CaM_{WT} (colored in green) bound to the C-terminus of *h*SK2 channel (colored in light brown). Side chains of key amino acids are shown using space-filling representation. **F.** Panel E rotated 90 degrees to the left around the Y-axis. Molecular modeling was performed in Ca^{2+} free conditions.

Figure 5.7

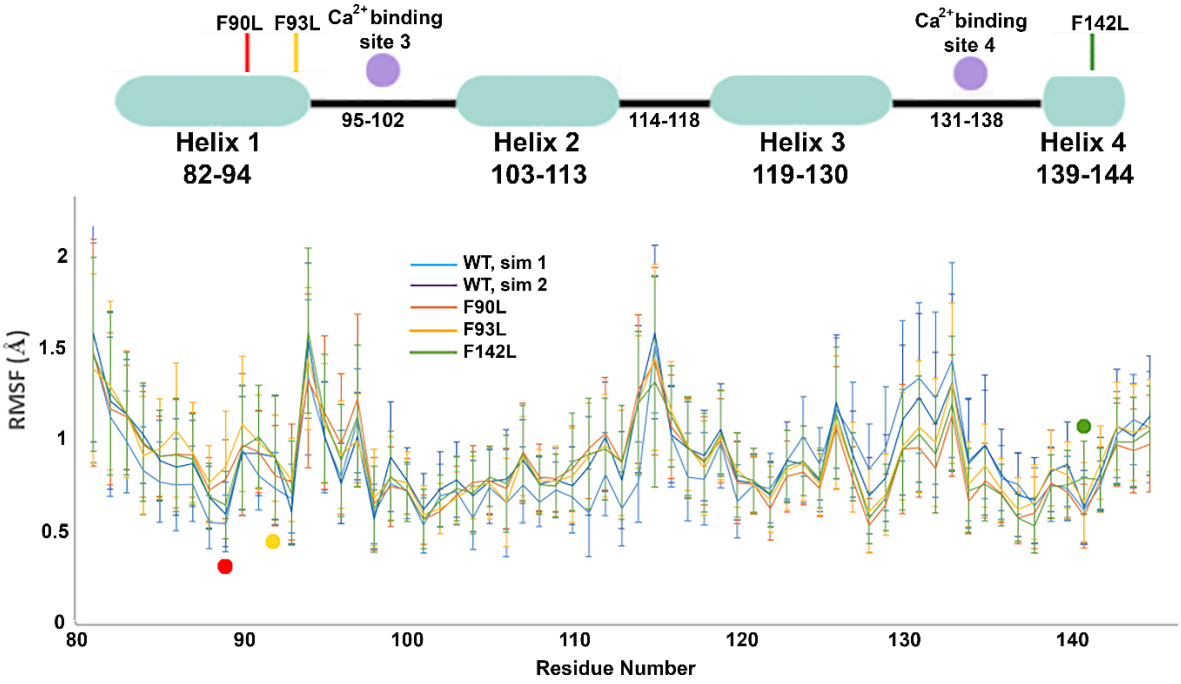

Figure 5.7: Graphs of RMSF showing regional changes in stability. C-lobe of apo-CaM_{WT} is shown in blue (first simulation) and purple (second simulation) while apo-CaM_{F90L}, apo-CaM_{F93L}, and apo-CaM_{F142L} mutants are shown in red, orange, and green, respectively. Diagrams above the graphs depict helices 1-4 from the C-lobe together with amino acid residues and are scaled to match the residue numbering of the graph. Locations of the three mutations are indicated by their respective colored dot on the graph and above the helices. Ca^{2+} binding sites are indicated with purple dots together with the numbers for the amino acid residues. Data shown are mean ± S.D.

Figure 5.8

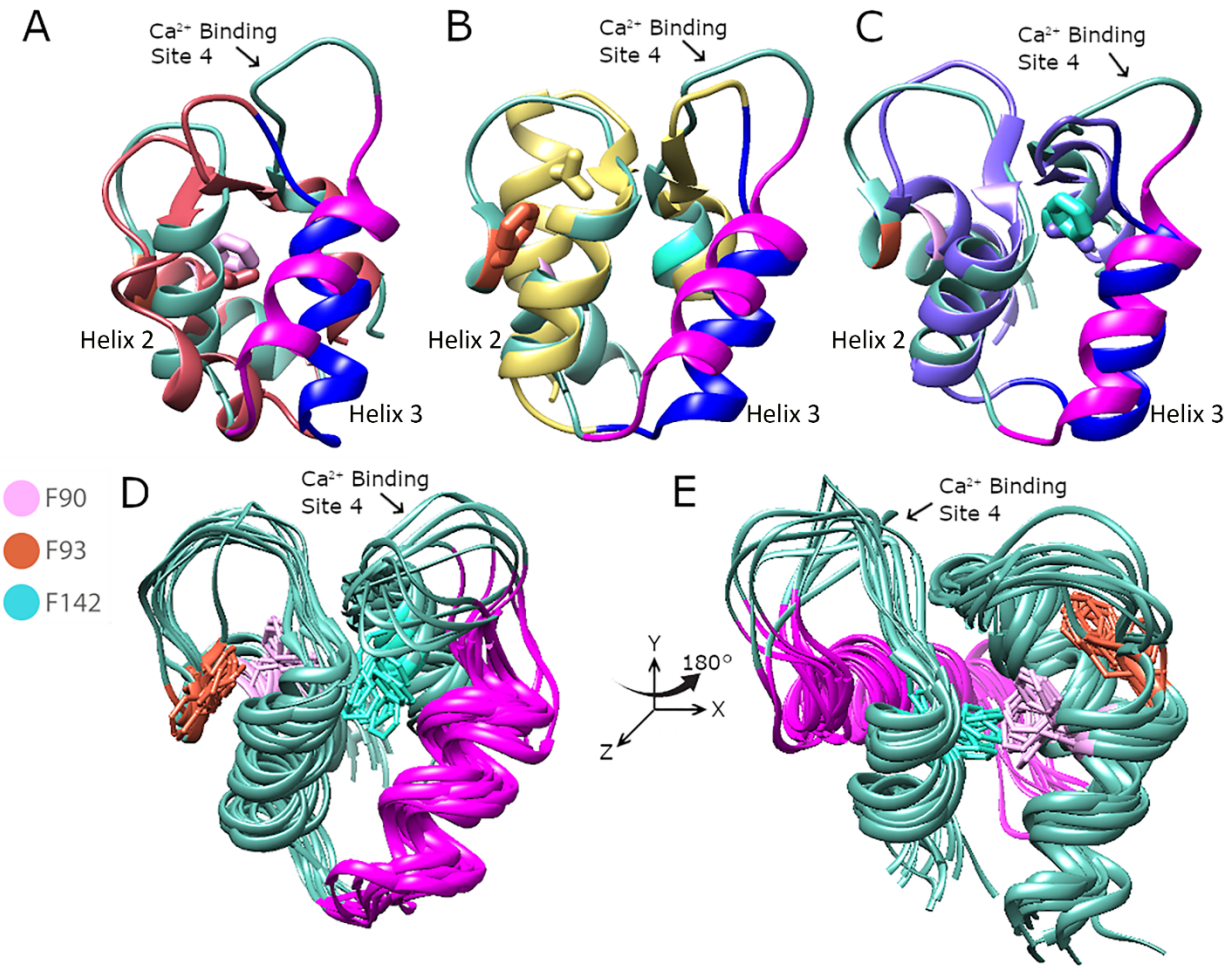

Figure 5.8: Graphical comparison from MD simulations of the C-lobe of apo-CaMs showing conformational changes in mutant CaMs with repacking of helices 2 and 3 with highly flexible Ca^{2+} binding site 4 in apo-CaM_{WT} compared to the CaM mutants confirming the RMSF results. Top clustered models of the C-lobe of apo-CaM_{F90L} (red), apo-CaM_{F93L} (yellow), and apo-CaM_{F142L} (purple) are aligned with apo-CaM_{WT} (green) in panels **A**, **B**, and **C**, respectively. Amino acid side chains of Phe^{90} (pink) and F90L (red) from apo-CaM_{WT} and apo-CaM_{F90L} (in **A**), amino acid side chains of Phe^{93} (red) and F93L (yellow) from apo-CaM_{WT} and apo-CaM_{F93L} (in **B**), and amino acid side chains of Phe^{142} (light blue) and F142L (light purple)

from apo-CaM_{WT} and apo-CaM_{F90L} (in **C**) are shown in ball and stick. Helix 3 from apo-CaM_{WT} (magenta) resides at a larger angle in reference to the Y-axis compared to helices 3 from Phe→Leu mutant CaMs (dark blue) in panels **A**, **B**, and **C** consistent with repacking of the structures. Quantification of the differences between apo-CaM_{WT} and mutant CaMs shown in **A, B** and **C** are summarized in Table 2 in Supplemental Data. **D.** Top ten clustered models of apo-CaM_{WT} aligned to represent an ensemble of possible states. Amino acid representation and color are conserved from panels A-C and legend. Helix 3 is in purple. Helix 3 is mostly in a similar angle in reference to the Y-axis with a much more extreme model present in the distribution. In addition, Ca^{2+} binding site 4 has a wide distribution of states which does not align with those from the mutants (panels **A-C**).

Supplemental Figures

Figure S5.1

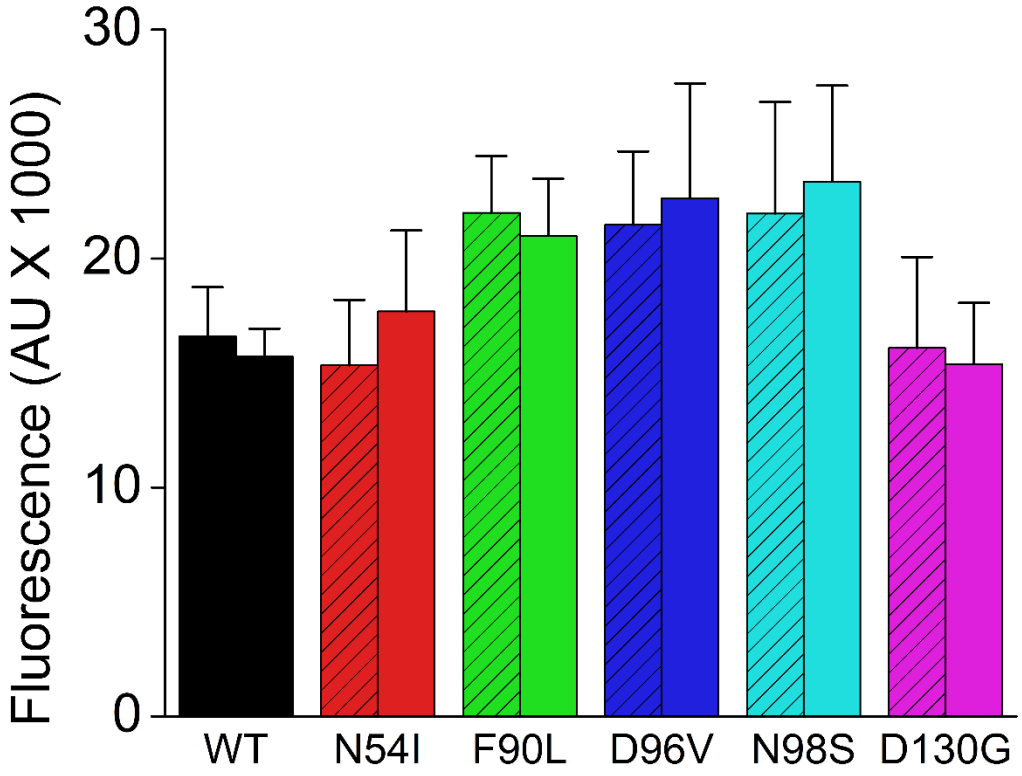

Fig. S5.1. Trafficking of hSK2 channels after co-expression with CaM_{WT} or mutant CaMs. HEK 293 cells expressing SK2 fusion protein with HA tag co-expressed with CaM_{WT} or mutant CaMs (N54I, F90L, D96V, N98S, and D130G) using non-permeabilized (NP) and permeabilized (P) conditions. Summary data showing fluorescence intensity under NP (left bars) and P (right bars) conditions (555 and 633 fluorescent intensity in arbitrary units X 1,000) (n = 15-20 cells, *P*=NS comparing NP vs. P for each group).

Figure S5.2

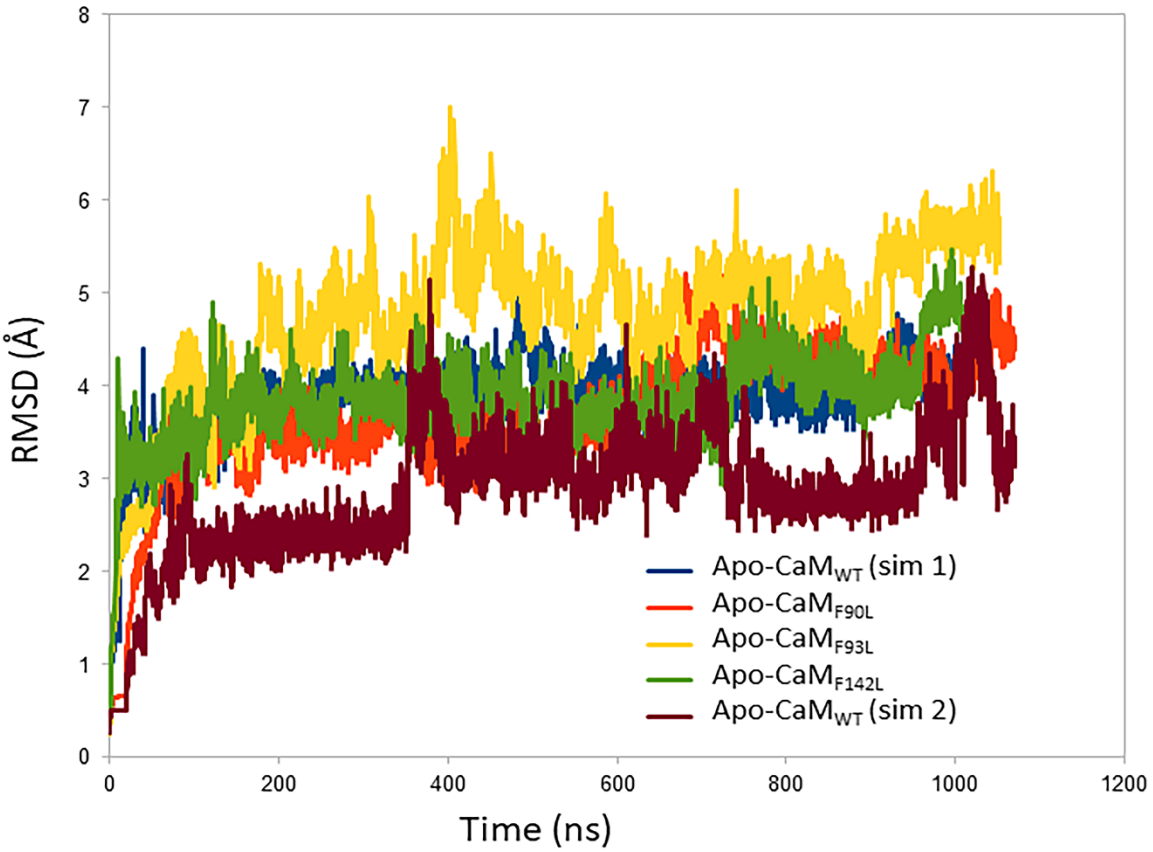

Fig. S5.2: Graphs of RMSD showing stability throughout the production run. RMSD graphs include the equilibration and production stages. The RMSD from the C-lobe of apo-CaM$_{WT}$ (simulation (sim) 1 and 2), apo-CaM$_{F90L}$, apo-CaM$_{F93L}$ and apo-CaM$_{F142L}$ are shown in blue, dark brown, red, yellow, and green, respectively. Runs are slightly different in length due to differences in equilibration time. The total simulation time is the same in all runs (1 μs).

Figure S5.3

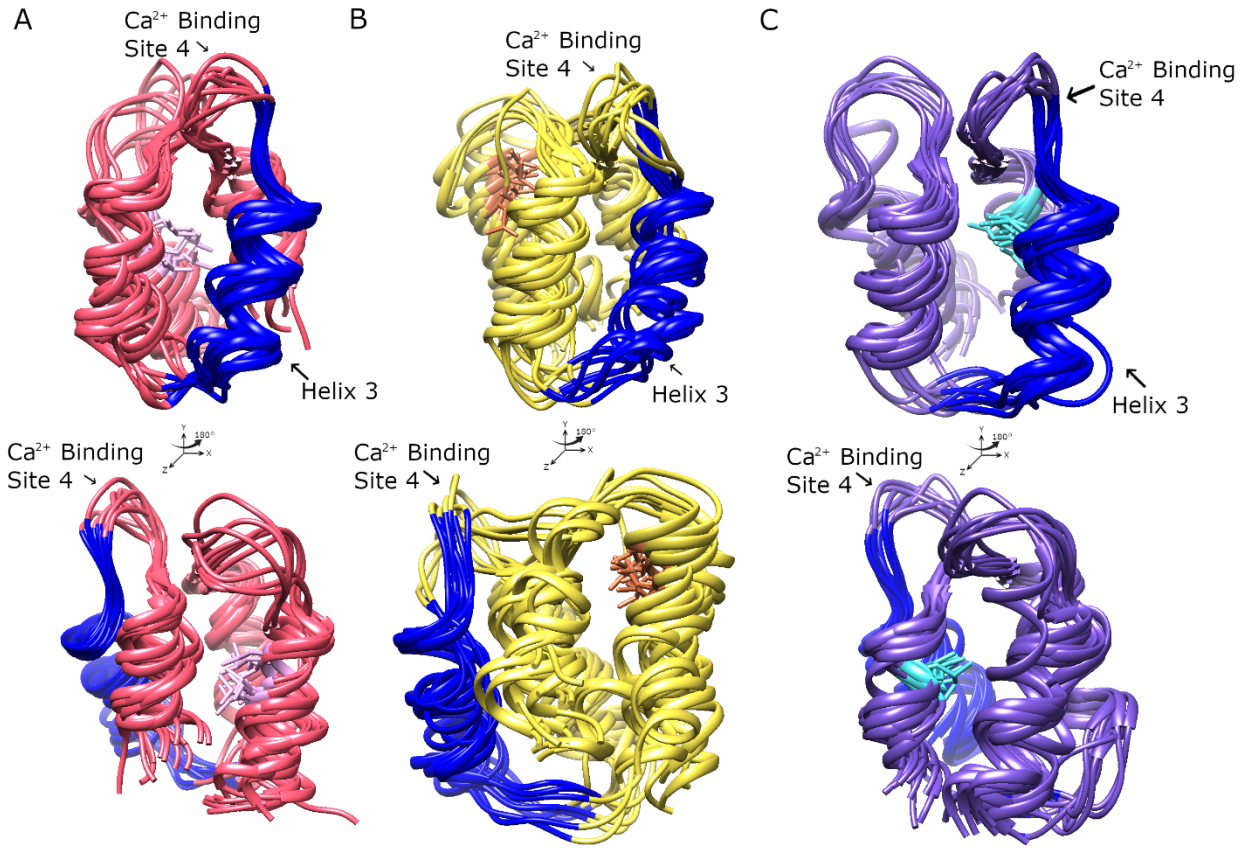

Fig. S5.3: Top ten clustered models of apo-CaM$_{F90L}$, apo-CaM$_{F93L}$, and apo-CaM$_{F142L}$ aligned to represent an ensemble of possible states showing the compact distribution of Helix 3 and Ca^{2+} binding site 4 regions. Ensembles of the aligned top ten clusters of the C-lobe of apo-CaM$_{F90L}$ (A, red), apo-CaM$_{F93L}$ (B, yellow), and apo-CaM$_{F142L}$ (C, purple). Helix 3 is in blue and Ca^{2+} binding site 4 is the loop immediately following Helix 3 and is labeled.

Figure S5.4

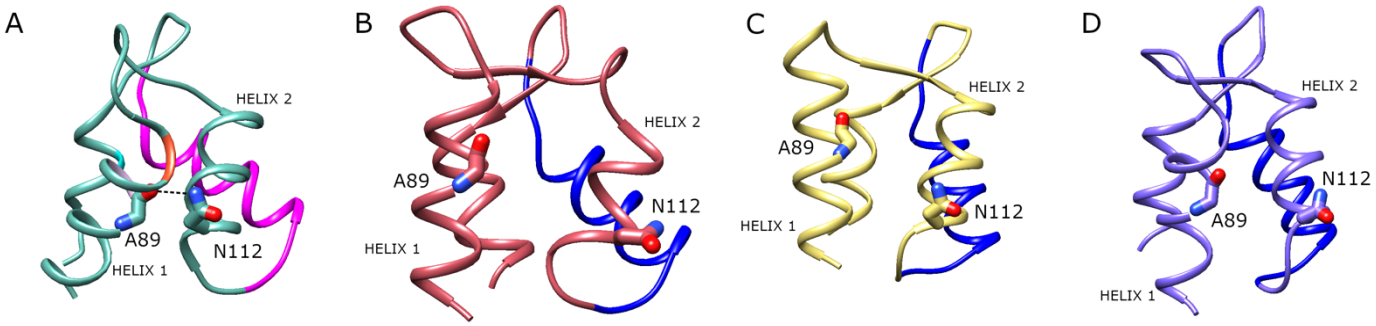

Fig. S5.4: Graphical comparisons from MD simulations of the C-lobe of apo-CaMs showing hydrogen bond in the apo-CaM$_{WT}$. Top clustered models of the C-lobe of apo-CaM$_{WT}$ (green in **A**), apo-CaM$_{F90L}$ (red in **B**), apo-CaM$_{F93L}$ (yellow in **C**), and apo-CaM$_{F142L}$ (purple in **D**), are shown, respectively. Helix 3 from apo-CaM$_{WT}$ is shown in magenta (in **A**) while helices 3 from Phe→Leu mutant CaMs are shown in dark blue in panels **B-D**. The side chain of Asn^{112} on the helix 2 in apo-CaM$_{WT}$ maintains a stable hydrogen bond with the carboxyl oxygen of Ala^{89} residue on the helix 1 during the simulations of the apo-CaM$_{WT}$, which is not observed in the simulations of the CaM mutants.

Figure S5.5

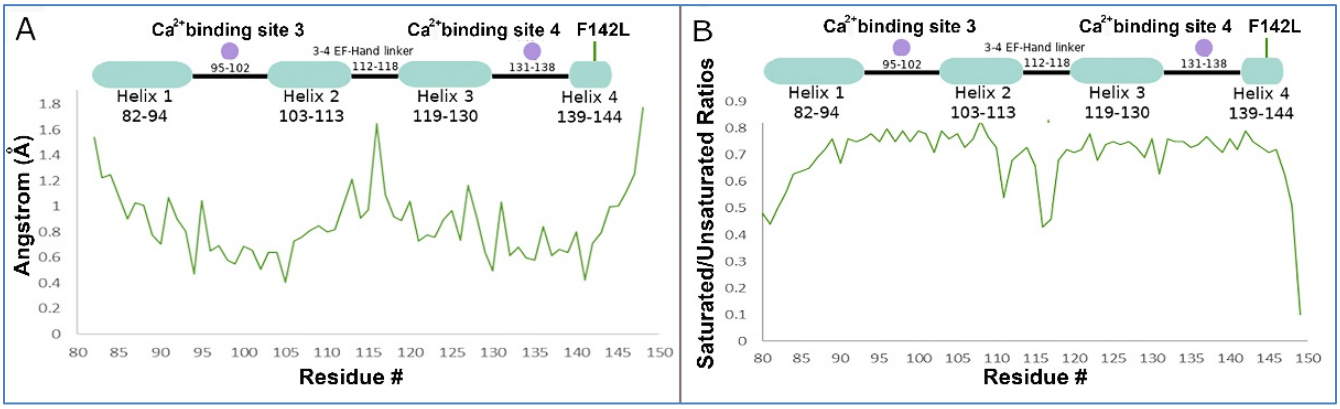

Fig. S5.5. Comparison of RMSF of Ca^{2+}-CaM_{F142L} from MD simulations (A) and N-H heteronuclear NOE saturated/ unsaturated ratio (B, BMRB: 34262) (Wang et al., 2018). There is similar flexibility including identification of the most flexible amino acid being Lys^{116} residue. NOTE: flexibility shown on graphs are inversed with higher values in RMSF and lower values in heteronuclear NOE denoting higher flexibility.

Table 1: Quantification of RMSD. Mean and standard deviations (mean ± S.D.) of RMSD calculated from the production portion of MD, presented in **Figure S5.2**.

Apo-CaM$_{WT}$ Simulation 1	**Apo-CaM$_{WT}$ Simulation 2**	**Apo-CaM$_{F90L}$**	**Apo-CaM$_{F93L}$**	**Apo-CaM$_{F142L}$**
3.9 ± 0.4	3.0 ± 0.5	3.8 ± 0.5	4.9 ± 0.6	3.9 ± 0.4

Table 2: Quantification of the differences in RMSD among WT and mutant CaMs. Data are presented as mean ± S.D., derived from the C terminal domain (residues 81-145) and Ca^{2+} binding site 4 (residues 131-138) as presented in **Figure 5.8**.

	C terminal domain	**Ca^{2+} binding site 4**
WT -> F90L	3.9 ± 3.0	6.8 ± 3.9
WT -> F93L	3.5 ± 2.4	4.1 ± 2.0
WT -> F142L	3.1 ± 2.1	5.2 ± 2.9

CHAPTER 9

Perspectives and Future Directions

9.1 Compartmentalization of AC isoforms in the SAN

Current knowledge gaps exist regarding the dominant AC isoforms and the specific roles of Ca^{2+}-activated and Ca^{2+}-inhibited ACs in the SAN. In contrast to atrial and ventricular myocytes that expressed only Ca^{2+}-inhibited isoforms of ACs, we have identified Ca^{2+}-activated AC_I as the predominant isoform mediating cAMP signaling in SAN, which resides within a functional microdomain with caveolin-3, HCN4, $Ca_v1.2$, and RyR-2. However, aside from AC_I, there are other AC isoforms, including Ca^{2+}-inhibited AC_V and AC_{VI} that are highly expressed in the SAN.

Our group has previously demonstrated that AC_{VI} is localized in the plasma membrane outside the T-tubule in ventricular myocytes. In contrast, AC_V is localized mainly in the T-tubular region, and the direct protein-protein interaction between caveolin-3 with AC_V and phosphodiesterase (PDE) is responsible for the compartmentalization of AC_V signaling.[1] In the current study, we found AC_I is critical in the sustained rise in local cAMP during β-AR stimulation and the actions of AC_I at these functional microdomains are balanced and modulated by the localized effects of PDE3 and 4 that degrade cAMP.

We have performed preliminary study that indicates the significance of Ca^{2+}-inhibited AC_V and AC_{VI} in mediating heart rate regulation. We utilized AC_V and AC_{VI} global knockout mice and performed ECG, action potential recordings, and cAMP-FRET experiments. Ablation of AC_V and AC_{VI} resulted in SAN dysfunction *in vivo*, reduced action potential firing frequencies *in vitro* and compromised cAMP response to β-AR stimulation. The mechanism remains to be explored. AC_I

forms compartmentalization almost exclusively with HCN4 and RyR-2 channels and regulate a subpopulation of L-type Ca^{2+} channels that are localized within caveolae. In contrast, AC_I does not functionally regulate T-type Ca^{2+} channels. Therefore, we hypothesize that different isoforms of ACs may regulate distinct components of the coupled clocks in the SAN, providing the necessary safety factors for the regulation of SAN *via* β-AR signaling. To this end, additional experiments including super resolution imaging and proximity ligation essay, electrophysiology, cAMP FRET experiments, are needed to directly decipher the subcellular microdomains of the Ca^{2+}-activated and Ca^{2+}-inhibited isoforms of ACs with second messengers, PDEs, different ion channels and transporters to determine how the expression and subcellular microdomains contribute to the coupled clocks of SAN. We have previously shown the functional expression of both $Ca_v1.2$ and $Ca_v1.3$ L-type Ca^{2+} channels in SAN.[2] Future studies are required to decipher the functional significance of compartmentalization for different isoforms of Ca^{2+} channels with ACs. Finally, computational studies are needed to further provide critical insights into the interplay between local cAMP concentrations and the functional regulation of SAN.

9.2 SAN dysfunction in heart failure

SAN dysfunction is well documented in patients with heart failure (HF); however, the underlying mechanisms are not fully understood. Our results showed that sinus bradycardia occurred concurrently with the development of HF in a murine model and provided evidence that impairment of mitochondria and their microdomain in the SAN could contribute to SAN dysfunction that occurs during HF.

To achieve a comprehensive understanding of SAN dysfunction in HF, additional approaches are needed. Mass spectrometry-based proteomics technologies allow us to investigate the

architecture of protein and signaling networks without biases.[3] A previous study demonstrated that pacemaking and ion channels are differentially expressed between the sinus node and atrial muscle using proteomics. Importantly, compared to the atria, proteins with higher expression in the sinus node are also enriched for functions related to actin cytoskeleton, contractile fibers, chromatin, neurofilament, carbohydrate metabolism, lipid metabolism, collagen and connective tissue.[4] Therefore, we proposed to take advantage of mass spectrometry-based proteomics to decipher the architecture of protein and signaling networks in chronic pressure-induced HF mouse models in future studies.

The SAN tissue is a highly complex structure with heterogeneous cell types, all of which are likely to contribute to sinus node physiology and pathophysiology. Further studies are needed to evaluate the transcriptome in HF SAN cells. Single-cell RNAseq will provide detailed mechanistic insights into the alterations in connectomics contributing to SAN dysfunction.

In summary, our successive and comprehensive studies have provided critical insights into the intricate and exquisite balance in the regulation of SAN cells and possible therapeutic targets for treatement of SAN dysfunction in diseased hearts.

References

1. Timofeyev V, Myers RE, Kim HJ, Woltz RL, Sirish P, Heiserman JP, Li N, Singapuri A, Tang T, Yarov-Yarovoy V, Yamoah EN, Hammond HK and Chiamvimonvat N. Adenylyl cyclase subtype-specific compartmentalization: differential regulation of L-type Ca2+ current in ventricular myocytes. *Circ Res*. 2013;112:1567-76.

2. Zhang Z, Xu Y, Song H, Rodriguez J, Tuteja D, Namkung Y, Shin HS and Chiamvimonvat N. Functional Roles of $Ca_v1.3$ (α_{1D}) calcium channel in sinoatrial nodes: insight gained using gene-targeted null mutant mice. *Circ Res*. 2002;90:981-7.

3. Boyett M and Lundby A. A New Window onto the Pacemaker of the Heart, the Sinus Node, Provided by Quantitative Proteomics and Single-Nucleus Transcriptomics. *J Cell Immunol*. 2020;2:38-41.

4. Linscheid N, Logantha S, Poulsen PC, Zhang S, Schrolkamp M, Egerod KL, Thompson JJ, Kitmitto A, Galli G, Humphries MJ, Zhang H, Pers TH, Olsen JV, Boyett M and Lundby A. Quantitative proteomics and single-nucleus transcriptomics of the sinus node elucidates the foundation of cardiac pacemaking. *Nat Commun*. 2019;10:2889.